



This is estimated to average 1 hour per response, including the time for reviewing instructions, searching existing data sources, gathering and reviewing the collection of information, sending comments regarding this burden estimate or any other aspect of this collecting this burden to Washington Headquarters Services, Directorate for Information Operations and Reports, 1215 Jefferson and to the Office of Management and Budget, Paperwork Reduction Project (0704-0188), Washington, DC 20503.

1. AGENCY USE ONLY (Leave blank)	2. REPORT DATE 1992	3. REPORT TYPE AND DATES COVERED <del>XXXXXX</del> /DISSERTATION		
4. TITLE AND SUBTITLE Four-Dimensional Data Assimilation of Gale Data Using a Multivariate Analysis Scheme and a Mesoscale Model with Diabatic Initialization		5. FUNDING NUMBERS		
6. AUTHOR(S) Dewey E. Harms, Major		8. PERFORMING ORGANIZATION REPORT NUMBER AFIT/CI/CIA- 92-029D		
7. PERFORMING ORGANIZATION NAME(S) AND ADDRESS(ES) AFIT Student Attending: North Carolina State University		10. SPONSORING / MONITORING AGENCY REPORT NUMBER		
9. SPONSORING / MONITORING AGENCY NAME(S) AND ADDRESS(ES) AFIT/CI Wright-Patterson AFB OH 45433-6583		11. SUPPLEMENTARY NOTES		
12a. DISTRIBUTION / AVAILABILITY STATEMENT Approved for Public Release IAW 190-1 Distribution Unlimited ERNEST A. HAYGOOD, Captain, USAF Executive Officer		12b. DISTRIBUTION CODE		
13. ABSTRACT (Maximum 200 words)				
<div data-bbox="974 1234 1387 1532" data-label="Text"> <p><b>S DTIC ELECTE DEC 08 1992 D</b></p> </div> <div data-bbox="346 1596 644 1670" data-label="Text"> <p><b>92-31037</b></p> </div> <div data-bbox="330 1649 619 1734" data-label="Image"> </div> <div data-bbox="264 1713 446 1766" data-label="Text"> <p>012200</p> </div> <div data-bbox="602 1713 743 1776" data-label="Text"> <p>23988</p> </div>				
14. SUBJECT TERMS		15. NUMBER OF PAGES 219		16. PRICE CODE
17. SECURITY CLASSIFICATION OF REPORT	18. SECURITY CLASSIFICATION OF THIS PAGE	19. SECURITY CLASSIFICATION OF ABSTRACT	20. LIMITATION OF ABSTRACT	

## ABSTRACT

HARMS, DEWEY ELVIN. Four-Dimensional Data Assimilation of GALE Data using a Multivariate Analysis Scheme and a Mesoscale Model with Diabatic Initialization. (Under the direction of Sethu Raman).

A method of assimilating 3-hourly sounding data is developed and successfully tested in this study. First, the successive corrections scheme of Bratseth (1986), which converges to optimum interpolation, is applied for the numerical analysis of data collected during the Genesis of Atlantic Lows Experiment (GALE). Univariate analyses of the mass and wind field are produced. The coupling of the mass and wind field is achieved by further iterations of the geopotential utilizing improving estimates of the geostrophic wind to extrapolate the geopotential to the grid points. The univariate wind analysis is then corrected for the new geostrophic wind.

Next, diabatic forcing is incorporated into a vertical mode initialization scheme to provide more realistic initial conditions and to shorten the spinup time of the Naval Research Laboratory / North Carolina State University (NRL/NCSU) mesoscale model. Latent-heating profiles are computed from 'spun-up' model-generated and observed rainfall. The latent heating is distributed in the vertical according to the cumulus convective parameterization scheme (Kuo scheme) of the model. Compatibility between the specified heating during initialization and the heating during early model integration is retained by merging the model integrated rainfall and heating rates with those rates from the initialization.

Finally, the multivariate, successive correction analysis scheme and the diabatic initialization procedure are combined with the NRL/NCSU model to form an intermittent data-assimilation system. Assimilations of the GALE data over a 2 1/2-day period were performed with differing update cycles of 3, 6, and 12 h. Twelve-hour NMC

hemispheric analyses served as the "no assimilation" control case for comparison. The assimilation of 3-hourly GALE data led to large decreases in background forecast rms errors and smaller decreases in analysis rms error. Better consistency in time was achieved between forecasts and analyses in the assimilation experiments. Rainfall prognoses from the assimilated states verified reasonably well with the observed rainfall and showed much more rapid spinup and better overall patterns than did the "no assimilation" precipitation forecasts.

Accession For	
NTIS CRA&I	<input checked="" type="checkbox"/>
DTIC TAB	<input type="checkbox"/>
Unannounced	<input type="checkbox"/>
Justification .....	
By .....	
Distribution)	
Availability Codes	
Dist	Avail and/or Special
A-1	

**DTIC QUALITY INSPECTED 2**

**FOUR-DIMENSIONAL DATA ASSIMILATION OF GALE DATA  
USING A MULTIVARIATE ANALYSIS SCHEME AND  
A MESOSCALE MODEL WITH DIABATIC INITIALIZATION**

by

**DEWEY E. HARMS**

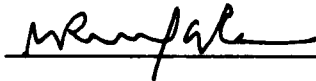
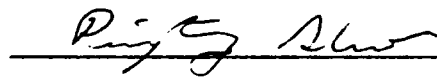
A thesis submitted to the Graduate Faculty of  
North Carolina State University  
in partial fulfillment of the  
requirements for the Degree of  
Doctor of Philosophy

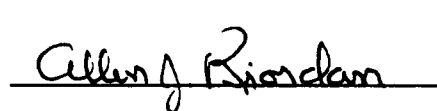
**DEPARTMENT OF MARINE, EARTH AND ATMOSPHERIC SCIENCES**

Raleigh

1992

**APPROVED BY:**

 \_\_\_\_\_  \_\_\_\_\_

 \_\_\_\_\_  \_\_\_\_\_

  
\_\_\_\_\_  
Chairman of Advisory Committee

## DEDICATION

I dedicate my Ph.D. dissertation to my wife and best friend, Sherilyn Mae (Carver) Harms. Her patience and encouragement to me have made this document possible. I also dedicate this work to my wonderful sons, Jeremy and Jared, who, besides the Lord Jesus Christ, are the joy of my life.

## BIOGRAPHY

Dewey Elvin Harms was born in Summerdale, Alabama on May 6, 1954. He was reared in the same community and graduated from Foley Senior High School, Foley, Alabama in 1972. In 1975, he received an Associate of Arts degree in Mathematics from Faulkner State Junior College, Bay Minette, Alabama. Two years later he enlisted in the United States Air Force (USAF).

He entered North Carolina State University (NCSU) in May of 1979 and received a Bachelor of Science degree with a major in Meteorology in August of 1980. Shortly afterwards, in November, he was commissioned as a second lieutenant in the USAF. The author held the position of Weather Support Unit Officer at the Eighth Air Force Headquarters, Barksdale Air Force Base, Louisiana. In August of 1983, he entered the Graduate School at NCSU and earned a Master of Science degree in Meteorology in May of 1985.

After a tour of duty as an environmental simulation analyst at the USAF Environmental Technical Applications Center at Scott Air Force, Illinois, he served as Commander of Detachment 19, 31st Weather Squadron at Incirlik Air Base, Turkey. Then, in January of 1990, the author again entered the Graduate School at NCSU and began studies toward the Degree of Doctor of Philosophy in Meteorology.

The author is married to the former Sherilyn Mae Carver and has two sons, Jeremy and Jared. The author's parents, Reverends Ronald and Marie Harms, are both living and still reside in Summerdale, Alabama.

## ACKNOWLEDGEMENTS

I would like to express my thanks and appreciation to the United States Air Force and, in particular, the Air Force Institute of Technology and Air Weather Service for their financial and moral support. I also thank Dr. Sethu Raman, the Chairman of my Advisory Committee, for his aid and advice in the preparation of this dissertation. Appreciation is also extended to Dr. Gerald Watson, Dr. Allen Riordan, and Dr. Ping-Tung Shaw for their assistance. I especially thank Dr. Rao Madala and Dr. Keith Sashegyi for sharing their knowledge and providing excellent guidance during the course of my research. I also thank my dear friends, Rob and Kathi Blevins, for their hospitality in sharing their home with me during my frequent visits to the Naval Research Laboratory, Washington, D.C. This work was partially supported by the Division of Atmospheric Sciences, National Science Foundation under Grant ATM-88-01650.

Finally, my deepest thanks and gratitude goes to my wife, Sherilyn, for her strength and caring during the past 2 1/2 years, to my sons, Jeremy and Jared, and to my parents and friends for their prayers and continued support, without which this study would not have been possible.

## TABLE OF CONTENTS

	Page
LIST OF TABLES.....	viii
LIST OF FIGURES.....	ix
LIST OF SYMBOLS.....	xv
1. INTRODUCTION.....	1
2. LITERATURE REVIEW OF DATA ASSIMILATION.....	4
2.1 Introduction.....	4
2.2 Quality Control.....	9
2.3 Objective Analysis Techniques.....	11
2.4 Initialization Techniques.....	15
2.5 Various Data-Assimilation Methods.....	23
2.6 Comparison of Operational Assimilation Techniques.....	29
2.7 FDDA Research: Implications and the Future.....	33
3. NRL/NCSU MESOSCALE MODEL.....	36
3.1 Dynamics of the Model.....	36
3.2 Numerics of the Model.....	39
3.2.1 Split-Explicit Time Integration.....	42
3.2.2 Lateral Boundary Conditions.....	43
3.3 Physics of the Model.....	44
3.3.1 Planetary Boundary Layer.....	44
3.3.2 Horizontal Diffusion.....	45
3.3.3 Cumulus Convection.....	46
3.3.4 Large-Scale Precipitation.....	47
3.3.5 Dry Convective Adjustment.....	48
3.3.6 Surface Parameters.....	49
3.4 Model Initialization.....	49

4. APPLICATION OF THE BRATSETH SCHEME FOR THE ANALYSIS OF GALE DATA.....	53
4.1 Introduction.....	53
4.2 The NRL/NCSU Objective Analysis Scheme.....	56
4.2.1 Data Preparation and Quality Control.....	57
4.2.2 Analysis Interpolation.....	62
4.3 Testing the Analysis Scheme.....	71
4.3.1 Experimental Design.....	72
4.3.2 The Synoptic Situation.....	74
4.4 Results.....	77
4.4.1 Comparisons of 25/12Z Analyses.....	77
4.4.2 Comparisons of Model Forecasts (25/12Z - 26/12Z).....	87
4.4.3 Comparisons using 26/00Z and 26/12Z Cases.....	102
4.5 Summary.....	122
5. DIABATIC INITIALIZATION EXPERIMENTS WITH CONVECTIVE HEATING.....	124
5.1 Introduction.....	124
5.2 Diabatic Heating in Model Initialization.....	126
5.3 Experimental Design.....	130
5.4 Results.....	131
5.4.1 Comparison of Initialized Vertical Velocity.....	131
5.4.2 Forecast Precipitation Comparisons.....	134
5.5 Summary.....	135
6. IMPACT OF ASSIMILATING 3-HOURLY GALE DATA.....	139
6.1 Introduction.....	139
6.2 The Data Assimilation System.....	142
6.3 Experimental Design.....	145
6.4 Results.....	153
6.4.1 Statistical Evaluation and Discussion.....	153

	vii
6.4.2 Subjective Evaluation and Discussion.....	164
7. CONCLUSIONS.....	204
8. LIST OF REFERENCES.....	208

**LIST OF TABLES**

<b>Table</b>		<b>Page</b>
4.1	Standard deviation of the observational errors and forecast error growth for a 6-h forecast period in parentheses.....	60
4.2	Analysis and forecast test cases.....	73
6.1	Average number of observations, before and after quality control and creation of super observations, in each analysis time window.....	149
6.2	Data-assimilation experiments.....	151
6.3	Standard deviation of the observational errors and updated forecast error growth for a 6-h forecast period in parentheses.....	162

## LIST OF FIGURES

Figure		Page
2.1	Successive reduction of wind error using a direct insertion of height data in a barotropic model. Corresponding results using height as well as from the derived geostrophic winds (McPherson 1975).....	8
2.2	Surface pressures for individual grid points for first 12 h of prognosis using an uninitialized analysis, after initializing two vertical modes, and after initializing two vertical modes using Dirichlet boundary conditions and Neumann boundary conditions (Bourke and McGregor 1983).....	18
2.3	Time trace of height field with no initialization and after two iterations of the implicit nonlinear normal mode initialization scheme (Temperton 1988).....	20
2.4	Gravity-wave activity (before and after initialization) for five vertical modes of a baroclinic model (Sugi 1986).....	21
2.5	Intermittent data assimilation using an analysis-forecast cycle (Bengtsson 1975a).....	24
2.6	A schematic of the assimilation-forecast cycle for various experiments (Ramamurthy and Carr 1987).....	30
3.1	Model domain with smoothed model topography for the coarse (outer) grid and the GALE (fine) grid.....	40
3.2	Horizontal staggered C-grid and vertical grid network utilized in the model for the simple case of $K = 2$ .....	41
4.1	The location of the data for the geopotential height at 500 mb and the sea level pressure (SLP) after quality control.....	63

4.2	The rms of the differences between the observation estimate (and the analysis value interpolated to the observation point) and the observation value for the geopotential at 500 mb.....	67
4.3	SLP and 1000-mb temperature and winds at 25/12Z, 26/12Z, and 27/12Z, and 500-mb geopotential, temperature, and winds at 25/12Z from the NMC analysis.....	75
4.4	SLP and 1000-mb temperature and winds and 500-mb geopotential, temperature, and winds at 25/12Z from case 4.1 and NRL analysis.....	78
4.5	250-mb geopotential, temperature, and winds at 25/12Z from case 4.1, NRL analysis, and NMC analysis.....	81
4.6	500-mb absolute vorticity and vertical motion at 25/12Z from case 4.1 and the NRL analysis.....	84
4.7	500-mb absolute vorticity and vertical motion at 25/12Z from the NMC analysis.....	86
4.8	The magnitude of the wind normal to CS1 and CS2 at 25/12Z for the NRL analysis.....	88
4.9	Ageostrophic circulation in CS1 at 25/12Z for NRL and NMC analyses....	89
4.10	Ageostrophic circulation and relative humidity in CS2 at 25/12Z for NRL and NMC analyses.....	90
4.11	Six-hour forecast of SLP, surface air temperature, and 1000-mb winds valid at 25/18Z for cases 4.4 and 4.3.....	93
4.12	GALE analysis of SLP deviation (from 1000 mb), surface temperature and wind for 25/18Z by Bosart (1988).....	94

4.13	Six-hour forecast of 500-mb vertical motion at 25/18Z for cases 4.3 and 4.4.....	95
4.14	Twelve-hour forecast of SLP and 1000-mb temperature and winds, and forecast of 6-h precipitation valid at 26/00Z for cases 4.3 and 4.4.....	96
4.15	Six-hour accumulation of observed precipitation valid at 26/00Z.....	99
4.16	Twelve-hour forecast of ageostrophic circulation and relative humidity in CS2 valid at 26/00Z for cases 4.3 and 4.4.....	100
4.17	SLP and 1000-mb temperature and winds from case 4.4 and NRL analysis and 500-mb absolute vorticity from from NMC and NRL analyses at 26/00Z.....	103
4.18	Wind normal to and relative humidity in CS2 for the NRL analysis and ageostrophic circulation in CS2 for NRL and NMC analyses at 26/00Z.....	105
4.19	Forecast precipitation (26/00Z - 26/06Z) for cases 4.5 and 4.6 and observed precipitation (26/00Z - 26/06Z).....	108
4.20	Twelve-hour forecast of SLP and 1000-mb temperature and winds and 250-mb geopotential, temperature, and winds at 26/12Z from case 4.5 and forecast precipitation (26/06Z - 26/12Z) for cases 4.5 and 4.6.....	110
4.21	Twelve-hour forecast for case 4.5 of wind normal to and ageostrophic circulation in CS3 and CS4 valid at 26/12Z.....	112
4.22	SLP and 1000-mb temperature and winds; 250-mb geopotential, temperature, and winds; and 500-mb absolute vorticity and vertical motion from NRL analysis at 26/12Z.....	115
4.23	Wind normal to and ageostrophic circulation in CS3 and CS4 from NRL analysis valid at 26/12Z.....	117

4.24	SLP and 1000-mb temperature and winds for a 12-h forecast valid at 27/00Z and a 24-h forecast valid at 27/12Z for case 4.7.....	119
4.25	12- and 24-h forecasts for case 4.7 of wind normal to and ageostrophic circulation in CS5 and CS6, respectively.....	120
5.1	Vertical motion fields for 500 mb valid at 27/00Z from 12-h forecast of case 5.1, after DVMI (case 5.2), and after AVMI (case 5.3).....	132
5.2	Forecasts of accumulated total precipitation (26/00Z - 26/06Z) originating from DVMI and AVMI.....	136
6.1	The locations of surface and upper-air data at 26/00Z and 26/03Z.....	147
6.2	Average analysis and background-forecast rms errors for geopotential from the 0000 and 1200 UTC update cycles.....	154
6.3	Average analysis and background-forecast rms errors for geopotential from the 0600 and 1800 UTC update cycles.....	156
6.4	Average analysis and background-forecast rms errors for u- wind component from the 0000 and 1200 UTC update cycles.....	157
6.5	Average analysis and background-forecast rms errors for v- wind component from the 0000 and 1200 UTC update cycles.....	158
6.6	Average analysis and background-forecast rms errors for relative humidity component from the 0000 and 1200 UTC update cycles.....	159
6.7	Average analysis and background-forecast rms errors for geopotential from the all update cycles of 06DI and 06AI.....	160
6.8	Average analysis and background-forecast rms errors for geopotential from 03DI for 03/15, 06/18, 09/21, and 12/00Z updates cycles.....	163

6.9	SLP, 1000-mb temperature and wind analyses at 25/12Z from control and 12DI.....	166
6.10	GALE analysis of sea-level pressure deviation (from 1000 mb), surface temperature and wind for 25/12Z by Bosart (1988).....	167
6.11	1000-mb specific humidity analyses at 25/12Z from control and 12DI.....	168
6.12	500-mb relative humidity analyses at 26/00Z from control, 12DI, 06DI, and 06AI.....	169
6.13	500-mb vertical velocity analyses at 26/00Z from control, 12DI, 06DI, and 06AI.....	172
6.14	Wind normal to CS2 at 26/00Z from control and 12DI.....	174
6.15	Ageostrophic circulation in CS2 at 26/00Z from control and 12DI.....	175
6.16	SLP, 1000-mb temperature and wind analyses at 27/00Z from 03DI and control, and at 27/03Z from 03DI.....	178
6.17	Wind normal to CS7 at 27/00Z from 03DI; ageostrophic circulation at 27/00Z from 03DI and control, and at 27/03Z from 03DI.....	180
6.18	SLP, 1000-mb temperature and wind analyses at 27/12Z from control and 03DI.....	183
6.19	Ageostrophic circulation in CS6 at 27/12Z from control and 03DI.....	184
6.20	Six-hour forecasts of SLP, surface air temperature, and 1000-mb winds valid at 26/06Z from control, 12DI, and 06DI.....	185
6.21	Same as Fig. 10, but for 26/06Z.....	188

6.22	Forecasts of precipitation (26/00Z - 26/06Z) from control, 06DI, and 06AI; and observed precipitation (26/00Z - 26/06Z).....	189
6.23	Forecasts of precipitation (26/06Z - 26/12Z) from control, 12DI, and 06DI; and observed precipitation (26/06Z - 26/12Z).....	191
6.24	Forecasts of precipitation (26/12Z - 26/18Z) from control, 12DI, and 06DI; and observed precipitation (26/12Z - 26/18Z).....	194
6.25	Six-hour forecasts of SLP and 1000-mb temperature and winds valid at 26/18Z from control, 12DI, 06DI, and 03DI.....	196
6.26	Forecasts of precipitation (26/12Z - 26/18Z) from control, 12DI, and 06DI (forecast start time of 26/12Z); and observed precipitation.....	199
6.27	12- and 24-h forecasts of SLP and 1000-mb temperature and wind valid at 27/00Z and 27/12Z, respectively, from control and 03DI.....	201

## LIST OF SYMBOLS

$\alpha_{ij}$	analysis weight for the observational estimate
$\alpha_{xj}$	analysis weight for the interpolated grid point value
$c$	geostrophy factor
$c_p$	specific heat at constant pressure for dry air [ $\text{J kg}^{-1} \text{K}^{-1}$ ]
$D$	mass divergence [ $\text{kg m}^{-1} \text{s}^{-3}$ ]
$\tilde{D}$	vertically integrated mass divergence [ $\text{kg m}^{-1} \text{s}^{-3}$ ]
$D_c$	vertically averaged moistening rate [ $\text{kg s}^{-5}$ ]
$d$	correlation length scale [m]
$E$	moisture flux [ $\text{kg m}^{-2} \text{s}^{-1}$ ]
$\varepsilon^2$	ratio of observation error variance to forecast error variance
$f$	Coriolis parameter [ $\text{s}^{-1}$ ]
$F$	forcing terms representing physical processes
$\Phi$	generalized geopotential [m]
$\phi$	geopotential [m]
$\phi_s$	surface geopotential [m]
$\phi^*$	average geopotential on a sigma surface [m]
$g$	acceleration of gravity [ $\text{m s}^{-2}$ ]
$h_x$	map factor for horizontal x coordinate
$h_y$	map factor for horizontal y coordinate
$H$	sensible heat flux [ $\text{K kg m}^{-2} \text{s}^{-1}$ ]
$H_s$	surface sensible heat flux [ $\text{K kg m}^{-2} \text{s}^{-1}$ ]
$K_H$	diffusion coefficient [ $\text{m}^2 \text{s}^{-1}$ ]
$\kappa$	ratio ( $\kappa = R/c_p$ )
$L_c$	latent heat of condensation [ $\text{J kg}^{-1}$ ]

$\lambda_k$	square of phase speed of the the free gravity modes [ $\text{m}^2 \text{s}^{-2}$ ]
$M$	horizontal moisture convergence [ $\text{kg m}^{-1} \text{s}^{-3}$ ]
$M_t$	total horizontal moisture convergence [ $\text{kg m}^{-1} \text{s}^{-3}$ ]
$m_j$	local data density
$P_c$	convective precipitation [cm]
$P_L$	large-scale non-convective precipitation [cm]
$p$	atmospheric pressure [ $\text{kg m}^{-1} \text{s}^{-2}$ ]
$p_o$	standard reference level of 1000 mb
$p_s$	surface pressure [ $\text{kg m}^{-1} \text{s}^{-2}$ ]
$q$	specific humidity [ $\text{kg kg}^{-1}$ ]
$q_s$	saturation specific humidity [ $\text{kg kg}^{-1}$ ]
$Q_c$	vertically averaged heating rate [ $\text{K kg s}^{-5}$ ]
$R$	gas constant for dry air [ $\text{J kg}^{-1} \text{K}^{-1}$ ]
$R_v$	gas constant for water vapor [ $\text{J kg}^{-1} \text{K}^{-1}$ ]
$r_m$	vertically averaged relative humidity
$\rho$	correlation function for observed and model variables
$\sigma$	vertical coordinate following terrain
$\dot{\sigma}$	vertical motion in terrain-following coordinate [ $\text{mb h}^{-1}$ ]
$\zeta$	mass-weighted vorticity [ $\text{kg m}^{-1} \text{s}^{-3}$ ]
$T$	temperature [K]
$T^*$	mean temperature varying only in vertical [K]
$t$	time coordinate [s]
$\Delta t$	integration time interval [s]
$\tau$	wind stress [ $\text{kg m}^{-1} \text{s}^{-2}$ ]
$\tau_s$	surface wind stress [ $\text{kg m}^{-1} \text{s}^{-2}$ ]
$\theta$	potential temperature [K]

$u$	east-west horizontal component of wind [ $\text{m s}^{-1}$ ]
$u_g$	east-west geostrophic wind component [ $\text{m s}^{-1}$ ]
$v$	north-south horizontal component of wind [ $\text{m s}^{-1}$ ]
$v_g$	north-south geostrophic wind component [ $\text{m s}^{-1}$ ]
$\vec{V}$	velocity vector [ $\text{m s}^{-1}$ ]
$\mu$	fixed non-dimensional diffusion coefficient
$\nu$	analysis iteration
$x$	east-west spatial coordinate [m]
$\Delta x$	grid interval distance in x-coordinate [m]
$\chi$	velocity potential [ $\text{kg m s}^{-3}$ ]
$y$	north-south spatial coordinate [m]
$\Delta y$	grid interval distance in y-coordinate [m]
$\Psi$	streamfunction [ $\text{kg m s}^{-3}$ ]

## 1. INTRODUCTION

Four-dimensional data assimilation, in the context of numerical weather prediction, is the process of specifying initial conditions for the integration of a numerical forecast model. In this process, new observational data are merged, using some analysis procedure, with the ongoing integration of the prediction model. Data analysis and model prediction, along with model initialization, make up the major components of the data-assimilation process. A short-range model forecast serves as a first guess for the subsequent analysis.

The overall purpose of this research is to develop a method of data assimilation, which includes a cost-effective multivariate analysis scheme, accounts for diabatic effects *in the model initialization*, and uses a fine-resolution mesoscale model, in order to produce improved analyses of mesoscale circulations and then more reliable forecasts of coastal frontogenesis/cyclogenesis and associated precipitation. The goal here is also to investigate the impact of assimilating high-frequency observational data using a mesoscale model. To achieve this goal, the following objectives were required: 1) develop and test a computationally efficient, multivariate objective analysis scheme, 2) shorten model spinup by including diabatic heating in the initialization procedure, and 3) combine these components with a mesoscale numerical model to form an intermittent data-assimilation system and then evaluate the results.

Four-dimensional data-assimilation methods, along with the most commonly used objective analysis and initialization techniques, are examined from a historical perspective in Chapter 2. Operational techniques, including intermittent data assimilation and Newtonian nudging, and next-generation methods (Kalman-Bucy filtering and the adjoint method) are briefly described. Several methods are compared, with primary emphasis

being placed on recent papers dealing with the operational assimilation techniques. Ongoing and future research is outlined, and some important implications of this research are discussed. Following this extensive literature review, the NRL/NCSU Limited-Area Numerical Weather Prediction Model (referred to hereafter as the NRL/NCSU mesoscale model) is described in Chapter 3. This model, which was developed jointly by the U.S. Naval Research Laboratory (NRL) and North Carolina State University (NCSU), is used throughout the course of this research. The description includes the model's dynamics, numerics, physics, and vertical mode initialization procedure.

In Chapter 4, the successive correction scheme of Bratseth (1986) is applied for the multivariate analysis of data collected during the Genesis of Atlantic Lows Experiment (GALE), which was conducted over the southeastern U.S. during the winter of 1986. The newly-developed multivariate analysis interpolation procedure is described in detail, and the utility of the analysis scheme is measured. After univariate analyses of the mass and wind fields are produced, the coupling of these fields is achieved through additional iterations of the geopotential, utilizing improved estimates of the geostrophic wind to extrapolate the geopotential to the grid points. The wind analysis is then corrected for the new geostrophic wind. This study revealed that the objective analysis scheme successfully resolved mesoscale structures and significantly improved the absolute vorticity and vertical velocity fields.

Diabatic forcing from convective heating, as applied in the model initialization procedure, is discussed in Chapter 5. Latent-heating profiles are computed from 'spun-up' model-generated and observed rainfall. The latent heating is distributed in the vertical according to the cumulus convective parameterization scheme (Kuo scheme) of the model. Compatibility between the specified heating during initialization and the heating during early model integration is retained by merging the model integrated rainfall and

heating rates with those rates from the initialization. The inclusion of convective heating in the model initialization substantially reduced the spinup of model rainfall.

In Chapter 6, the multivariate, successive correction analysis and the diabatic initialization components are combined with a mesoscale numerical weather prediction model to form an intermittent data-assimilation system. A thorough evaluation of the assimilation system was performed using GALE data. Finally, a summary and major conclusions are presented in Chapter 7.

## 2. LITERATURE REVIEW OF DATA ASSIMILATION

### 2.1 Introduction

Two major motivations for using data assimilation exist: as an analysis/diagnostic/research tool and for operational weather forecasting. Data assimilation has been applied not only in meteorology (air pollution and planetary boundary layer studies, forecast case studies, quantitative assessment of new observing systems, among others), but also in oceanography for describing ocean currents (Ghil 1989; Robinson 1986). To summarize all relevant work pertaining to data assimilation is indeed a difficult task because the contents are spread so widely. The purpose of this review is only to provide an overview of *four-dimensional data assimilation with primary emphasis on assimilation methods currently useful for operational weather forecasting*. To make this review more complete, attention has also been given to the state-of-the-art or "next-generation" techniques, but to a lesser extent. Excellent reviews covering the early days of data assimilation research in both simulation and real-data studies are available in the literature. The interested reader is referred to Bengtsson (1975a), McPherson (1975), Hollingsworth (1986), and Bourke et al. (1985). Plus, a comprehensive history of data analysis and assimilation is given by Daley (1991), whereas a more abbreviated examination of data assimilation techniques is rendered by Harms et al. (1992b).

Numerical weather prediction (NWP) has classically been viewed as an initial-value problem where the governing equations of geophysical fluid dynamics are integrated forward in time from a set of initial values. The quality of NWP is strongly dependent on the accuracy of specifying these initial conditions and on the ability to model mathematically the dynamics and physical processes of the atmosphere. In a

pioneering paper, Charney et al. (1969) suggested combining past and current data in a numerical model such that the model's equations provide time continuity and dynamic coupling among the atmospheric fields. This concept, which has merged objective numerical analysis and numerical weather prediction, has become known as four-dimensional data assimilation (FDDA) and has proven to be a major advance in NWP during the past 20 years.

What inspired this major advance, or in other words, what spurred this development of data assimilation? The advent of meteorological satellites in the 1960s raised the possibility that nearly continuous atmospheric temperature observations would be available on a global basis. However, these space-based observing systems measure only radiance (or temperature) distributed in space and time, rather than at fixed locations and times. In order to fully utilize this new source of data, the numerical weather prediction techniques had to be adjusted. Beginning with Charney et al. (1969), Smagorinsky et al. (1970), Rutherford (1972), and Morel and Talagrand (1974), research progressed in reconstructing unobserved variables from the observed variables through the numerical model's dynamical coupling between those variables. By combining information about the state of the atmosphere, earlier observations are carried forward to provide an independent source of information to be added to the newly acquired observations.

Morel (1981) further illustrated why data assimilation is essential in NWP by listing five key reasons: 1) the inadequate distribution (spatial gaps) of the twice-daily upper-air sounding data, 2) the discrepancy between the conventional observations as point measurements and the true volume averages required by numerical models, 3) the inherently synoptic character of remote observations obtained from sunsynchronous orbiting satellites, 4) the inadequate vertical resolution of remote observations of cloud motions from geostationary satellites, and 5) the significant random and systematic

errors involved in the data processing required for reconstructing atmospheric fields from remotely measured physical quantities. He concluded that any weather prediction model must be initialized by merging the new observations with the currently estimated meteorological fields, computed on the basis of earlier observations, while taking into account the dynamical constraints between successive model states, specified by the governing dynamical equations.

This process of merging new observational data with the ongoing integration of a numerical forecasting model is known as "data assimilation" or, equivalently, "four-dimensional data assimilation" in consideration of the time-space distribution of the data base. Then, as stated by Warner (1987), "the overall objective of the assimilation process is to provide the best possible initial state from which to begin a forecast, where the term "best" implies an appropriate balance as well as reflects optimal use of four-dimensional data (*synoptic as well as asynoptic*) to define the structures on all scales at the initial time."

In the past 20 years, many techniques have been developed to insert data into dynamic models. However, the first data-assimilation experiments were simplistic and of limited success. The observation simply replaced the model forecast value at the model grid point nearest the observation location (Jastrow and Halem 1970). This technique, known as direct insertion, is inadequate from the initialization point of view (Bengtsson 1975b). Direct insertion shocks the system and generates large-amplitude waves, or gravitational oscillations. For example, if observations of the mass field are inserted into a primitive equation model, an imbalance is created between the mass and wind fields. When the model integration is resumed, this imbalance is manifested as large-amplitude gravitational oscillations; this is the model's attempt to restore the dynamic balance which was disrupted by the data insertion. Techniques such as damping time integration schemes and time filters were developed to dampen these non-meteorological waves.

However, this damping must be rather strong and can be harmful to the meteorological modes. Bengtsson (1975b) stated that the shock effect will be reduced if locally analyzed data (interpolating the observation to several nearby grid points) are inserted into the model instead of observations only (indirect insertion). For example, applying a local multivariate analysis, or correspondingly, relating wind and geopotential by the geostrophic relation and inserting both height and winds simultaneously proved successful by speeding the updating considerably (see Fig. 2.1). The multivariate procedure mentioned here produces a simultaneous weighting of mass and motion observations, subject to the constraint of geostrophy (Petersen 1968; Eddy 1973; Daley and Puri 1980).

Of the several FDDA methods that have been investigated over the last two decades, some have been implemented operationally while others have not yet been used or are in the developmental stage. In the 1970s, regional/mesoscale weather forecasting models were developed, normal mode initialization was introduced, and global data assimilation became operational. With the advent of mesoscale modeling, FDDA applications are also geared toward the mesoscale, with the emphasis shifting from applications on the global scale.

In operational numerical prediction systems, FDDA can be categorized into two broad areas: continuous methods and intermittent (analysis-forecast cycle) methods. The former refers to the insertion of data into a model as it is received, in a temporally continuous fashion. The analysis-forecast cycle clearly illustrates the four components of data assimilation: quality control, objective analysis, initialization, and an initial guess from a short-range forecast. With this method, the data are assimilated intermittently at specified intervals. So-called next-generation data-assimilation methods are being researched today, with the two most prevalent being the adjoint method based on the variations of calculus and the Kalman-Bucy filter technique.

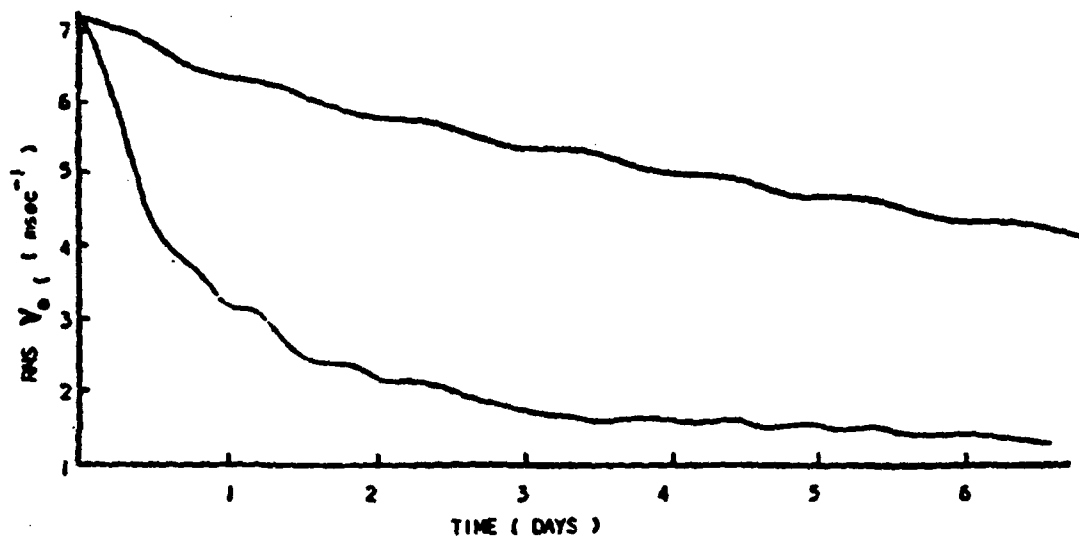


Figure 2.1. Successive reduction of wind error using a direct insertion (upper curve) of height data in a barotropic model. Corresponding results using height as well as from the derived geostrophic winds (lower curve) (McPherson 1975).

Since quality control, objective analysis, and initialization are intricate parts of data assimilation, it is appropriate to consider each of these components in the present discussion. Quality-control methods and the most commonly used objective analysis and initialization techniques are overviewed, followed by a discussion of various data-assimilation methods. Then, two studies, comparing operational data-assimilation techniques, are reviewed, and some important implications of FDDA and ongoing and future research in data assimilation are outlined.

## 2.2 Quality Control

Quality control is an integral part of a data-assimilation system. Quality-control algorithms are designed to modify or reject erroneous meteorological data. Following Daley (1991), observational data errors can be classified into two groups: natural error and gross (or rough) error. The natural error includes instrument error and error of representativeness. The data describe the behavior of the instrument itself, not the behavior of the meteorological parameter it is intended to measure. Every instrument is approximate by its very nature. Errors of representativeness are deviations caused by small-scale perturbations and are also referred to as micrometeorological errors. Gross errors originate from improperly calibrated or malfunctioning instruments, incorrect registration of observations, incorrect coding of observations, and telecommunication errors. These errors (natural and gross) can be either random or spatially or temporally correlated, and there can be systematic biases. The systematic errors can result from improper calibration of an instrument or from the influence of some persistent factor that is not accounted for or is accounted for inaccurately.

Several quality-control techniques are used routinely to screen bad data. These techniques can be divided into four major categories (following Gandin 1988). The first

two, plausibility check and check for contradictions, are used to identify gross errors based on the physical reasonableness of the data. Plausibility checks are the most widely used quality-control methods. These checks analyze each datum independently of other data. A simple plausibility check is one that rejects data values that can never occur in reality--for example, positive temperatures ( $^{\circ}\text{C}$ ) at 300 mb. Other versions compare the datum with the climatological mean or with a background field (numerical forecast). If the deviation is too large, the datum may be rejected. The check for contradictions is based on an analysis of two or more parameters at the same point. An example is the occurrence of rain in the absence of clouds.

The remaining quality-control procedures include checks that rely on some common information and redundancy between observations. The spatial continuity (or consistency) check compares a datum with data at adjacent locations. This method, also known as the buddy check, demands spatial consistency among the data. A temporal continuity check can also be made in which temporal continuity is required with past observations. Finally, checks using dynamic relations such as the geostrophic or hydrostatic relation can be used to check geopotential height with temperature and mass with wind. These checks require the data to obey the dynamic relation at least approximately, otherwise the data are suspected or rejected.

The necessity for including automated quality control in operational NWP was recognized during the early era of NWP. Significant advances have been made in quality control, including the development of methods using optimum interpolation (Rutherford 1976; Lorenc et al. 1977; Lorenc 1981). Recent advances include the complex quality-control method of Gandin (1988) and the Bayesian approach of Lorenc and Hammon (1988). Reviews on various quality control methods have been authored by Belousov et al. (1968), Gustavsson (1981), and Lorenc (1985).

### 2.3 Objective Analysis Techniques

Objective analysis (the second major component of FDDA) and quality control have become intertwined and, as a result, the data-assimilation process is more internally consistent. Excellent reviews on objective analysis have been presented by McPherson (1976) and Gustavsson (1981). The present discussion contains a synopsis of selected topics from these two reviews. According to McPherson (1976), objective analysis is a process in which meteorological observations distributed in space and time are combined with forecasts from previous analyses and perhaps with climatology to form a numerical representation of the state of the atmosphere. This representation takes the form of values of the meteorological variables at regularly spaced grid points subject to various mathematical and physical constraints.

The objective analysis process consists of three subprocesses which are essential for the overall success or effectiveness of the FDDA system: 1) filtering of small amplitude random and systematic errors; 2) interpolation to a regular network of grid points or, in the case of spectral analysis, integration of the representing mathematical space functions over the irregularly spaced observations; and 3) forced adjustment of the meteorological variables using dynamic relationships among these variables.

Within a relatively short period of time, objective (numerical) analysis schemes were independently developed by several meteorologists. Panofsky (1949) devised the first objective analysis method--polynomial interpolation, or the so-called surface-fitting type. An extension of this method was developed by Gilchrist and Cressman (1954) and became the first operational objective analysis. In this technique, mathematical (polynomial) functions are adjusted to observed data in the close vicinity of the grid point, for which analyzed values are required. The adjustment or fit is obtained by a least squares technique. The polynomial method is nonlinear since nonlinear functions are

used to approximate the variation of the analyzed variable. However, the resulting analyzed value at the grid point is a linear function of the observed data and, in this respect, this method is similar to the other analysis methods that will be described.

Bergthorsson and Döös (1955) introduced the successive correction method, and a similar method was devised by Cressman (1959). Cressman's successive correction technique essentially replaced the polynomial interpolation method because the latter produced unreasonable analyses at the edge of data-rich and data-sparse areas. In the successive correction technique, a forecast model provides the preliminary estimate (first guess) of the field to be analyzed. The basic idea of the method is to correct this preliminary field iteratively during several analysis "scans"; the results of one scan become the first guess for the next scan. The estimate is modified by a combination of corrections computed for each grid point. The corrections, which are proportional to the difference between the observed and first guess values, are weighted empirically with observations nearest the grid point weighted the most heavily.

By using a short-range forecast based on a previous analysis as the first guess, the effect of past data is allowed to influence the analysis and thereby contributes to the temporal continuity and spatial coherence of the analysis. For many years, successive correction methods were most widely used in operational forecast centers.

This early dominance of the successive correction methods was taken over during the last decade by statistical (optimal) interpolation schemes, which were originally introduced by Eliassen (1954) and Gandin (1963). Statistical interpolation was also studied extensively by Alaka and Elvander (1972) and Phillips (1976). This analysis technique is based on statistical linear regression and provides a systematic framework for blending observations of differing error characteristics with recent predictions or climatology. More accurate data receive more weight in the analysis. As in the successive correction method, the analyzed value at the grid point is the sum of the first

guess and a linear combination of corrections, which are proportional to the difference between observational and first guess values. The weighting coefficients are determined from the condition that the mean-square-error of the analyzed values be minimum, and they depend on the spatial covariances among the analyzed variables. This method is, in principle, spatially coherent and, like its counterpart of successive correction, incorporates temporal continuity through the use of a short-range forecast from the preceding analysis as a first guess.

The polynomial interpolation method mentioned earlier reappeared in the British Meteorological Office analysis (Dixon et al. 1972) and in the spectral analysis method devised by Flattery (1971). In the spectral analysis technique, mathematical functions are globally adjusted to fit observed data. One additional analysis method that has been utilized in the FDDA context (see discussion in section 5) is the variational technique introduced by Sasaki (1958). This method is a post-analysis adjustment technique based on the calculus of variations and is very effective in making the analyzed fields compatible with a forecast model. A functional is used, which minimizes the analyzed-minus-observed difference, filters undesirable high-frequency and high-wavenumber features, and employs dynamical constraints. These constraints may be strong (satisfied exactly) or weak (satisfied approximately).

Over the past 30 years, numerous variations of these different objective-analysis methods have been developed. Some versions are hybrids belonging to more than one of the aforementioned techniques.

According to McPherson (1976), objective analysis methods used in operational meteorology can be divided into two basic categories. The first represents an analyzed field as a series expansion (spectral analysis):

$$Z_g = a_1 f_1 + a_2 f_2 + \dots + a_m f_m \quad 2.1$$

where  $Z_g$  represents the departure of the field from its mean value. The  $f_i$  represents a set of orthogonal functions--for example, a cosine series. The analysis procedure involves determining the time-dependent coefficients  $a_i$  which make the series expansion best fit the observed data by, for example, a least-squares technique. Analysis methods of this type are in operational use at the National Meteorological Center (NMC) (Flattery 1971; Hayden 1976) and the United Kingdom Meteorological Office (UKMO) (Dixon 1976).

The second basic method, called the "gridpoint" method, includes statistical interpolation and successive correction techniques. Here, the analyzed value  $Z_g^a$  at a discrete point  $g$  is given by a linear combination of observations that are nearby in time and space:

$$Z_g^a = a_1 Z_1^o + a_2 Z_2^o + \dots + a_n Z_n^o \quad 2.2$$

where  $Z^o$  represents observed values at the several stations within some predetermined influence radius of point  $g$ , and the coefficients  $a_i$  determine the influence of each observation on the analyzed value. In this case, the analysis involves determining the coefficients  $a_i$  in the linear combination for each point of the analysis grid.

Two forms of representation are associated with these two basic methods of analysis: the discrete form and the spectral form. In the former, the analysis is a set of values at discrete points in space and time; in the latter, the analysis is represented by a series expansion such as Eq. 2.1. The spectral form has been used primarily for global and hemispheric applications. The discrete form has been extensively used for limited-area applications in mesoscale meteorology.

## 2.4 Initialization Techniques

The objective-analysis methods described in the previous section generally do not provide balanced mass and wind fields to initiate a forecast. Uncompensated errors in wind and pressure-temperature observations, interpolation of observations to model grids, and the numerical model's inability to exactly describe the atmosphere are the primary sources of this dynamical inconsistency. The dynamical imbalances in the initial data lead to the generation of spurious inertia-gravity-wave oscillations, or "meteorological noise." Primitive equation models, unlike geostrophic models, admit these higher-frequency gravity-wave solutions that can have amplitudes much greater than their counterpart in the real atmosphere. These gravity wave oscillations can obscure the lower-frequency Rossby-mode component of the model, which constitutes the meteorological signal. Early numerical modelers called attention to the need to eliminate the spurious high-frequency oscillations, which can compromise the forecast procedure. First of all, these fast-moving gravity waves require short computational time steps; second, they can seriously interfere with very short-range forecasts (<12 h); and third, they can impair vertical motion and, hence, precipitation forecasts (Daley 1981). Therefore, a long-standing approach has been to eliminate or effectively reduce the amplitude of these fast-moving inertia-gravity waves at initial forecast time. This process is known as model initialization. Charney (from unpublished letter to Phillip Thompson, 12 February 1947) provided insight for rectifying this initialization problem by suggesting that one should modify the initial state or modify the governing equations; that is, use filtered models.

The first and simplest approach was to exclude any possibility of the high-frequency oscillations by using a "filtered system" such as the balance equations which simply reduce the model dynamics to the quasi-geostrophic response. However, this

approach severely restricts the model dynamics, which results in very poor forecasts beyond 24 hours. The so-called primitive equations account for more atmospheric dynamics and can yield much better forecasts, so they are generally used. However, the primitive equations do allow the amplification of fast-moving gravity waves which requires some modification of the initial conditions to achieve the desired dynamical balance.

Over the years, many initialization methods have been developed. A summary of the more widely used techniques are presented here. For a more detailed review, the reader is referred to Daley (1991). In static initialization, the data are adjusted at a single time level to conform to some dynamical constraints. That is, certain time derivatives are identified as vanishing in order to eliminate or reduce the generation of inertia-gravity wave noise. In the conventional static initialization, a standard practice is to first analyze the geopotential field using pressure-height data and use wind observations to estimate the gradient of the geopotential using the geostrophic relation. The analyzed geopotential fields on pressure surfaces are then used in the mass balance equation to obtain the streamfunction of the nondivergent wind, from which the rotational wind component can be computed. A major limitation in using the balance equation to determine a rotational wind for initializing a primitive equation model is that the lack of a divergent wind component insures the presence of gravitational modes (Haltiner and Williams 1980).

The most common approach of initialization in intermittent FDDA is normal mode initialization, which achieves dynamical balance using the normal modes of the linearized dynamical equations. The direct use of normal modes was introduced by Dickinson and Williamson (1972). They proposed that the amplitudes of the unwanted, fast-moving modes be set to zero. Their method was effective in suppressing the spurious noise in linear models, but failed in the nonlinear case. A nonlinear normal mode scheme was independently developed by Machenhauer (1977) and Baer (1977). In nonlinear normal

mode initialization, the tendency of the unwanted modes are set to zero, versus setting the amplitude of these modes to zero. The solution of the nonlinear equation requires an iterative process. Unfortunately, this nonlinear scheme, without the inclusion of diabatic effects, suppressed the meridional circulation in the tropics. Puri and Bourke (1982) used the idea that the tropical divergent circulations driven by convection influence mainly the low frequency gravity modes. Therefore, they excluded these low frequency modes from the initialization using a frequency cutoff. Wergen (1982) introduced another method in which average diabatic heating is obtained by integrating the model for a few time steps prior to initialization. This model-produced diabatic heating is then included in the nonlinear forcing in the iterative process.

In global models, (Andersen 1977; Daley 1979; Temperton and Williamson 1981; for example), after the normal modes of the model are computed, the high-frequency inertia-gravity waves can be removed by projecting the inertial wind and mass fields onto these normal modes. However, in limited-area models it is not possible to define the horizontal structure of the normal modes.

Bourke and McGregor (1983) introduced a method of initializing a limited-area model without explicitly computing horizontal normal modes. In this technique, termed vertical mode initialization, the free modes of oscillation of the prediction model are identified by linearizing the equations about a basic state of rest. This linearization permits a simple decomposing of the three-dimensional eigenvalue problem into a series of two dimensional problems. The vertical decomposing leads to a number of characteristic vertical modes, one corresponding to each discrete level in the model. Balance conditions on the horizontal structure equations are then derived for each vertical mode. Filtering conditions, in which the tendencies of divergence and ageostrophic vorticity are set to zero, are applied to derive linear diagnostic equations for the mass and divergence fields. In Fig. 2.2, from Bourke and McGregor (1983), graphs of surface

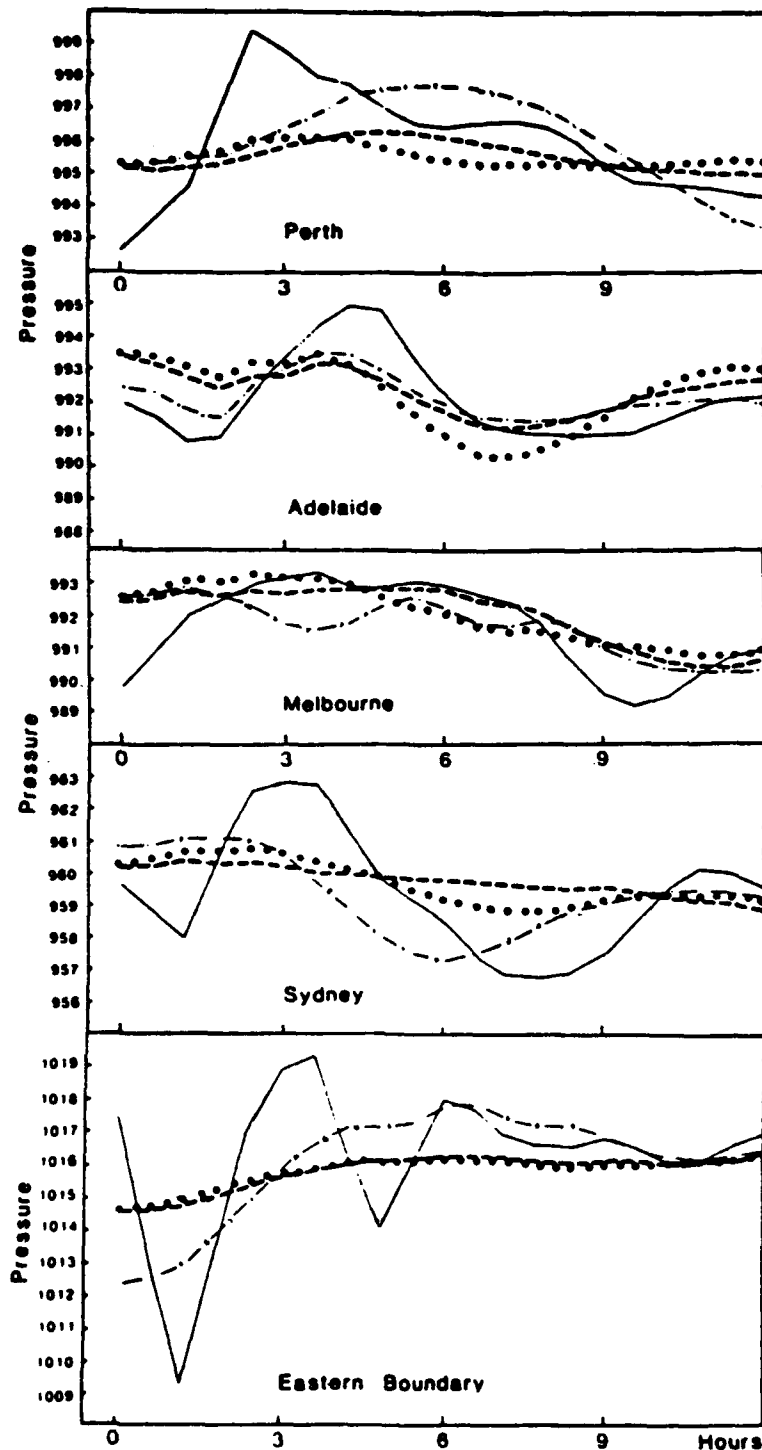


Figure 2.2. Surface pressures (mb) for individual grid points for the first 12 h of prognosis using an uninitialized analysis (solid curves), after initializing two vertical modes (dot-dash), and after initializing two vertical modes (dashes--using Dirichlet boundary conditions and dots--using Neumann boundary conditions) (Bourke and McGregor 1983).

pressure before and after initialization using the Australian regional primitive equation model are shown. It is obvious that the initialization procedure successfully removed noise from the integrations.

Temperton (1988) devised a method of applying Machenhauer's criterion without requiring the computation of the coefficients of the individual modes. Figure 2.3 (from Temperton 1988) shows graphs of 500-mb geopotential before and after the application of Temperton's implicit normal mode initialization for the Canadian finite-element model. This method is also successful in removing the high-frequency noise.

Although appropriate for intermittent FDDA, the normal mode initialization is a distinct, separate step from the objective analysis and usually leads to changes in model parameters. As a result, the initialized analysis may no longer fit the observations as closely as desired. An alternative, known as dynamic initialization, has the advantage of *avoiding the complications of computing normal modes*. In this method, which was introduced by Miyakoda and Moyer (1968), observations are inserted (intermittently or continuously) over a period of time. The method has the added advantage of simplicity and can balance physical processes as well as the mass and wind fields. In dynamic initialization, the model equations were integrated forward and backward through time under controls that encourage time derivatives to become small compared to spatial derivatives, which in turn selectively dampened the high-frequency components of the solutions. Early versions of this technique required several repetitions of the integration cycle to successfully reduce the gravity-wave oscillations and, as a result, these schemes were computationally expensive. Another disadvantage was that the slow modes of the model were dampened.

More recently, researchers including Bratseth (1982), Sugi (1986), and Satomura (1988) have developed schemes which are more computationally efficient and have more selective damping properties. Figure 2.4 (from Sugi 1986) depicts graphs of the gravity-

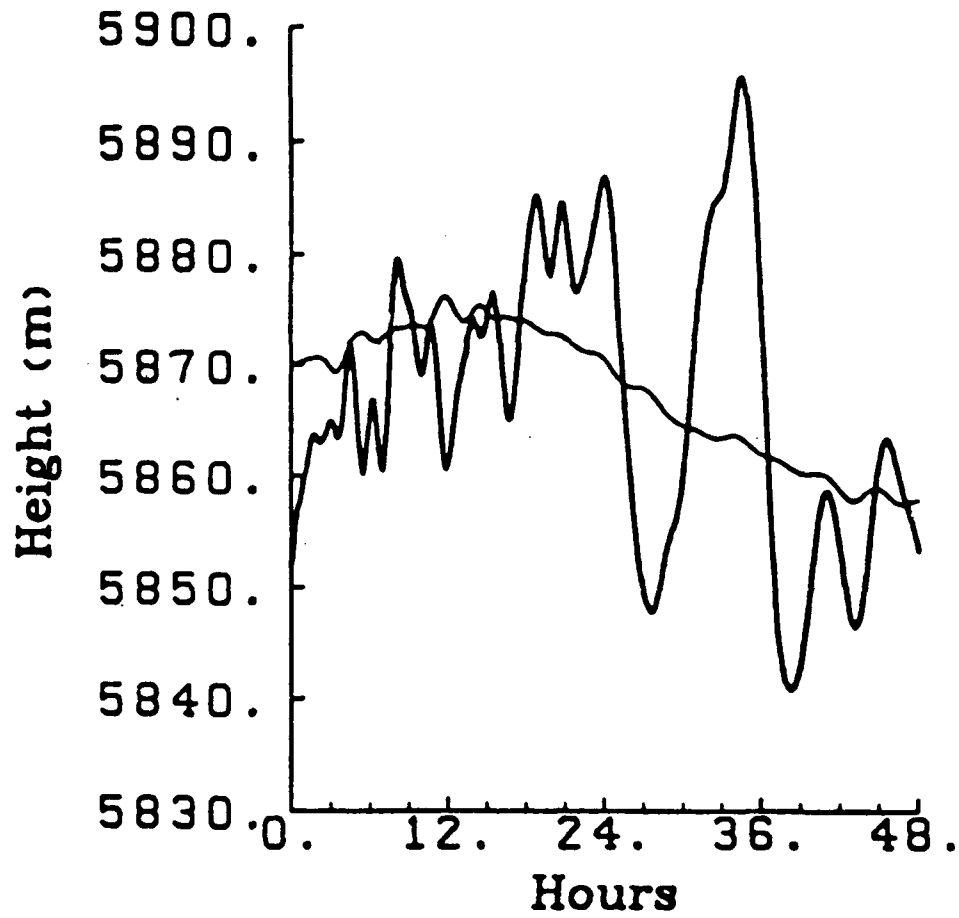


Figure 2.3. Time trace of height field. Heavy line: no initialization. Light line: after two iterations of the implicit nonlinear normal mode initialization scheme (Temperton 1988).

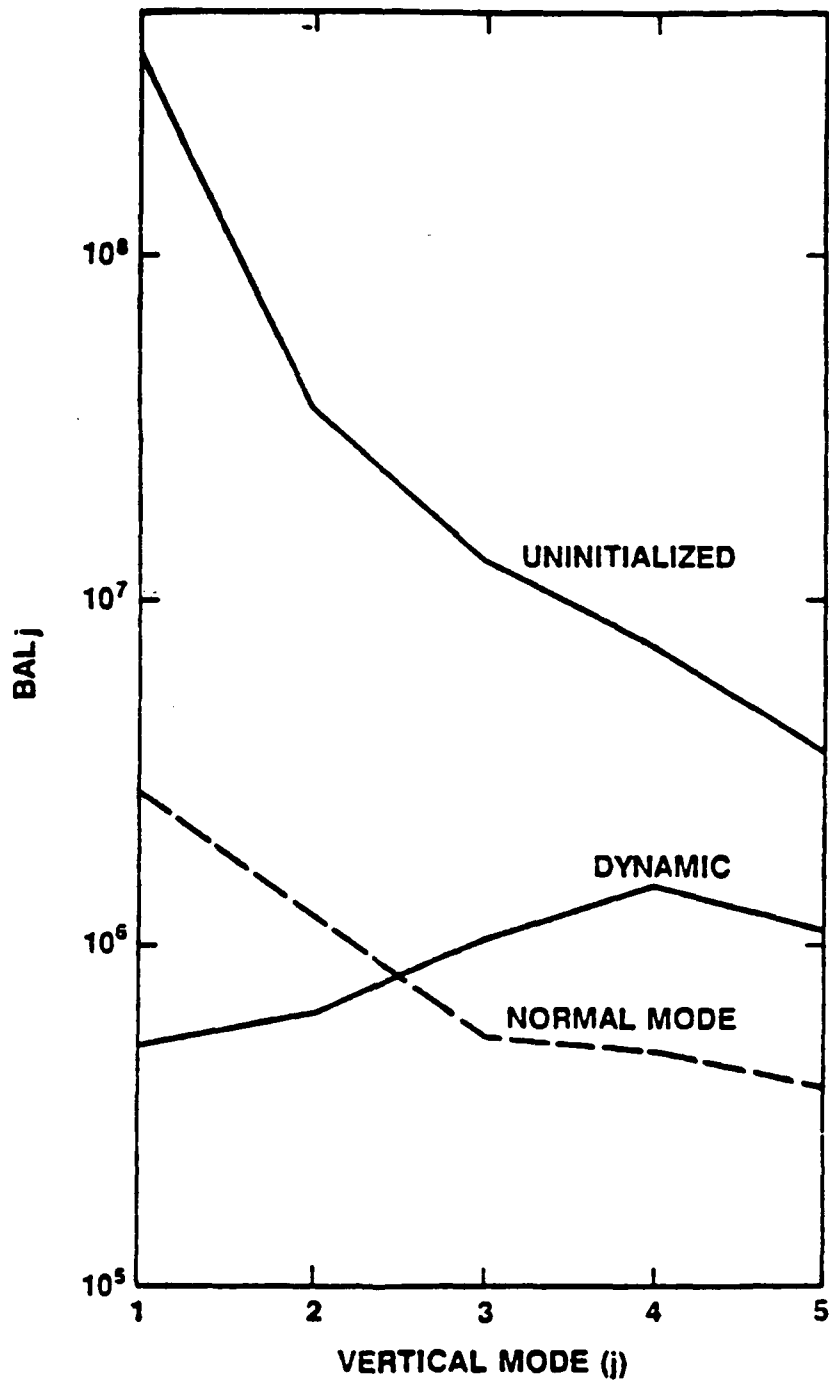


Figure 2.4. Gravity-wave activity (before and after initialization) for five vertical modes of a baroclinic model (Sugi 1986).

wave activity (before and after initialization) for five vertical modes of a baroclinic model. The gravity-wave noise is dramatically reduced, particularly for the modes of large equivalent depths. Dynamic initialization, as well as the Laplace transform and bounded derivative methods (described below), is well suited for initializing data on a limited domain.

Lynch (1985a) developed an effective method of initialization based on a filtering scheme which uses a modified inverse Laplace transform. This technique is equivalent to the nonlinear normal mode initialization method, but it has the advantage of not requiring a transformation of the model equations into normal mode space. Therefore, the Laplace transform method is well suited for initializing limited-area models with complex boundary conditions. Lynch (1985b) used his method to initialize data for a barotropic limited-area model, successfully removing high-frequency gravity wave oscillations during the model integration. This technique has also been applied in a filtering integration scheme for continuous data assimilation.

Another technique, which has been used to initialize models of limited domain, is the bounded derivative method. Kreiss (1979) developed the methodology of controlling the amplitudes of the high-frequency inertia-gravity waves by requiring the derivatives of the model's dependent variables with respect to time to be bounded, i.e., of order unity, at the initial time. First, the equations of motion are nondimensionalized so that certain terms are multiplied by a small parameter,  $\epsilon$ . Then, if the first derivatives are bounded, the equations can only be satisfied if the model atmospheric flow is geostrophic and nondivergent to order  $\epsilon$ . If the second-order time derivatives are bounded, the resulting diagnostic relationships are the quasi-geostrophic omega equation and the nonlinear balance equation.

## 2.5 Various Data-Assimilation Methods

An assimilation method extensively used in operational meteorology is the analysis-forecast cycle technique, commonly referred to simply as intermittent data assimilation (see Fig. 2.5). This process consists of four steps which are repeated at each assimilation cycle (typically every 3-12 h). After the data have been checked (quality controlled), a static three-dimensional objective analysis (typically successive correction or optimal interpolation) is performed using observations and a background field. The background or "first guess" is usually a prior model forecast valid at the analysis time, or can simply be climatology or a combination of both. Then, the analyzed fields are adjusted, or initialized, to conform to some dynamical constraint(s) in order to reduce or eliminate inertia-gravity-wave noise. The final step consists of a short-range *numerical forecast to obtain first-guess fields for the analysis at the next assimilation cycle*. Thus, the new estimates (analyzed fields) are clearly based on the past observations, being carried forward in time by the model forecast, and on the current observations. The intermittent updating process is entirely appropriate as long as most available data are taken at the same time, for example, at synoptic times. This technique is currently used at most of the world's major operational forecasting centers, including the NMC (DiMego 1988), the Norwegian Meteorological Institute (Gronas and Midtbo 1986), and the European Centre for Medium-Range Weather Forecasts (ECMWF) (Hollingsworth 1986).

The extensive operational use of intermittent data assimilation is primarily due to its computational efficiency. In addition, this method normally includes a normal mode initialization scheme that produces a balanced mass/wind initial state. A disadvantage of this method is that it is not totally suited for asynoptic data types; that is, it can not

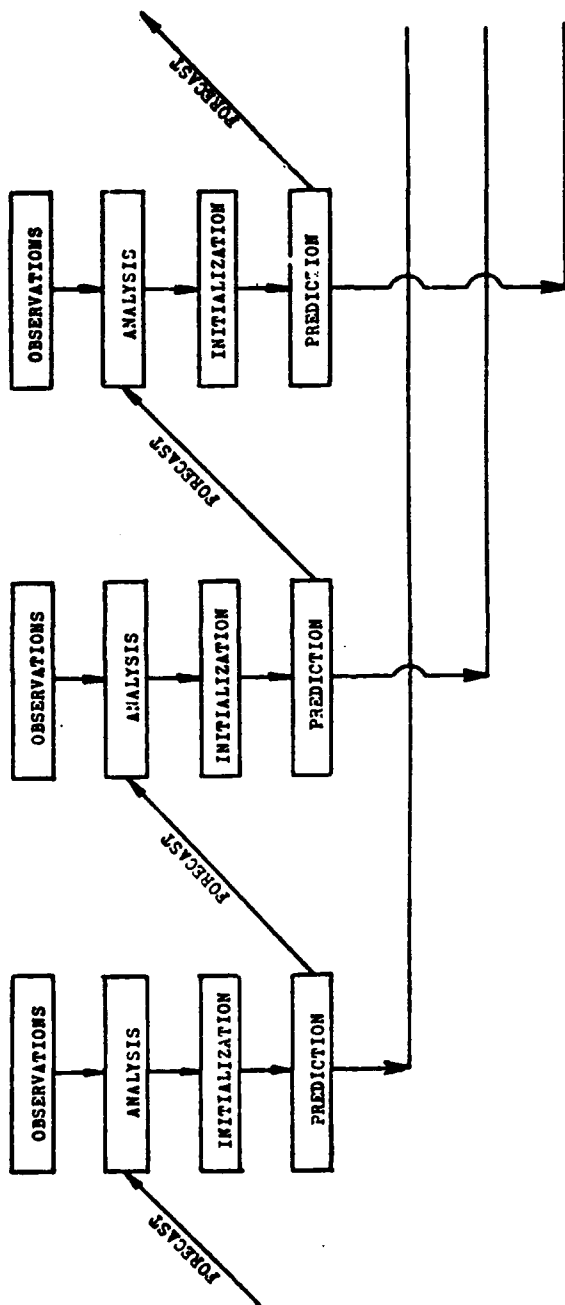


Figure 2.5. Intermittent data assimilation using an analysis-forecast cycle (Bengtsson 1975a).

assimilate data continuously. However, updates on the order of every 2 to 3 h can be made, allowing some asynoptic data into the assimilation.

Two other mathematically elegant methods, Kalman-Bucy filtering and the adjoint method using variational techniques, have emerged as state-of-the-art methodology in FDDA. The latter is briefly reviewed first. For a more rigorous and complete discussion of the general theory of these two techniques, the reader is referred to Daley (1991).

Variational assimilation, based on the calculus of variations, involves the incorporation of dynamical constraints in a variational treatment and has been pursued by Sasaki (1969), Stephens (1970), and others for several years. In variational calculus, stationary points (extrema) of integral expressions known as functionals are determined.  $J$  is a functional of the function  $q(t)$  in the interval  $(t_m, t_n)$ , if it depends on all the values  $q(t)$  for  $t_m \leq t \leq t_n$ . In this approach, successive analyses are mutually adjusted to *effectively increase the database at each time step by using information at other analysis times through the forecast equations*. The objective is to produce initialized values of  $q$  subject to certain constraints such as the hydrostatic relation, the continuity equation, the geostrophic relation, or the nonlinear balance equation. The approach is designed to keep the initialized fields close to the observations while satisfying the constraint (Daley 1991).

Lewis (1972) developed a variational scheme using a thermal wind relationship and the hydrostatic equation as constraints. A more recent variational approach, known as the adjoint method (Lewis and Derber 1985), uses a complete dynamic model as a strong constraint. This method fits a model to observational data distributed over a finite period by computing derivatives of model output. An iterative method minimizes the weighted squared difference between the original analyses at several times and the coincident solutions to the model (constraint) for a given output variable. The final analyses are constrained to satisfy the model forecast from a set of initial conditions. The functional,  $J$ , is minimized by finding the gradient of  $J$  with respect to the initial conditions.

The output of any model depends upon a set of input variables: initial conditions, boundary conditions, and even modeling parameters of physical processes. Because of this dependence, the "adjoint" can be used to determine the sensitivity of the model output to any input parameter, i.e., initial conditions. Neglecting forecast errors over the assimilation period (time period spanning the observations), this technique can produce the optimal initial state (end of the assimilation period) such that the model best fits the observations through the entire period.

The alternate "next-generation" FDDA method is called Kalman-Bucy (K-B) filtering. The K-B method can be thought of as a continuous dynamic FDDA where the weighting factors are optimally determined by explicitly calculating the error covariance of the analysis. In 1960, Kalman developed the basic theory for the linear, unbiased data assimilation scheme known as the Kalman filter (Kalman 1960).

The K-B filter (Kalman and Bucy 1961; Ghil et al. 1979 and 1981), which is the time-continuous counterpart to Kalman's original scheme, uses the forecast model itself to predict the background error statistics. The goal of this method is to obtain the most accurate analysis value for all time during the assimilation period using only present and past observations. The weight given to the current observations is inversely proportional to their variance, and the accuracy of the analysis is the sum of the accuracies of the forecast, based on the past observations, and of the current observations. The K-B filter minimizes the analysis error variance not only at every time step, but over the entire assimilation interval in which data are provided (Ghil 1989). Through an application of Bayesian ideas in a dynamical sense (Kalman 1960; Lorenc 1986), the filter is able to extract all useful information from the observational increment/residual at each time step, thus, allowing observations to be discarded as soon as they are assimilated. As a result, the method is sequential.

The K-B filter and the adjoint method are very promising assimilation techniques. Both methods have been shown to produce improved assimilated states for model forecast integration as compared to those from the operational techniques. However, these "next-generation" data assimilation methods are of limited practicality at the present because of their complexity and extensive computational requirements. Therefore, operational implementation is still several years away (Stauffer and Seaman 1990). However, Lorenc (1988) has pursued approximations to the adjoint technique in a quest to make it operational in numerical weather prediction.

Most research has been directed toward the less elegant but more practical method of dynamic assimilation, in which the numerical prediction model serves as an integrator of observations distributed in time and space. In this approach, which has become known simply as "nudging" or Newtonian relaxation, the model integration is interrupted periodically and the current model state is updated with the new observations. During the assimilation cycle, or preforecast integration period, the model variables are gradually driven, or nudged, toward the observations by extra forcing terms in the equations (Anthes 1974; Kistler 1974; Hoke and Anthes 1976; Davies and Turner 1977). As a result, the model fields are gradually corrected and no further dynamic balancing through initialization is required. The general form of the predictive equation of variable  $S$  is:

$$\frac{\partial S}{\partial t} = F(S, \tilde{x}, t) + G \cdot W (S_0 - S) . \quad 2.3$$

All of the model's physical forcing terms (Coriolis, advection, etc.) are represented by  $F$ , where  $S$  represents a model dependent variable,  $S_0$  represents observations of  $S$ ,  $\tilde{x}$  is the independent spatial variable, and  $t$  is time. The second term on the right is the nudging term, where  $G$  is the nudging constant (generally  $10^{-3}$  to  $10^{-4}$ ) and  $W$  represents a four-

dimensional weighting function. The data to be nudged can be either derived or measured, analyzed to a grid for assimilation into the model, or inserted as individual observations.

This technique, which has been successful in bringing the data and the model in harmony and providing a relatively noise-free start for the forecast, has been widely used on the global scale (Lyne et al. 1982; Krishnamurti et al. 1988) and on the regional scale in limited-area models (Anthes 1974; Hoke and Anthes 1977). Of late, several researchers have developed a new interest in this technique (Stauffer et al. 1985; Bell 1986; Ramamurthy and Carr 1987; Kao and Yamada 1988; Wang and Warner 1988; Kuo and Guo 1989; Stauffer and Seaman 1987, 1990). It is currently used operationally at the UKMO for both global (Lyne et al. 1982) and regional (Bell 1986) data assimilation.

The nudging technique mentioned above does possess a few desirable attributes; these were summarized by N. L. Seaman (from his lecture notes presented at the 1990 Summer Colloquium on Mesoscale Data Assimilation, Boulder, Colorado):

- 1) The assimilating model is complete, so irreversible processes are included without difficulty.
- 2) Any data type that can be represented as a tendency of a prognostic variable can be assimilated.
- 3) Observation-nudging can easily assimilate asynoptic and single-level data.
- 4) Analysis-nudging requires that the analyses be performed only once prior to model integration, i.e., it is economical.
- 5) Nudging does not require a separate balancing/initialization step.
- 6) Nudging is conceptually and computationally simple.

On the other hand, this method has a few disadvantages:

- 1) The nudging constant is generally assigned in an application-dependent semi-arbitrary manner.
- 2) Observation-nudging is based on "continuous analysis" during model integration and can become computationally expensive.
- 3) Analysis nudging is not well-suited for asynoptic data types.
- 4) Use of accurate data in observation-nudging may cause assimilation of local or unrepresentative components, e.g., microscale observations spread over a large area.

## 2.6 Comparisons of Operational Assimilation Techniques

Two papers from the recent literature (Ramamurthy and Carr 1987; Kuo and Guo 1989) compared different data-assimilation methods. Unlike the purpose of the present discussion, both of the aforementioned articles advocated Newtonian nudging. The sole purpose here is to offer a short review of the available comparative studies.

Ramamurthy and Carr (1987) studied the applicability of several assimilation techniques currently being employed in operational models. A prime scientific objective was to determine the "best" way to assimilate asynoptic observations in limited-area models. A sequence of ten assimilation experiments was conducted using different update procedures. In each experiment, their limited-area model was initialized with ECMWF FGGE level III-b data, and then 12-h assimilations were performed using level II-b data from the 1979 Summer Monsoon Experiment (SMONEX). Forecasts were then made from these assimilated states. The first experiment served as the control run since no assimilation was performed. Figure 2.6 is a schematic of the overall assimilation-forecast strategy; four types of data assimilation were compared: 1) In the static assimilation, the model was updated only once at the end of the preforecast (assimilation) period. An initialization step was then taken to suppress the noise associated with the external inertia-gravity mode; the internal modes were not initialized. 2) The intermittent data-assimilation experiment was similar to the static case, except the model was updated twice during the assimilation period. 3) Four experiments were conducted using continuous indirect data assimilation in which the model was updated whenever new observations became available. 4) Newtonian relaxation was used in the last three experiments; the model state was nudged toward analyses produced from the observations. The reader should see Ramamurthy and Carr (1987) for a detailed description of the experiments.

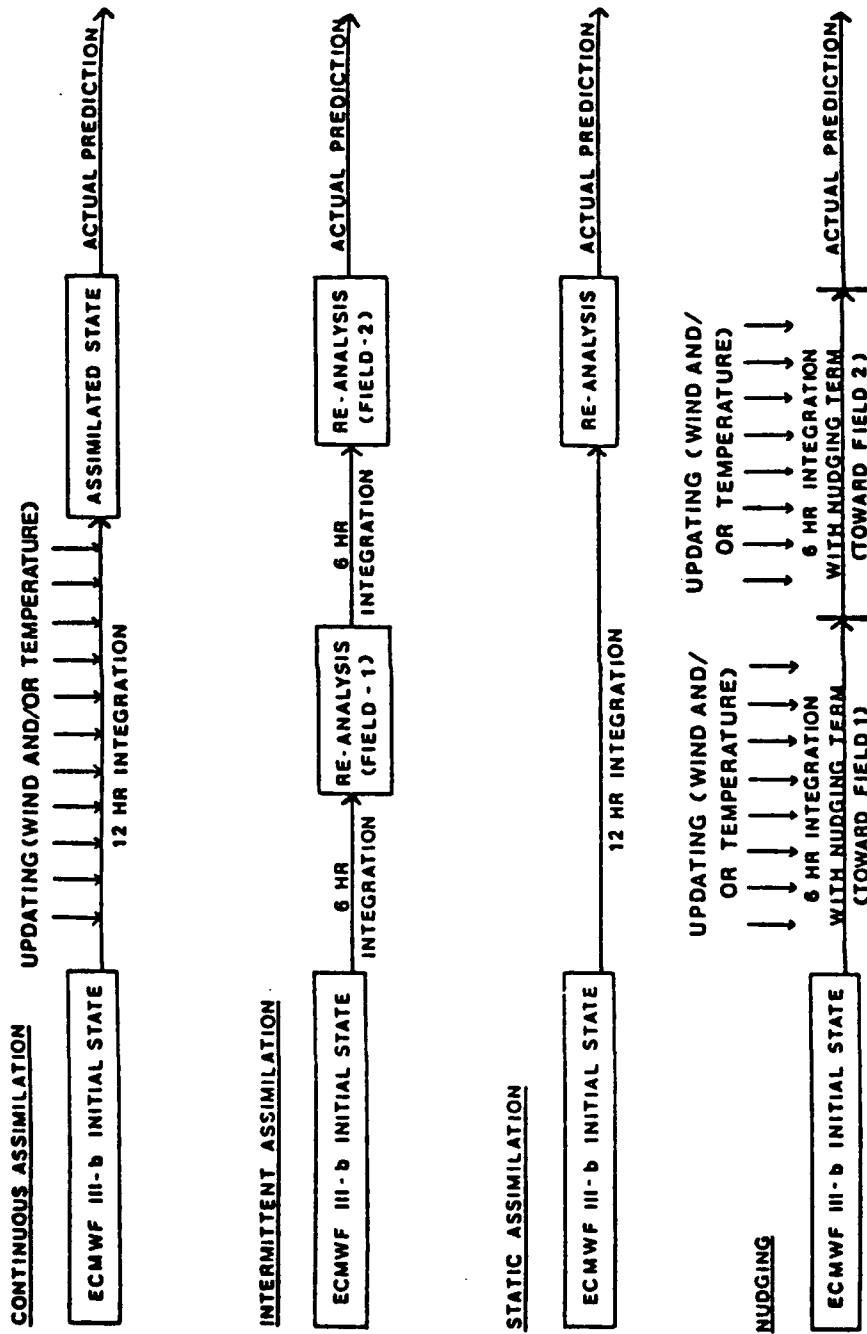


Figure 2.6. A schematic of the assimilation-forecast cycle for various experiments (Ramamurthy and Carr 1987).

Comparisons among these differing techniques were made by examining assimilated states (analyses obtained at the end of the 12-h assimilation period). Newtonian nudging produced better assimilated states than did the continuous assimilations via indirect insertion. Also, the continuous assimilation experiments produced noisy assimilated fields due to insertion shocks.

From each of the assimilated states, 24-h forecasts were made and the results were compared against each other and with the observations. The continuous assimilation (via indirect insertion) continued to suffer from the ill effects of the insertion shock. However, the forecasts from the nudging experiments had a minimal amount of noise.

The degree of spinup was examined in terms of the development of precipitation. The excessive shocking associated with continuous insertion was detrimental to the spinup process and consequently to the rainfall predictions. The rotational nudging experiment (*only the rotational component of the wind was nudged*) produced the most accurate rainfall predictions. The lack of divergence-related shock in this approach aided in the evolution of the physical processes.

The predicted tracks of the cyclone in the SMONEX case study were compared. During the first 12 h (assimilation period), the cyclone's movement was erratic in all of the experiments due to the rapid mutual adjustment between the mass and wind fields that occurred in the early stages of integration. In the static and intermittent assimilation experiments in which the fields were replaced completely at the end of the assimilation period, this problem extended into the forecast stage for another 12 h. Overall, the nudging experiments predicted more accurate tracks than the other experiments.

In another comparative study, Kuo and Guo (1989) examined different data-assimilation strategies. They conducted a series of observing-system simulation experiments (OSSEs) to test a Newtonian nudging technique for continuous assimilation of observations from a hypothetical network of profilers. Twenty experiments were

described in their paper. Similar to the work of Ramamurthy and Carr, they investigated static initialization, intermittent assimilation, and Newtonian nudging.

Comparisons of the three assimilation techniques were made by obtaining time series of wind and temperature errors during the assimilation period. With nudging, the errors decreased gradually during the period. The intermittent assimilation produced a stepwise decrease in the errors and the results after four assimilation cycles were considerably better than in the static assimilation case. This reveals that intermittent data assimilation was also effective in producing an improved initial state for the model forecast.

When considering model noise generated during the preforecast period, a strong difference emerged between continuous nudging and the intermittent assimilation. In the nudging experiment, the model noise gradually decreased during the assimilation period. In contrast, the *intermittent data* assimilation produced model noise with large spikes immediately after each reanalysis of the wind field. However, this noise could have been reduced substantially if a normal mode initialization procedure had been incorporated.

The two papers reviewed above suggest that Newtonian nudging is the best assimilation method among those compared. However, the investigators' findings may be scientifically inconclusive due to their incomplete tests (notably, their failure to include an effective normal mode initialization procedure in the intermittent data assimilation experiments). Furthermore, their comparisons were limited to operational data assimilation techniques. The next-generation methods will produce more optimal assimilated states for initiating a numerical weather prediction model. But as stated previously, these methods are still in the developmental research stage and computationally efficient versions are not currently available for operational use.

## 2.7 FDDA Research: Implications and the Future

FDDA has been developed tremendously during the past 15 years and is now an essential component of numerical analysis and prediction systems in both research and operations. The improving performance of medium-range global and hemispheric prediction and the rapid development of limited-area and mesoscale models at centers such as the NMC, ECMWF, and UKMO clearly illustrate the practical benefits of research in data assimilation.

The systematic development of data assimilation methods has made possible the use of unconventional and asynoptic observations from satellites, aircraft, drifting buoys, and soon from wind profilers and doppler radars. As a result, the accuracy of short-range forecasts has significantly improved, although only minor changes have occurred in the *global observing system since the Global Weather Experiment in 1979* (Bengtsson and Shukla 1988). According to Lange and Hellsten (1986), the 3-day rms forecast error for the Northern Hemisphere dropped by more than 35% between 1979 and 1986. During the same period, medium-range weather prediction has been usefully extended in the time scale from 3 - 4 days to about 7 days in the Northern Hemisphere and to 4 days in the Southern Hemisphere (Bengtsson 1985; Bourke et al. 1985). The largest improvement has occurred at middle and high latitudes of the Northern Hemisphere. Weather prediction in the tropics has not improved nearly as much, due to insufficient observations and deficiencies in the formulation of critical physical processes.

Lorenz (1982) addressed the limit of medium-range predictability and concluded that it is possible to predict instantaneous weather patterns with better accuracy than guesswork nearly two weeks in advance. Such extensions in predictability will depend on the ability to improve current data-assimilation systems as well as the numerical prediction models themselves.

Research is ongoing to find ways to improve data assimilation methods. A number of research centers are investigating higher-resolution models, better numerical techniques, improved physical parameterizations, and improved models of auto- and cross-correlation functions for prediction error. Another area of interest is in specifying the diabatic heating at the initial forecast time. A detailed specification is necessary in order to correctly analyze and forecast the divergent wind field over the tropics. A few universities are making major strides in developing the next-generation FDDA techniques and enhancing existing methods. For example, adjoint methods are being intensely investigated at the University of Oklahoma; K-B filtering at McGill University, Montreal, Canada; and Newtonian relaxation at the Pennsylvania State University.

Several other critical research topics need attention during the 1990s. They include: assimilation of moisture processes (rainfall data and integrated liquid water), lateral boundary conditions and mesoscale predictability (predictive skill of limited-area models is strongly controlled by the lateral boundary conditions), assimilation of surface conditions/characteristics, and quality control, which will continue to be a priority as new data types are applied in FDDA. Data assimilation is relatively new on the meso-alpha and sub-alpha scales and needs considerable research with improved datasets. Existing first-generation assimilation systems must be improved to effectively forecast on these small scales.

During the next decade, FDDA will play a role in solving or alleviating important environmental issues such as air pollution and climate control (increasing CO<sub>2</sub> and the ozone hole). Recent clean-air legislation requiring the use of low-sulfur fuels and extremely expensive equipment will make accurate numerical models of atmospheric-chemistry transport and removal more important than ever. FDDA can be used to obtain accurate meteorological fields for input to complex air-chemistry models. Bengtsson and Shukla (1988) have suggested that a comprehensive analysis of global observations

based on an FDDA system with a realistic physical model should be used to produce internally consistent, homogeneous datasets for the earth's climate system. These global observations will include many new environmental variables such as external forcing variables, concentrations of radiatively and chemically important rare species, and land surface and oceanic variables. New remote-sensing systems such as EOS (Earth Observing System) will monitor these variables.

With these environmental issues in mind, Daley (1991) elaborated on a possible vision of the future of data assimilation:

"Firstly, data assimilation will no longer be entirely or even primarily concerned with short (or medium) range weather forecasting. Secondly, the data base will become incredibly diverse in both variables measured and type of observing system. Thirdly, assimilating models will be much more comprehensive, involving ocean, land surface and stratospheric components. Finally, there will be considerably more emphasis on the long term stability of algorithms to facilitate climate change signal detection."

### 3. NRL/NCSSU MESOSCALE MODEL

The forecast model used throughout this data-assimilation research study was developed at the Naval Research Laboratory and North Carolina State University and is described in detail by Madala et al. (1987), Holt et al. (1990), and Sashegyi and Madala (1990, 1992b). The use of the full model is based in the philosophy that no compromise should be made in any components of the assimilation system. The model generates forecast of temperature, wind, surface pressure, humidity, geopotential height, vorticity, vertical velocity, and precipitation.

#### 3.1 Dynamics of the Model

The prediction model is based on the primitive equations. The horizontal momentum equations, thermodynamic energy equation, moisture conservation equation, and pressure tendency equation make up the set of prognostic equations. The hydrostatic and continuity equations are used as diagnostic equations for geopotential height and vertical motion. The prognostic equations include forcing terms, diabatic heating terms, and sink/source terms, which are regarded as physical processes and are treated separately. The primitive equations can be written in flux form in the sigma coordinates as

$$\begin{aligned} \frac{\partial(p_s u)}{\partial t} + \frac{1}{h_x h_y} \left[ \frac{\partial}{\partial x} (p_s u h_y u) + \frac{\partial}{\partial y} (p_s v h_x u) \right] + \frac{\partial}{\partial \sigma} (p_s \sigma u) - f p_s v \\ = - \frac{p_s}{h_x} \frac{\partial \phi}{\partial x} - \frac{R T}{h_x} \frac{\partial p_s}{\partial x} + p_s F_u \end{aligned} \quad 3.1$$

$$\begin{aligned} \frac{\partial(p_s v)}{\partial t} + \frac{1}{h_x h_y} \left[ \frac{\partial}{\partial x} (p_s u h_y v) + \frac{\partial}{\partial y} (p_s v h_x v) \right] + \frac{\partial}{\partial \sigma} (p_s \dot{\sigma} v) + f p_s u \\ = - \frac{p_s}{h_y} \frac{\partial \phi}{\partial y} - \frac{R T}{h_y} \frac{\partial p_s}{\partial y} + p_s F_v \end{aligned} \quad 3.2$$

$$\begin{aligned} \frac{\partial(p_s T)}{\partial t} + \frac{1}{h_x h_y} \left[ \frac{\partial}{\partial x} (p_s u h_y T) + \frac{\partial}{\partial y} (p_s v h_x T) \right] + \left[ \frac{p}{p_0} \right]^k \frac{\partial}{\partial \sigma} (p_s \dot{\sigma} \theta) \\ - \frac{R T}{c_p} \left[ -\tilde{D} - \frac{u}{h_x} \frac{\partial p_s}{\partial x} - \frac{v}{h_y} \frac{\partial p_s}{\partial y} \right] = p_s F_T \end{aligned} \quad 3.3$$

$$\frac{\partial(p_s q)}{\partial t} + \frac{1}{h_x h_y} \left[ \frac{\partial}{\partial x} (p_s u h_y q) + \frac{\partial}{\partial y} (p_s v h_x q) \right] + \frac{\partial}{\partial \sigma} (p_s \dot{\sigma} q) = p_s F_q \quad 3.4$$

$$\frac{\partial p_s}{\partial t} = -\tilde{D} \quad 3.5$$

with the hydrostatic and continuity equations given by

$$\frac{\partial \phi}{\partial \sigma} = - \frac{R T}{\sigma} \quad 3.6$$

$$\frac{\partial(p_s \dot{\sigma})}{\partial \sigma} = \tilde{D} - D \quad 3.7$$

where the horizontal components of the wind  $u$  and  $v$ , the temperature  $T$ , specific humidity  $q$ , and the surface pressure  $p_s$  are the model prognostic variables. The geopotential, potential temperature, and vertical motion in sigma coordinates are represented by  $\phi$ ,  $\theta$ , and  $\dot{\sigma}$ , respectively. The vertical sigma coordinate ( $\sigma$ ) is defined by the ratio of the pressure  $p$  to the surface pressure  $p_s$  (Phillips 1957),  $h_x$  and  $h_y$  are the map factors for the horizontal  $x$  and  $y$  coordinates, and  $p_0$  is a standard reference level of 1000 mb.  $\kappa$  is given by the ratio of  $R$ , the gas constant for dry air, to  $c_p$ , the specific heat at constant pressure for dry air. The mass divergence  $D$  is defined by

$$D = \nabla \cdot (p_s \vec{V}) = \frac{1}{h_x h_y} \left[ \frac{\partial}{\partial x} (p_s u h_y) + \frac{\partial}{\partial y} (p_s v h_x) \right] \quad 3.8$$

and  $\tilde{D}$  is the vertically integrated mass divergence given by

$$\tilde{D} = \int_0^1 \nabla \cdot (p_s \vec{V}) d\sigma \quad 3.9$$

The terms  $F_u$ ,  $F_v$ ,  $F_T$ , and  $F_q$  on the right-hand side (RHS) are forcing terms and represent physical processes such as friction, diffusion, heating and moistening due to cumulus convection and large-scale precipitation, among others. The boundary condition at the model top ( $\sigma = 0$ ) and bottom ( $\sigma = 1$ ) is  $\dot{\sigma} = 0$ .

The model dynamical equations in flux form can then be written in finite difference and vector notation. Details of the vector and matrix elements can be found in the report by Madala et al. (1987).

### 3.2 Numerics of the Model

This hydrostatic, primitive equation model uses a terrain-following coordinate system and has a one-way interacting nested grid network. The domains of the fine and coarse grids, with the smoothed model topography used on each, are shown in Fig. 3.1. The coarse grid domain includes the continental United States and extends from 40°W to 140°W and 10°N to 70°N with a horizontal resolution of 2° longitude (170 km at 40°N) by 1.5° latitude (166.5 km). The GALE (inner or fine) grid covers a smaller domain including the eastern half of the United States and extending out over the Gulf Stream from 58°W to 102°W and 23.5°N to 56.5°N with a finer horizontal resolution of 2/3° longitude (56.7 km at 40°N) by 0.5° latitude (55.5 km). With this grid resolution, the integration time step used is 180 seconds on the coarse grid and 60 seconds on the fine grid. The continuous governing equations are written in flux form and the finite difference scheme is a second-order quadratic conserving scheme. The Arakawa C-grid (Arakawa and Lamb 1977) in spherical coordinates is used for horizontal differencing. Lateral boundary conditions suggested by Davies (1976, 1983) are emphasized in the present version of the model at each grid boundary.

In the vertical, both grids use 10 equally spaced sigma levels. The vertical layers and the horizontal staggered C-grid are illustrated in Fig. 3.2 for the simple case of only two model levels. In the vertical, the layers are of varying thickness  $\Delta\sigma_k$  with the prognostic variables  $u$ ,  $v$ ,  $T$ , and  $q$ , and the geopotential  $\phi$  defined at sigma levels  $\sigma_k$ . The vertical motion  $\sigma$  in the sigma coordinate is staggered in the vertical, being defined at sigma levels  $\sigma_k + \Delta\sigma_k/2$  at the boundaries between the vertical layers.

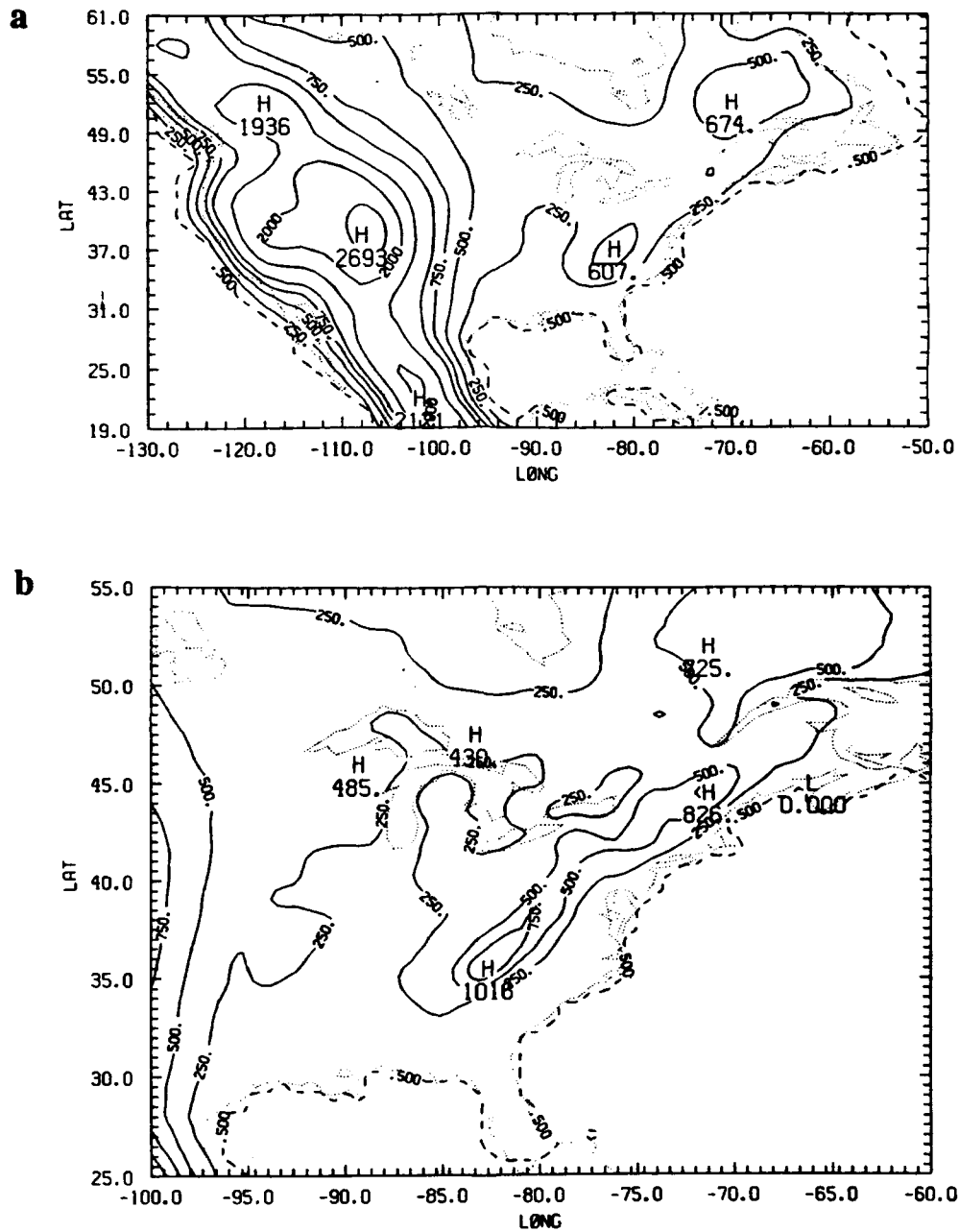


**Figure 3.1. Model domain with smoothed model topography for (a) the coarse (outer) grid and (b) the GALE (fine) grid. The contour intervals are 500 m for elevations above 1000 m, and 250 m below 1000 m. Model grid indicated by small tick marks along axes.**



### 3.2.1 Split-Explicit Time Integration

The model's time integration scheme is the split-explicit method which allows larger time steps by effectively separating various terms in the prognostic equations into parts governing the slow-moving Rossby modes and fast-moving gravity modes. In applying the split-explicit scheme of Madala (1981) to the nested model, the time step on each grid satisfies the non-linear CFL condition with centered differencing for the phase speed of the fourth internal vertical gravity mode of the model. Initial estimates of the tendencies of the model variables for all the terms are computed with a large time step  $\Delta t$ . These explicit first estimates of the tendencies of the mass (surface pressure  $p_s$  and temperature  $T$ ) and wind components ( $u$  and  $v$ ) are then corrected for the motion of the higher frequency gravity modes (external and first two internal modes).

These corrections to the mass and momentum tendencies are computed by integrating, at shorter time steps, the amplitudes of the deviations of the divergence and generalized geopotential from their values at time  $t$ , for each of the first three vertical modes. Time steps of  $\Delta t/8$ ,  $\Delta t/4$ , and  $\Delta t/2$  are used for the external modes and first two internal vertical modes, respectively. The average of these deviations, over the interval of twice the large time step, is then used to correct the initial estimate of the variables, with the non-linear forcing held constant. Madala's split-explicit scheme is extremely cost-effective, requiring only 20-25% of the computer time expended by explicit methods. Plus, Sashegyi and Madala (1990) showed that this technique reduces the amplitude of the freely-propagating higher-frequency gravity waves.

### 3.2.2 Lateral Boundary Conditions

To update the flow at the horizontal boundaries of each grid during the integration of the NRL/NCSU mesoscale model, boundary conditions are required for the horizontal components of the wind field and for the mass and humidity fields. Surface pressure  $p_s$ , temperature  $T$ , and specific humidity  $q$  are defined at the lateral boundary. The wind components are staggered in the C grid, which allows the tangential wind to be defined at the boundary and the normal wind to be staggered half a grid point in from the boundary. Idealized boundary values and tendencies for the coarse grid are derived from 12-hourly NMC 2.5° hemispheric analyses. The fine-grid boundary values are obtained from the coarse grid integration.

Computed model variables are relaxed to the boundary values in a boundary zone of six points using the *Davies scheme* (1976, 1983). The model variables are adjusted at each time step according to:

$$a = (1 - \alpha) a_m + \alpha a_b \quad 3.10$$

where 'a' is the independent model variable  $p_s u$ ,  $p_s v$ ,  $p_s$ ,  $p_s T$ , or  $p_s q$ , and is a linear combination of the model computed value  $a_m$  and the prescribed boundary value  $a_b$ . Following Gronas et al. (1987),  $\alpha$  is defined as a quadratic function of the distance ( $n$ ) from the lateral boundary in units of the grid spacing:

$$\alpha = \begin{cases} 1 & \text{for } n = 0 \\ \left[ \frac{6.5 - n}{6} \right]^2 & \text{for } 1 \leq n \leq 5 \\ 0 & \text{for } n \geq 6 \end{cases} \quad 3.11$$

Coarse-grid boundary values are computed at each time step by a linear interpolation in time from the 12-hourly NMC analyses. At each time step, model variables on the coarse grid are linearly interpolated to the six points in the boundary zone

of the fine mesh. Then these values are linearly interpolated in time to the intermediate time steps for the fine grid.

### 3.3 Physics of the Model

Physical parameterizations suitable for simulating extratropical cyclones are used. These model physics are described below.

#### 3.3.1 Planetary Boundary Layer

The planetary boundary layer is parameterized using a single layer with the fluxes of heat, momentum, and humidity computed using a generalized similarity theory, in which the *drag coefficients are stability dependent* (Chang 1981). The exchange of momentum, moisture, and sensible heat between the surface and the lowest model layer is proportional to the differences in the wind velocity, humidity, and temperature between those two levels and is given by:

$$\frac{\partial p_s V}{\partial t} = -g \frac{\partial \tau}{\partial \sigma} = -\frac{g \tau_s}{\Delta \sigma} \quad 3.12$$

$$\frac{\partial p_s T}{\partial t} = g \frac{\partial H}{\partial \sigma} = \frac{g H_s}{\Delta \sigma} \quad 3.13$$

where  $\tau$  is the stress,  $H$  is the sensible heat flux, and  $\tau_s$  and  $H_s$  are the respective surface values. A similar relationship holds between the specific humidity  $q$  and the moisture flux  $E$ . The magnitudes of the surface stress and surface fluxes of sensible heat and humidity are related to the values of the wind, potential temperature, and specific

humidity in the lowest model layer. In this parameterization, only positive heat and moisture fluxes are computed. Heat and moisture loss to the ocean surface is not considered.

### 3.3.2 Horizontal Diffusion

The model has horizontal diffusion to control noise accumulation during integration. The diffusion is of second order and is applied directly on the horizontal sigma surfaces using a forward time differencing scheme. The model variables for the flux form of the equations are smoothed by application of the two dimensional diffusion operator  $\nabla \cdot K_H \nabla$ . The operator is applied directly to the wind components  $p_s u$  and  $p_s v$ , while for the temperature  $p_s T$ , specific humidity  $p_s q$ , and surface pressure  $p_s$ , the operator is applied on the deviations from values computed at the same sigma levels for the U.S. standard atmosphere. The diffusion coefficient varies with latitude as the square of the longitudinal map factor  $h_x$ , so that the coefficient of diffusion decreases as the longitudinal grid distance decreases with increasing latitude. We define the diffusion coefficient  $K_H$  as

$$K_H = \frac{[h_x \Delta x]^2 \mu}{2 \Delta t} \quad 3.14$$

where  $\mu$  is a fixed non-dimensional diffusion coefficient,  $\Delta x$  and  $\Delta t$  are the latitudinal grid spacing and time step, respectively. A value of  $\mu = 0.005$  was found to provide sufficient smoothing, without excessively damping the synoptic scale waves on the coarse grid. On the fine grid, a value of  $\mu = 0.006$  is used to provide a little more damping of the small scale features.

### 3.3.3 Cumulus Convection

Convective heating, precipitation, and moistening of the environment are parameterized using the method developed by Kuo (1974) and modified by Anthes (1977). Convective heating is released in an atmospheric column when there is conditionally unstable stratification and moisture convergence. Kuo assumed that deep convection occurs in a conditionally unstable environment where there is large-scale convergence at low levels in the troposphere. It is further assumed that the deep clouds dissipate and mix horizontally with the environmental air, releasing heat and moisture. The total moisture used to form the clouds in a given area is given by the total horizontal convergence of moisture into that area. The converged moisture is partitioned into moistening and heating parts where the ratio is determined by the vertically averaged *relative humidity of the column*. The vertical heating profile is determined by the difference between the predicted temperature sounding and the moist adiabat constructed from the boundary layer temperature and humidity.

First, the horizontal moisture convergence  $M$  is computed for all model layers using

$$M = \nabla \cdot (p_s \vec{V} q) = \frac{1}{h_x h_y} \left[ \frac{\partial}{\partial x} (p_s u h_y q) + \frac{\partial}{\partial y} (p_s v h_x q) \right] \quad 3.15$$

The total horizontal moisture convergence  $M_t$  is computed by summing over all the layers except the top layer, where  $M_t$  is given by

$$M_t = -\frac{p_s}{g} \int_{\Delta\sigma}^1 \nabla \cdot (p_s \vec{V} q) d\sigma \quad 3.16$$

The moisture convergence in the top layer is computed separately, since it is assumed that clouds do not penetrate into the top layer. The air column is tested for convectively

unstable lapse rates if the total moisture convergence  $M_t$  exceeds a critical value. The total moisture used in cloud formation is dependent on the vertically averaged relative humidity  $r_m$  in the environment. This moisture can be partitioned into a fraction  $(1-b) M_t$ , which is condensed and precipitated out in the cloud, and a fraction  $b M_t$  which moistens the cloud (or condenses and re-evaporates at the same level), where the fraction is defined as  $b = 1-r_m$ . Assuming the cloud dissipates and mixes with the environmental air, then the moistening and heating rates of the environment can be easily computed. The vertically averaged heating rate  $Q_c$  and moistening rate  $D_c$  satisfy

$$(1 - b) M_t = \frac{c_p Q_c}{g L_c} \quad 3.17$$

$$b M_t = \frac{D_c}{g} \quad 3.18$$

where  $L_c$  is the latent heat of condensation. The precipitation  $P_c$  from cumulus clouds follows from

$$P_c = (1 - b) g M_t \quad 3.19$$

### 3.3.4 Large-Scale Precipitation

The parameterization of large-scale or non-convective precipitation/heating follows Manabe et al. (1965); that is, the excess moisture in a supersaturated layer within a stably stratified environment is condensed out isobarically, leaving the layer saturated. The evaporation of precipitation in unsaturated layers below the cloud base is also accounted for.

Following the outline in Haltiner and Williams (1980), if  $q$  and  $T$  are the initial values of the specific humidity and temperature of the supersaturated layer, then the resulting saturation specific humidity  $q_s$  is given by

$$q + \Delta q = q_s(T + \Delta T) \equiv q_s(T) + \left[ \frac{\partial q_s}{\partial T} \right]_p \Delta T \quad 3.20$$

where  $\Delta q$  and  $\Delta T$  are the changes (assumed small) in the specific humidity and temperature of the layer. Using the Clausius-Clapeyron equation to define the saturation vapor pressure as a function of the temperature and rearranging, the change in the specific humidity is given by:

$$\Delta q = \frac{q - q_s}{1 + L_c^2 q_s / c_p R_v T^2} \quad 3.21$$

where  $R_v$  is the gas constant for water vapor.  $\Delta q$  is reduced at each model level by a factor to account for that fraction which re-evaporates in the next layer below. The corresponding  $\Delta T$  at each level is given by  $c_p \Delta T = -L_c \Delta q$ , and the total large-scale non-convective precipitation  $P_L$  is given by:

$$P_L = -\frac{P_s}{g} \int_0^1 \nabla q \, d\sigma \quad 3.22$$

### 3.3.5 Dry Convective Adjustment

Also following Manabe et al. (1965), a dry convective adjustment is applied to remove any absolutely unstable lapse rates in the model atmosphere. In the real atmosphere, unstable lapse rates, which can develop due to large surface fluxes of sensible heat for example, are removed through dry convection (plumes, rolls, etc). In the model, these mechanisms are sub-grid scale. However, such unstable lapse rates will produce unrealistically large vertical velocities in the model. To resolve this problem, the

vertical column at each grid point in the model domain is tested for any absolutely unstable lapse rates. Then, for each sequence of unstable layers in the vertical, the sub-grid scale vertical mixing is parameterized in the model following Manabe et al. (1965). It is assumed that parcels in unstable layers are lifted adiabatically to the next layer, exchanging their heat at constant pressure, while conserving the total enthalpy. The exchange of heat takes place until the temperatures of the unstable layer and the first stable layer above the unstable layers are adjusted to a neutral lapse rate.

### 3.3.6 Surface Parameters

At the earth's surface, weekly-averaged sea surface temperatures (SST) of 0.5° resolution, taken from the GALE datasets, are interpolated to the model's fine grid. Climatological SSTs for the months of January and February of one degree resolution, taken from Reynolds (1982), are interpolated temporally to obtain a weekly mean and interpolated spatially to the coarse grid of the model. A sea/ice boundary is derived from the U.S. Navy's climatological sea/ice boundaries for month of January. Model topography for both grid domains is obtained from Navy 10-minute global topographical data.

### 3.4 Model Initialization

The vertical mode initialization scheme of Bourke and McGregor (1983), as applied by Sashegyi and Madala (1990, 1992a) and Harms et al. (1992a), is used to reduce the undesirable gravity wave oscillations in numerical integrations of the NRL/NCSU mesoscale model. The scheme applies a correction to the Rossby modes by averaging a separate integration for those gravity modes whose phase speeds are much

larger than meteorological systems. In this scheme, filtering conditions for the inertia-gravity waves are applied to the model dynamical equations to derive linear diagnostic equations for the mass and divergence fields for the first few vertical modes of the limited-area model. The process sets time derivatives of the gravity-wave oscillations resulting from imbalances between the initial mass and momentum fields to zero by decomposing the total model tendencies into normal modes. With suitable boundary conditions, the equations are then solved iteratively for the first three vertical modes of the numerical model to remove the high frequency gravity waves from the initial conditions. The scheme has been shown to be an application of the normal mode initialization scheme, developed by Machenhauer (1977) and Baer (1977) and used in global models (for example Andersen 1977; Daley 1979; Williamson and Temperton 1981), without the horizontal structure of the normal modes having to be computed (Juvanon du Vachat 1986; Temperton 1988).

As in Bourke and McGregor (1983), the mass field remains fixed at the lateral boundaries of the model. Bourke and McGregor assumed that the divergence does not change at the boundary. To provide a more realistic boundary condition, an approximate mass divergence is computed inside the lateral boundary using the thermodynamic equation. In the present scheme, the resulting changes to the tangential and normal wind are computed assuming no change in the stream function and velocity potential along the lateral boundaries of the model domain. By using the C grid and defining the tangential wind at the lateral boundary and the normal wind staggered half a grid point inside the lateral boundary, the changes in the wind field along the boundary are then naturally consistent with the changes in the integrated vorticity and mass divergence over the model domain.

Following Temperton and Williamson (1981), the vertical structure of the model's normal modes is obtained by separating the linear and non-linear terms of the

governing equations and then linearizing about a basic state at rest with a mean temperature  $T^*(\sigma)$ , which varies only in the vertical. A generalized geopotential is defined whose derivative gives the horizontal pressure gradient in the horizontal equations of motion and whose time tendency is related to the divergence. A separation of the vertical structure of the model variables is then possible. The model dynamical equations are expressed as time tendencies of mass-weighted vorticity  $\zeta$ , mass divergence  $D$ , and generalized geopotential  $\Phi$ . The equations with the  $\beta$  term included with the non-linear terms on the RHS are written as:

$$\frac{\partial \zeta}{\partial t} + f D = A_{\zeta} \quad 3.23$$

$$\frac{\partial D}{\partial t} + \nabla^2 \Phi - f \zeta = A_D \quad 3.24$$

$$\frac{\partial \Phi}{\partial t} + \lambda_k D = A_{\Phi} \quad 3.25$$

The freely-propagating inertia-gravity waves in the model are solutions to these linearized equations with the forcing terms on the RHS of the equations equal to zero. Here,  $f$  is the Coriolis parameter,  $D$  is the mass divergence,  $u$  and  $v$  are the horizontal wind components, and  $\Phi$  is the generalized geopotential, defined as:

$$\Phi = p_s \left[ \phi - \phi_s + R T^* - \phi^* \right] \quad 3.26$$

where  $p_s$  is the surface pressure,  $\phi$  is the geopotential,  $\phi_s$  is the surface geopotential,  $R$  is the gas constant for dry air, and  $\phi^*$  is the average geopotential on the sigma surface of the model. Equations 3.23 - 3.25 describe the shallow water equations, where the phase speed of the free gravity modes is given by  $\lambda_k^{1/2}$ , where  $\lambda_k$  (which can be represented as

an equivalent depth multiplied by the acceleration due to gravity) is the eigenvalue for the  $k^{\text{th}}$  mode.

The filtering conditions of Bourke and McGregor,

$$\frac{\partial D}{\partial t} = \frac{\partial}{\partial t} \left[ f \zeta - \nabla^2 \Phi \right] = 0 \quad 3.27$$

on the divergence  $D$  and the ageostrophic "vorticity"  $f \zeta - \nabla^2 \Phi$ , need to be applied to Eqs. 3.23 - 3.25 for only the first three vertical modes, whose phase speeds of the gravity modes are much larger than about  $25 \text{ m s}^{-1}$ . Since the terms on the RHS of Eqs. 3.23 - 3.25 depend on the vorticity, divergence, and geopotential, the resulting set of equations is solved iteratively (Bourke and McGregor 1983).

The resulting changes to the horizontal wind field are computed from the changes in the mass divergence and mass weighted vorticity by solving the following Poisson's equations:

$$\nabla^2 \Delta \chi = \Delta D \quad 3.28$$

$$\nabla^2 \Delta \Psi = \Delta \zeta \quad 3.29$$

for the changes in the velocity potential  $\Delta \chi$  and the stream function  $\Delta \Psi$  for each sigma level of the model. Then changes to the mass weighted wind follow from:

$$\Delta(\bar{p}_s u) = \delta_x \Delta \chi - \delta_y \Delta \Psi \quad 3.30$$

$$\Delta(\bar{p}_s v) = \delta_y \Delta \chi + \delta_x \Delta \Psi \quad 3.31$$

Finally, following Temperton (1984), the changes in the surface pressure  $p_s$  and the temperature  $T$  can be derived directly from changes in the generalized geopotential.

## 4. APPLICATION OF THE BRATSETH SCHEME FOR THE ANALYSIS OF GALE DATA

The mesoscale weather prediction model described in Chapter 3 provides a short-range forecast which serves as the background field, or first guess, for our numerical analysis. Following a brief introduction of various analysis techniques, an in-depth description of the NRL/NCSU objective analysis scheme, which was developed and tested during the course of this research, is given.

### 4.1 Introduction

During the 1960s and 70s, the most widely used objective analysis technique in operational data assimilation and forecast systems was the method of successive correction. This type of analysis was first introduced by Bergthorsson and Döös (1955), and a number of versions have been developed by Cressman (1959), Barnes (1973), and others. It is still widely used for the analysis of mesoscale systems in the research community (Koch et al. 1983; Benjamin and Seaman 1985; for example). However, these successive correction schemes possess a couple of undesirable attributes. First, the analysis converges to the data, and if a first guess is used, then too much attention is paid to the observations relative to the first guess. Second, observations in regions of high data density are given excessive weight relative to observations in areas of low data density.

In the 1980s, emphasis shifted in operational community toward the more mathematically complex and computationally expensive method of statistical

interpolation, or better known as optimal interpolation. With optimal interpolation, analysis errors are minimized with respect to the spatial structure of observational and forecast errors. A concise review of objective analysis can be found in the paper by Schlatter (1988). Recently the method of optimum interpolation has been applied with success to operational limited-area modelling systems (DiMego 1988; Benjamin 1989; Mills and Seaman 1990).

A paper by Bratseth (1986) has caused a recent resurgence of the successive correction method. He introduced a successive correction scheme, in which the solution converges toward the solution obtained by optimal interpolation. His technique alleviates the aforementioned shortcomings of previous successive correction methods by utilizing the forecast error covariance to define weights which are reduced in regions of higher data density by use of a normalizing factor. Additionally, the Bratseth method requires much less computational expense than does optimal interpolation methods. Therefore, it is very attractive for use for a limited-area forecast system when only limited resources are available. This approach to successive correction methodology is currently being used operationally in a multivariate analysis for the limited-area forecast system at the Norwegian Meteorological Institute (Gronas and Midtbo 1986). An algorithm similar to the Bratseth scheme has been applied at the U.K. Meteorological Office to directly insert data into both the global and regional models (Lorenc et al. 1991). With each iteration of the scheme, the mass and wind variables are updated in a sequential fashion. To maintain balance in their models, changes to the geostrophic component of the wind are derived from any mass changes; the wind changes are non-divergent and the divergence during integration is damped.

A simplified multivariate, successive correction objective analysis scheme using the Bratseth method has been developed at the U.S. Naval Research Laboratory (NRL) and North Carolina State University (NCSU) to analyze data collected during the Genesis

of Atlantic Lows Experiment. During intensive observing periods, more frequent upper air soundings were taken at selected National Weather Service (NWS) sites over the region of the eastern U.S., supplemented by additional sites along the coast, dropsondes deployed from aircraft offshore, and a denser set of surface observations (Dirks et al. 1988; Raman and Riordan 1988). As has been the practice with limited-area forecast systems using optimal interpolation, the length scales of the correlation functions in the Bratseth scheme are reduced from those used with global models to provide more detail at the smaller scales (DiMego 1988). After a number of iterations of the scheme, the length scale of the correlation functions is further reduced for subsequent iterations to speed the convergence of the scheme (Gronas and Midtbo 1986; Seaman 1988). A prior forecast generated by the NRL/NCSU mesoscale model is used, as in the operational limited-area models, to provide a first guess for the analysis scheme. With the coarse resolution of the upper-air network, it is only by using such a mesoscale model to generate a first guess, is there any hope that any realistic mesoscale features generated by the model will be preserved or even enhanced by the analysis. The analysis of the deviations of the data from the first guess covers a region similar to the model's fine grid but at a lower resolution of  $1.5^\circ$  in latitude and longitude. The grid spacing used is consistent with the average upper air station spacing of about 350 km over the eastern U.S. To remove bad data or data inconsistent with the scales resolved by the numerical model, an efficient quality control procedure was implemented in a manner similar to DiMego (1988).

In this chapter, a general description of our objective analysis method is given and a qualitative evaluation of the scheme is provided. Experiments with the analysis scheme are described. The vertical mode initialization scheme of Bourke and McGregor (1983) is used to diagnose the divergent circulations associated with the analyzed mesoscale features and upper-level jet streaks. The interaction of these secondary circulations in the jet streaks can be important for cyclone development (see Uccellini et al. 1984; Uccellini

and Kocin 1987; for example). The impact of these mesoscale circulations produced by the analysis on subsequent forecasts is tested and precipitation forecasts are compared to observed values.

#### 4.2 The NRL/NCSU Objective Analysis Scheme

A simplified application of the Bratseth (1986) scheme has been developed, as compared to the full multivariate implementation used at the Norwegian Meteorological Institute by Gronas and Midtbo (1986). In our scheme, univariate analyses of the mass and wind fields are first performed using the successive correction approach of Bratseth. The deviations from our first-guess field, which is derived from a prior 12-h forecast valid at the analysis time, are analyzed. To provide the coupling between the wind and mass fields, the analyzed wind is used as an initial estimate of the geostrophic wind in a further iteration on the geopotential. The geostrophic wind is used to extrapolate the geopotential to the grid point locations in a fashion similar to Cressman (1959), but consistent with the Bratseth scheme. In each subsequent iteration, an improved geostrophic wind estimate is then defined by the new geopotential gradient, and not by the original wind as is widely used with the Cressman scheme. The wind analysis is then corrected for the new geostrophic wind as in Kistler and McPherson (1975). A further analysis of the wind is performed to improve the larger scales of the ageostrophic wind. The temperature is then corrected with the new geopotential thicknesses. The resulting analysis corrections are interpolated to the model sigma coordinates to update the first-guess forecast, so as to not destroy any balance or small mesoscale features generated by the model.

A set of upper-air soundings, which were interpolated to 10-mb levels from the surface up to 100 mb, and surface data for the second Intensive Observing Period (IOP)

of GALE were obtained from the GALE Data Center (GDC) at Drexel University (Mercer 1987). The data domain included the eastern U.S. and western North Atlantic from 115°W to 45°W in longitude and from 10°N to 60°N in latitude. A higher density of upper-air soundings and surface data is found in the inner GALE region covering the Carolinas and southern Virginia from the Gulf Stream to the Appalachians. An analysis grid covered the data domain with a resolution of 1.5° in latitude and longitude extending from 116°W to 44°W in longitude and from 9°N to 61.5°N in latitude. To correct the model forecast first guess in areas with no data over the ocean and around the lateral boundaries of the analysis grid, bogus data derived from the NMC analysis are used. After the analysis is complete, the resulting corrections are merged with corrections to the first guess derived from the NMC analysis in a zone along the lateral boundaries of the analysis grid. The corrections are then bicubically interpolated to the model fine grid and added to the original first guess on the pressure surfaces to provide a final analysis. The corrections themselves are also interpolated in the vertical to the sigma surfaces of the model to correct the original first-guess model forecast. By applying the vertical mode initialization scheme, both the divergent and the ageostrophic wind are derived from the analysis.

A further important part of any analysis scheme of real data is the quality control of the data prior to the analysis. Data, which are inconsistent with the first guess or with neighboring observations or are of a scale too small to be resolved by the analysis scheme, must be removed to prevent aliasing into the larger scales in the analysis.

#### 4.2.1 Data Preparation and Quality Control

An efficient quality control procedure has been developed for use with the analysis scheme, similar to those at operational weather centers. The soundings are first

checked for hydrostatic consistency and smoothed, retaining data at 50-mb levels, to be more representative of our 10-layer model vertical resolution. Similar procedures to those used at NMC in the regional analysis (DiMego 1988) are followed by performing a "gross" check in which observations with large deviations from the first-guess values and any missing data are removed. In a simplified "buddy" check, observations not agreeing with neighboring observations are removed. Close observations are replaced by an average "super" observation and any remaining isolated observations are eliminated. To smoothly merge with the NMC analysis at that synoptic hour, bogus data derived from the NMC analysis at that time are added in data void regions such as over the ocean or at the lateral boundary of the analysis domain. Over the ocean, the NMC analysis acts as a test of our scheme. A further advantage of the quality control is that by removing bad and missing data prior to the analysis our analysis code is able to be vectorized to run rapidly on a supercomputer. Using these procedures, the influence of any data errors and biases is reduced. The details of each of the components of the data preparation and quality control follow.

#### a) Hydrostatic check and smoothing

After being checked for hydrostatic consistency, the soundings are smoothed in the vertical. The temperatures and the u and v wind components were averaged over 20-mb intervals weighted by the log of pressure for the temperatures and by the mass for the u and v wind components. The humidities, which were more noisy (Kreitzberg, personal communication), were smoothed by averaging over 50-mb intervals using the mixing ratios weighted by the mass. Consistent geopotentials were then recomputed and variables retained only for levels every 50 mb. For each sounding, a "daily average" surface temperature is computed by linear extrapolation from levels above the boundary

layer. The sea level pressure is computed by extrapolation of the average surface temperature to sea level, and a plateau correction is added (Saucier 1955). To extrapolate heights to pressure levels below ground level, an average of the surface temperature and the daily average is used. For efficiency, the soundings are sorted into 5° latitude/longitude boxes for each pressure level, at 50-mb increments from sea level to 100 mb.

b) Gross errors

At each pressure level, data are checked for gross errors, as compared to the first-guess analysis, which has been interpolated to the pressure surfaces from the earlier 12-h model forecast. In this gross check, those upper-air observations that differ in magnitude by more than four standard deviations from the first guess are rejected. Any missing data specified in the sounding are also removed. For the sea-level pressure, those values that differ in magnitude by more than two and a half times the standard deviation are rejected. Estimates of the standard deviation of the observations from the first-guess forecast are obtained by adding a forecast error growth to the observational error. The values used are slight modifications to those used at operational centers (DiMego 1988; Shaw et al. 1987). For sea-level pressure, an observational error of 1.5 mb is used with forecast error growth of 1.0 mb in 6 h to give a first-guess error of 3.5 mb for a 12-h forecast using our limited-area model. For the upper-air variables, the values used for the observational error and the forecast error growth are listed in Table 4.1. For the remaining quality-control procedures and the analysis, only the deviations of the data from the first guess are retained.

TABLE 4.1. Standard deviation of the observational errors and forecast error growth for a six-hour forecast period in parentheses. These are the input error statistics for the objective analysis.

Pressure (mb)	Height (m)	Temperature (°C)	Rel humidity (%)	u,v Wind (m s <sup>-1</sup> )
100	20 (17)	2.0 (0.7)	----	3.5 (1.3)
150	18 (18)	1.8 (0.6)	----	4.0 (1.4)
200	15 (18)	1.8 (0.5)	----	4.0 (1.5)
250	14 (18)	1.5 (0.6)	----	4.0 (1.6)
300	14 (18)	1.0 (0.6)	17 (4)	4.0 (1.6)
350	14 (17)	1.0 (0.5)	15 (4)	4.0 (1.7)
400	12 (16)	1.0 (0.5)	13 (4)	3.5 (1.7)
450	10 (14)	1.0 (0.4)	13 (4)	3.5 (1.6)
500	9 (12)	1.0 (0.3)	13 (4)	3.0 (1.6)
550	8 (10)	1.0 (0.3)	13 (3)	3.0 (1.5)
600	7 (9)	1.0 (0.3)	12 (3)	3.0 (1.4)
650	6 (8)	1.2 (0.3)	12 (3)	3.0 (1.3)
700	6 (8)	1.3 (0.3)	12 (2)	2.5 (1.2)
750	6 (8)	1.4 (0.3)	12 (2)	2.5 (1.2)
800	6 (8)	1.5 (0.4)	13 (2)	2.5 (1.1)
850	6 (8)	1.5 (0.5)	13 (2)	2.5 (1.1)
900	5 (8)	1.8 (0.5)	13 (2)	2.5 (1.1)
950	5 (8)	1.8 (0.6)	13 (2)	2.5 (1.1)
1000	5 (8)	1.8 (0.6)	13 (2)	2.5 (1.1)

c) Buddy check

A simplified buddy check procedure is used, in which deviations of the observations from the first guess are compared with the deviations from all neighboring observations including itself. Each observation is compared with itself and all the others, within a maximum distance of 833 km (equal to  $7.5^\circ$  of latitude). The maximum allowed deviations for a pair of observations is a linear function of the cartesian distance between the observations, and is equal to one standard deviation at zero distance and increases to 3.5 times the standard deviation at the maximum distance.

d) Average close observations and eliminate isolated observations

To speed the convergence of the iterative analysis scheme, observations in close geographical proximity are combined into a single "super" observation. Each  $5^\circ$  box is divided into smaller boxes of  $1.25^\circ$  longitude by  $1^\circ$  latitude, and an average of all the data within each smaller box is computed, assigning the average latitude and longitude for the position. To further prevent isolated data from adversely affecting the analysis (generating circular corrections), any remaining isolated data are removed. For each data box with less than two of the surrounding eight boxes having any data, the data in that box are removed.

e) Merge with NMC analysis

In regions of no data over the ocean, additional "bogus" soundings, derived from the difference between the first-guess forecast and the NMC  $2.5^\circ$  hemispheric analysis, are used to merge our analysis smoothly with the NMC analysis over the ocean at

synoptic hours. At off-synoptic times, no bogus soundings are added and the analysis returns to the background in regions of no data. To match the resolution of the NMC analysis, two bogus soundings spaced  $5/3^\circ$  apart in latitude and longitude are used in each empty interior box requiring bogus data, and one sounding is used at the center of each boundary box requiring bogus data. The requirement for adding bogus data to an empty box depends on the availability of data in the neighboring boxes. In this case, additional bogus soundings have been added over the Gulf of Mexico and off the east coast of the U.S. An example for 1200 UTC January 25 in Fig. 4.1a shows the locations of the geopotential height data at 500 mb after the quality control. Very few upper-air real observations (shown by the crosses) are found over the oceans, where NMC "bogus" data (shown by stars) have been added. For the sea-level pressure, shown in Fig. 4.1b, many more observations were available over the ocean, many of which are superobs.

#### 4.2.2 Analysis Interpolation

The attractive features of the Bratseth successive correction scheme (1986) for the interpolation of the observations to the analysis grid are: 1) the weights are dependent on the covariance between observations and, therefore, are dependent on the accuracy of the observations, 2) the weights are reduced in regions of higher-data density, and 3) the scheme converges to that obtained by optimal interpolation. As has been done in the operational implementation of this scheme in Norway by Gronas and Midtbo (1986), the width of the modelled covariance function is reduced after three or four iterations to speed the convergence of the scheme at the smaller scales. Further passes of the analysis scheme on a smaller grid can be easily added in regions of higher observational density, such as in regions of drifting buoys or dropwindsondes. This was applied to the case of

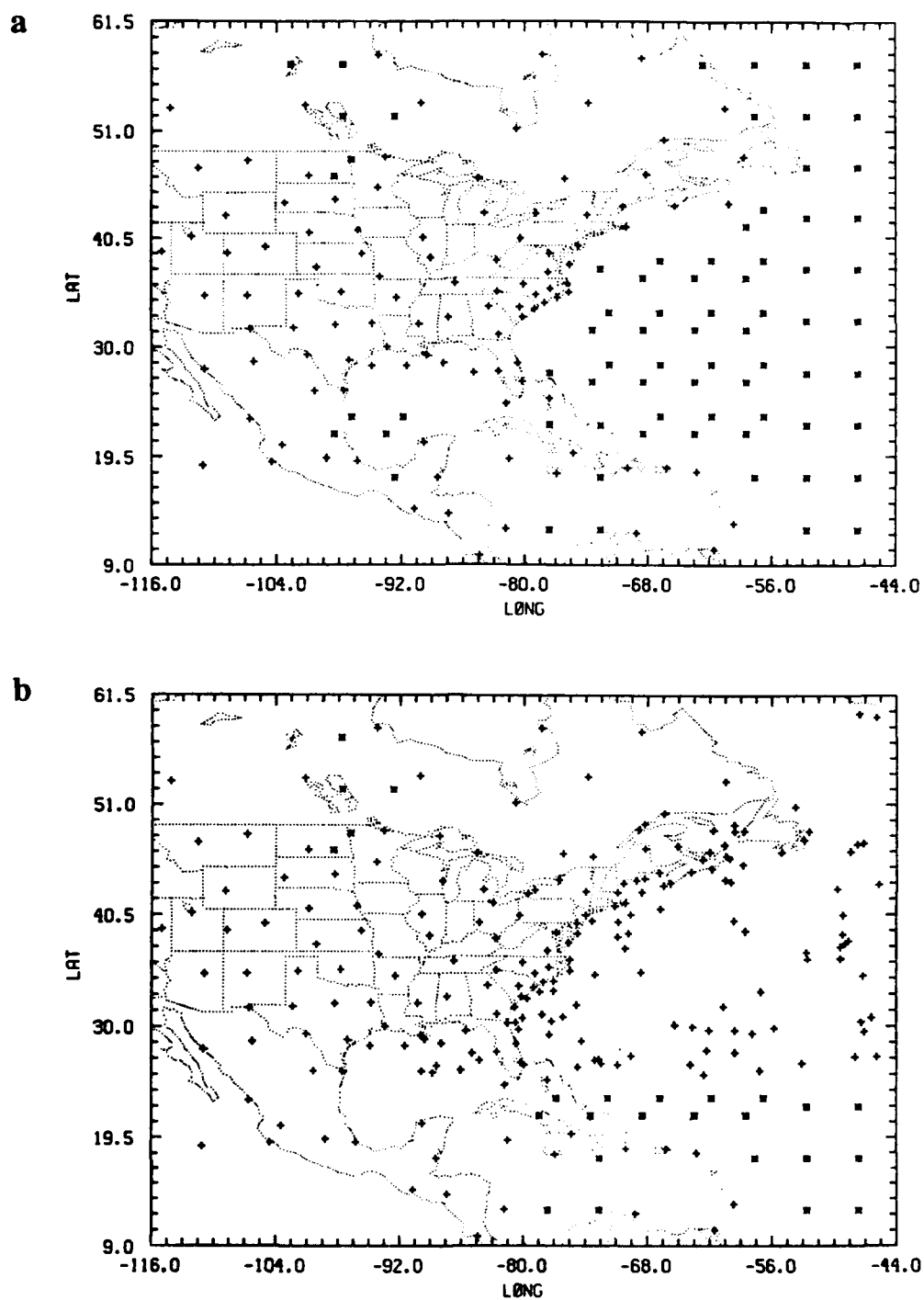


Figure 4.1. The location of the data for (a) the geopotential height at 500 mb and (b) the sea level pressure after quality control. The observations are indicated by the '+', while bogus values are indicated by '\*'. The analysis grid is indicated by the tick marks along the domain boundary.

a hurricane with an earlier version of the analysis based on the Barnes scheme by Shi et al. (1991). The steps are further described below.

a) Univariate analysis of the mass and wind field

In the first step of the analysis scheme, univariate analyses of sea-level pressure, geopotential, temperature, and humidity corrections to the first guess are successively adjusted at each iteration. In the Bratseth scheme, estimates of both the interpolated correction and the observation correction are computed using the iterative formulas. For the geopotential corrections  $\phi$  to the first-guess values of geopotential provided by an earlier 12-h forecast, the interpolated value at the grid point "x" is given by:

$$\phi_x^{(v+1)} = \phi_x^{(v)} + \sum_{j=1}^n \alpha_{xj} \left[ \phi_j^{\circ} - \phi_j^{(v)} \right] \quad 4.1$$

and the estimate of the value of observation correction is given by:

$$\phi_i^{(v+1)} = \phi_i^{(v)} + \sum_{j=1}^n \alpha_{ij} \left[ \phi_j^{\circ} - \phi_j^{(v)} \right] \quad 4.2$$

where  $\phi_j^{\circ}$  is the value of the observation, and  $\phi_x^{(v)}$  and  $\phi_j^{(v)}$  are the interpolated values at the grid point and the estimate of the observation value, respectively, for the  $v^{\text{th}}$  iteration.

The starting corrections  $\phi_x^{(1)}$  and  $\phi_j^{(1)}$  are zero. The weights, which are dependent on the covariance of the corrections for the first guess, are in each case given by:

$$\alpha_{xj} = \frac{\overline{\phi_x^{(1)} \phi_j^{(1)}}}{m_j \sigma^2} = \frac{\rho_{xj}}{m_j} \quad 4.3$$

$$\alpha_{ij} = \frac{\overline{\phi_i \phi_j}}{m_j \sigma^2} = \frac{\rho_{ij} + \varepsilon^2 \delta_{ij}}{m_j} \quad 4.4$$

where the covariances are defined in terms of a correlation function  $\rho$  for the true values  $\phi^t$ , and  $\varepsilon^2$  is the ratio of the observation error variance  $\sigma_\varepsilon^2$  to the first-guess (forecast) error variance  $\sigma^2$ . For the forecast error variance, we use the same variance used in the quality control for the variance of the observations from the first-guess forecast listed in Table 4.1. A "local data density"  $m_j$  is defined at the observation location by

$$m_j = \frac{1}{\sigma^2} \sum_{k=1}^n \overline{\phi_j \phi_k} = \sum_{k=1}^n \left[ \rho_{jk} + \varepsilon^2 \delta_{jk} \right] \quad 4.5$$

The correlation function  $\rho(r)$  for the geopotential corrections  $\phi$  is modeled as a Gaussian,

$$\rho(r) = e^{-(r/d)^2} \quad 4.6$$

which is a function of the distance  $r$  between observations. The correlation length scale "d" is defined by 500 km for the first 3 or 4 iterations and by 275 km for one additional iteration. Since our mesoscale model can resolve smaller scale mesoscale features than can operational regional models, a somewhat smaller length scale is used, as compared to that used at NMC (577 km) by DiMego (1988). After the first pass of our analysis scheme, the data are again checked for inconsistency with the first-pass analysis itself. Any inconsistent data, which differ more than 2.5 times (1.5 times for sea-level pressure) the standard deviation from the first pass, are removed and the first pass is repeated. The same correlation function is used for the univariate analysis of sea-level pressure, temperature, and relative humidity. With observation errors included, the estimate of observation is not equal to the analyzed value interpolated to the observation location, but

it converges rapidly to the value of the observation itself (Bratseth 1986). For a fixed length scale of 500 km, the convergence of the observation estimate and the convergence of the analyzed value at the observation location are shown in Fig. 4.2. The convergence is measured with respect to the number of analysis iterations. When the length scale is reduced after just 3 or 4 iterations, the resulting rms differences for both the observation estimate and analyzed value are substantially reduced, as depicted in Fig. 4.2. It can be noted however, that if there was no observation error, they would be the same.

For the univariate analysis of wind corrections to the first-guess wind field, different correlation functions are used. The correlation functions for the wind components can be derived from the correlation function  $\rho(r)$  for the geopotential (Gronas and Midtbo 1986). The functional form of the correlation functions  $\rho_u$  and  $\rho_v$  for the components of the wind field are given by

$$\rho_u = \left[ 1 - \frac{(y-y_j)^2}{d_u^2} \right] \rho(r) \quad 4.7$$

$$\rho_v = \left[ 1 - \frac{(x-x_j)^2}{d_u^2} \right] \rho(r) \quad 4.8$$

where  $\rho(r)$  is the correlation function for the geopotential,  $(x,y)$  and  $(x_j,y_j)$  are the cartesian positions of two observations. These correlations effectively give smaller weights across the direction of the wind than along it without having to compute wind direction as in Benjamin and Seaman (1985). A modified length scale " $d_u$ " is used which is different from the length scale " $d$ " used for  $\rho(r)$ . A value of 700 km is assigned for  $d_u$ , whereas the length scale for  $\rho(r)$  is 500 km. This value of  $d_u$  fits the length scale found by Hollingsworth and Lonnberg (1986), where the transverse correlations in the

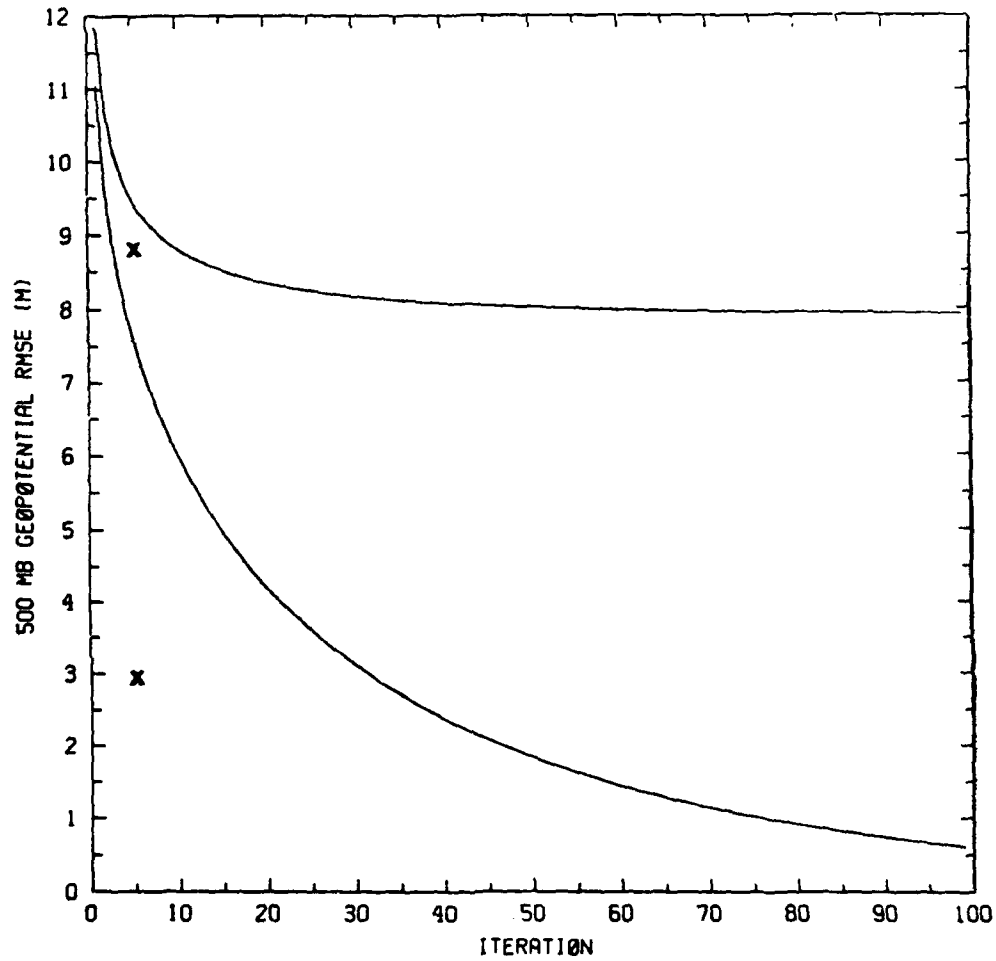


Figure 4.2. The root mean square (rms) of the difference between the observation estimate and the observation value for the geopotential at 500 mb (lower curve) as a function of the iteration number. The upper curve shows the rms of the difference between the analysis value interpolated to the observation point and the observation value. The rms values obtained after four iterations followed by a further iteration with a reduced length scale are indicated by the X's.

wind reach zero. After 3 to 4 iterations, the length scales,  $d_u$  and  $d$ , are reduced to 380 km and 275 km, respectively, for one more iteration to again speed convergence.

b) Geostrophic enhancement of the geopotential

A further four iterations are used for the geopotential correction, using improving estimates of the geostrophic wind at each iteration to extrapolate the geopotential correction to the grid points. An initial estimate of geostrophic wind is obtained from the previous univariate  $u$ ,  $v$  wind corrections by linear interpolation. The interpolated value  $\phi_x^{(v+1)}$  at the grid point is now given after the  $v^{\text{th}}$  iteration by

$$\phi_x^{(v+1)} = \phi_x^{(v)} + \sum_{j=1}^n \alpha_{xj} \left[ \begin{aligned} &\phi_j^o - \phi_j^{(v)} - c_j (y - y_j) f_j \left\{ u_g^{(v)} - u_g^{(v-1)} \right\}_j \\ &+ c_j (x - x_j) f_j \left\{ v_g^{(v)} - v_g^{(v-1)} \right\}_j \end{aligned} \right] \quad 4.9$$

and the observation estimate  $\phi_i^{(v+1)}$  is

$$\phi_i^{(v+1)} = \phi_i^{(v)} + \sum_{j=1}^n \alpha_{ij} \left[ \begin{aligned} &\phi_j^o - \phi_j^{(v)} - c_j (y_i - y_j) f_j \left\{ u_g^{(v)} - u_g^{(v-1)} \right\}_j \\ &+ c_j (x_i - x_j) f_j \left\{ v_g^{(v)} - v_g^{(v-1)} \right\}_j \end{aligned} \right] \quad 4.10$$

where  $\phi_j^o$  is the value of the observation and  $u_{g,j}^{(v)}$  is an estimate of the geostrophic wind correction at the observation point for the  $v^{\text{th}}$  iteration.  $\phi_j^{(v)}$  and  $u_{g,j}^{(v-1)}$  are the prior estimates of the value of the observation of geopotential and the geostrophic wind, respectively, at the observation point. For the next iteration, an improved estimate of the geostrophic wind correction  $(u_{g,j}^{(v+1)}, v_{g,j}^{(v+1)})$  is obtained at the observation point by linear

interpolation of grid point values computed from the interpolated values of the geopotential at the grid points.

$$u_{g,x}^{(v+1)} = - \frac{\bar{c}^y \delta_y \phi_x^{(v+1)}}{f^* \Delta y} \quad 4.11$$

$$v_{g,x}^{(v+1)} = - \frac{c \delta_x \phi_x^{(v+1)}}{f^* \Delta x} \quad 4.12$$

$u_{g,x}^{(v)}$  is the value of the geostrophic wind at the grid point, derived from the geopotential  $\phi_x^{(v)}$ , and  $u_{g,j}^{(v)}$  is the value at the observation point obtained by bilinear interpolation from  $u_{g,x}^{(v)}$ , for the  $v^{\text{th}}$  iteration. "f" is the Coriolis parameter, and  $f^* = \max(f(15^\circ\text{N}), |f| \text{sign}(f))$ . "c" is a geostrophy factor depending on the latitude  $\theta$  in degrees as

$$c = \begin{cases} 1 & \text{for } |\theta| > 30^\circ \\ 0.5 [ 1 + \cos(12\theta) ] & \text{for } 15^\circ \leq |\theta| \leq 30^\circ \\ 0 & \text{for } |\theta| < 15^\circ \end{cases} \quad 4.13$$

The four iterations use a single correlation scale "d" of 500 km. Only the larger scales are corrected, without changing the smaller scales which are not as geostrophic. In a 9-point zone along the boundary of our analysis grid, the analyzed values are merged with values interpolated from the NMC analysis. The analyzed values in the first six points closest to the boundary are replaced by the NMC values, while a linear weighting of (.25,.75), (.5,.5), (.75,.25) is used to merge the analyzed values with the NMC values.

c) Enhancements to the wind field and temperature gradients

Following Kistler and McPherson (1975), the geostrophic part of the corrections to the wind field is adjusted to match the new corrections for the geopotential. That is, the univariate wind corrections are modified by adding the difference in the geostrophic wind between the geostrophic and univariate analysis of the geopotential. Four additional passes of the univariate wind analysis are then performed to enhance the corrections of the ageostrophic wind. A similar merging with wind derived from the NMC analysis is performed in the 9-point boundary zone as was done with the geopotential. After the corrections have been computed at all analysis pressure levels of the analysis, the univariate temperature corrections are adjusted to match the computed thickness corrections. The final corrections are then bicubically interpolated to the model horizontal grid and added to the first guess on the pressure surfaces.

The analysis deviations are interpolated in the vertical to the model sigma levels and the model background forecast is updated. Before interpolating in the vertical, an initial estimate of new surface pressure is computed from the analyzed full fields on the p levels. The surface pressure of the background forecast is similarly computed from the fields of temperature and geopotential height on the pressure levels. The difference in surface pressure between the two is then added to the original surface pressure of the background forecast to obtain the corrected surface pressure. The analysis deviations are then linearly interpolated in the vertical to the model sigma levels and added to the first-guess model forecast. The thermodynamic variables (temperature, humidity) are interpolated to the model sigma levels, assuming they are linear in the log of pressure, while the wind components are interpolated assuming they are linear in the pressure.

### 4.3 Testing the Analysis Scheme

The utility of an analysis scheme may be judged in several ways, including its ability to: 1) define accurately the amplitude and phase of meteorological waves, 2) fit data within the accuracy of observations, 3) distinguish between accurate and erroneous data, and 4) provide initial conditions for numerical weather prediction models such that forecast error is minimized. In section 4.2, it was shown that our analysis scheme fits the data to a desirable limit. Here, we will concentrate on items 1) and 4) from a qualitative viewpoint by comparing our analyses and subsequent model forecasts based on these fields with the mesoscale analyses of Bosart (1988) and Doyle and Warner (1990) and the NMC 2.5°-resolution hemispheric analyses, and forecasts produced from these NMC fields by our limited-area model. Application of the vertical mode *initialization scheme* on both the NMC and our analyses is used to compare the mesoscale vertical motion and ageostrophic wind derived from the NRL and NMC analyses. Model forecast precipitation is compared in each case to observed values. Analyses of GALE raingauge data from GDC (Mercer 1987) on a polar stereographic grid of about 84 km resolution were interpolated to a 0.5° latitude/longitude grid. To provide values outside of the region of the GDC precipitation analyses, precipitation estimates on a 1°-resolution grid derived from satellite by Martin et al. (1988) at the Cooperative Institute for Meteorological Satellite Studies at the University of Wisconsin were also interpolated to the 0.5° grid. These rainfall estimates were derived from digital infrared images of the GOES-6 satellite using the Global Precipitation Index technique of Arkin (1983). This technique assumes that rainfall ( $R$  in mm) is linearly related to the fractional cloud cover ( $f$ ):

$$R = k \times f \quad 4.14$$

where the coefficient  $k$  has a value of 72 mm/day.

#### 4.3.1 Experimental Design

A number of cases were performed to test the effectiveness of the NRL/NCSU objective analysis scheme; these are outlined in Table 4.2. The analyses were made using surface and atmospheric sounding data collected during IOP 2 of GALE. Twelve-hourly NMC 2.5° hemispheric analyses for the period 0000 UTC 25 January to 1200 UTC 26 January 1986 (25/00Z to 26/12Z) were used for the initial conditions to generate the first-guess 12-h forecasts and for comparison to our analyses. Six model variables were analyzed: sea level pressure, geopotential height, u- and v- wind components, temperature, and relative humidity. Analyses were performed at 19 vertical levels from 1000 mb to 100 mb at 50-mb increments on a horizontal grid with a resolution of 1.5° latitude by 1.5° longitude. These analyses produced from the NRL/NCSU objective analysis scheme are referred to as simply NRL analyses.

In case 4.1, the model is initialized from the 25/00Z NMC analysis. The 12-h forecast serves as the background, or first guess, for univariate (case 4.2) and multivariate (case 4.3) analyses using the NRL/NCSU scheme. For each case, 24-h forecasts are then produced. The 25/12Z NMC analysis and a 24-h subsequent forecast (case 4.4) serve as a baseline for comparison. Cases 4.5 and 4.6 are identical to cases 4.3 and 4.4, except the analyses are valid at 26/00Z and the 12-h forecast from case 4.4 serves as the first guess for the NRL analysis in case 4.5. The analyses in cases 4.7 and 4.8 are valid 12 h later at 26/12Z. These 8 cases essentially serve as 3 separate experiments: 1) 25/12Z analyses and subsequent forecasts, 2) 26/00Z analyses and forecasts, and 3) those at 26/12Z.

TABLE 4.2. Analysis and Forecast Test Cases

Case	
4.1	25/00Z NMC analysis and 12-h model integration
4.2	25/12Z univariate analysis with 12-h forecast from case 4.1 as first guess and 24-h integration
4.3	25/12Z multivariate analysis with 12-h forecast from case 4.1 as first guess and 24-h integration
4.4	25/12Z NMC analysis and 24-h integration
4.5	26/00Z multivariate analysis with 12-h forecast from case 4.4 as first guess and 24-h integration
4.6	26/00Z NMC analysis and 24-h integration
4.7	26/12Z multivariate analysis with 12-h forecast from case 4.6 as first guess and 24-h integration
4.8	26/12Z NMC analysis and 24-h integration

### 4.3.2 The Synoptic Situation

During the period 25/00Z to 27/12Z, coastal frontogenesis and cyclogenesis took place along the eastern seaboard. Riordan (1990) and Doyle and Warner (1990) describe the initial stages of the coastal frontogenesis from 24 January. At 25/00Z, coastal frontogenesis had begun offshore along the Carolina coast in an onshore easterly flow regime and by 25/12Z a 1000-km long coastal front paralleled the coastline. Cold air damming east of the Appalachians and warming of the easterly air over the Gulf Stream were the major factors contributing to the strong thermal gradient along the coast. The easterly flow regime can be seen in the coarse NMC 1000-mb analysis in Fig. 4.3a, which is however unable to resolve the strong thermal gradient along the coast. In the upper levels of the atmosphere, a broad, long-wave trough was present over the central U. S. (Fig. 4.3b). An associated 250-mb jet with maximum winds of  $55\text{-}60\text{ m s}^{-1}$  extended from northeast Texas across the Ohio River Valley. During the next 24 h, the trough moved eastward and deepened rapidly due to a second short wave digging southward in the large-scale trough. By 26/00Z, the coastal front extended from Georgia to southern New England and a weak low moved up the coast along the front, reaching the Chesapeake Bay by 26/12Z (Fig. 4.3c). In the next 12 h, the coastal low merged with a weak trough seen in Fig. 4.3c moving eastwards from the Great Lakes.

The disturbance which ultimately became the first of the major cyclones of GALE was present as a minor frontal wave in extreme southeast Texas at 25/12Z. The surface disturbance remained weak as it advanced along the Gulf coast and on 26 January the surface wave weakened further as it moved across Georgia. In response to the strong upper-level short wave reaching the east coast, a new center formed off Cape Hatteras and deepened rapidly as it moved north and combined with the pre-existing waves associated with the northward-moving coastal low and eastward moving trough. By

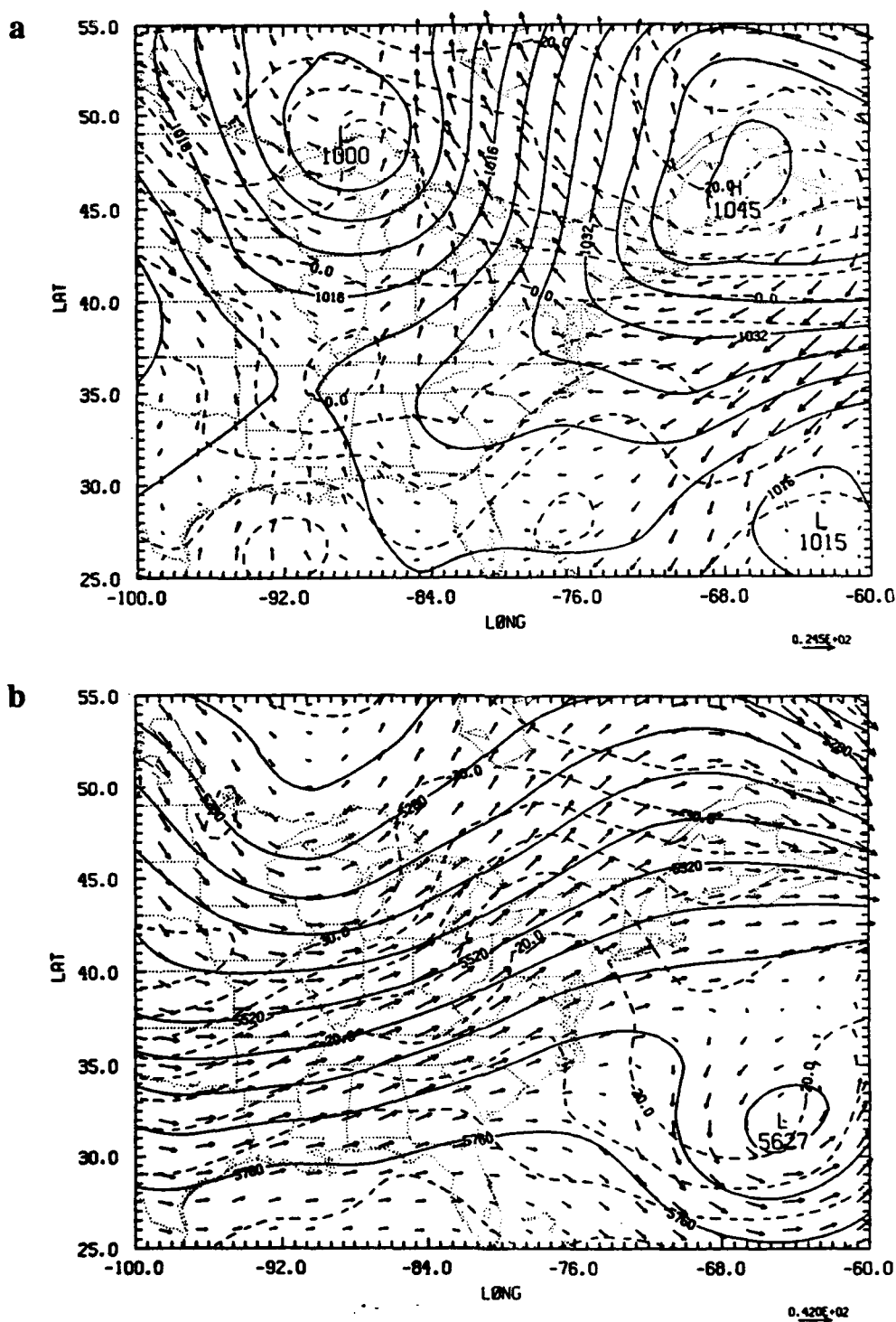


Figure 4.3. (a) Sea-level pressure (mb) and temperature (°C) and winds at 1000 mb, and (b) geopotential height (m), temperature (°C) and winds at 500 mb for the NMC analysis on 25/12Z. (c) and (d) as in (a) except for 26/12Z and 27/12Z, respectively. Contours of sea-level pressure and temperature at 1000 mb are 4 mb and 5°C, respectively. Maximum wind vector indicated by labelled arrow in m s<sup>-1</sup>.

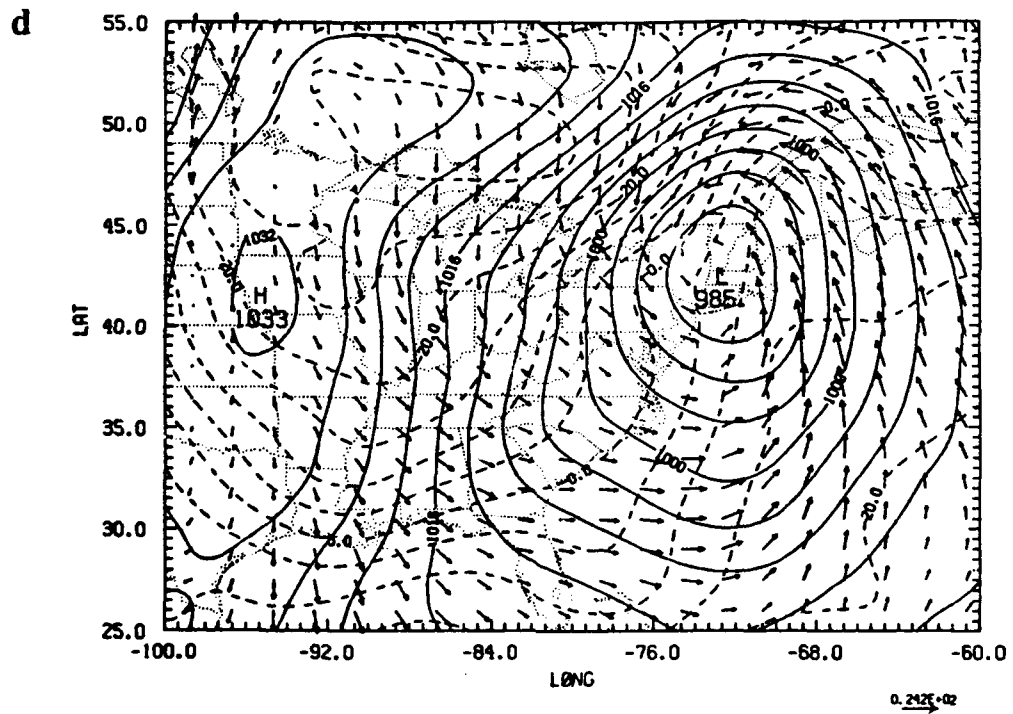
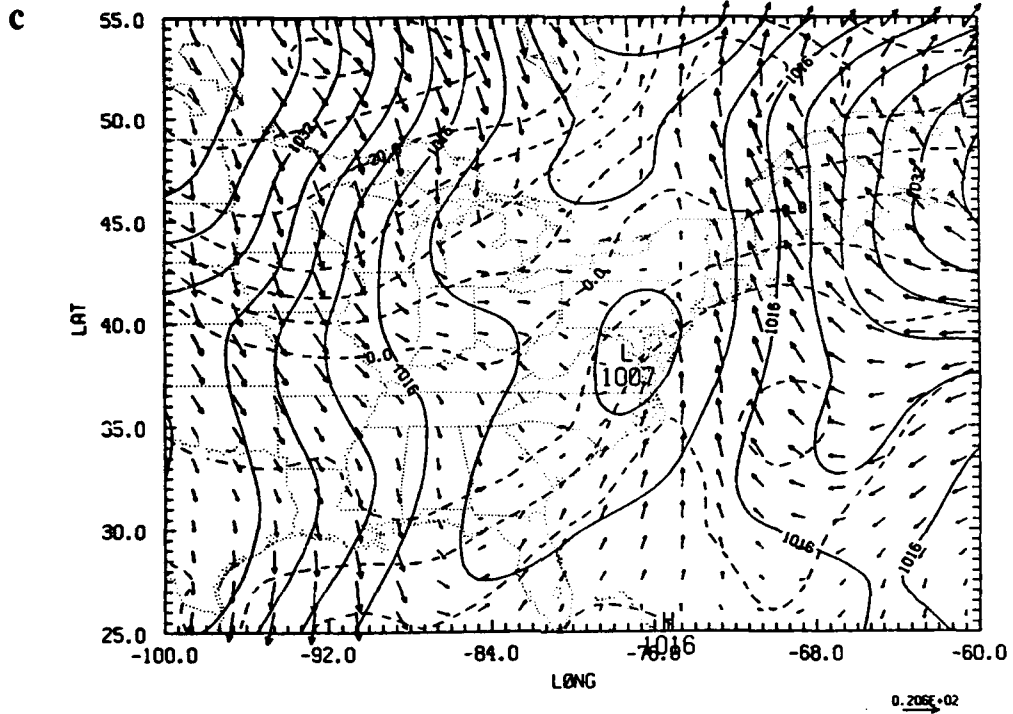


Figure 4.3. Continued.

27/12Z, the well-developed low pressure center crossed the New England coast, as shown in Fig. 4.3d.

#### 4.4 Results

Comparisons between first-guess forecast fields, univariate analyses, multivariate analyses, NMC analyses, and Bosart's detailed hand analyses are made at 25/12Z and 26/00Z. Also, model forecasts resulting from these analyses are compared with each other and with the Bosart analyses valid at specific forecast times.

##### 4.4.1 Comparison of 25/12Z Analyses

Sea-level pressure, surface temperature, and 1000-mb winds for the first guess (12-h forecast from case 4.1), and the NRL analysis at 25/12Z are shown in Figs. 4.4a and b. The first guess, shown in Fig. 4.4a, had the cold air damming with strong ridging east of the Appalachians. The presence of a strong temperature gradient along the Carolina coast signified the existence of a coastal front. The NRL analysis shown in Fig. 4.4b retained these features, suggesting that they were present in the data. The 25/12Z analysis of Doyle and Warner (1990) verifies that the coastal front and the cold air damming were present (see Fig 2b. of Doyle and Warner). Note that the coarse NMC analysis shown in Fig. 4.3a is unable to resolve the tight thermal gradient along the coast. The NRL analyses also retained the strong onshore flow from the first guess and which is readily apparent in Doyle and Warner's analysis along the Carolina coast. The overall pressure pattern from the NRL analysis matched Doyle and Warner's analysis much better than the coarse NMC analysis was able to do. Note the position and magnitude of the "low" of 1000 mb over Lake Superior and the "high" of 1046 mb over the Gulf of

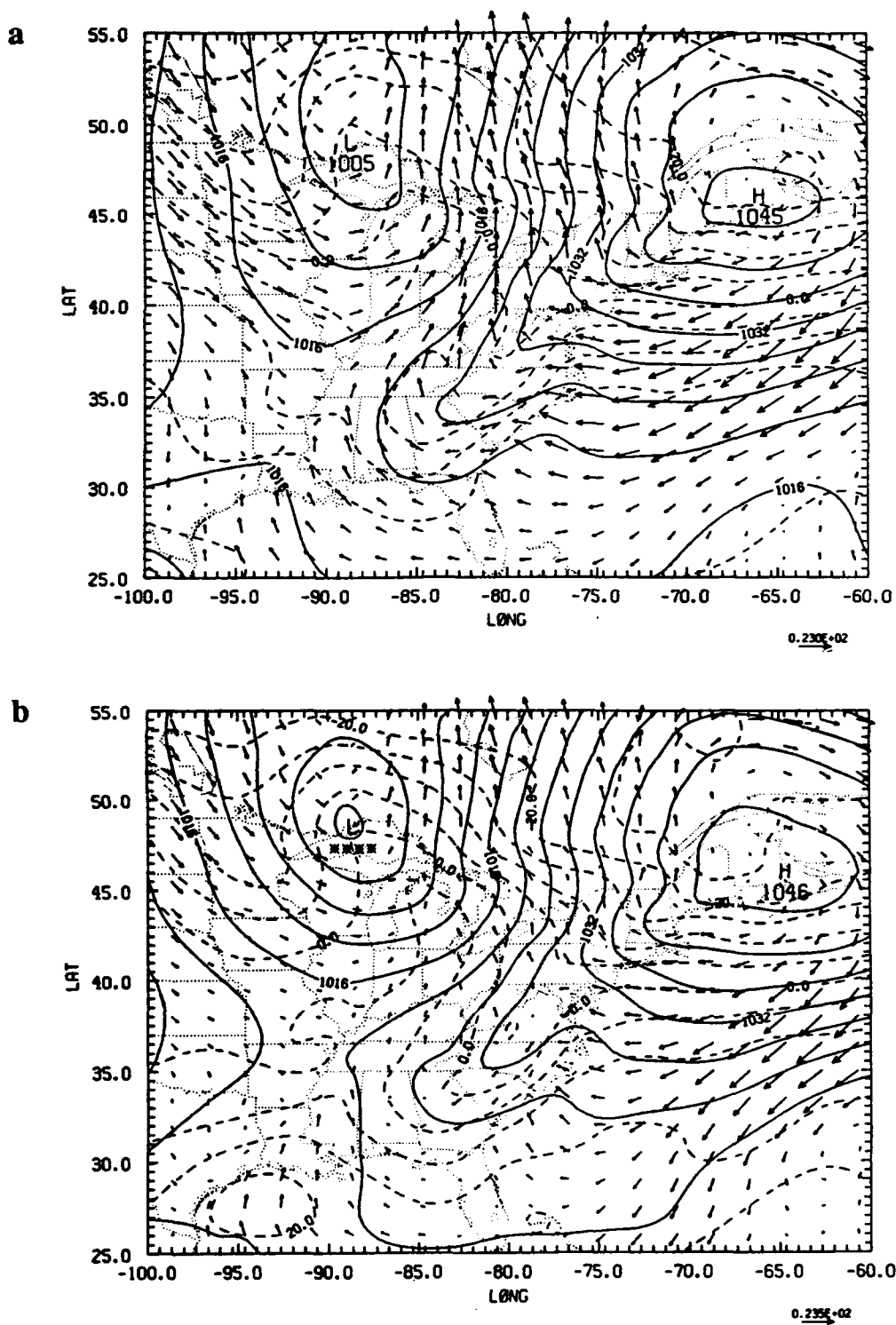


Figure 4.4. Sea-level pressure (mb) and 1000-mb temperature ( $^{\circ}\text{C}$ ) and winds at 25/12Z for (a) the first guess, a 12-h forecast from case 4.1 and (b) NRL analysis. (c) and (d) as in (a) and (b) but for the geopotential height (m), temperature ( $^{\circ}\text{C}$ ), and winds at 500 mb. Contours of geopotential and temperature at 500 mb are 60 m and  $2.5^{\circ}\text{C}$ , respectively.

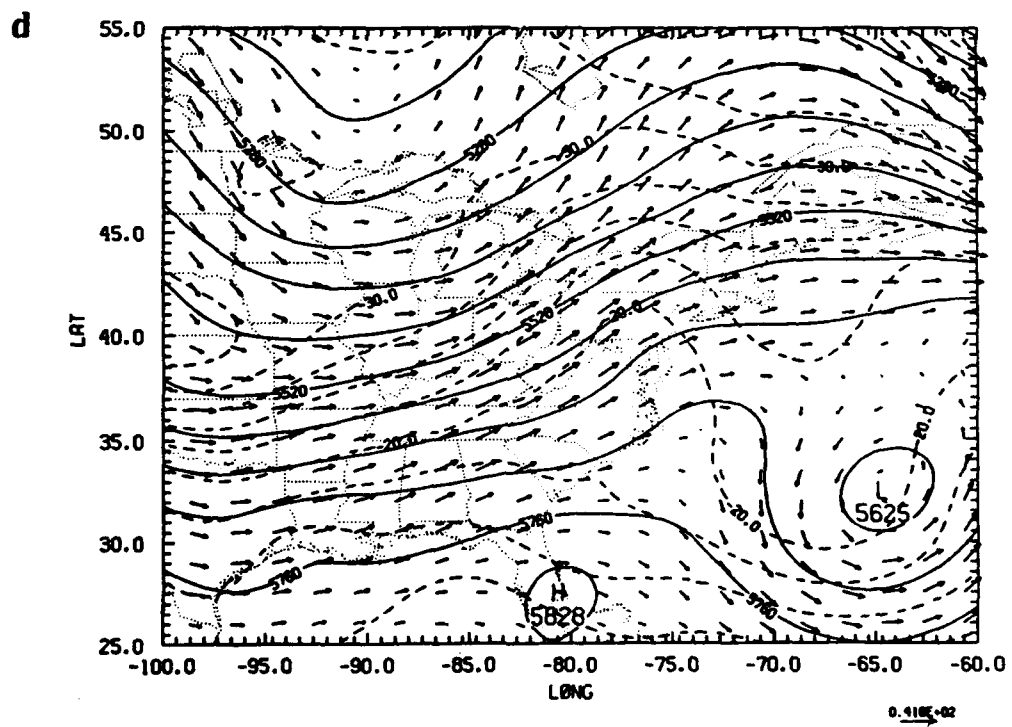
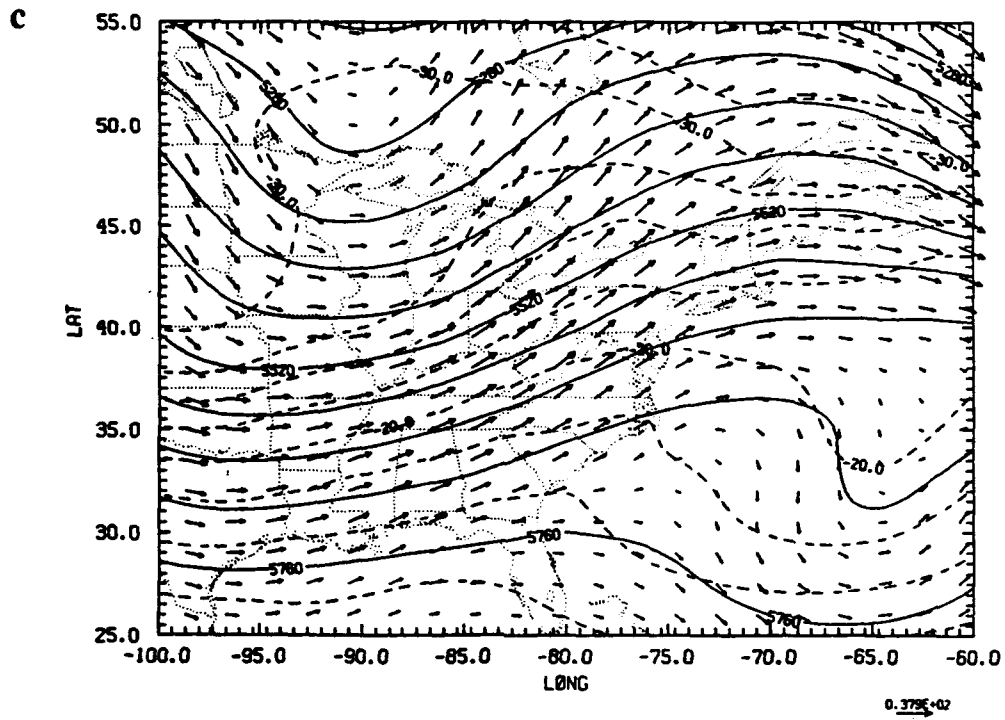


Figure 4.4. Continued.

St. Lawrence. The first-guess "low" was in error by 5 mb and was corrected totally by the NRL analysis.

The analysis of 500-mb geopotential height, temperature and winds are compared to the first guess in Figs. 4.4c and d. The NMC 500-mb analysis shown in Fig. 4.3b shows a cutoff low of 5627 m over the western Atlantic. The first-guess field provided by the model forecast failed to deepen the low significantly, and only a weak trough is present. The univariate NRL analysis (not shown) does capture this feature, but the low is not quite deep enough (5634 m). The multivariate analysis (Fig. 4.4d) is able to deepen the low even more to 5625 m by extrapolating geopotential heights using wind information, and the associated winds are somewhat stronger. It is worth noting that the data used in the NRL analysis in the vicinity of the cutoff low are in fact bogus values derived from the NMC analysis (see Fig. 4.1a). The NRL multivariate analysis, as noted above, reproduced the NMC analysis for the cutoff low with remarkable accuracy, considering the coarse resolution of the bogus data supplied to the analysis. The first-guess 500-mb temperature field is out of phase in the Great Lakes region. The  $-30^{\circ}\text{C}$  isotherm in the NMC analysis is over Lake Michigan, whereas the first-guess forecast has it lagging too far to the west over Minnesota. Some improvement is gained with the NRL univariate analysis, but the phase error is totally corrected by the multivariate analysis.

The NRL analysis is successful in pushing the first-guess 500-mb relative humidity field toward the NMC analysis (not shown). In particular, a high moisture tongue off the Carolina coast was absent in the first-guess field. The NRL analysis was successful in moistening the model environment to the appropriate level. The 250-mb jet associated with the upper-level long wave trough is depicted in Fig. 4.5. The jet from the first guess is too weak and broad with a jet maximum of about  $50 \text{ m s}^{-1}$ , compared to the NMC analysis which has a jet maximum of  $55 \text{ m s}^{-1}$ . Both the univariate and

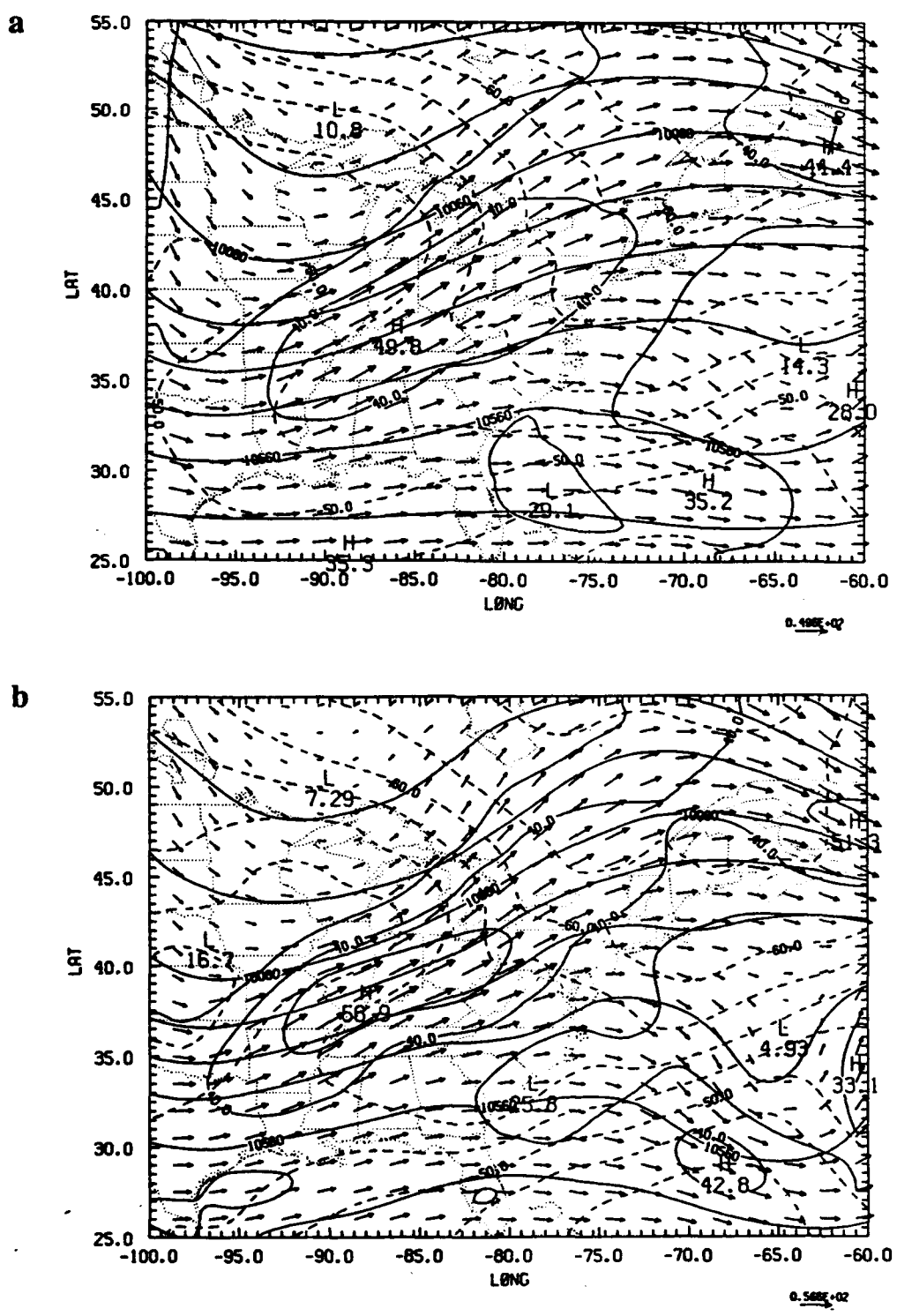


Figure 4.5. Geopotential height (m), temperature ( $^{\circ}\text{C}$ ), and winds at 250 mb for (a) the first guess, a 12-h forecast from case 4.1, (b) the NRL analysis, and (c) the NMC analysis on 25/12Z . Contours of geopotential are every 120 m and isotachs above  $30 \text{ m s}^{-1}$  are shown every  $10 \text{ m s}^{-1}$ .

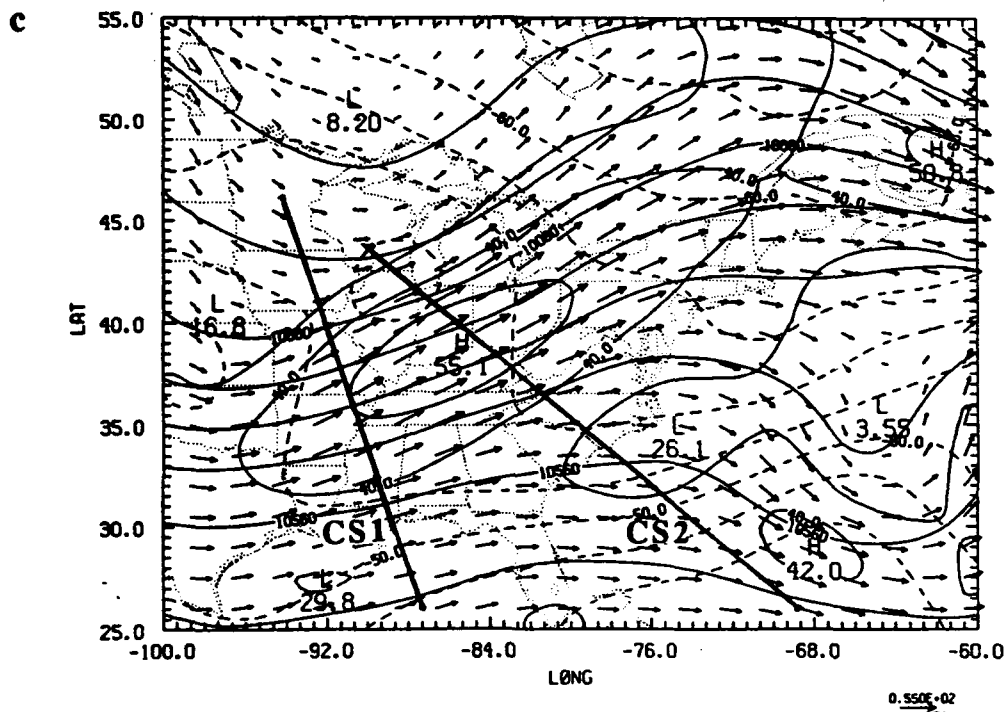


Figure 4.5. Continued.

multivariate analyses corrected the wind speeds and sharpened the jet, with the multivariate analysis having a slightly smaller maximum than the univariate analysis. Actually the analyzed jet maximum in the multivariate case is still  $2 \text{ m s}^{-1}$  stronger than that in the NMC analysis. However, this is not alarming since our analysis is on a finer scale than the NMC analysis.

The first-guess second-order fields of absolute vorticity and the vertical motion are significantly improved by the NRL objective analysis. The 500-mb absolute vorticity and vertical motion fields for the first guess and NRL analysis are shown in Fig. 4.6. For comparison, the vorticity and vertical motion derived from the NMC analysis are shown in Fig. 4.7. The vertical motion from the analyses is derived by application of the vertical mode initialization procedure. The NRL multivariate analysis greatly improved the overall pattern, including the gradients of vorticity, when compared to the first-guess field. The vorticity maxima for the multivariate analysis are close in value to those in the NMC analysis. In the first-guess vertical motion field, the subsidence west of the cutoff low is strengthened by the NRL analysis and is in close agreement with that derived for the NMC analysis. However, the rising motion associated with the developing coastal front in the first-guess field is retained in the NRL analysis. The rising motion, associated with the surface cyclone located on the southeast Texas coast and a secondary circulation of the upper-level jet's entrance region, is evident over eastern Texas and northern Mississippi. These two centers of ascending motion are better defined in the NRL analysis than either the first guess or the NMC analysis.

Cross sections were produced to further investigate the secondary ageostrophic circulations, associated with the upper-level jet and the coastal front. The locations of the cross sections are displayed in Fig. 4.5c. Cross section CS1 ( $94^{\circ}\text{W}$ ,  $46^{\circ}\text{N}$  to  $87.3^{\circ}\text{W}$ ,  $26^{\circ}\text{N}$ ), which extends from Minnesota to the central Gulf of Mexico, cuts across the entrance region of the upper-level polar jet. The second cross section (CS2 from  $90^{\circ}\text{W}$ ,

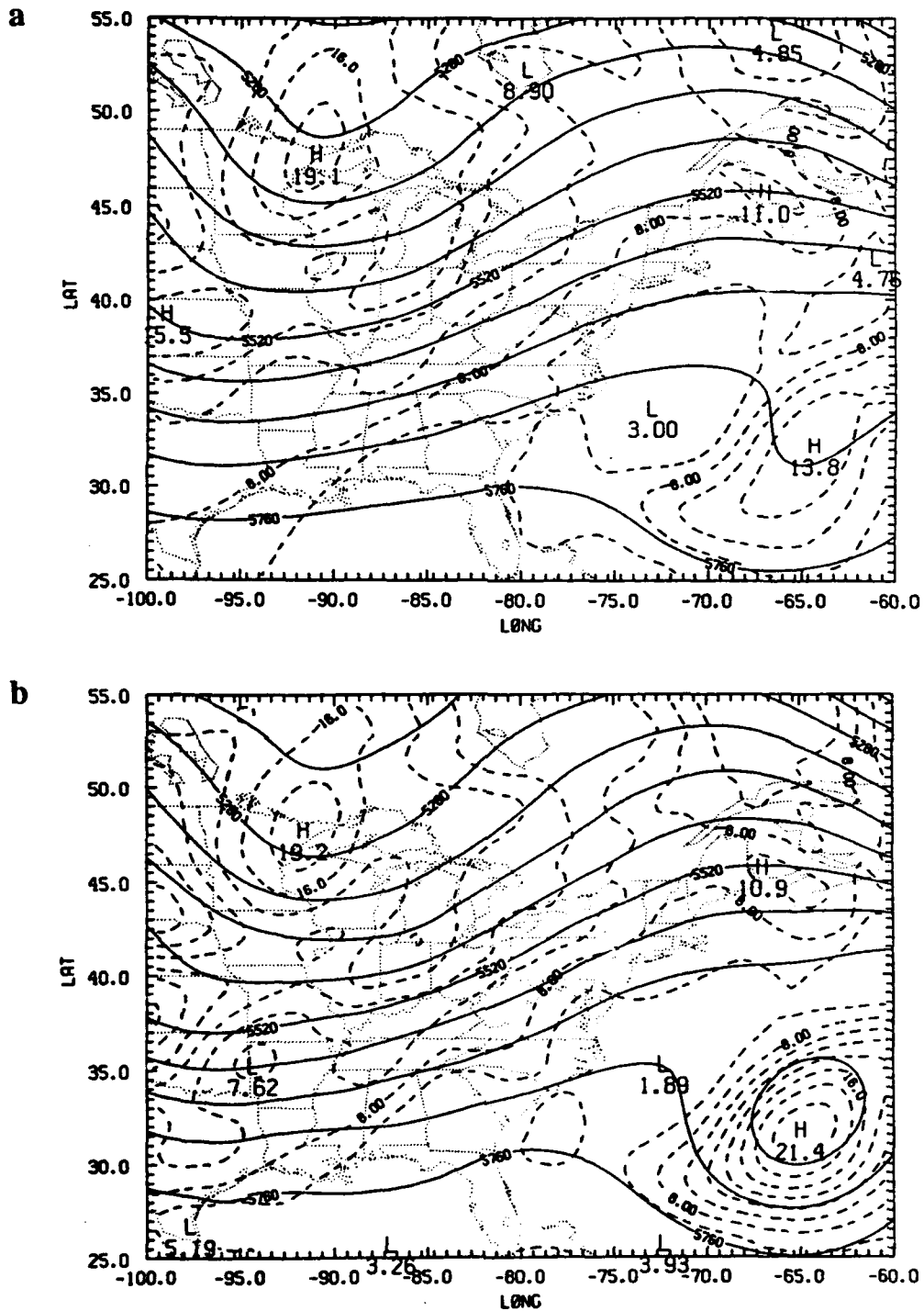


Figure 4.6. Absolute vorticity (in units of  $10^{-5} \text{ s}^{-1}$ ) with geopotential height (m) at 500 mb on 25/12Z for (a) the first guess 12-h forecast from case 4.1, and (b) the NRL analysis. The vertical velocity motion in  $\text{mb h}^{-1}$  at 500 mb for (c) the first guess and (d) the NRL analysis. Contours of vorticity are shown for 6 units and above every 2 units.

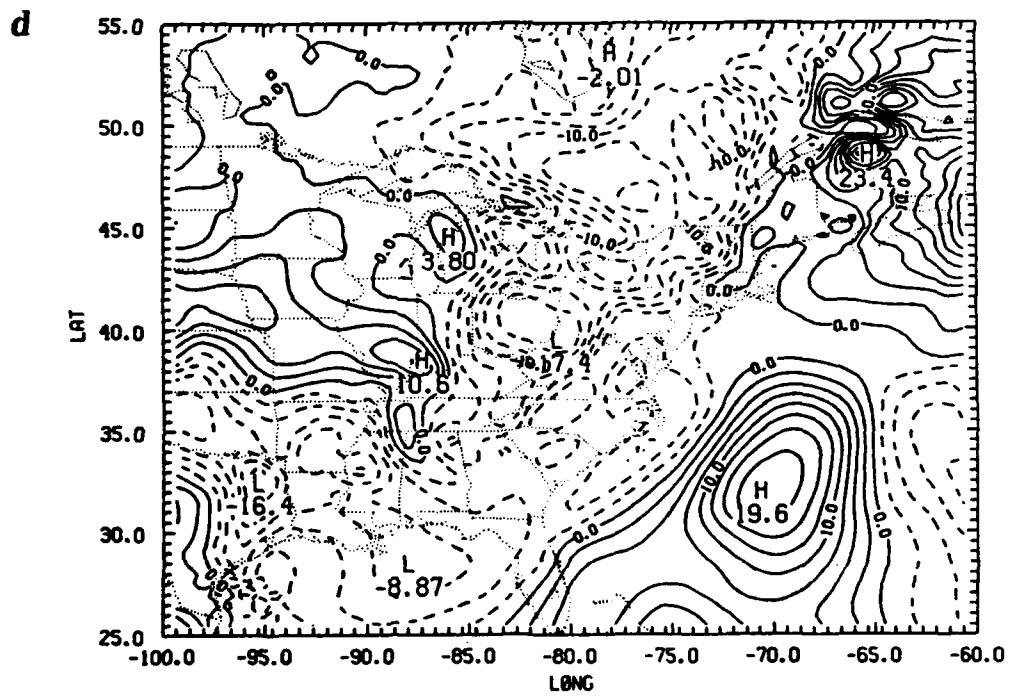
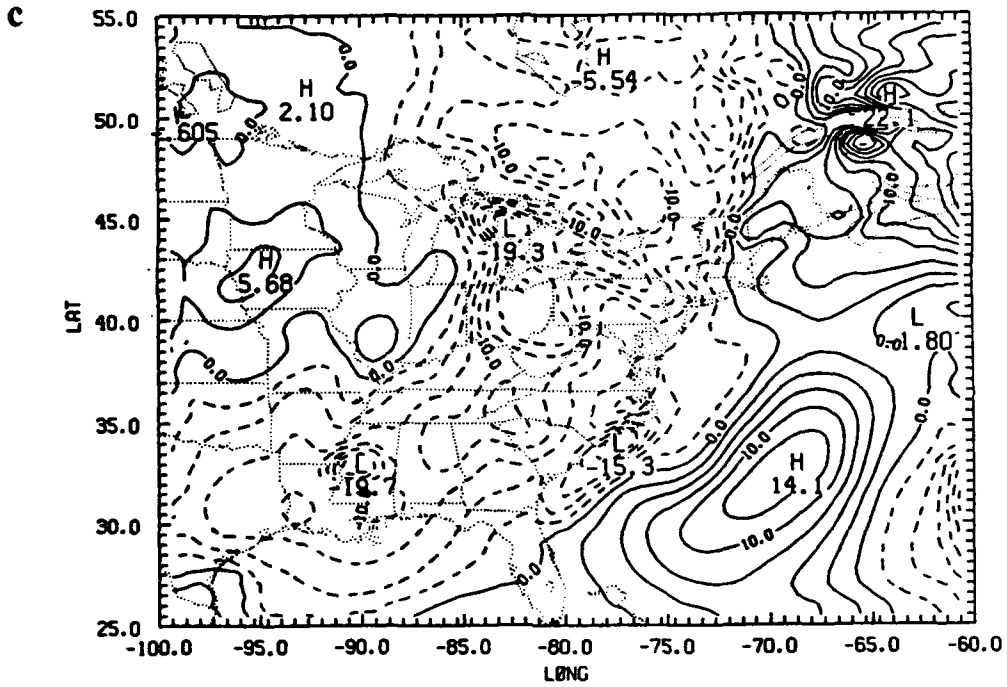


Figure 4.6. Continued.

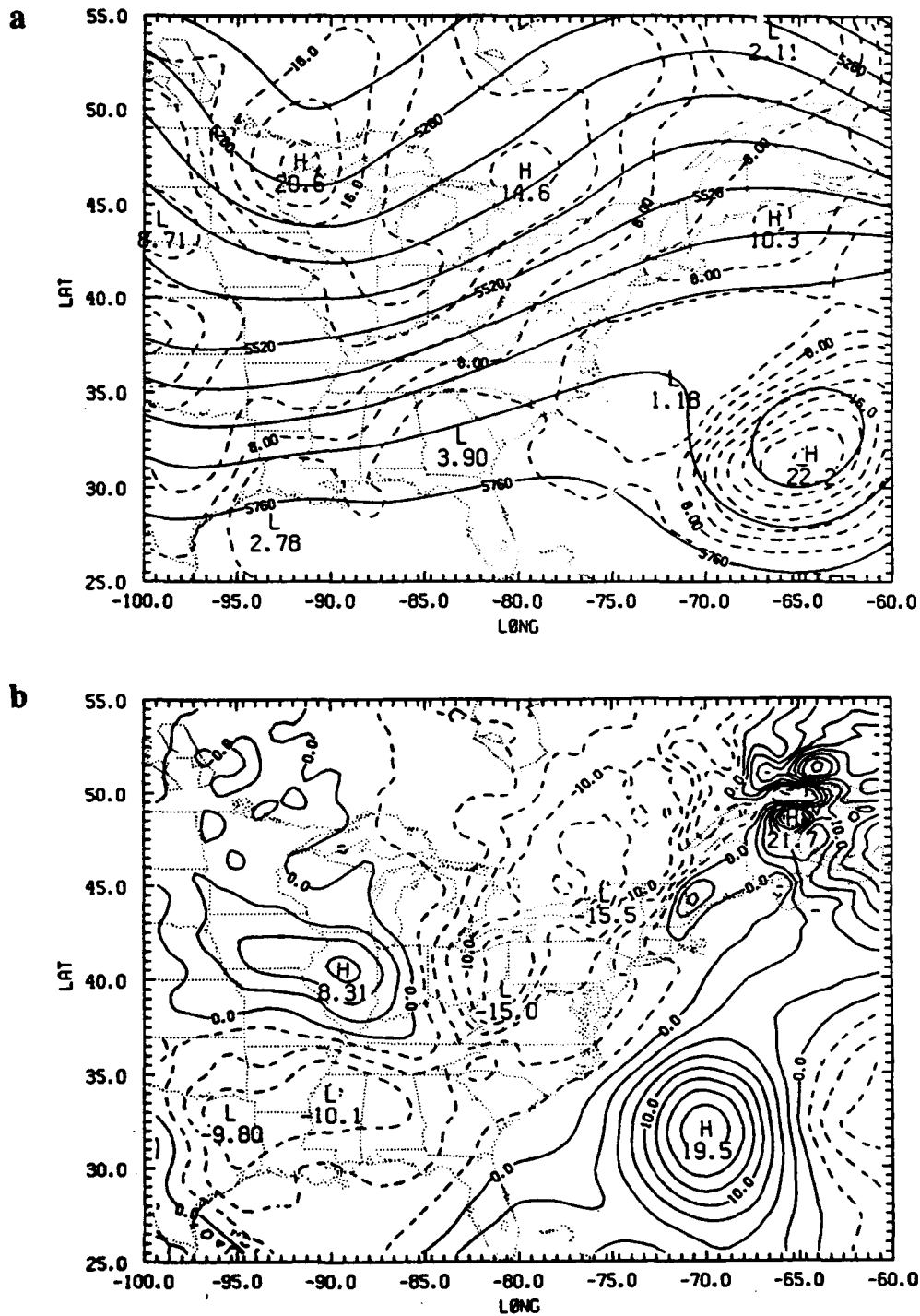


Figure 4.7. (a) Absolute vorticity (in units of  $10^{-5} \text{ s}^{-1}$ ) with geopotential height (m) and (b) the vertical velocity in  $\text{mb h}^{-1}$  at 500 mb on 25/12Z for the NMC analysis. Vertical motion of magnitudes  $-20 \text{ mb h}^{-1}$  or greater are contoured every  $2.5 \text{ mb h}^{-1}$ .

43.5°N to 68.7°W, 26°N) is perpendicular to the Carolina coast. In all figures displaying cross sections, the positions of the grid points every 0.5° in latitude are denoted by the inner tick marks for facilitation in locating meteorological features of interest. The wind speed normal to each cross section is shown in Fig. 4.8. In the cross section across the Gulf of Mexico, the NMC analysis at 25/12Z (Fig. 4.9b) shows a broad region of ascending motion in the right rear flank of the polar jet. The NRL analysis (Fig. 4.9a) has enhanced the secondary circulation in this region. The maximum vertical velocity is 40% greater than in the NMC analysis ( $-14 \text{ mb h}^{-1}$  vs.  $-10 \text{ mb h}^{-1}$ ). Also, more evident in the NRL analysis is the ascent associated with the subtropical jet stream to the south. Figure 4.10 depicts the cross section perpendicular to the Carolina coast for both the NRL and NMC analyses. As shown in Fig. 4.10a, the NRL analysis is successful in maintaining the shallow ascent associated with the coastal front, which was generated in the first-guess forecast. Note the maximum ascent of  $-18.3 \text{ mb h}^{-1}$  about 15000 km from the northernmost end (left side of cross section) in Fig. 4.10a. This circulation is much stronger and more well-defined than the corresponding circulation from the NMC analysis (Fig. 4.10b). The subsidence west of the cutoff low in the subtropical jet stream and ascent east of the approaching upper-level trough (see Fig. 4.6) are also seen in both cases. Increased humidities at low levels offshore and over the coastal front, with dryer values behind the front, are seen in Fig. 4.10c for the NRL analysis. A narrower tongue of high humidity is also found at mid-levels.

#### 4.4.2 Comparison of Model Forecasts (25/12Z-26/12Z)

Forecasts using the different analyses to derive the initial conditions are compared in cases 4.3 and 4.4. After 6 h of model integration (at 25/18Z), the forecast based on the NMC analysis (case 4.4) still contained a relatively weak thermal gradient in the

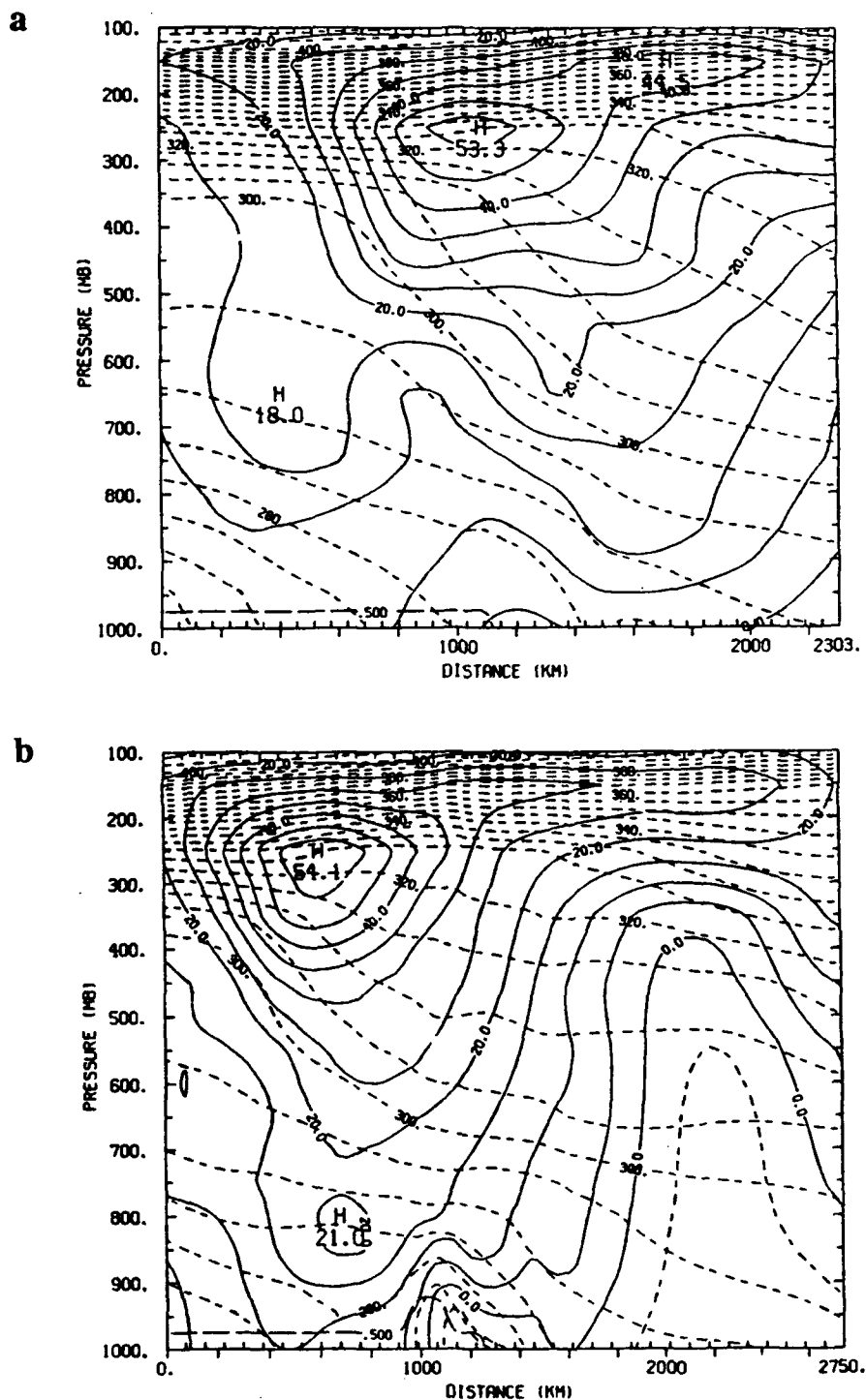


Figure 4.8. Magnitude of the wind normal to the plane of cross sections (a) CS1 and (b) CS2 at 25/12Z for the NRL analysis (see Fig. 4.5c). Contours every  $5 \text{ m s}^{-1}$ . Potential temperature ( $^{\circ}\text{K}$ ) is also shown by the dashed contours every  $5^{\circ}\text{K}$  in the troposphere. The position of the grid points every  $0.5^{\circ}$  in latitude are shown by the inner tick marks.

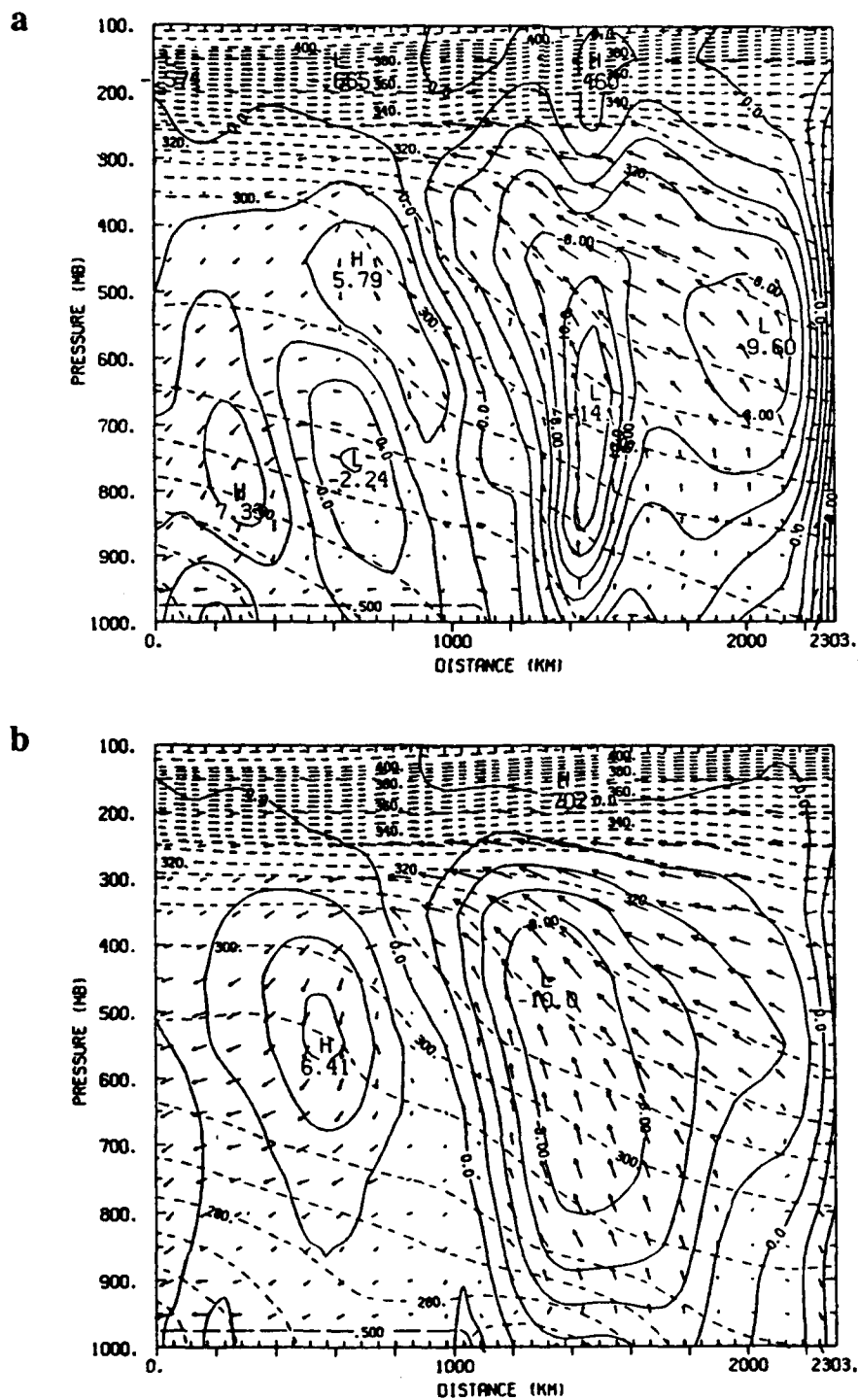


Figure 4.9. The vertical motion and ageostrophic wind in the plane of cross section CS1 at 25/12Z for (a) the NRL analysis and (b) for the NMC analysis. The magnitude of the vertical motion is represented by the solid contours at -40, -25, -20, -15, -12.5, and every 2 mb h<sup>-1</sup> for values -10 and above.

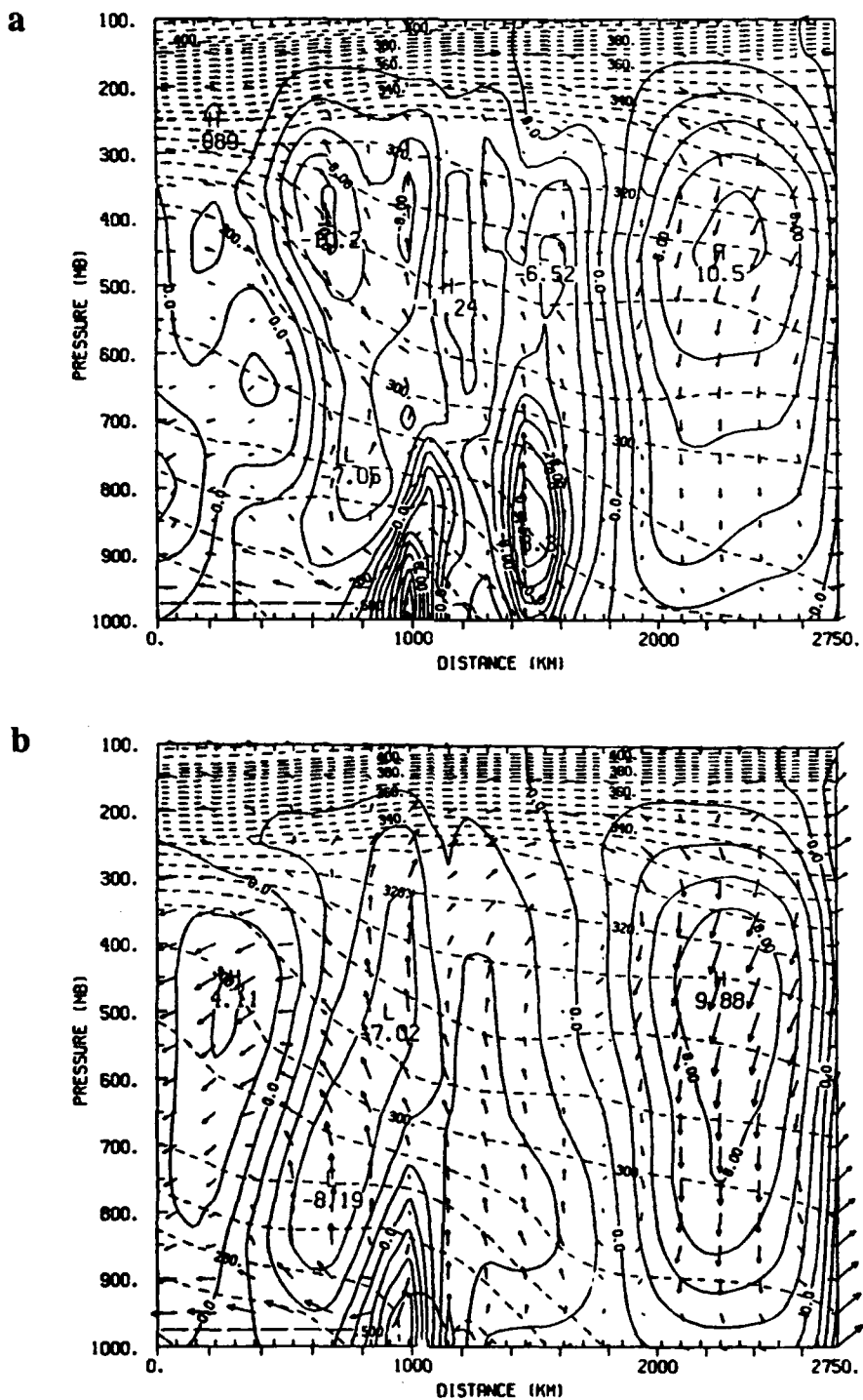


Figure 4.10. The vertical motion and ageostrophic wind in the plane of cross section CS2 at 25/12Z for (a) the NRL analysis and (b) for the NMC analysis. (c) and (d) as in (a) and (b) but for the relative humidity, contoured every 10% for 30% and above. Contours of vertical motion as in Fig. 4.9. See Fig. 4.5c for location of CS2.

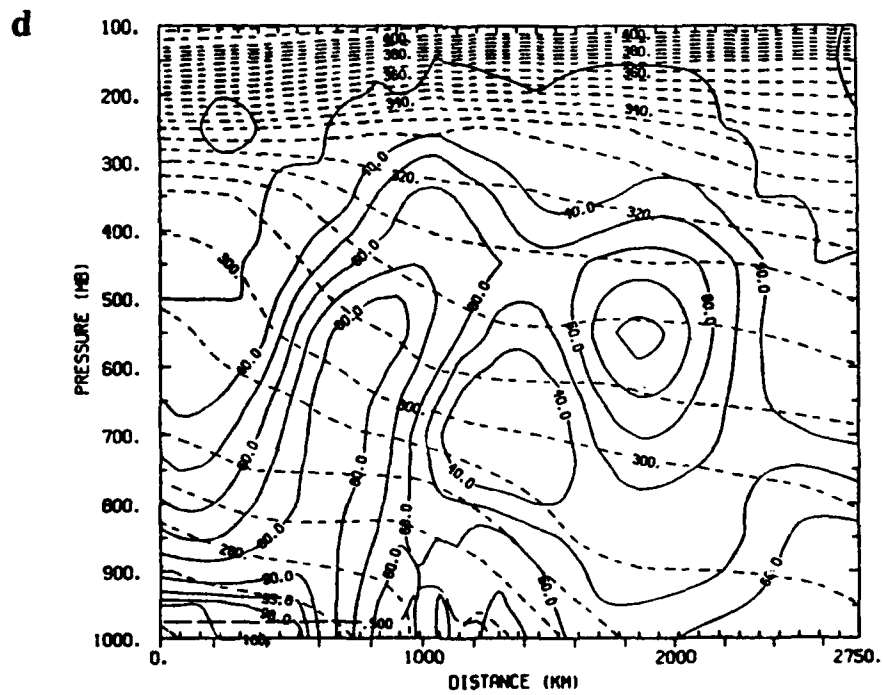
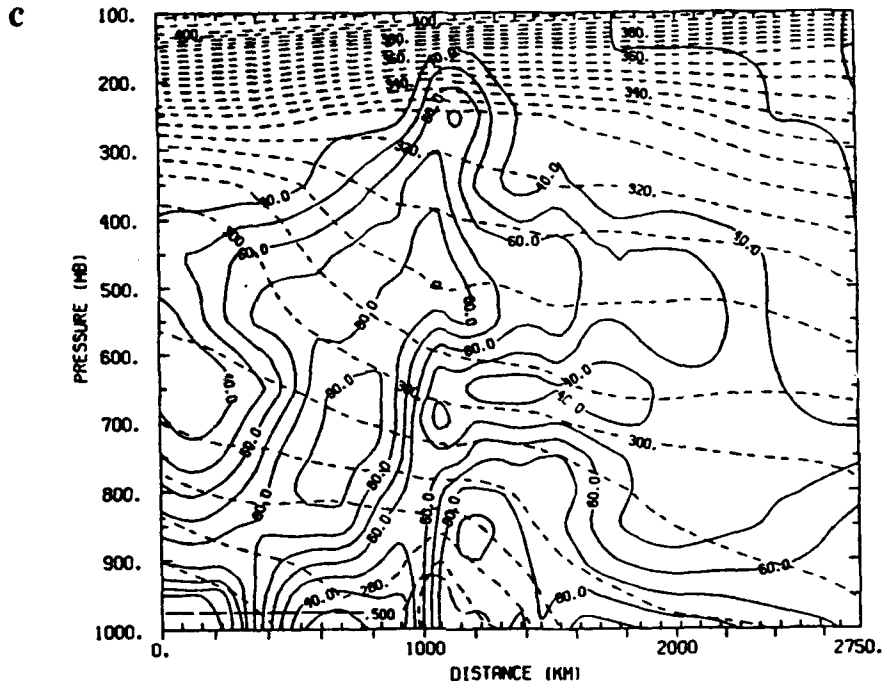


Figure 4.10. Continued.

vicinity of the coastal front (shown in Fig. 4.11a), since the model was still in a spin-up mode. An inverted surface trough is present near Jacksonville, Florida in Fig. 4.11b in the case using the NRL analysis (case 4.3). This feature is weaker and further east in the NMC case. Bosart's analysis (Fig. 4.12) verifies the presence of the trough with the genesis of a cyclonic circulation. A weak surface low is also indicated just north of New Orleans in better agreement with the Bosart analysis, than the NMC case. The weak coastal circulation, which forms a low pressure center that moves northeast along the coast, is handled better in the NRL case compared to that using the NMC analysis.

The 500-mb mass and wind fields are very similar from both cases at 25/18Z. However, differences do exist in the 500-mb vertical motion (Fig. 4.13) and moisture fields (not shown). In the NRL case 4.3, a significant upward vertical motion had developed off the Carolina coast. These vertical velocities are missing in the NMC case 4.4. As a result, no precipitation was forecast along the coastal front during the first 6 h of integration in the case originating from the NMC analysis. Case 4.3 also produced stronger vertical motions over the Mississippi Gulf coast associated with the secondary jet circulation and an area of positive vorticity advection at 500 mb. Both 25/12Z analyses, NMC and NRL, had a strong 500-mb moisture tongue off the Carolina coast. Unlike that of the NMC case, the stronger coastal front circulation from the NRL case had pushed the moisture tongue inland by 25/18Z.

At 26/00Z, the coastal front has developed from Georgia to southern New England in an onshore easterly flow regime. Figure 4.14a illustrates that NRL case still retains a stronger thermal gradient associated with the front than does the NMC case 4.4 (Fig. 4.14b). The inverted surface trough of low pressure remains more pronounced in the NRL case as compared to the NMC case. In both cases, the surface low along the Alabama coast is in good agreement with the analyses of Bosart and Doyle and Warner for position and intensity.

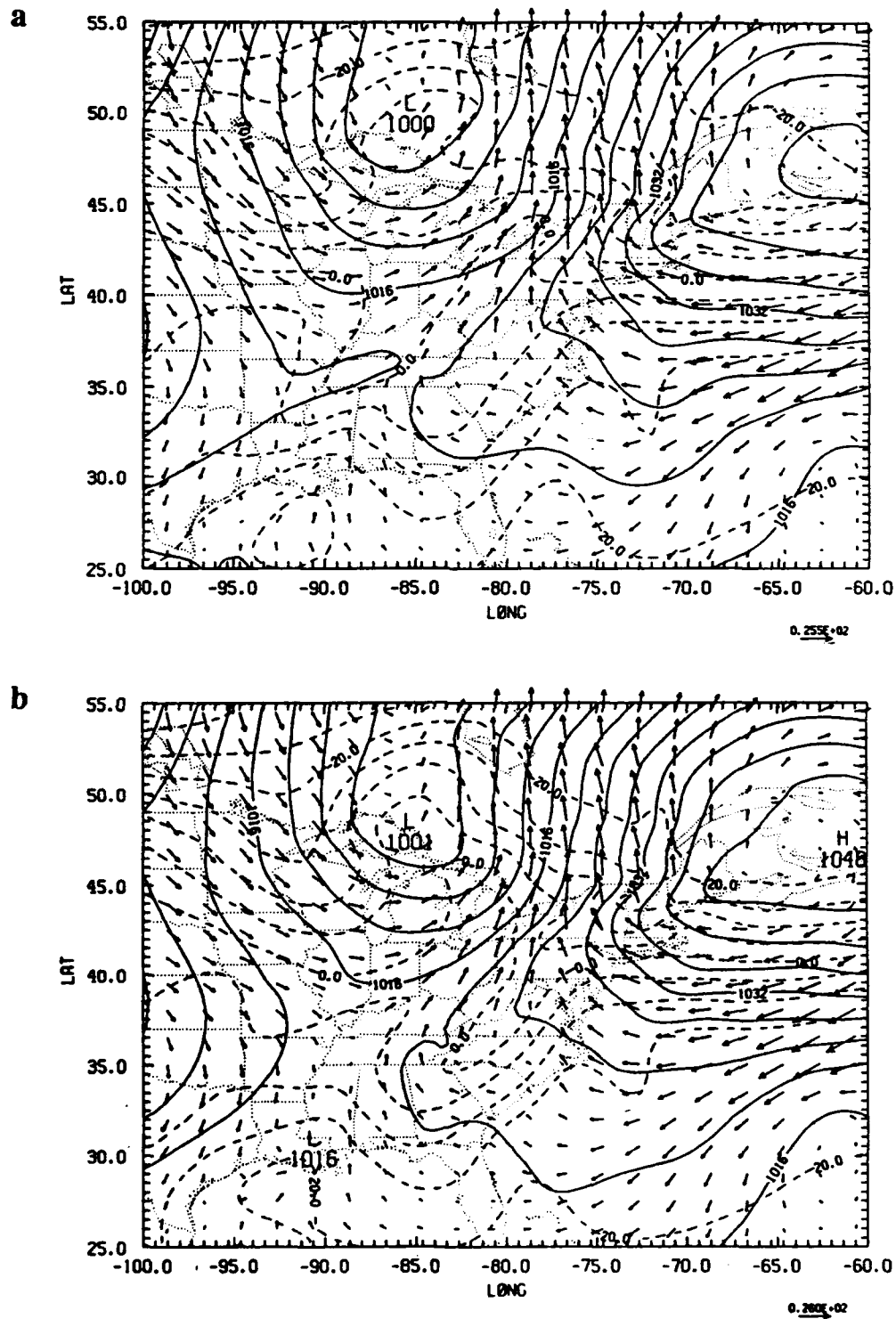


Figure 4.11. Six-hour forecast of sea-level pressure (mb), surface air temperature ( $^{\circ}$ C), and 1000 mb winds valid at 25/18Z for (a) case 4.4 from the NMC analysis and (b) case 4.3 from the NRL analysis. Contours as in Fig. 4.3.

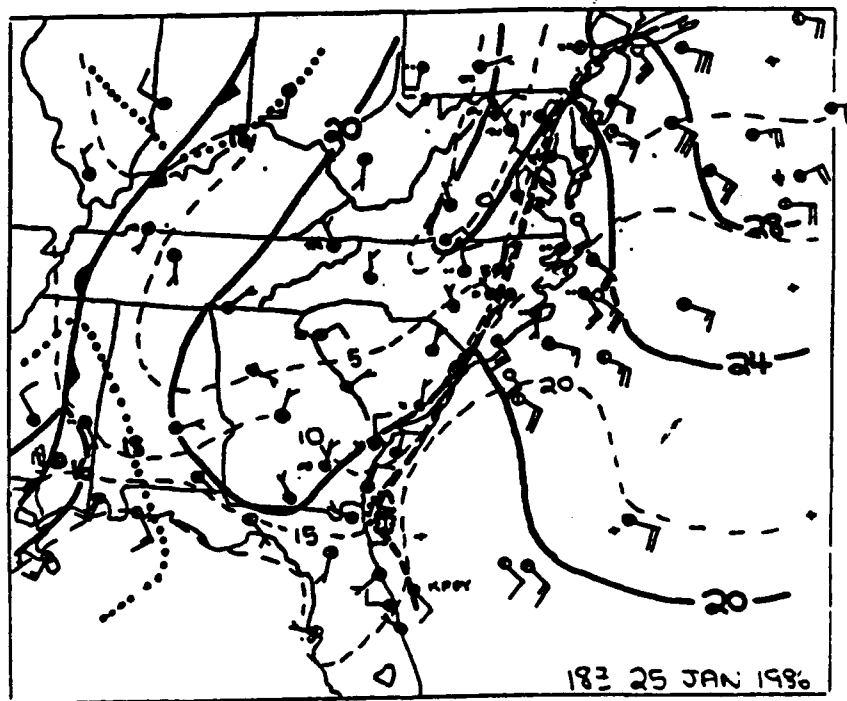


Figure 4.12. GALE analysis of sea-level pressure deviation (from 1000 mb), surface temperature ( $^{\circ}\text{C}$ ) and wind for 25/18Z by Bosart (1988). Surface temperature contours every  $5^{\circ}\text{C}$ .



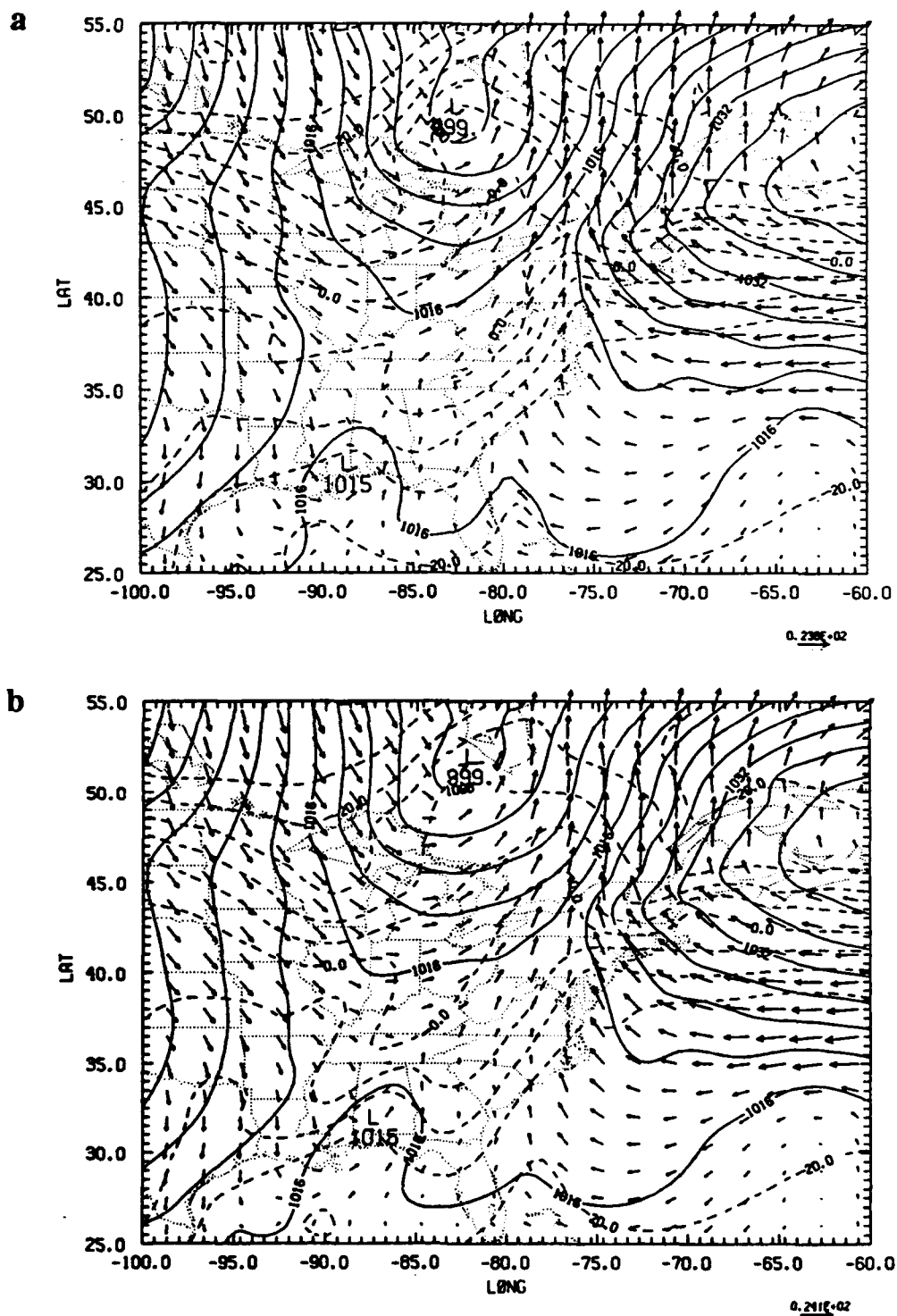
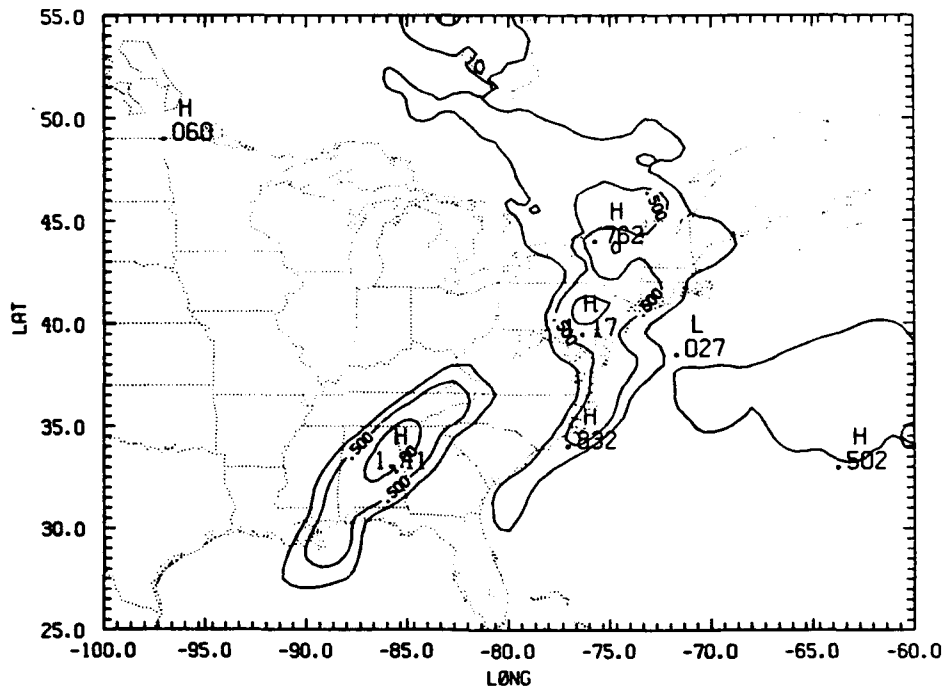


Figure 4.14. Twelve-hour forecast of sea-level pressure (mb), temperature ( $^{\circ}$ C) and winds at 1000 mb valid at 26/00Z for (a) case 4.3 from the NRL analysis and (b) case 4.4 from the NMC analysis. (c) and (d) as in (a) and (b) but for the forecast of six-hour accumulated precipitation (25/18Z- 26/00Z) in cm. Contours of precipitation at 0.25 and every 0.5 cm for 0.5 and above.

c



d

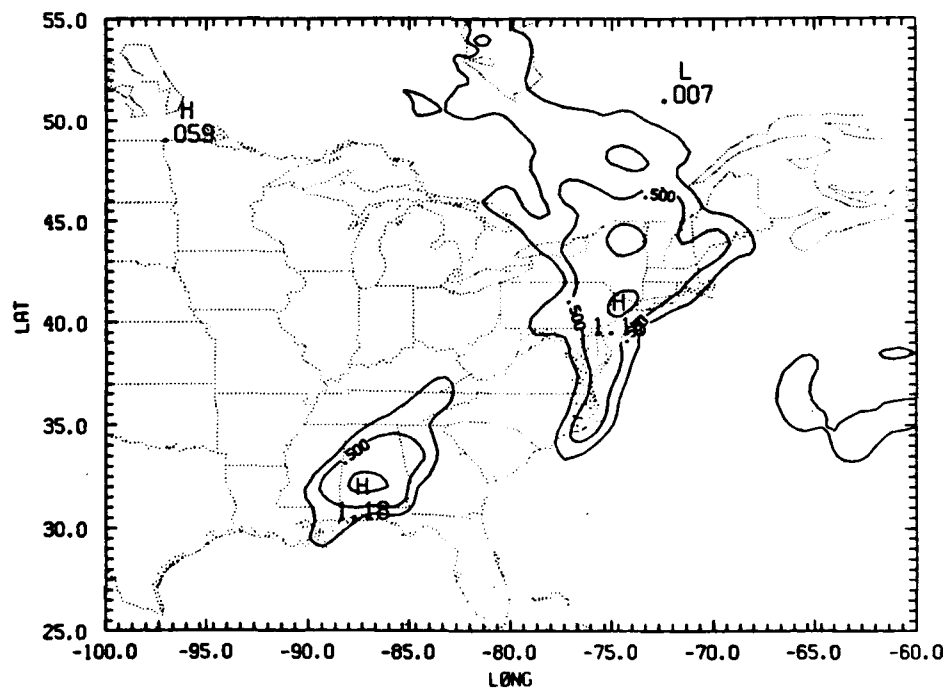


Figure 4.14. Continued.

The 500-mb relative humidity fields are now very similar; after 12 h of integration, model spinup in the NMC case is essentially complete. Still, the 500-mb absolute vorticity in the NRL case over Georgia associated with the surface cyclone along the central Gulf coast is much stronger than that in the NMC case. In addition, the upward vertical motion associated with the inverted surface trough, i.e. the southern extent of the coastal front, over the Georgia coast is much better developed in the forecast originating from the NRL multivariate analysis. Figures 4.14c and d depict the accumulated 6-h rainfall ending at 26/00Z for the NRL and NMC cases. The key difference is again that the NRL case is able to produce precipitation due to mesoscale circulations associated with the coastal front along the Georgia and South Carolina coasts; whereas, the NMC case fails to develop any rainfall in this region. The NRL case is in more agreement with the observed precipitation shown in Fig. 4.15, which does show rainfall associated with the coastal front and with the low along the Gulf coast.

The effects of starting with stronger secondary circulations in the entrance region to the jet and in the coastal front are illustrated in cross sections of the ageostrophic flow and the relative humidity across the Carolina coast in Fig. 4.16. The main difference is the stronger secondary circulation associated with the jet entrance region in the NRL case. In the NRL case (Fig. 4.16a), the coastal circulation is clearly captured by the jet's circulation, which also intensifies the subsidence in the cutoff low offshore and the ageostrophic flow across the coastal front. Higher low-level humidities are also advected over the front in the NRL case (Fig. 4.16b) to produce the forecast precipitation.

The cyclonic circulation which formed near Jacksonville, Florida continues up the coast as a weak low. By 26/06Z, it is located near Wilmington, North Carolina. The low along the central Gulf coast is just a few miles southeast of Pensacola, Florida. The positions of these circulations from the NRL case are in excellent agreement with Bosart's analysis (not shown). Once again, the 500-mb ascending vertical velocities

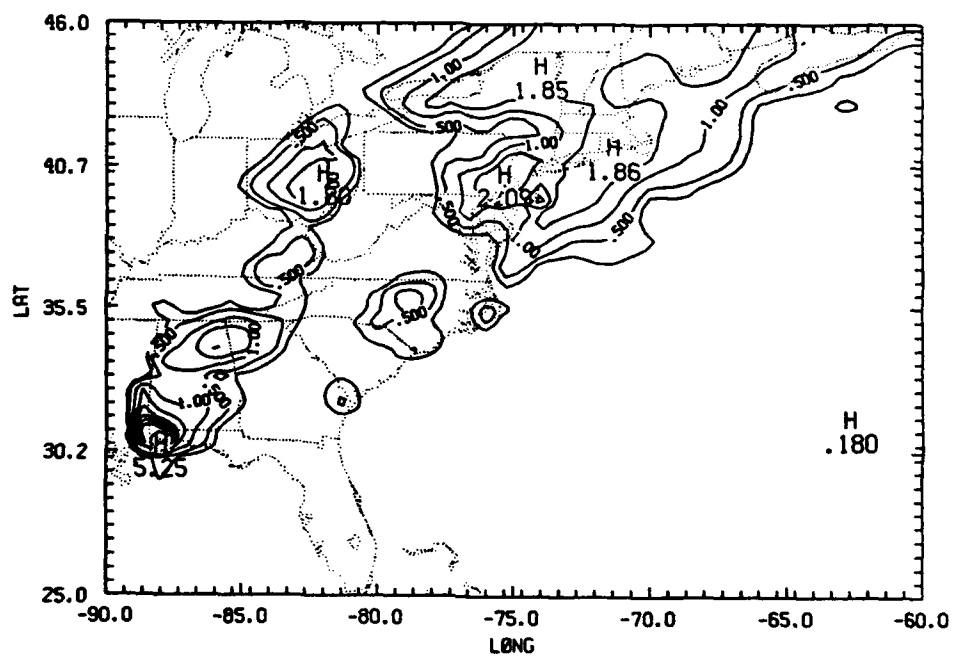


Figure 4.15. Six-hour accumulation of observed precipitation in cm for the same period as in Fig. 14 c and d. Contours of precipitation as in Fig. 4.14.

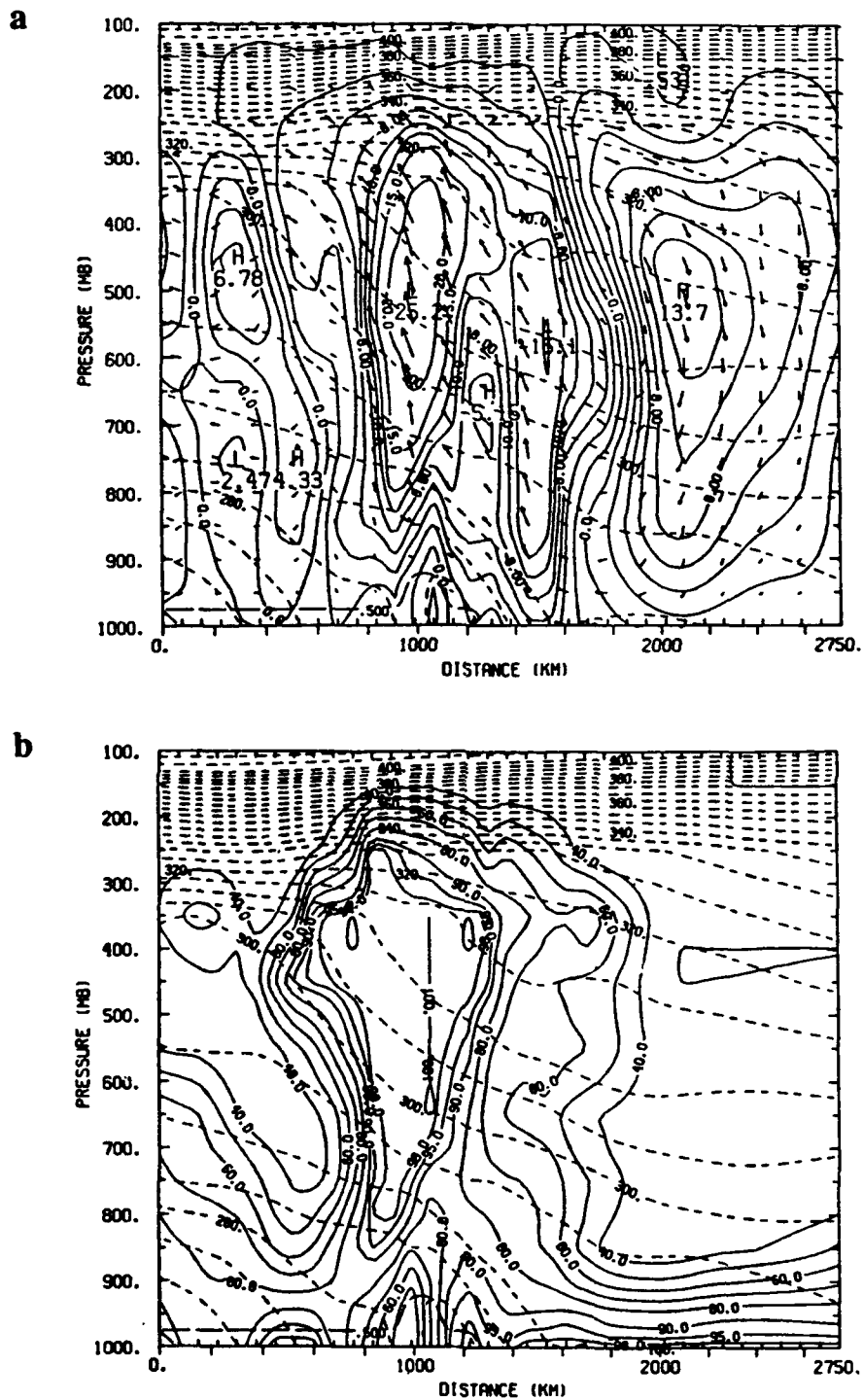


Figure 4.16. Twelve-hour forecast of (a) the vertical motion ( $\text{mb h}^{-1}$ ) and ageostrophic wind ( $\text{m s}^{-1}$ ) and (b) relative humidity (%) in the plane of cross section CS2 valid at 26/00Z for case 4.3 from the NRL analysis. (c) and (d) as in (a) and (b) but for case 4.4 from the NMC analysis. See Fig. 4.5c for location of CS2.

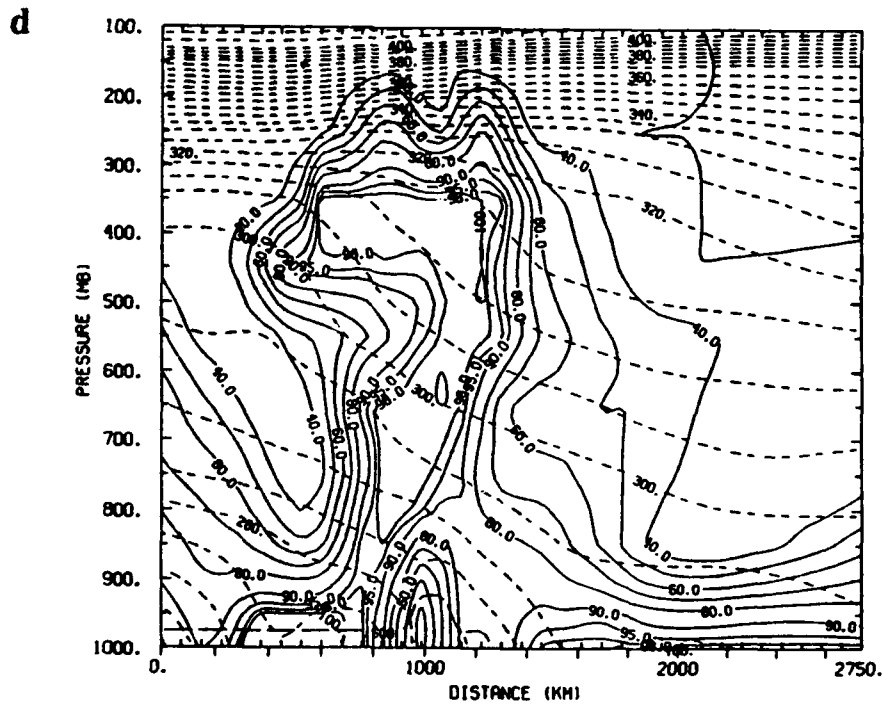
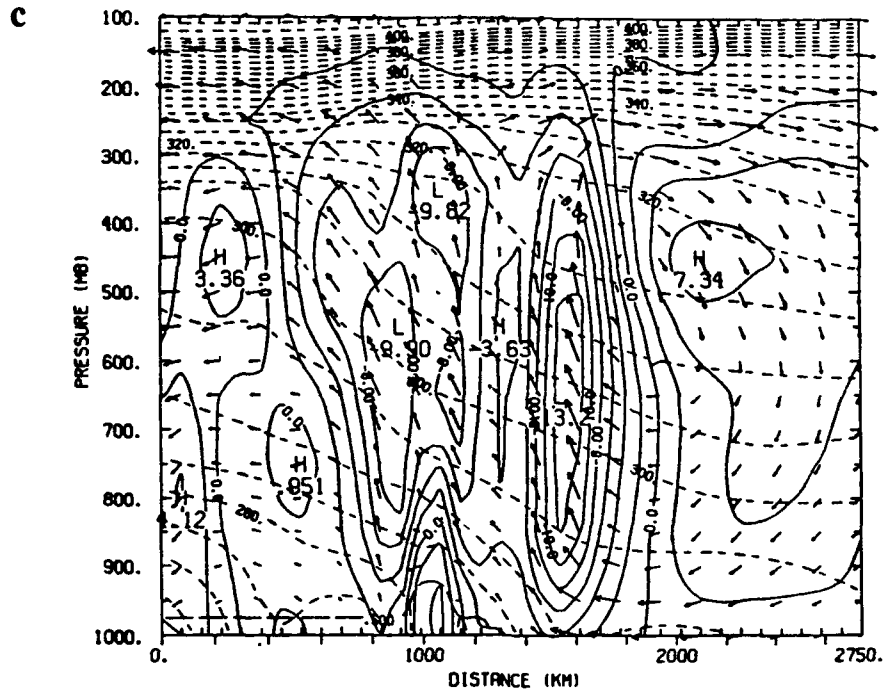


Figure 4.16. Continued.

along the coastal front and associated with the surface wave over the Florida panhandle are about 25% greater in the NRL case versus the NMC case.

#### 4.4.3 Comparisons using 26/00Z and 26/12Z Cases

The analyses for 26/00Z and the subsequent forecasts are compared in cases 4.5 and 4.6. At 26/00Z, the NRL analysis once again produced a much tighter thermal gradient across the coastal front than shown by the coarser NMC analysis. In this case however, the NRL analysis was able to significantly sharpen the first-guess temperature gradient across the Carolina coast. The cold air damming is missing in the first-guess field (Fig. 4.17a) and NMC analysis (not shown), but is still evident in the NRL analysis (Fig. 4.17b). The NRL/NCSU analysis scheme was able to use the observational data to enhance the background's weaker gradient generated by our mesoscale model.

At 500 mb, the NRL analysis in case 4.5, like in case 4.3, is successful in correcting the background fields. The phase of the temperature field is again adjusted and the cutoff low has been deepened by 48 m and is within 6 m of the NMC analyzed value. The strong vorticity maximum at the base of the large-scale trough at 500 mb is of the same magnitude in both cases. A weak vorticity maximum is present over Georgia in the NRL analysis (Fig 4.17d) which is not discernible in the NMC analysis (Fig 4.17c). This is a reflection of the stronger secondary circulation in the entrance region of the jet over the eastern U.S. as it interacts with the coastal low. At 250 mb, this jet is also stronger and sharper in the NRL analysis (not shown). As the short wave over the Great Lakes moves eastward, it produces confluence of the flow into the jet thereby strengthening it. The secondary circulation in the entrance region of the jet has begun to absorb and deepen the coastal front's ageostrophic circulation as shown in the cross sections (CS2) in Fig. 4.18. However, the coastal front circulation is still a distinct

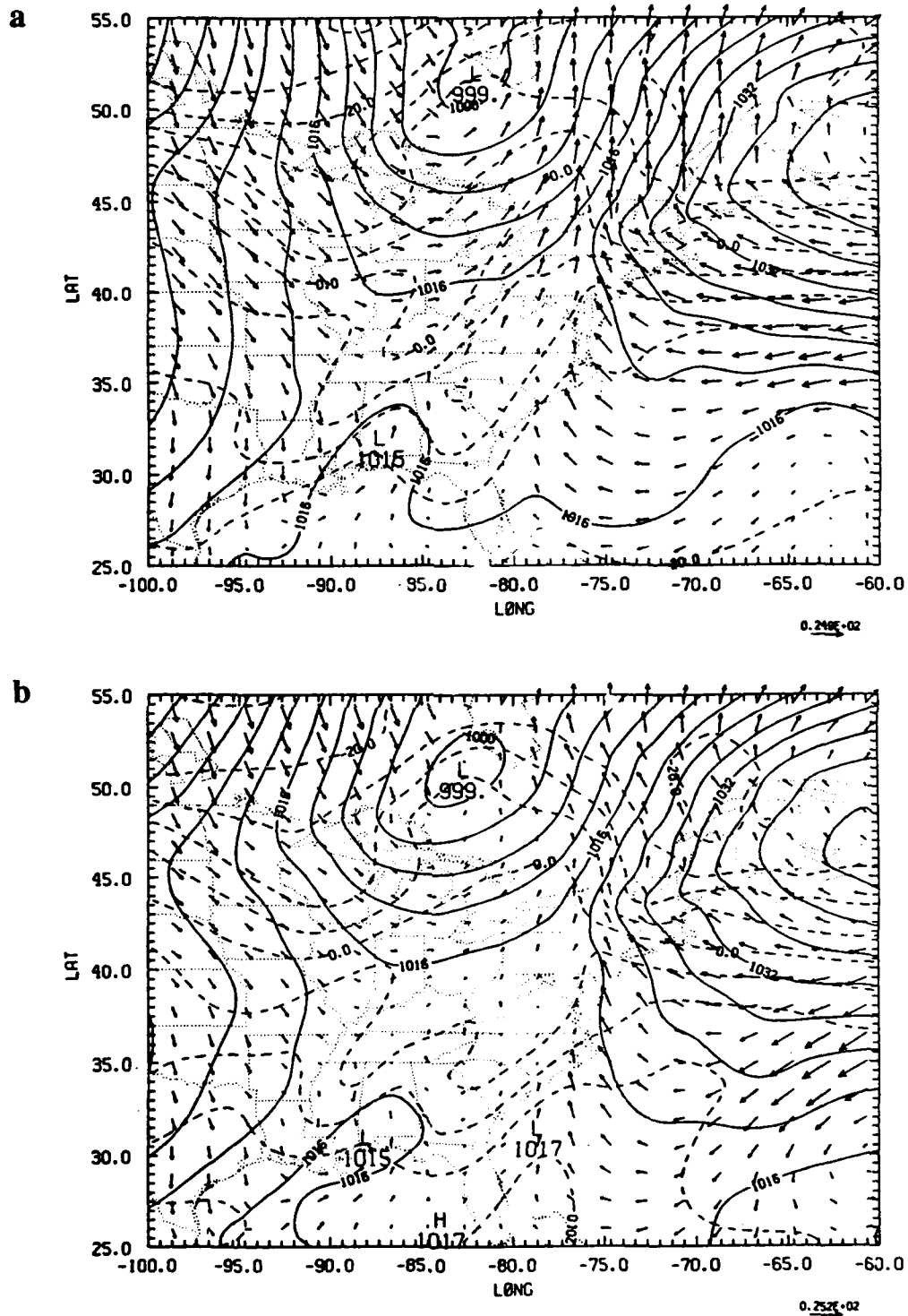


Figure 4.17. Sea-level pressure (mb) and 1000-mb temperature ( $^{\circ}\text{C}$ ) and winds at 26/00Z for (a) the first guess, a 12-h forecast from case 4.4 and (b) the NRL analysis. Absolute vorticity (in units of  $10^{-5} \text{ s}^{-1}$ ) with geopotential height (m) at 500 mb at the same time for (c) the NMC analysis and (d) the NRL analysis.

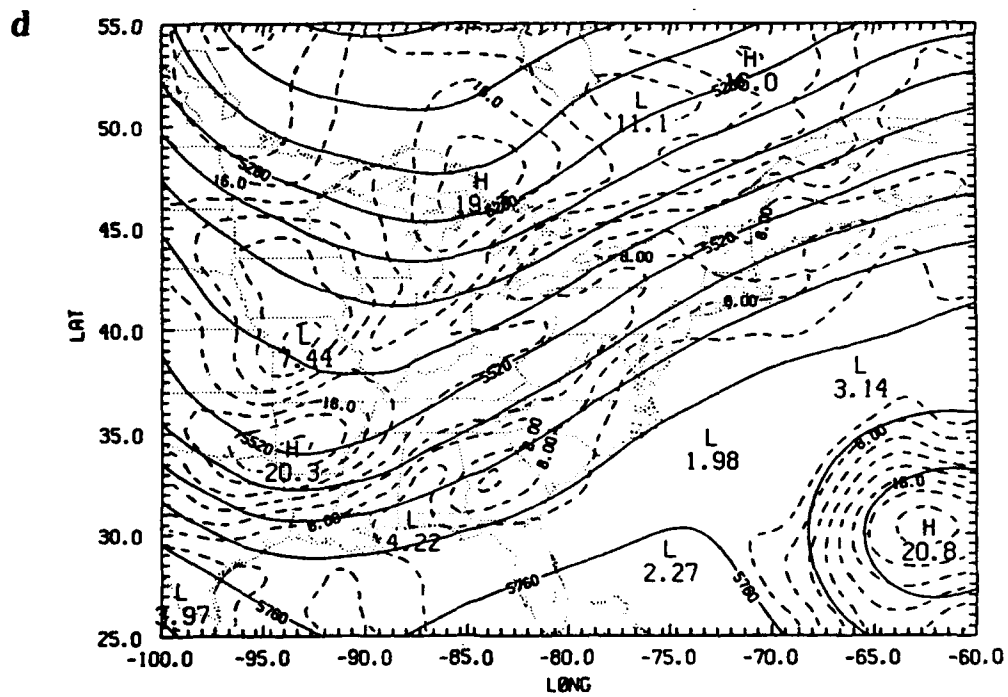
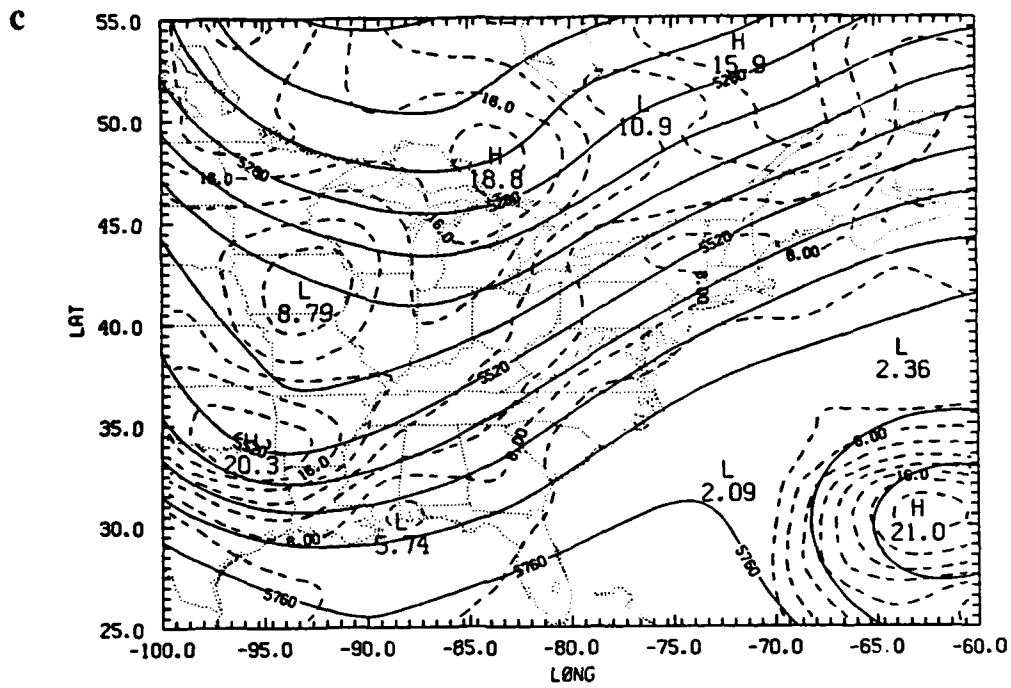


Figure 4.17. Continued.

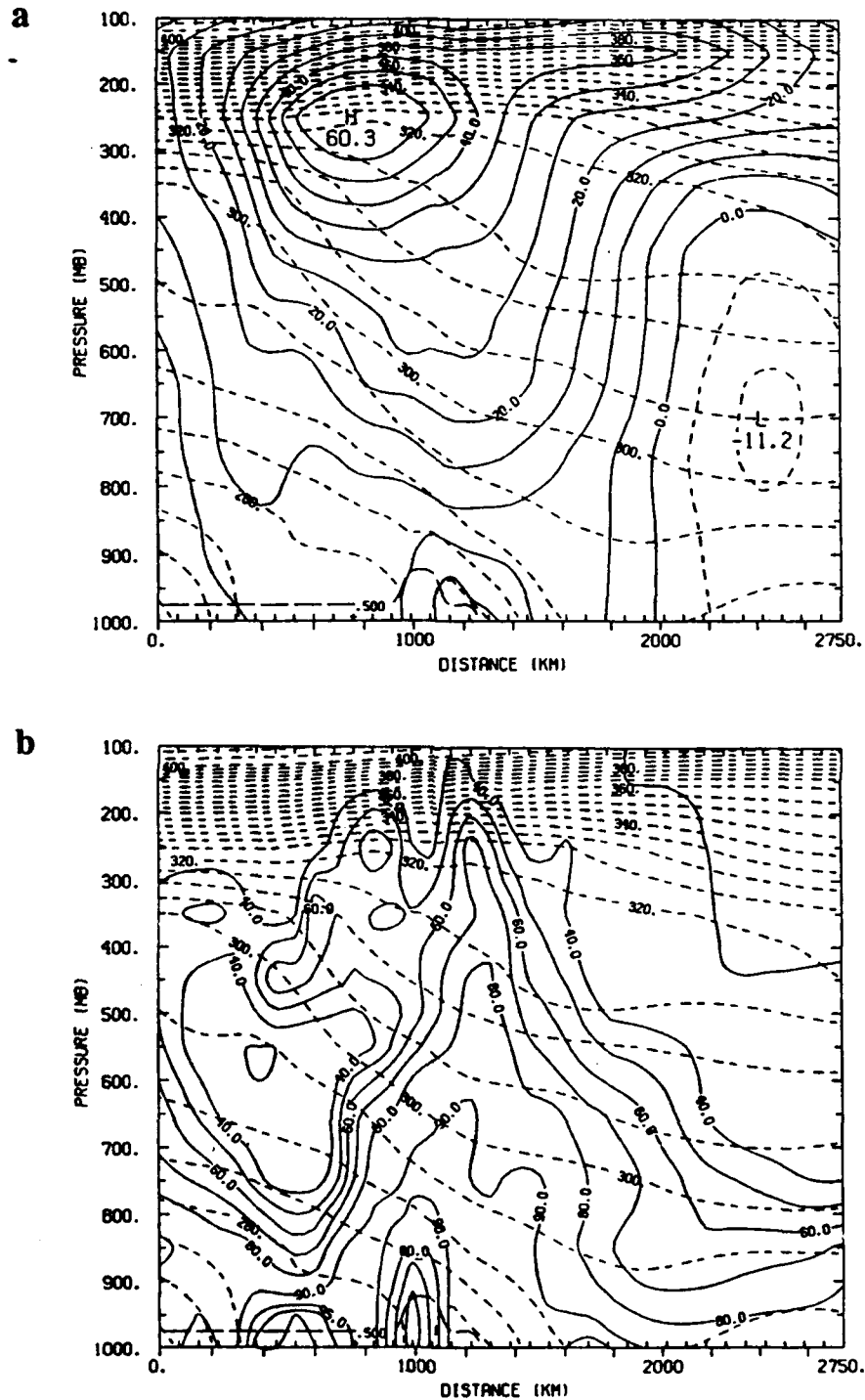


Figure 4.18. The magnitude of (a) the wind ( $\text{m s}^{-1}$ ) normal to the plane of the cross section and (b) the relative humidity (%) in the cross section CS2 for the NRL analysis at 26/00Z. The vertical motion and ageostrophic wind in the plane of cross section CS2 at 26/00Z for (c) the NRL analysis and (d) for the NMC analysis.

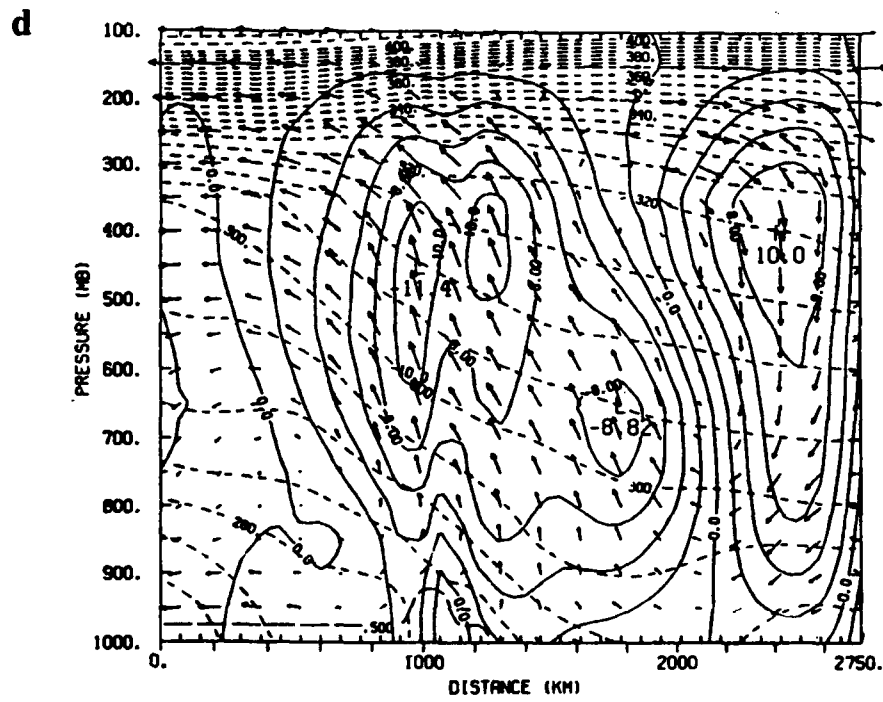
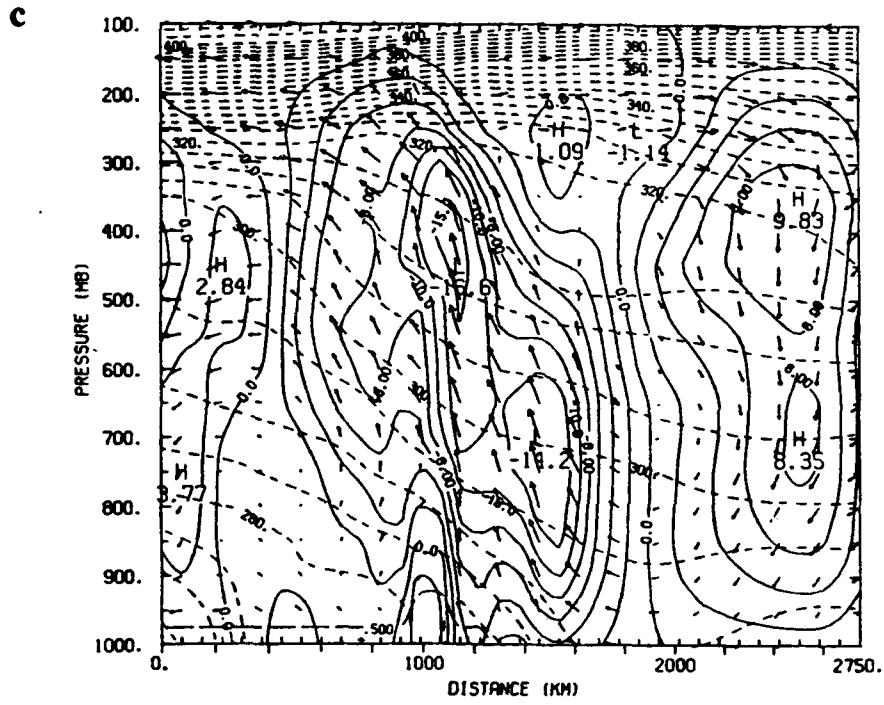


Figure 4.18. Continued.

feature in the cross section, particularly for the NRL analysis shown in Fig. 4.18c. The ageostrophic circulation due to the coastal front remains stronger and sharper in the NRL analysis as compared to the NMC analysis in Fig. 4.18d. Higher humidities are also found over the region of the coastal front in the NRL analysis (Fig. 4.18b). The mesoscale circulation derived from our analysis is also consistent with the 12-h forecast produced in case 4.3, giving confidence in our diagnosed secondary circulations. Also, the horizontal temperature gradient in the lowest 100 mb of the atmosphere in the vicinity of the front (1200 - 1600 km from northernmost end of CS2) is much greater in case 4.3.

By 26/06Z, the forecast from the NRL case 4.5 possessed stronger 500-mb vorticity and vertical velocities along the east coast than in the NMC case 4.6. The resulting 6-h precipitation pattern is much better in case 4.5 (Fig. 4.19a). With a fine-resolution model forecast serving as the first guess, the NRL analysis has the advantage of possessing the strong mesoscale circulations and higher initial humidities which help to force the precipitation. Whereas, the forecast in case 4.6 (Fig. 4.19b) originates from the coarse NMC analysis, which fails to capture these features and leads to a substantial model spin-up which is readily apparent in the precipitation pattern, when compared to the observed rainfall in Fig. 4.19c.

After 12 h of model integration, the surface temperature gradient in the coastal trough is still markedly stronger, and heavier precipitation is generated in the lee of the Appalachians in the forecast originating from the NRL analysis (Fig. 4.20). However, by this time, the upper-level features in the two cases 4.5 and 4.6 are very similar. A cross section (CS3 from 84°W, 43.5°N to 62°W, 27.5°N) across the coast in the region of the coastal low shows a strong vertical circulation in the coastal low merged with the secondary circulation in the jet entrance region (Fig. 4.21a and b). A cross section (CS4 from 70°W, 53°N to 80°W, 28°N) along the coastline cutting through this jet and the one at the base of the large-scale trough is shown in Fig. 4.21c and d. The coastal low

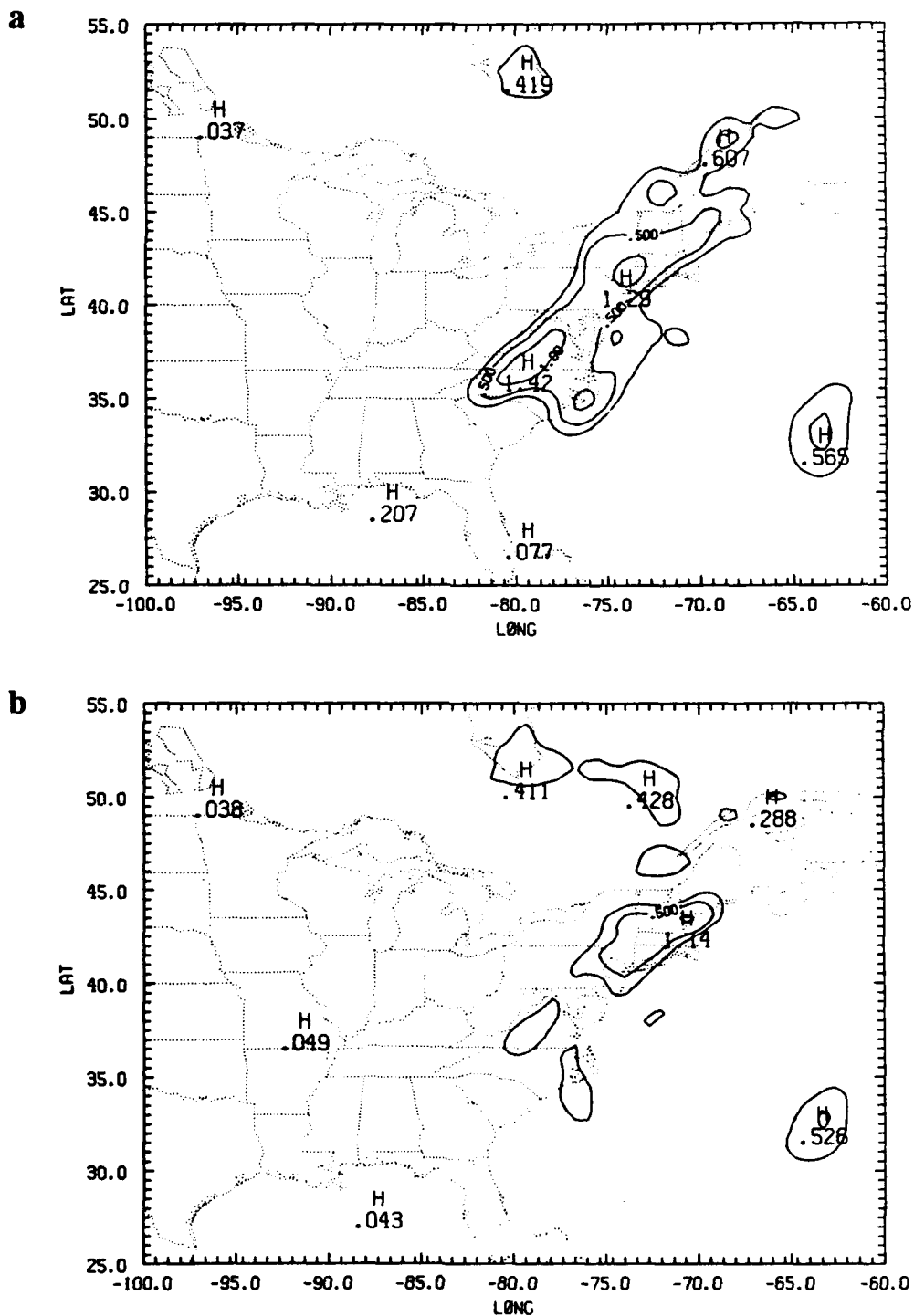


Figure 4.19. Forecast of accumulated total precipitation (26/00Z- 26/06Z) in cm for (a) case 4.5 from the NRL analysis and (b) case 4.6 from the NMC analysis. (c) Six-hour accumulation of observed precipitation (26/00Z- 26/06Z) in cm.

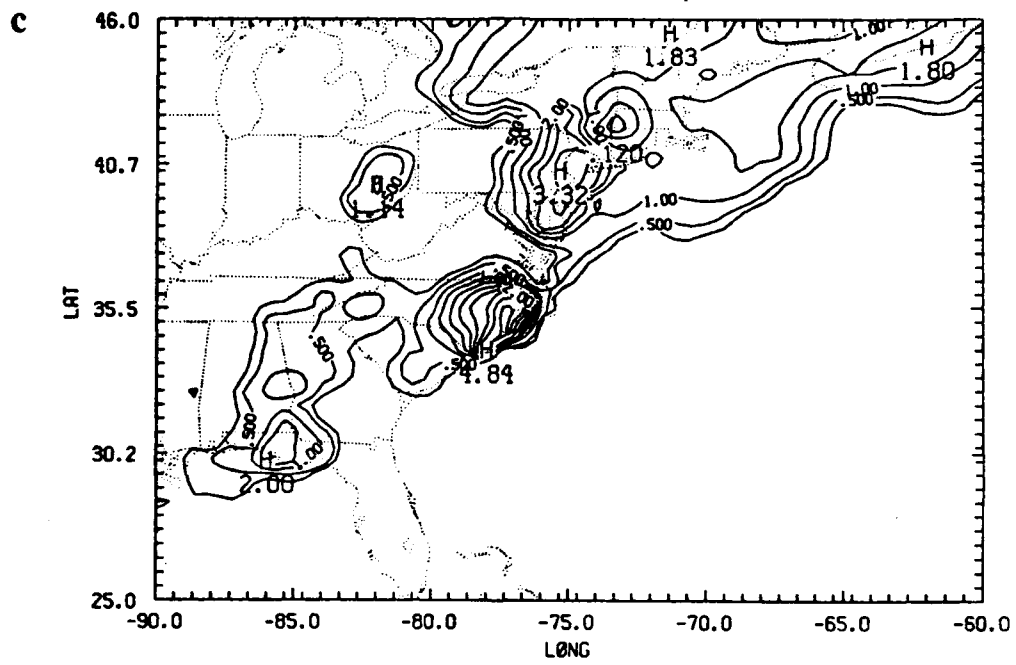


Figure 4.19. Continued.

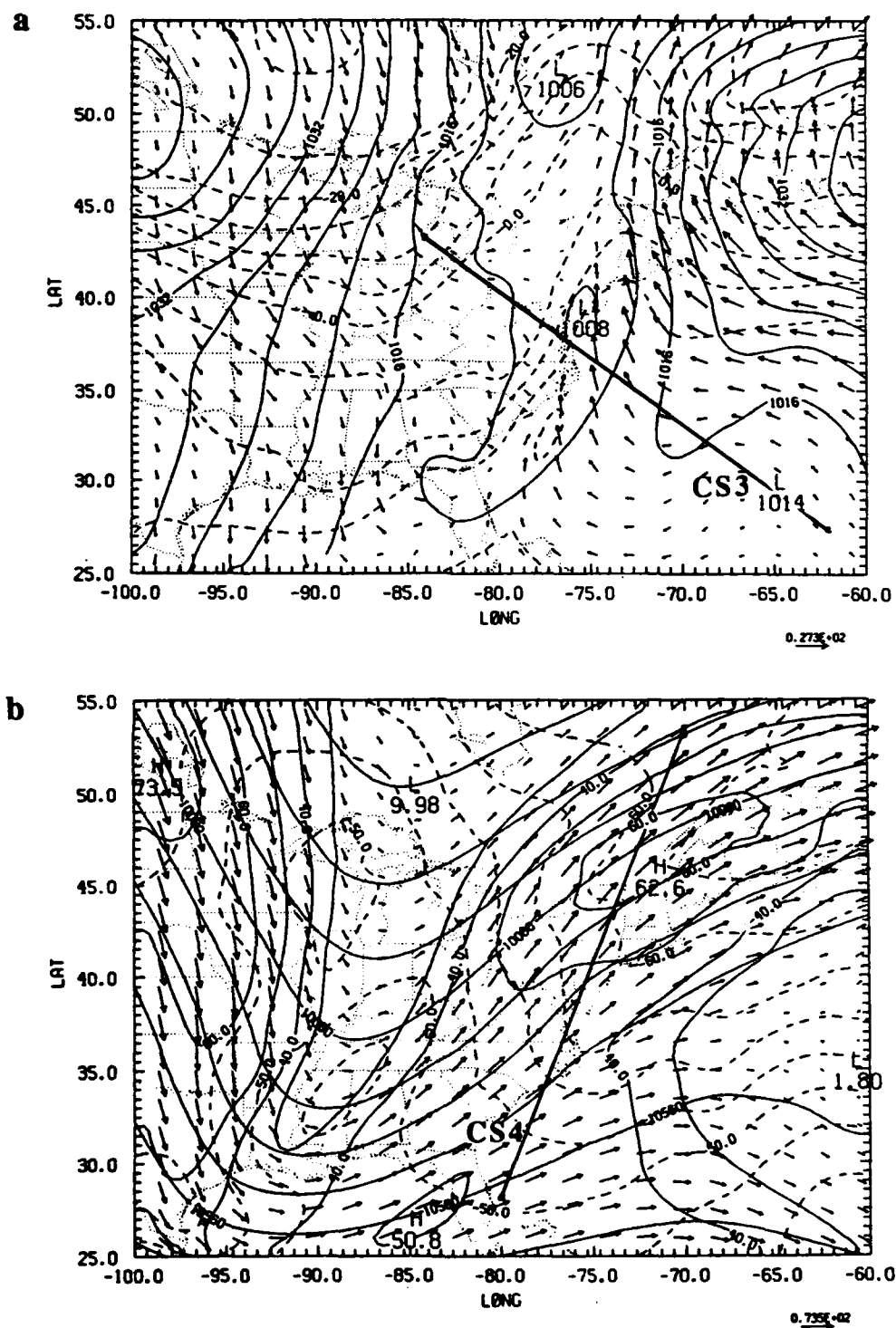


Figure 4.20. Twelve-hour forecast of (a) sea-level pressure (mb) and 1000-mb temperature (°C) and winds and (b) the geopotential height (m), temperature (°C), and winds at 250 mb valid at 26/12Z for case 4.5 from the NRL analysis at 26/12Z. The forecast 6-h accumulated precipitation in cm, valid at 26/12Z for (c) case 4.5 from the NRL analysis and (d) case 4.6 from the NMC analysis.

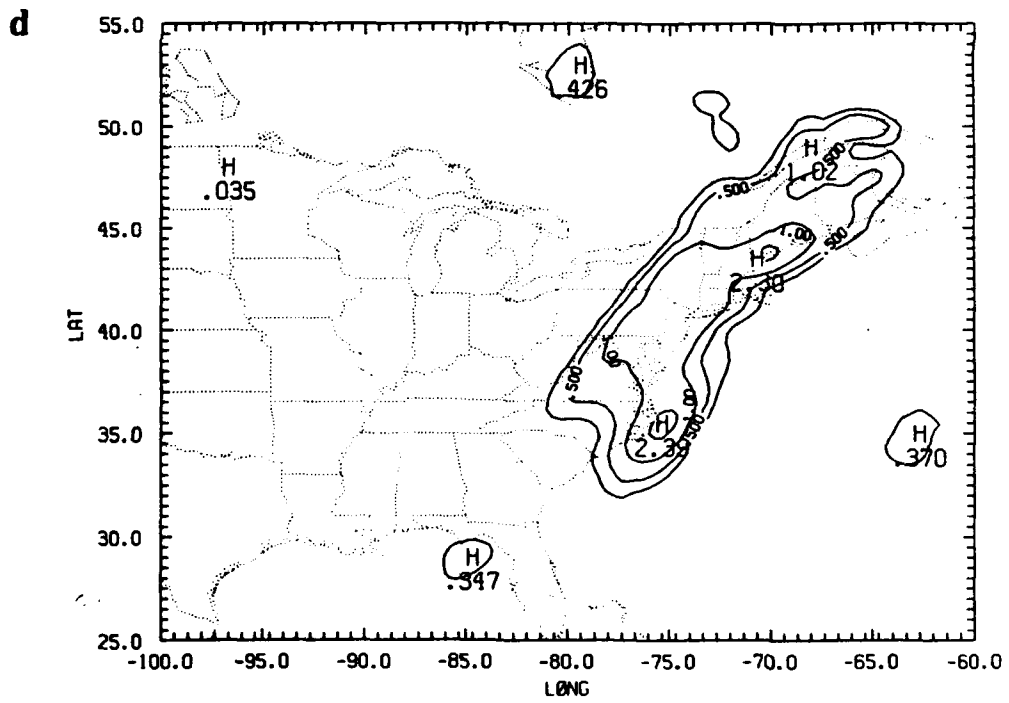
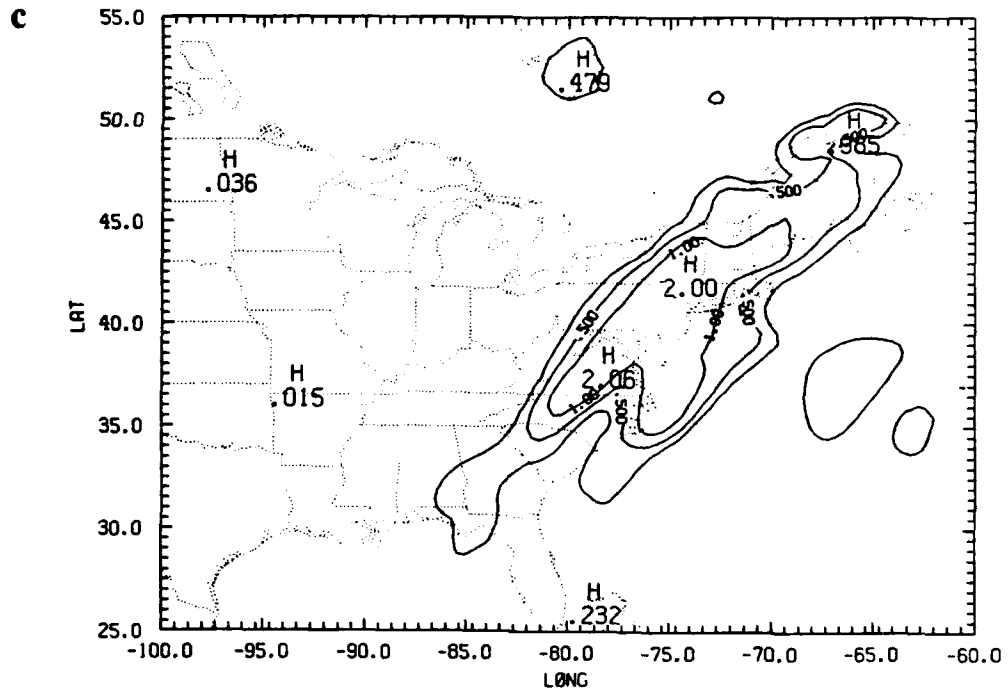


Figure 4.20. Continued.

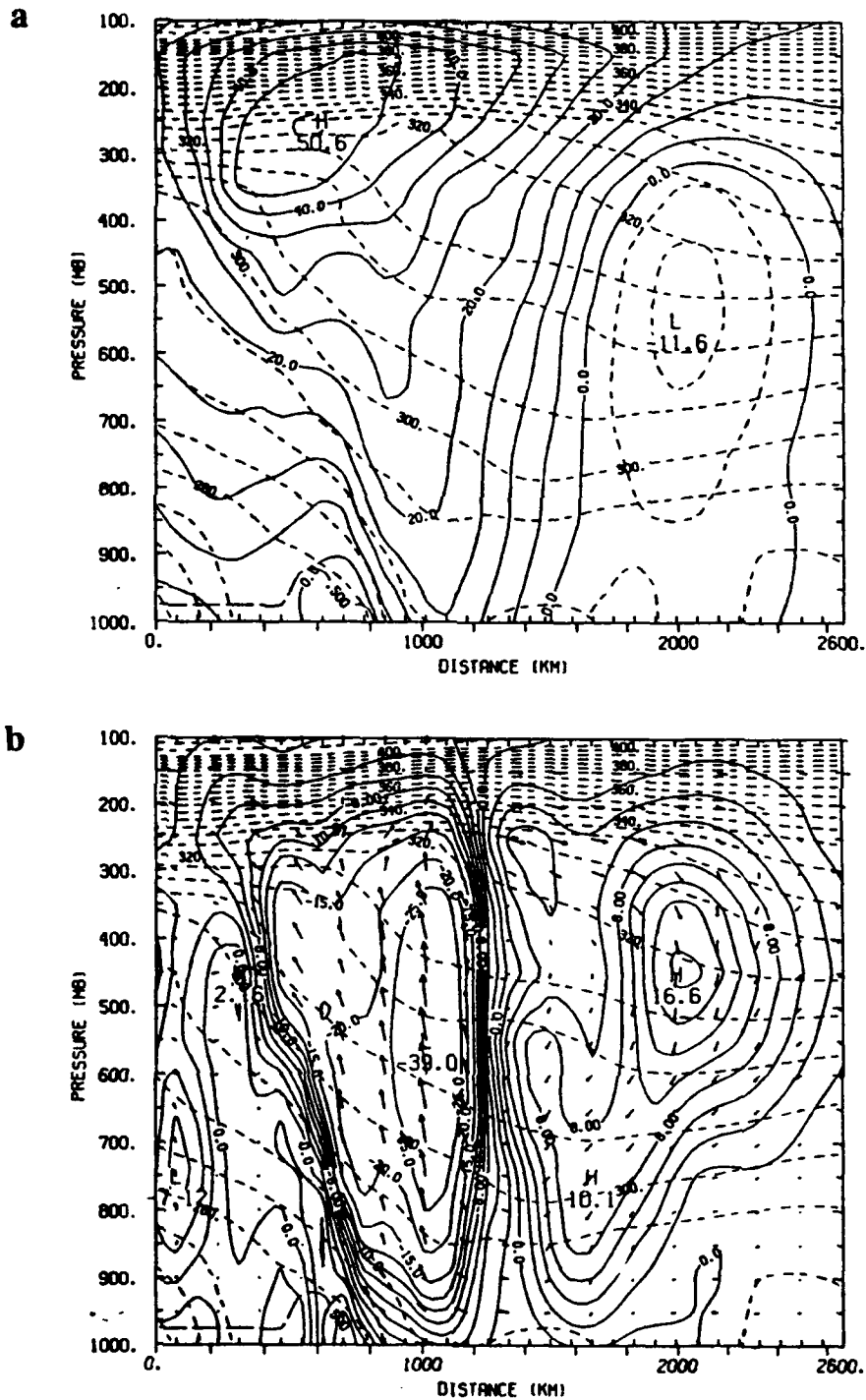


Figure 4.21. Twelve-hour forecast for case 4.5 of the (a) wind ( $\text{m s}^{-1}$ ) normal to cross section CS3 (see Fig. 4.20a) and (b) the vertical motion ( $\text{mb h}^{-1}$ ) and ageostrophic wind ( $\text{m s}^{-1}$ ) in the plane of CS3, valid at 26/12Z. (c) and (d) as in (a) and (b) but for the cross section CS4 (see Fig. 4.20b).

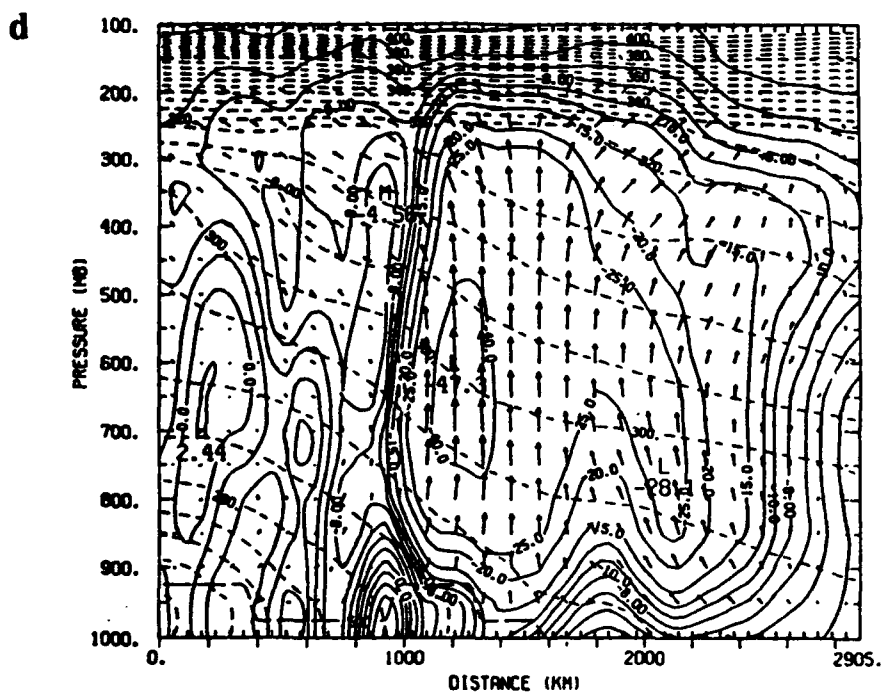
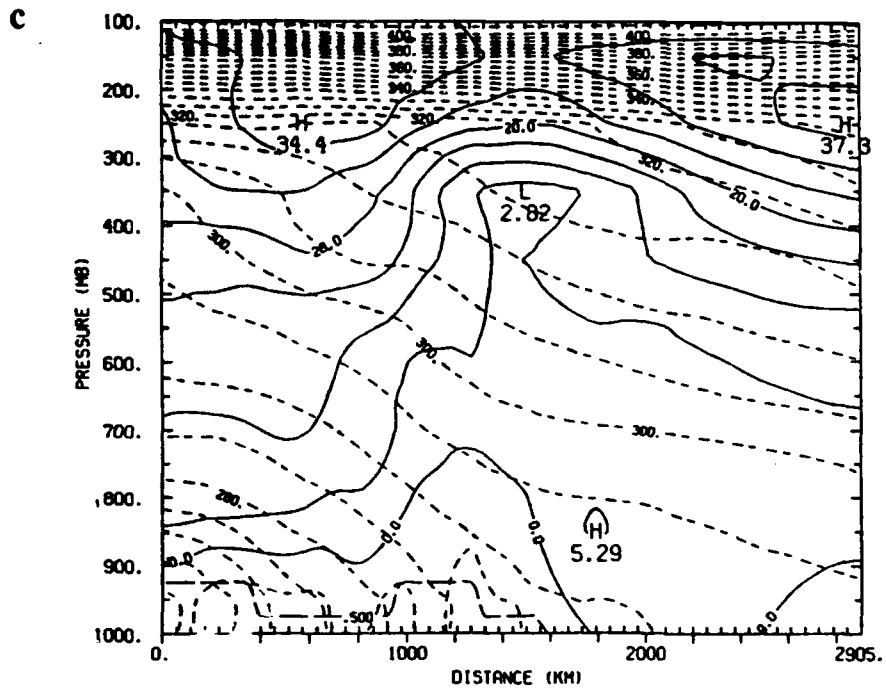


Figure 4.21. Continued.

circulation is shown to the rear of the strengthening direct secondary circulation in the entrance region of the northern jet. Ascent to the south, which is stronger in the forecast from the NRL analysis, is associated with the exit region of the jet at the base of the large-scale trough. This ascent leads to the increased precipitation over western Georgia, which is confirmed by the observed precipitation.

The analyses shown in Fig. 4.22 at 26/12Z confirm the large scale of the developing surface low pressure and upper-air trough, as the strong short wave reaches its base and the northern jet is strengthened by the short wave from the Great Lakes. Due to this large scale, the differences between the NRL and NMC analyses are less apparent. The merging of the circulations associated with the entrance region of the northern jet and the coastal low is still better resolved however by the NRL analysis. Cross sections along (CS4) and across (CS3) the coastline in Fig. 4.23 show the merging of the two circulations. Two circulations can be clearly seen in the cross section across the coast in the region of maximum ascent in the coastal low. As a result of the larger scale of the new developing system, the subsequent forecasts from the NRL (case 4.7) and NMC (case 4.8) analyses reveal less differences than previously. The 12- and 24-h surface forecasts for the NRL case 4.7 (Fig. 4.24) show the development of a new low off Hatteras, which moves northward and deepens rapidly to overshadow the earlier coastal low. In Fig 4.25, cross sections (CS5 from 70°W, 50.5°N to 76°W, 28°N and CS6 from 68.7°W, 55.5°N to 76.7°W, 25.5°N; see Fig. 4.24) along the coast show the secondary circulation in the exit region of the southern jet catching up with the circulation in the entrance region of the northern jet, so that they cooperate in strengthening the ascent in the rapidly developing low. Such has been found in other cases analyzed by Uccellini and Kocin (1987).

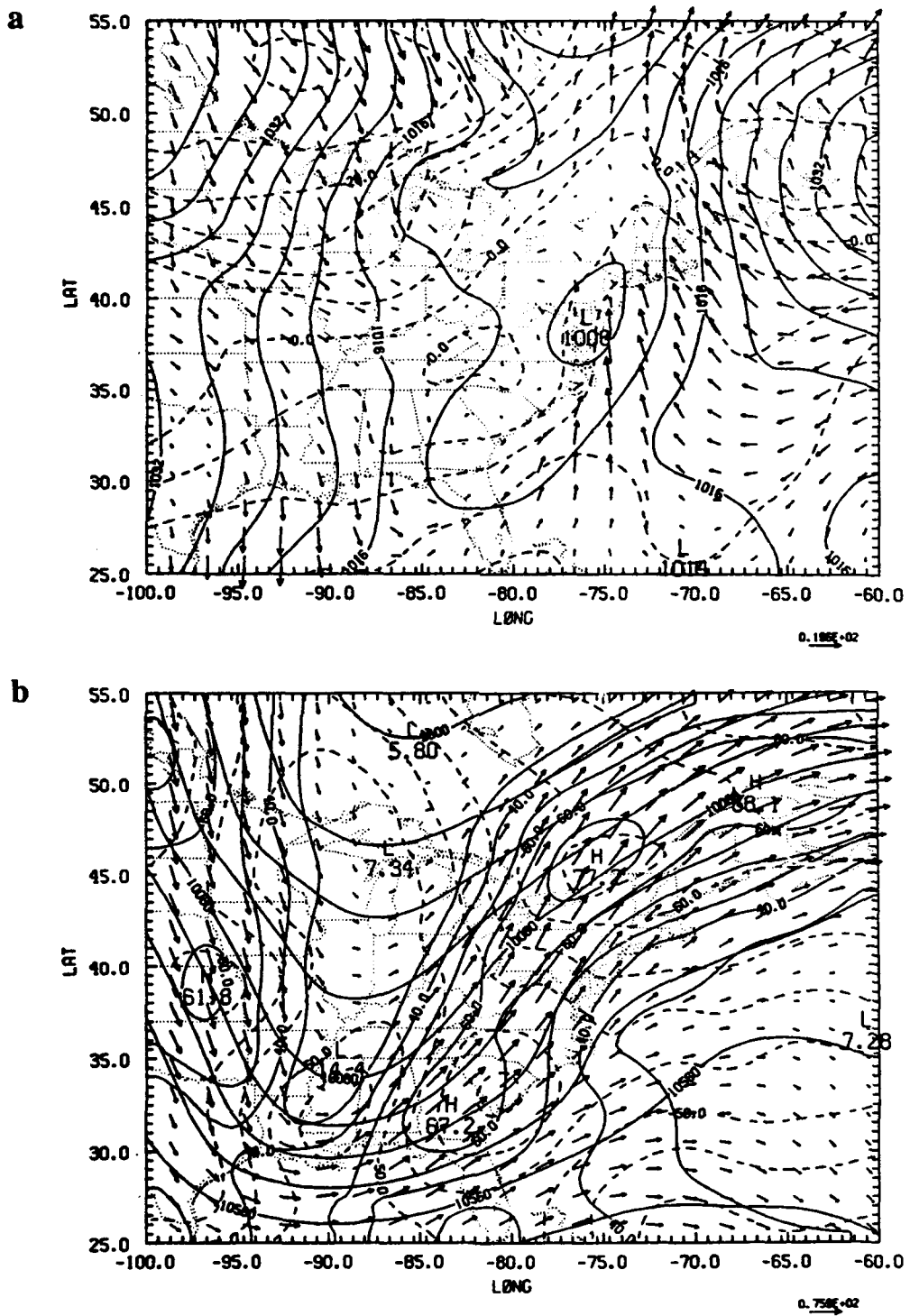


Figure 4.22. (a) Sea-level pressure (mb) and 1000-mb temperature (°C) and winds, (b) the geopotential height (m), temperature (°C), and winds at 250 mb, (c) absolute vorticity (in units of  $10^{-5} \text{ s}^{-1}$ ) with geopotential height (m) at 500 mb, and (d) the vertical velocity in  $\text{mb h}^{-1}$  at 500 mb for the NRL analysis at 26/12Z.

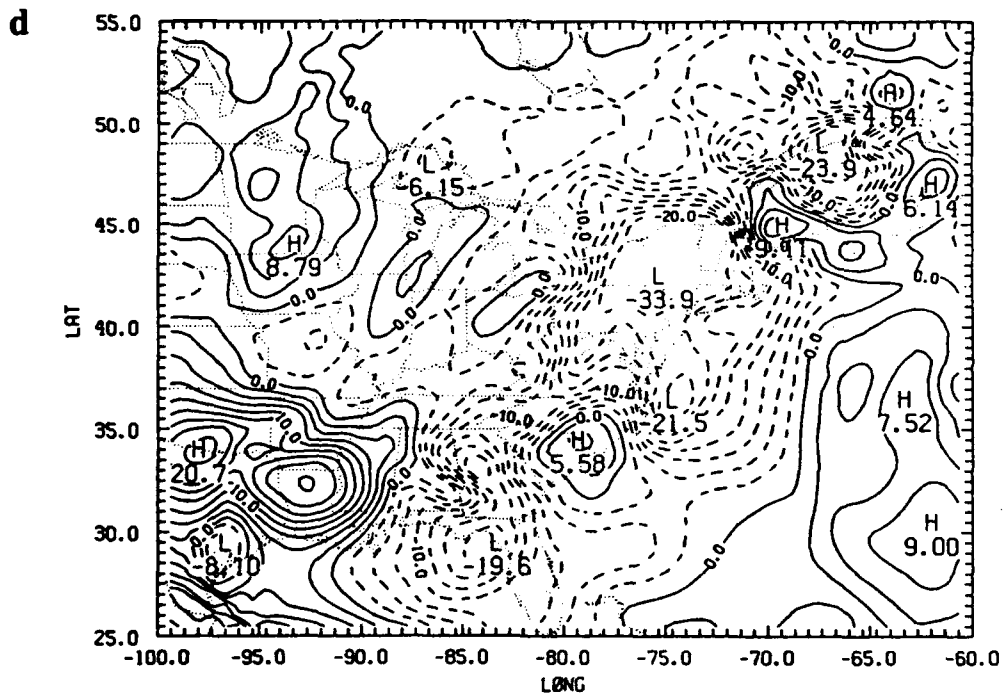
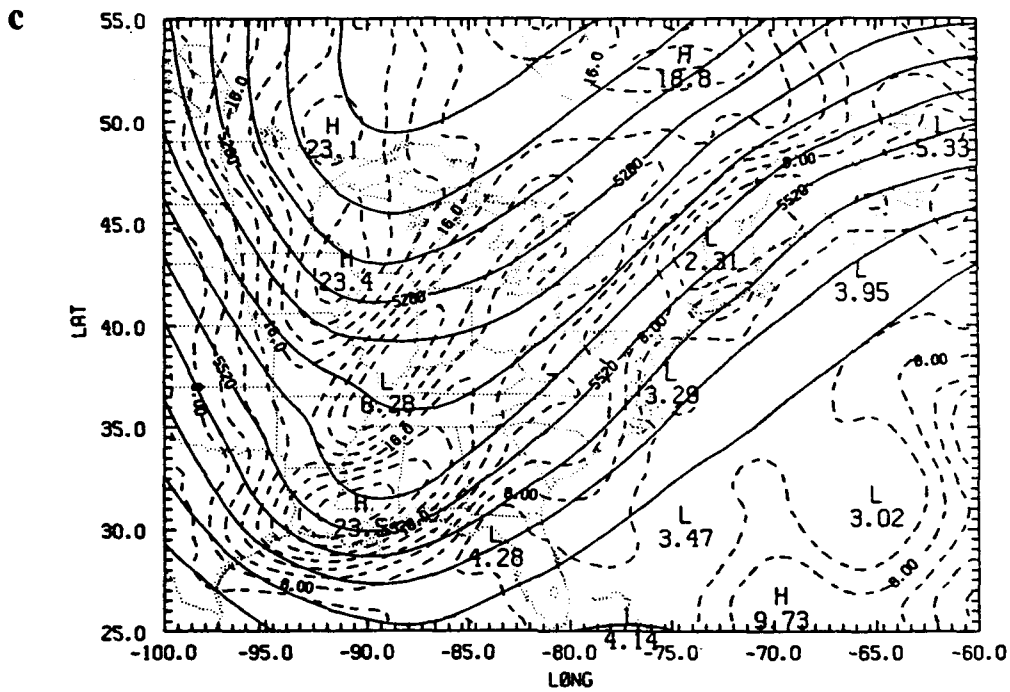


Figure 4.22. Continued.

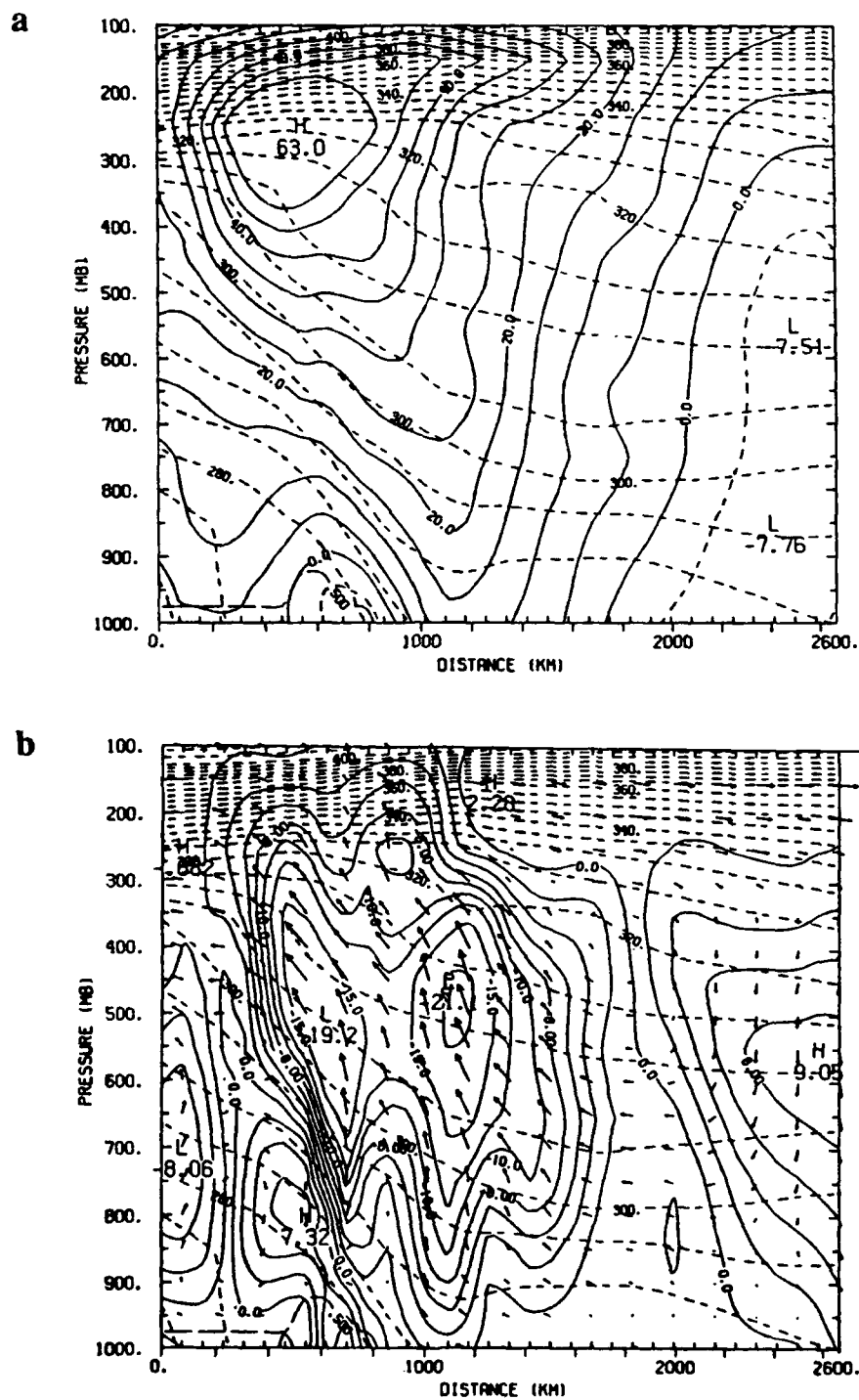


Figure 4.23. (a) The wind ( $\text{m s}^{-1}$ ) normal to the cross section CS3 and (b) the vertical motion ( $\text{mb h}^{-1}$ ) and ageostrophic wind ( $\text{m s}^{-1}$ ) in the plane of CS3 for the NRL analysis valid at 26/12Z. (c) and (d) as in (a) and (b) but for the cross section CS4.

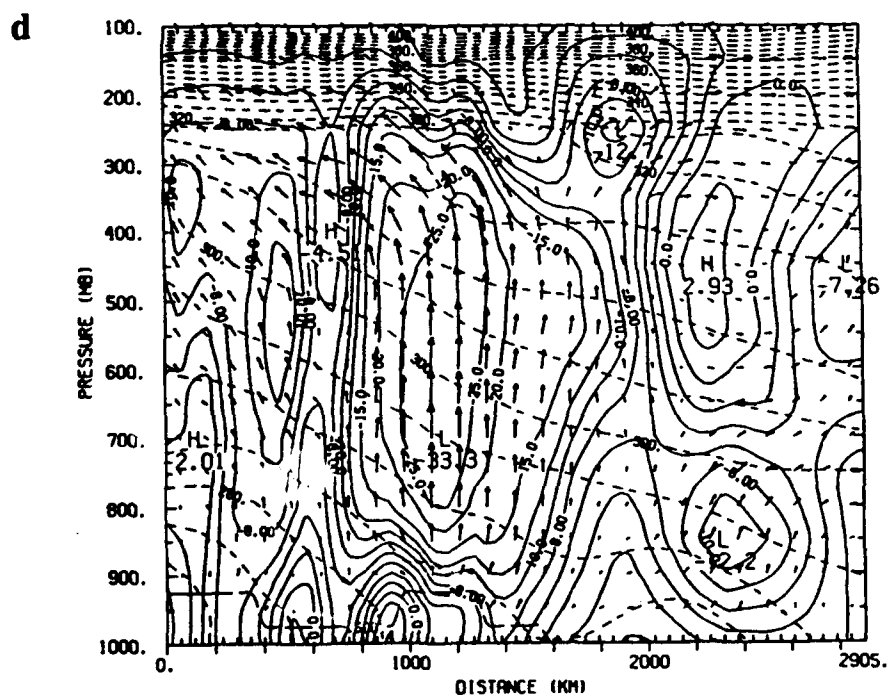
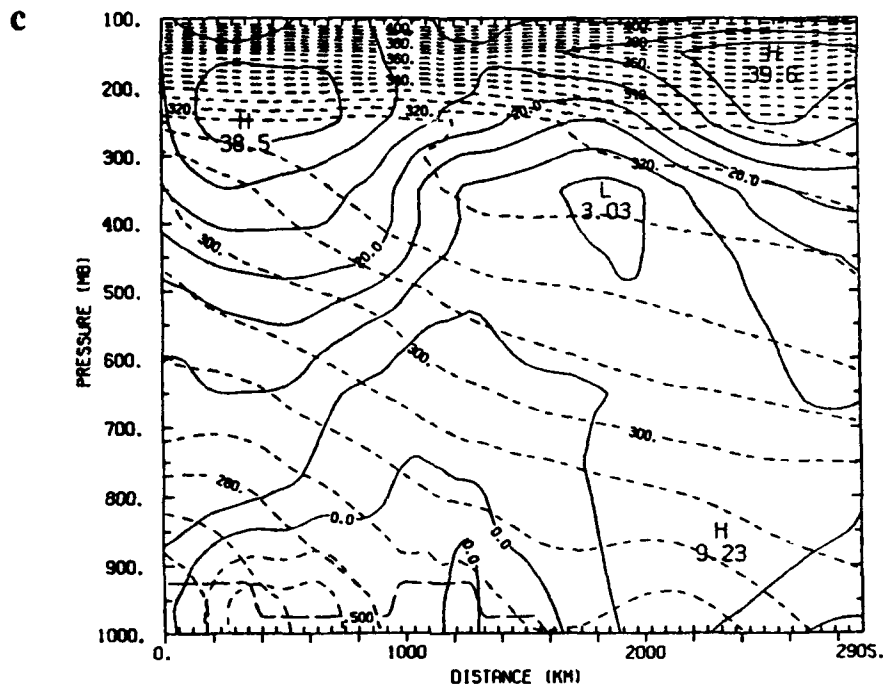


Figure 4.23. Continued.

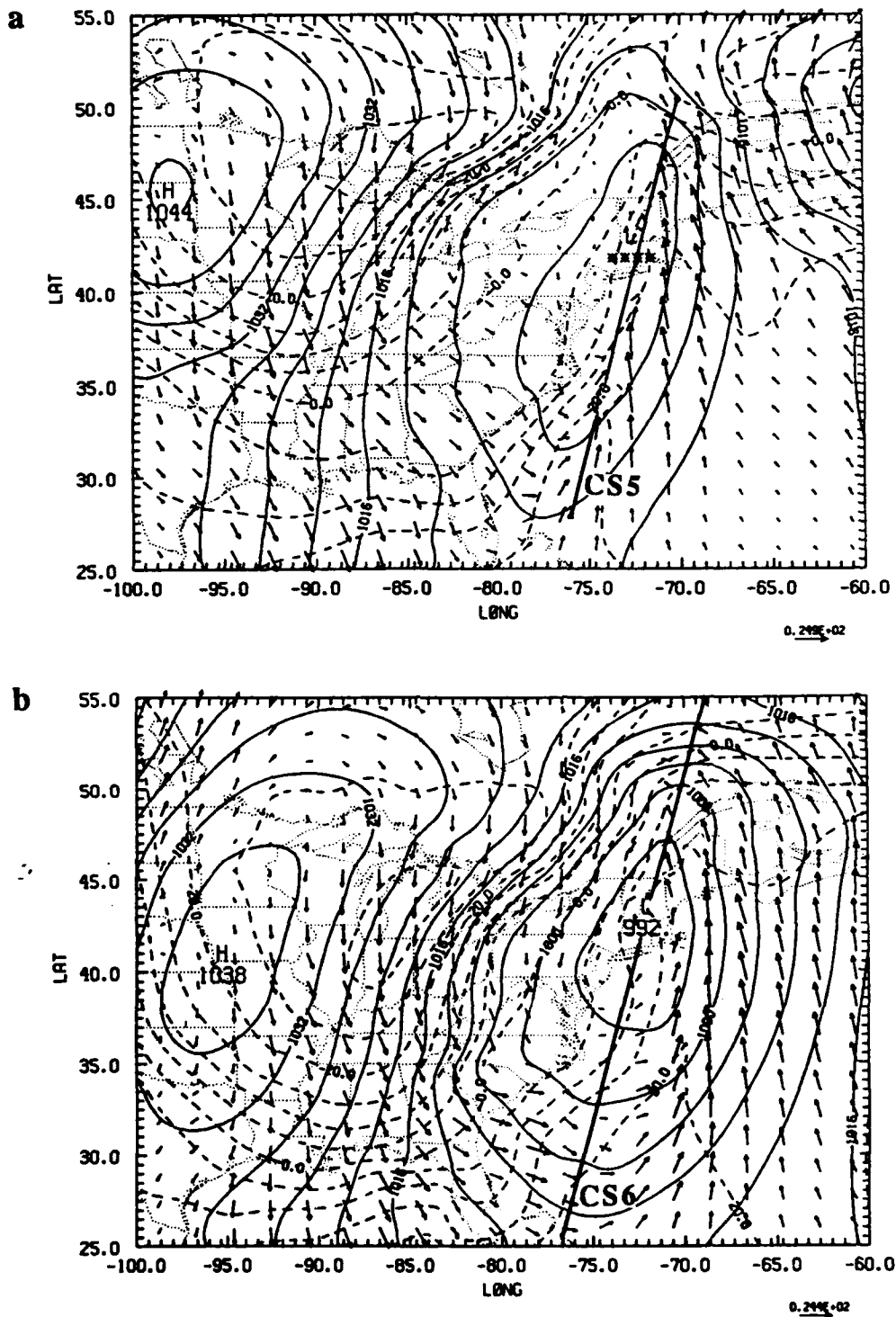


Figure 4.24. (a) Sea-level pressure (mb) and 1000-mb temperature ( $^{\circ}\text{C}$ ) and winds for (a) a 12-h forecast valid at 27/00Z and (b) a 24-h forecast valid at 27/12Z for case 4.7 integrated from the NRL analysis at 26/12Z.

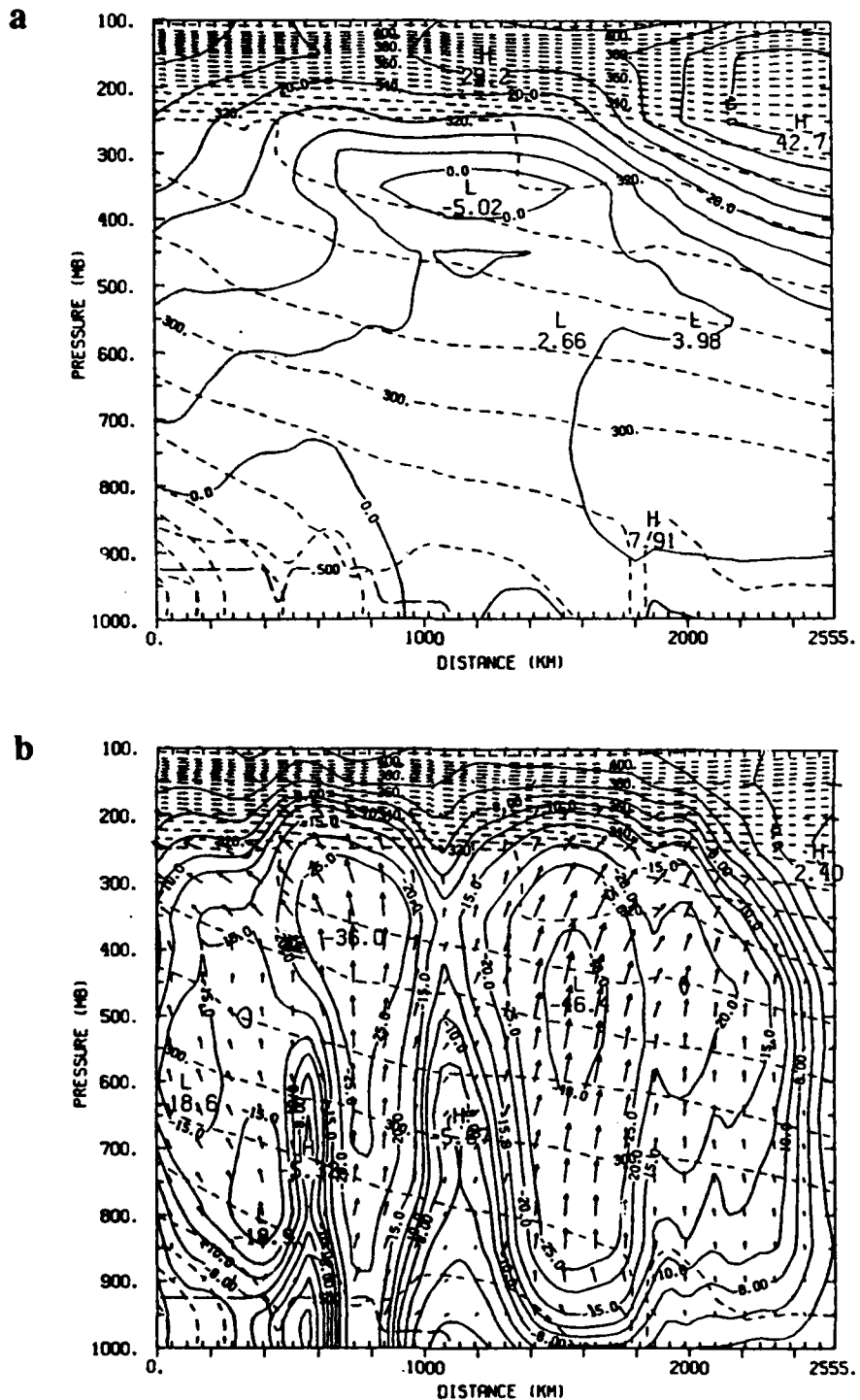


Figure 4.25. Twelve-hour forecast for case 4.7 of the (a) wind ( $\text{m s}^{-1}$ ) normal to cross section CS5 (see Fig. 4.24a) and (b) the vertical motion ( $\text{mb h}^{-1}$ ) and ageostrophic wind ( $\text{m s}^{-1}$ ) in the plane of the same cross section valid at 27/00Z. (c) and (d) the same as (a) and (b) but for a 24-h forecast for cross section CS6 (see Fig. 4.24b) valid at 27/12Z.

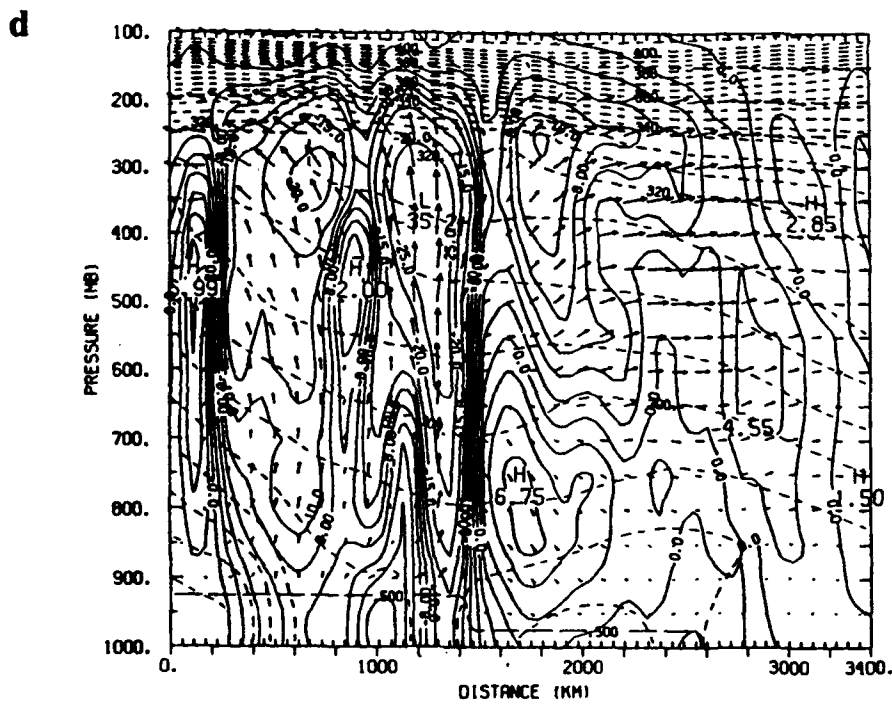
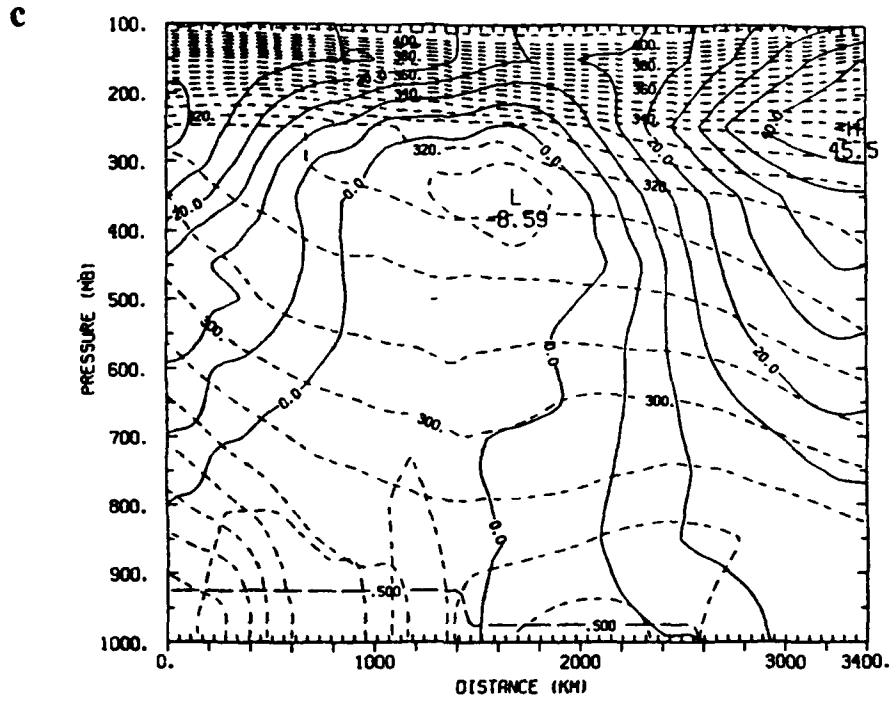


Figure 4.25. Continued.

#### 4.5 Summary

During the last decade, optimal interpolation replaced successive correction methods as the dominant objective analysis technique in operational weather forecasting systems. However, with the advent of Bratseth's (1986) analysis scheme, which converges to the optimal interpolation solution, the less expensive approach of successive correction has become a powerful and attractive alternative analysis method. The objective analysis scheme developed for use with the NRL/NCSU mesoscale model utilizes the Bratseth scheme, in which the data weights are dependent on the covariance between observations, are reduced in regions of higher data density, and include observational errors.

A computationally inexpensive multivariate methodology for linking the mass and momentum fields has been devised and is different from earlier methods reported in the literature. The key element is obtaining the gradient of the geopotential change from the change in  $u$ - and  $v$ - through the geostrophic relation at each iteration of the analysis process.

A qualitative evaluation of the NRL/NCSU objective analysis scheme has been accomplished. Several tests were conducted using a GALE IOP 2 data set. NRL analyses verified well against Bosart's hand analyses. The multivariate analysis was successful in deepening the cutoff low over the western Atlantic. The univariate analysis showed some improvement, but as expected, the multivariate analysis proved to be superior by using wind information to achieve gradients of geopotential through the geostrophic relationship. The NRL multivariate analysis was also successful in bringing the first-guess temperature pattern into proper phase.

A very encouraging finding was that the second-order fields of absolute vorticity and vertical motion were significantly improved by the objective analysis. Gradients and

maxima and minima were pushed toward those found in the NMC analyses. In addition, the upper-level jet from the background field was strengthened and tightened.

In the cases where the forecast originated from an NRL analysis, the forecast fields maintained the mesoscale features better than those originating from an NMC analysis. The first-guess fields from a prior model forecast already contains those finer scale features. The objective analysis was not only successful in retaining those finer scale features, but also was able to correct their phases and magnitudes. The mesoscale circulations associated with the coastal front on 25-26 January 1986 were forecast more accurately when the NRL multivariate analysis was incorporated.

## 5. DIABATIC INITIALIZATION EXPERIMENTS WITH CONVECTIVE HEATING

The analyses presented in the previous chapter were initialized adiabatically for model integration. That is, the vertical mode initialization procedure did not include forcing due to diabatic heating. Here, convective heating is accounted for in the model initialization.

### 5.1 Introduction

The dominant forcing in the troposphere within areas of precipitation is diabatic heating (convective and radiative heating and large-scale condensation). The present study deals strictly with diabatic heating from cumulus convection. A convective heating term is incorporated in the balance condition for the high frequency normal modes (Bengtsson 1981; Errico and Rasch 1988; Kitade 1983; Wergen 1983). With the inclusion of heating corresponding to observed rainfall data in the diabatic forcing term, the initialization can force the model state toward the real atmospheric state. As a result, the diabatic initialization corrects the model's forecast fields. Possibly the primary benefit of initialization with diabatic forcing is that the spinup problem (the extent that the initial amplitude of the divergent part of the wind and the precipitation are in error) can be minimized. That is, diabatic vertical mode initialization (DVMI), also referred to as diabatic nonlinear normal mode initialization, produces an initial model state which already includes convective heating.

Model spinup appears in all numerical forecast systems both in midlatitudes and tropics (Kasahara et al. 1988). It is one of the most serious problems in numerical

weather prediction and has been documented in research and operational models. Girard and Jarraud (1982) and Heckley (1985) documented spinup in the operational models used by the European Centre for Medium Range Weather Forecasts. Whereas, Miyakoda et al. (1978) and Donner (1988) illustrated different aspects of the spinup phenomena in research models at the Geophysical Fluid Dynamics Laboratory and National Center for Atmospheric Research, respectively.

Inadequate physical parameterizations and incorrect initial specifications of divergence, moisture and thermal fields are the primary causes of spinup (Mohanty et al. 1986). Until recently, most normal mode initialization methods were adiabatic in nature; that is, the existing latent heating at the initial model time was excluded leaving out a significant heat source which affected the adjustment between the mass and momentum fields. Lejenas (1980) found that adiabatic normal mode initialization, while providing improved vertical velocity profiles, does not alleviate the spinup problem. Data-assimilation techniques which incorporate a spun-up background field in the analysis of observed data have been developed. At the start of each update cycle of the assimilation, the background forecast field is corrected using the observed mass and momentum fields. During this process, the divergent part of the wind is lost primarily because the divergence has the same order of magnitude as the errors in the wind field. This divergent circulation associated with upward vertical motion can be regained if the analysis at each cycle of the assimilation is initialized with a diabatic initialization procedure. Turpeinen et al. (1990) concluded that the inclusion of observed low-level latent heat sources with a consistent and higher-resolution moisture analysis are critical components in reducing the underestimation of initial divergence, and hence precipitation rates.

Throughout the 1980s, NWP models incorporating initial latent heating based on rain rates have been developed. Turpeinen et al. (1990) summarized the main features of some of these models. Mohanty et al. (1986) investigated the inclusion of diabatic

heating in the vertical mode initialization (VMI) and found that the divergent circulation was rapidly destroyed by the integrated model heating if it differed too much from the observed heating. In the present study, we have merged the model-produced heating, during the first few hours of integration, with the heating used in the initialization.

The major thrust here is to incorporate the latent-heat forcing into the vertical mode initialization of the NRL/NCSU mesoscale model in an effort to shorten the spinup time. The goal is also to demonstrate that VMI with diabatic forcing provides improved initialized fields over adiabatic VMI. A diabatic heating term, derived from 'spinup' model convective rainfall and observed rainfall, has been included in the vertical mode initialization to better define the initial conditions for model integration. Several model runs (test cases) are made to test the effectiveness of DVMI as compared to initialization excluding the heating term, or adiabatic VMI (AVMI). The procedure for computing the diabatic heating for the initialization is described, followed by the experimental design and results.

## 5.2 Diabatic Heating in Model Initialization

Until recently the NRL/NCSU model was initialized exclusively using an adiabatic vertical mode initialization. The procedure is detailed by Sashegyi and Madala (1990, 1992a) and is discussed briefly in Chapter 3 of this document. In their VMI only the first three modes, the external mode and first two internal modes of the model, are initialized. Sashegyi and Madala (1990) showed that the first two modes require only two iterations of the scheme to converge. The third mode converged after five iterations. The phase speeds of these modes are much faster than typical meteorological systems, which move at speeds less than  $20 \text{ m s}^{-1}$ .

Adiabatic VMI has proven to be extremely effective in controlling spurious large-amplitude gravity wave oscillations due to initial imbalances between the mass and wind fields in primitive equation models (Puri and Miller 1990; Sashegyi and Madala 1990). However, the use of AVMI leads to a drastic depletion of the divergent circulation.

Wergen (1983 and 1987) introduced a procedure to overcome this problem, in which average diabatic heating is obtained by integrating the model for a few time steps prior to the initialization. The average heating is then included in the nonlinear forcing of the iterative initialization process. The fixed diabatic heating is determined as the time-mean heating generated by model physics (cumulus parameterization and large-scale heating) during the short integration. Unfortunately, most forecast models do not produce realistic heating rates during the first few hours, leading to the spinup problem. Therefore, for present experiments, the choice was made to integrate the model for 9 h before accumulating the model latent heating and convective rainfall from which our time-mean heating and rainfall rates were derived. The diabatic VMI (DVMI) used in this study is similar to Wergen's, but it is original in that 'spun-up' model heating is applied in the initialization, rather than the heating from the first few hours of integration as is usually done. The procedure involves the following steps:

- The model is integrated for 12 h from adiabatically initialized fields. Convective rainfall, from which the diabatic heating is derived, is accumulated from 9-12 h of this initial integration (control run), allowing ample time for model spinup.

- Time average convective rainfall rates over the 3-h period are derived for all grid points.

- The average rain rates are converted into vertical profiles of heating using a reverse Kuo cumulus parameterization. This vertical distribution of the latent heating is based on the cumulus convective scheme of the model. Thus, no simplifying hypotheses are needed. The advantage of the present approach is an improved consistency obtained

with the physical parameterization scheme of the model. In future studies, observed rainfall will be combined with our model rainfall rates in this procedure to obtain more objectivity.

-- This three-dimensional diabatic heating field is then added as a forcing term in the VMI thermodynamic energy balance equation as the implicit DVMI is performed. As a result, diabatic effects are implicitly included in the specification of the heating field.

The diabatic initialization described above is primarily for heating associated with convective precipitation. The heating is nearly zero in the lower troposphere and varies significantly from case to case in the upper troposphere. The first three modes of the model account for 40 to 50% of the convective heating in the upper troposphere. Therefore, we assume that the method described here accounts for a significant part of the divergence field.

The conversion of rainfall rates into vertical profiles of convective heating depends on the stability of the environment as determined by the cumulus parameterization. If convective instability occurs, a heating function is computed using the reverse Kuo scheme. This heating function is then used to distribute the diabatic heating, derived from the average rainfall rates, in the vertical direction. If the environment is convectively stable, the diabatic heating associated with the two-dimensional rainfall distribution will be taken as zero. Therefore, non-convective precipitation does not contribute to the diabatic heating in the present initialization scheme.

The persistence of balance achieved by DVMI during the early stages of the model integration depends heavily on the compatibility between the specified heating during initialization and the model-produced heating during integration (Puri and Miller 1990). Puri (1987) suggested that one possible way of retaining this compatibility in the heating rates would be to adjust the moisture field until the model-produced heating rates determined by the convective parameterization in the model are similar to those used

during DVMI. Here, two procedures are used to retain this desired compatibility in heating rates. First, the model rainfall and heating rates produced during the first 3 h of integration are merged with the corresponding rates from the initialization. A nonlinear weighting factor ( $\alpha$ ) is employed where  $\alpha=1$  at  $t=0$  h and  $\alpha=0$  at  $t=3$  h. The relation is given by:

$$R_m = \alpha R_i + (1-\alpha) R_c \quad 5.1$$

where  $R_i$  is the convective rainfall rate used in the diabatic VMI,  $R_c$  is the model-produced convective rainfall rate,  $R_m$  is the merged rain rate, and  $\alpha$  is given by:

$$\alpha = 1 - \frac{[1 + \sin(\pi t / 3 - \pi / 2)]}{2} \quad 5.2$$

The above relations allow the influence of the initialized heating and rain rates to approach zero in a smoother manner than a simple linear relationship would allow. Merging is applicable only for DVMI cases since AVMI, by definition, does not include a diabatic heating term in its balance equation.

The second method involves adjusting the humidity fields prior to initialization. The importance of moisture adjustment in diabatic initialization was emphasized by Wolcott and Warner (1981). They argued that if the environment is not humid enough, the upward motion associated with the initialized divergence field will not be sustained by latent heat release. In the present study, specific humidity is enhanced only at grid points where convective rainfall is occurring and the relative humidity is less than 95%. At those points, the specific humidity is increased to 95% of the saturation specific humidity at the three lowest model levels. However, our findings indicated that the changes in the humidity fields were small, and, as a result, the adjustment had minimal affect on the convective rainfall. Since the modeled large-scale condensation occurs only upon

supersaturation, not at 95% relative humidity, this moisture adjustment would have little affect on non-convective precipitation.

### 5.3 Experimental Design

Initially, three test cases (model runs) were performed to determine improvements (if any) in the model initial state and subsequent forecasts using DVMI versus AVMI. The first is a control run (case 5.1) in which the model is initialized at 1200 UTC 26 January 1986 (26/12Z) using the NMC analyzed data. These data of 2.5° resolution are first interpolated to the model grid and then initialized with the AVMI for the first three vertical normal modes of the model. The model is then integrated for 24 h. The 12-h forecast from the control run serves as the initial fields for cases 5.2 and 5.3. In case 5.2, the model is initialized using DVMI on the forecast fields from case 5.1 valid at 27/00Z. Model-generated rainfall (26/21Z to 27/00Z of the control) is used to compute heating rates at each vertical level of the model for the DVMI. The model is then integrated for 12 h, with heat/rain merging. The initialization for the next case (case 5.3) is simply an AVMI on the control run's 12-h forecast.

For this study, the control run is considered the "truth" for comparison against the other two cases. From 26/12Z to 27/00Z of the control run, the model should have sufficient time to spin up, or in other words, develop the divergent part of the wind. By using model-generated rainfall rates in the DVMI (case 5.2), one would expect a negligible spinup during the subsequent forecast. Also, one might expect little change due to the initialization using model rain since the model heating function is consistent with other model parameters. By comparing the initialized and subsequent forecast fields from case 5.2 with the corresponding fields from the control, one can determine if the

model-generated rainfall, which is a two-dimensional (2-D) distribution, can re-create the 3-D distribution of vertical heating rates accurately.

#### 5.4 Results

The following results were obtained by making qualitative comparisons of meteorological fields from the different model initializations and forecasts of the three test cases. The differences between cases 5.2 and 5.3 of their respective initialized fields of 1000 mb, 500 mb, and 250 mb geopotential height, temperature, and winds are extremely small. As expected, the first-order analysis fields (12-h forecast from the control run) changed little with each initialization in these test cases and, as a result, the forecasts (valid at 27/12Z) of these variables from these two runs are almost identical and agree well with the control run forecast.

##### 5.4.1 Comparison of Initialized Vertical Velocity

Since vertical velocity or omega ( $dp/dt$ ) is directly related to diabatic heating, we can expect noticeable differences between the initial states of omega from cases 5.2 and 5.3. Furthermore, the effectiveness of diabatic heating in inducing divergent circulations can be seen by comparing omega fields from DVMI and those resulting from AVMI. As expected, in geographic areas absent of precipitation, vertical velocity patterns in cases 5.2 (DVMI) and 5.3 (AVMI) are approximately the same and very close to the "truth" (Fig. 5.1). Off the east coast, an area of strong ascent stretches along the eastern seaboard and is associated with the old frontal boundary and the developing cyclone off the North Carolina coast. In this region where the control run ("truth") predicts heavy rain at initialization time (27/00Z), the initialized state for case 5.2 is very close to the

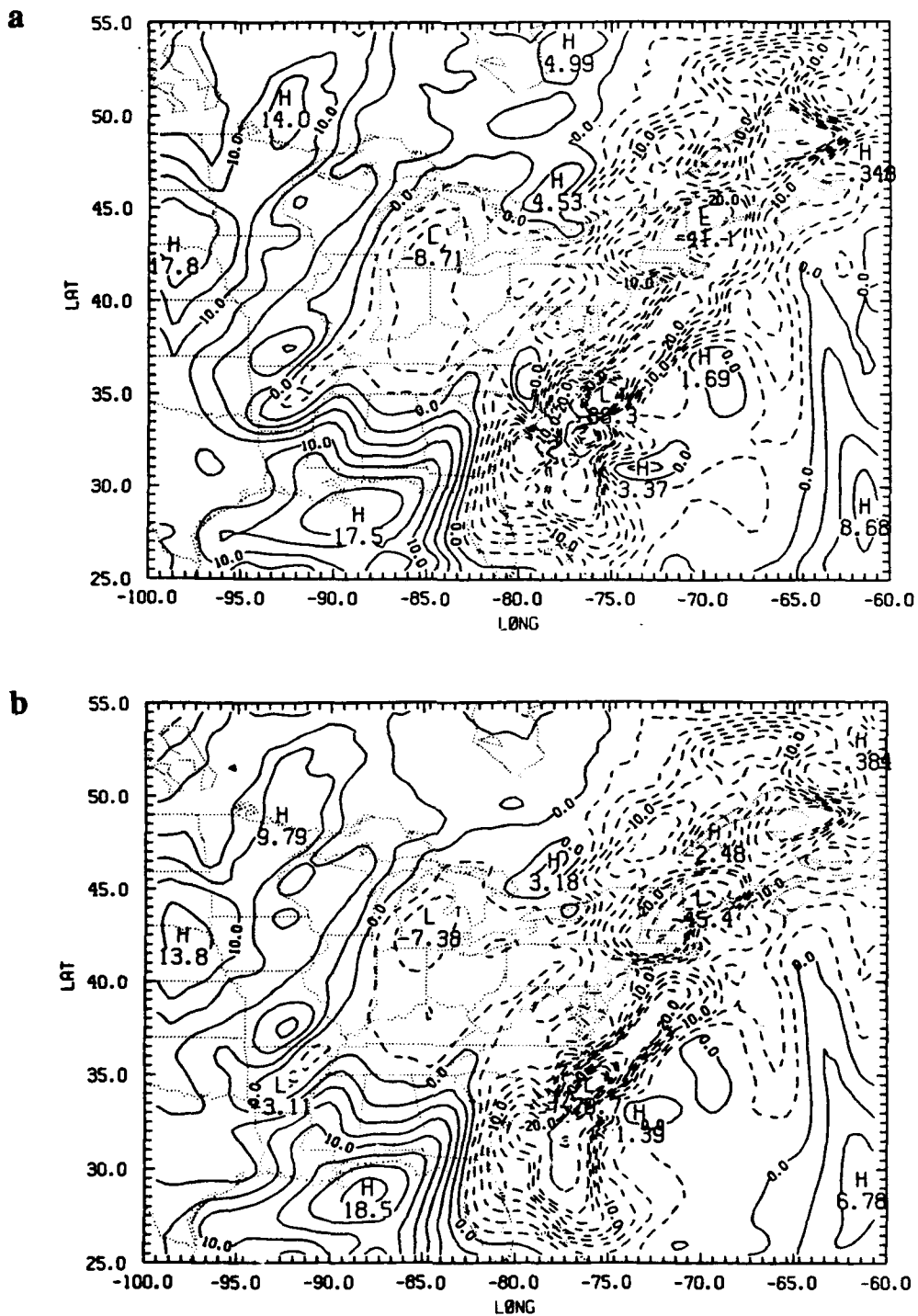


Figure 5.1. 500-mb vertical motion fields valid at 27/00Z: (a) from 12-h forecast of the control (case 5.1), (b) after DVMI (case 5.2), and (c) after AVMI (case 5.3). Vertical motion of magnitude of  $-20 \text{ mb h}^{-1}$  or more are contoured every  $2.5 \text{ mb h}^{-1}$ .



"truth." The pattern and positions of maxima and minima in the omega field show little change from the control run, suggesting the 3-D structure of model convective heating can be re-created from a 2-D rain distribution. A further comparison between case 5.2 and case 5.3 reveals the deficiency of AVMI. In the vicinity of the developing cyclone off Cape Hatteras, the magnitude of omega has changed substantially using AVMI; the maximum upward velocity is only about 60% of that resulting from DVMI. Since a significant amount of the divergence (and hence vertical motions) associated with heavy precipitation events may be forced by latent heat release, and since the nonlinear step in the AVMI does not include this diabatic forcing, the divergence due to this forcing will be removed as if it were associated with unwanted gravity waves. As a result, the vertical velocities are underestimated.

#### 5.4.2 Forecast Precipitation Comparisons

The patterns of 12-h (27/00Z - 27/12Z) convective rainfall in cases 5.2 and 5.3 are very similar to each other and to the control in areal coverage and accumulation. The 12-h convective rainfall forecast from the adiabatically initialized fields is just as good as the forecast originating from the diabatically initialized fields. Since the physics and dynamics of the nonlinear normal mode procedure are internally consistent with the numerical model (which provided the analysis fields), the initialization procedure, whether with or without diabatic heating, changes the model forecast fields only a small amount. As a result, the subsequent forecasts are essentially the same. Therefore, additional model experiments were performed in which GALE 3-hourly surface and upper-air data were analyzed using a multivariate, successive correction objective analysis scheme (Sashegyi et al. 1992). Model forecast fields served as the first guess for the analyses. Adiabatic (AVMI) and diabatic (DVMI) initializations were performed on the

analysis fields. In the latter case, observed rain data was combined with the model-produced rainfall for computation of the 3-dimensional heating function in the model initialization procedure.

Figure 5.2 shows 6-h observed rainfall and accumulated forecast rainfall valid 26/00Z - 26/06Z. The forecast in Fig. 5.2a was initialized with DVMI at 26/00Z. The rainfall pattern is similar to the observed; in particular, over Alabama and along the central Gulf coast region, the model was able to predict the precipitation during this short-range forecast. However, the forecast originating from AVMI (Fig. 5.2b) fails to capture any rainfall over the Gulf coast associated with the developing short wave. The absence of diabatic heating from the VMI has caused a spinup problem in this case. RMS differences between these forecasts and observed rainfall were computed. The differences were computed only at gridpoints in which at least 0.01 cm of either forecast or observed rainfall accumulated during the 6-h period. When initializing with AVMI and DVMI, the rms differences were 0.9 cm and 0.7 cm, respectively. The larger rms difference in the AVMI case is due to model spinup. The disparity between these two cases would be even greater, if only the accumulated rainfall from the first 3 h of model integration was compared. A complete description of these experiments and discussion of results within the context of four-dimensional data assimilation is given by Harms et al. (1992c)

## 5.5 Summary

In this study, the viewpoint taken was that the "best" initialized states were those which were least altered by initialization. From comparisons of vertical velocity fields, we found that DVMI with model rain produced an initial state very similar to the "truth" and, thus, successfully re-created the 3-D distribution of convective heating from the 2-D model rain distribution. The AVMI (case 5.3) changed the "true" analysis significantly

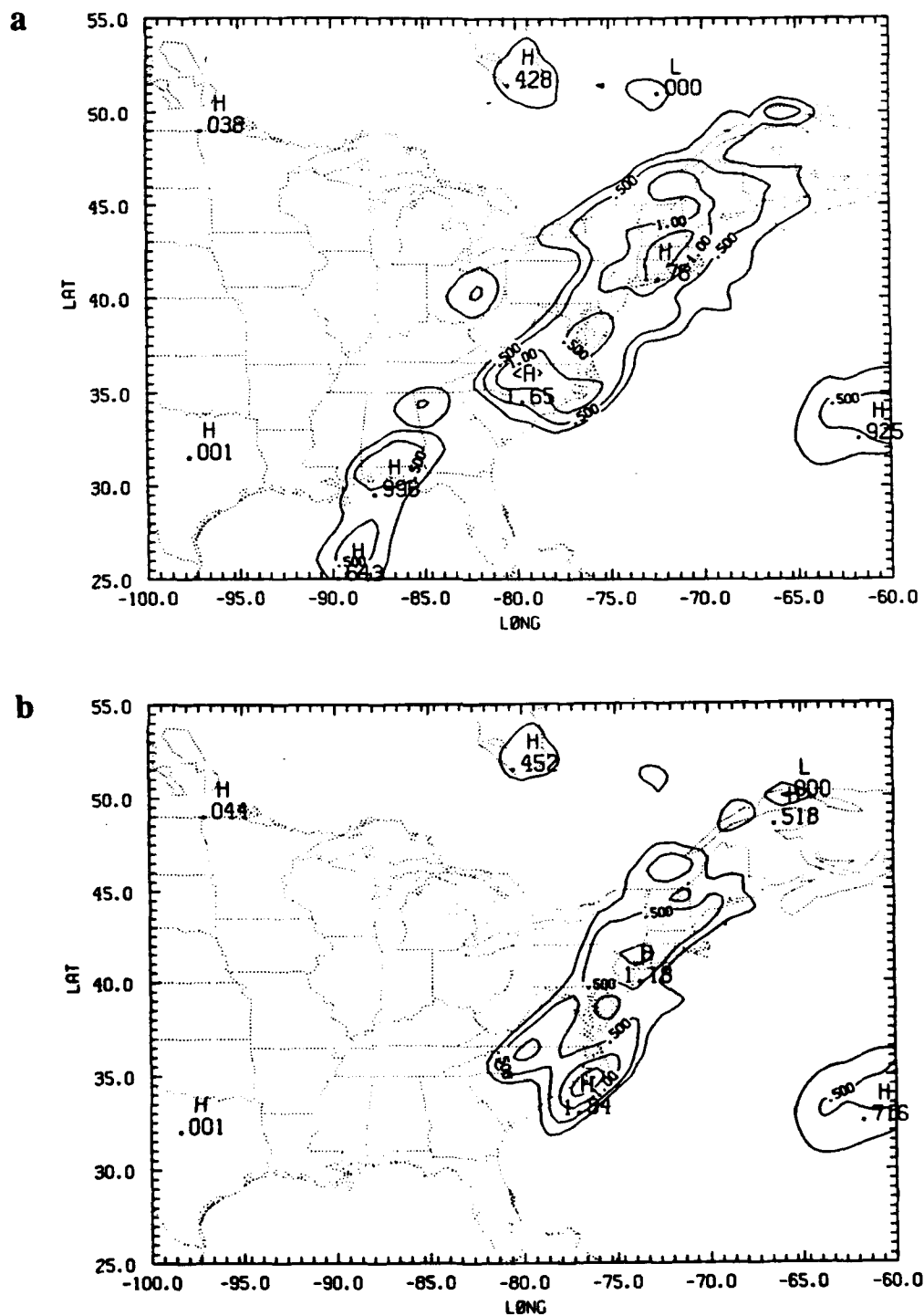


Figure 5.2. Forecasts of accumulated total precipitation in cm (26/00Z - 26/06Z) originating from (a) DVMI and (b) AVMI. (c) Observed precipitation in cm for the same period. Contours at 0.25 cm and every 0.5 cm for 0.5 and above.

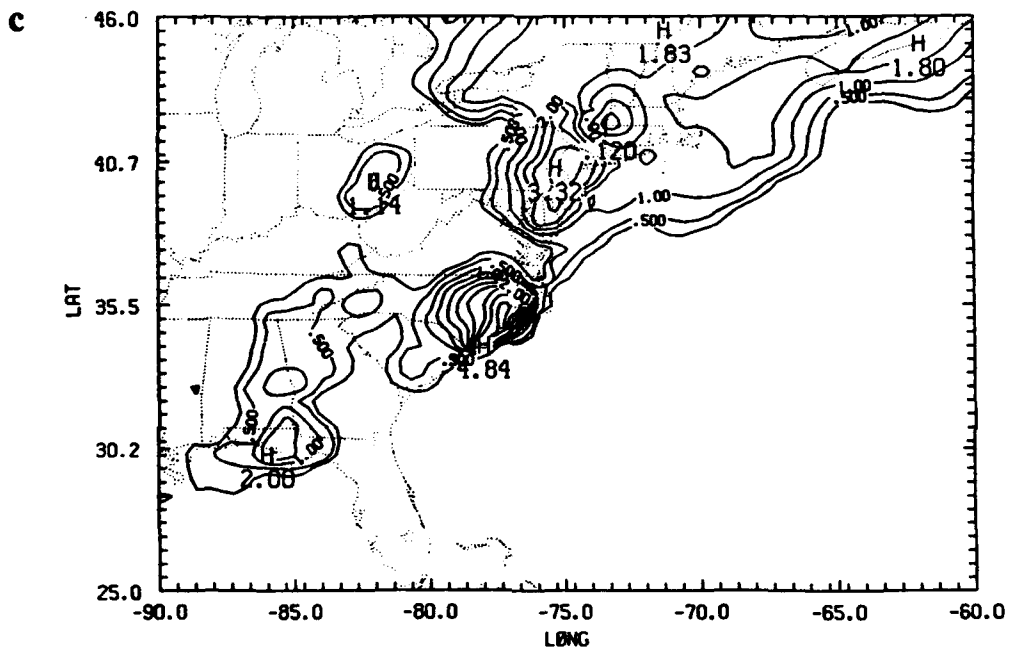


Figure 5.2. Continued.

by reducing the maximum vertical velocities to about 60% of that resulting from DVMI. With the diabatic heating term which forces, to a large degree, convective precipitation, the DVMI (unlike the AVMI) retains the divergence (or vertical motion) associated with the convection.

When DVMI is performed on the analysis fields, model spinup time is reduced. The pre-forecast integration of the model ensures that the analyses are spunup and that the circulations in these analyses are consistent with the model resolution and external parameters such as topography. The initializations and forecasts were performed in this study for the midlatitudes, which dictates a relatively short spinup. In the data-sparse tropics, spinup can be expected to be much greater. In the tropical case, DVMI with merging will be critical in reducing spinup time.

## 6. IMPACT OF ASSIMILATING 3-HOURLY GALE DATA

The discussion to this point has dealt with the major components of data assimilation: objective analysis, initialization, and model forecast. In the following discussion, these components are linked together to form a four-dimensional data-assimilation system.

### 6.1 Introduction

A limited-area intermittent data-assimilation system is used to assimilate 3-hourly data collected during the Genesis of Atlantic Lows Experiment (GALE), which was conducted over the southeastern U.S. during the winter of 1986. The system, developed jointly by NRL and NCSU, is used to generate initial conditions for the NRL/NCSU mesoscale model. The NRL/NCSU data-assimilation system consists of a multivariate, successive correction objective analysis, a diabatic vertical mode initialization (VMI), and a mesoscale numerical forecast. The development of four-dimensional data-assimilation systems for limited areas is being driven by a need to optimally utilize data from the new observing systems of the 1990s (e.g., Next Generation Radar [NEXRAD], Special Sensor Microwave/ Imager [SSM/I], and Wind Profilers) in mesoscale models. Until these new observing systems become operational, other data sources must be used to test assimilation techniques.

During intensive observing periods (IOPs) of GALE, 3-hourly upper-air soundings were taken at selected National Weather Service (NWS) sites over the eastern U.S., supplemented by more frequent and higher density soundings taken at sites along the east coast and by dropsondes deployed offshore by aircraft (Dirks et al. 1988). These

3-hourly asynoptic upper-air observations from the GALE experiment are ideal for testing the impact of assimilating high-frequency observations in a mesoscale model.

The influence of GALE data on the regional analyses and assimilation system at the National Meteorological Center (NMC) has been investigated by Rodgers et al. (1990) and DiMego et al. (1989). Using the higher density GALE soundings along the east coast at the synoptic hours of 0000 and 1200 UTC only, Rodgers et al. (1990) found only a minimal impact on the NMC operational regional analyses and the subsequent forecasts which were rerun for IOPs 1 and 2. Some noise and bias problems were found however in the geopotential in the mid-troposphere in the supplemental soundings along the east coast, which may have contributed to the negative result. Also, at the time of their study, a 6-h forecast from the global spectral model was being used as the first guess for the operational regional analyses (Hoke et al. 1989) and no feedback between the regional model and the analysis could take place. To test an intermittent assimilation for use with future high-frequency wind profiler data, DiMego et al. (1989) used a 3-h update cycle, with the regional model providing the first guess, to assimilate the 3-hourly GALE asynoptic data from a single 12-h period during IOP 1. For their single case, an improvement in the analysis at the end of the 12-h period of assimilation was demonstrated. A stronger jet with stronger horizontal and vertical shears in the final analysis led to a better definition of the indirect circulation in the exit region of the jet in the initialized field. They also asserted that the low-level cyclogenesis was improved in the first 12 h of the subsequent forecast. Even assimilating the winds alone improved the final analysis when compared to the operational analysis which did not use the GALE asynoptic data.

In the present paper, a finer-resolution mesoscale model is used in the assimilation experiments with the GALE asynoptic data, and the model and analysis domains are centered on the GALE region. The horizontal resolution of the fine grid in the

NRL/NCSU model is about 50 km at 45°N, whereas the fine mesh of NMC's nested grid model used by DiMego et al. (1990) had at that time a resolution of about 85 km at the same latitude (Hoke et al. 1989). In the present case, the data assimilation is extended for a full 2 1/2-day period for the second IOP of GALE, during which time a substantial number of asynoptic observations were available. During this time, several upper troposphere jets propagated across the region of the GALE data, and a cyclone developed in the region along the east coast. Since the ultimate test of any data-assimilation system's usefulness is the quality of the forecast produced from the assimilated states, focus is placed heavily on comparisons of subsequent forecasts as well as on the analyses from which they were initialized.

As noted by Kanamitsu (1989), a number of advantages are realized when using a four-dimensional data assimilation system (such as the one described in this paper) for *specifying the initial state for a numerical forecast*: 1) Using a comprehensive assimilation model with full physics as the assimilation model provides the most accurate first guess for the following objective analysis. This allows optimum use of model feedback in regions where data are sparse in time and space. Plus, it ensures that the initial state specification possesses a resolution compatible with the high-resolution forecast model. 2) Using the model forecast as the first guess for the next analysis enables information from earlier observations to be carried forward to provide an independent source of information to be added to the newly-acquired data. That is, the background forecast feeds information forward to the next forecast. 3) Using a multivariate objective analysis ensures a degree of balance between the mass and momentum fields, which helps minimize changes due to the initialization. 4) A multivariate analysis scheme also enables one model variable to be updated from observations of another variable.

The primary purpose here is three-fold: 1) to describe our data assimilation system, 2) to evaluate the effectiveness of the system, and 3) to assess what impact the high-density 3-hourly GALE data have on the NRL analyses and forecasts. More specifically, the analysis performance is addressed both by data-fitting statistics and by comparison with operational analyses. Also, precipitation forecasts are compared using predictions originating from NMC operational analyses, from assimilated fields excluding the 3-hourly data, and from assimilated analyses including the GALE asynoptic data.

## 6.2 The Data-Assimilation System

The NRL/NCSU four-dimensional data-assimilation system uses the intermittent data-assimilation method (or analysis/forecast cycle) in which a model forecast serves as the background field, or first guess, for the analysis of new data. The assimilation system analyzes asynoptic GALE surface and upper-air data every 3, 6, or 12 h using the NRL/NCSU multivariate, successive correction scheme. The analyzed mass and momentum fields are balanced by an initialization procedure. A short-range forecast is then made to serve as the first guess for the next analysis. The NRL/NCSU mesoscale model is used as the assimilation model to generate the background fields for the analysis at each cycle of the assimilation. The same model is used to produce subsequent forecasts from the assimilated states, thus ensuring compatibility of model resolution and physical processes between assimilated and forecast states. In addition, Bell (1986) documented that model spinup time can be substantially reduced if the forecast model being initialized is also the assimilation vehicle. He recognized that the analyzed fields from the assimilation must contain detail compatible with the resolution of the forecast model grid; otherwise, the model will require time to generate the small scale circulations. Furthermore, with a fine grid resolution of approximately 50 km, the NRL/NCSU

mesoscale model is designed to capture and retain the mesoscale information from the GALE data network.

The NRL/NCSU data-assimilation system is also fully diabatic incorporating 3-hourly observed and model-generated precipitation rates in its vertical mode initialization. The initialization scheme is used to correct the divergent part of the wind produced by the analysis and to provide initial conditions for model integration at the next assimilation cycle.

At the start of each update cycle of the assimilation, the analysis procedure corrects the background forecast field using the observed mass and momentum fields. During this process, the divergent part of the wind is lost primarily because the divergence has the same order of magnitude as does the errors in the wind field. This divergent circulation can be regained if the analysis at each cycle of the assimilation is initialized with a diabatic initialization procedure. In the present assimilation system, the interpolated analyses are initialized separately on both coarse and fine grids for the first three vertical modes of the numerical model using the vertical mode scheme of Bourke and McGregor (1983), as applied to the NRL/NCSU model by Sashegyi and Madala (1992a) and Harms et al. (1992a). This scheme generates a balanced divergent part of the wind field, while producing only small changes to the geopotential and vorticity.

Harms et al. (1992a) discussed the importance of including diabatic forcing in the model initialization. With the inclusion of heating corresponding to observed rainfall in the diabatic forcing term of the thermodynamic balance equation, the initialization can force the model state toward the real atmospheric state and substantially reduce model spinup. In our diabatic vertical mode initialization procedure, diabatic heating rates are computed from a merged field of observed and model-produced rainfall.

Model convective rainfall is accumulated during the integration of the previous assimilation cycle from 3 h before the current initialization time to 3 h past that initial

time. In other words, the model convective precipitation is accumulated for 6 h centered around the beginning of the current assimilation cycle. As a result, the model integration for each assimilation cycle is 3 h longer than the cycle duration (period between updates). For cycle durations of 3, 6, and 12 h, the model is integrated for 0, 3, and 9 h, respectively, before the rainfall accumulation begins. Therefore, in the latter two assimilation cases, the model is spunup prior to collecting the model convective rain. During the vertical mode initialization, this model-produced rainfall is combined with analyzed 6-h observed rainfall (satellite-derived and GALE 3-hourly raingauge data, described in the next section) valid for the same period, a time frame extending to 3 h beyond the current analysis time. This procedure requires the assimilation to occur at least 3 h after real time. However, in this sense, diabatic heating rates used in the initialization are derived from rainfall accumulations which are time-centered at the *appropriate time (valid at initialization)* and, therefore, are temporally representative rates. The observed values are used where available over the model grid; otherwise, the model values are used.

This 6-h combined rainfall field is converted into time-average rainfall rates for all grid points. The average rain rates are converted into vertical profiles of heating using a reverse Kuo cumulus parameterization. This vertical distribution of the latent heating is based on the cumulus convective scheme of the model. Thus, no simplifying hypotheses are needed. The advantage of the present approach is an improved consistency obtained with the physical parameterization scheme of the model. This three-dimensional diabatic heating field is then added as a fixed forcing term in the thermodynamic energy balance equation as each iteration of the vertical mode initialization is performed.

During the first 3 h of model integration of each assimilation cycle, the model-produced convective rainfall and heating rates are merged with the corresponding rates used in the previous initialization, thus ensuring the desired compatibility with the heating

rates at initialization. As mentioned earlier, the heating rates used in the initialization are derived from a 6-h accumulation of rainfall centered on the initialization time. Therefore, this 6-h amount includes rainfall accumulated for 3 h beyond the valid time of the initialization, that is, the same 3 h of subsequent model integration in which the merging of heat/rain rates occurs. Thus, these heating rates used in the initialization and first 3 h of subsequent "assimilation" model integration are representative of "observed" heating rates for this period. Thus, the merging process forces the subsequent model heating toward the "observed" heating.

### 6.3 Experimental Design

The system was tested using data collected over a 2 1/2-day period from 1200 UTC 25 January to 0000 UTC 28 January 1986 (25/12Z to 28/00Z). This data included a set of upper air soundings, which were interpolated to 10-mb levels from the surface up to 100 mb, and surface observations for IOP 2 of GALE. These datasets were obtained from the GALE Data Center (GDC) at Drexel University (Mercer 1987). The data domain included the eastern U.S. and western North Atlantic from 115°W to 45°W in longitude and from 10°N to 60°N in latitude. A higher density of upper-air and surface data is found in the inner GALE region covering the Carolinas and southern Virginia from the Gulf Stream to the Appalachians. The sounding network for GALE consisted of 39 National Weather Service (NWS) sites which made launches at 3-h intervals when weather events dictated. These observing sites were supplemented by seven Cross-chain LORAN-C Atmospheric Sounding System (CLASS) sites, which made launches as often as every 90 minutes, in North Carolina and South Carolina. Plus, numerous dropwindsondes were deployed over the Atlantic Ocean and the Gulf of Mexico during IOP 2, as well as observing systems aboard two ships in Atlantic coastal waters (Mercer

and Kreitzberg 1986). The GALE datasets included upper-air observations (primarily synoptic) from several other NWS sites, the Canadian Weather Service sites, and a few sites in Mexico. The GALE observations were grouped into data windows of 3 h centered on the analysis times of 0000, 0300, 0600, 0900, 1200, 1500, 1800, and 2100 UTC.

As mentioned in Chapter 4, in regions of no data over the ocean, bogus data, derived from the difference between the first guess forecast and the NMC 2.5° hemispheric analysis, are used to merge the analysis smoothly with the NMC analysis over the data-sparse ocean regions at synoptic hours. At off-synoptic times, no bogus soundings are added and the analysis returns to the background in regions of no data. As an example, Fig. 6.1 shows the locations of surface and upper-air data at 26/00Z and 26/03Z after the quality control. Very few upper-air real observations (shown by the crosses) are found over the oceans, where NMC "bogus" data (shown by stars) have been added at the synoptic hours (Figs. 6.1a and c). At the asynoptic hours (Figs. 6.1b and d), the number and aerial coverage of the data is much less than at the synoptic times as noted above. Table 6.1 shows the average number of surface and upper-air observations, before and after quality control, available at each analysis time, with the number of bogus data shown in parentheses. As was also clear in Fig. 6.1, there is considerable variation. At the asynoptic times, only a limited number of sounding data is available with these being solely from the GALE network. The actual number of data analyzed is less than the number of real GALE observations, particularly in the case of surface data. In the quality control procedures, gross error checks and buddy checks eliminate a few data. Data in close proximity of each other or observations from the same location within a given 3-h data window are averaged to create super observations.

Three-hour observed rainfall amounts from IOP 2 of GALE are used in the diabatic vertical mode initialization. The raingauge data obtained from the GALE Data Center at

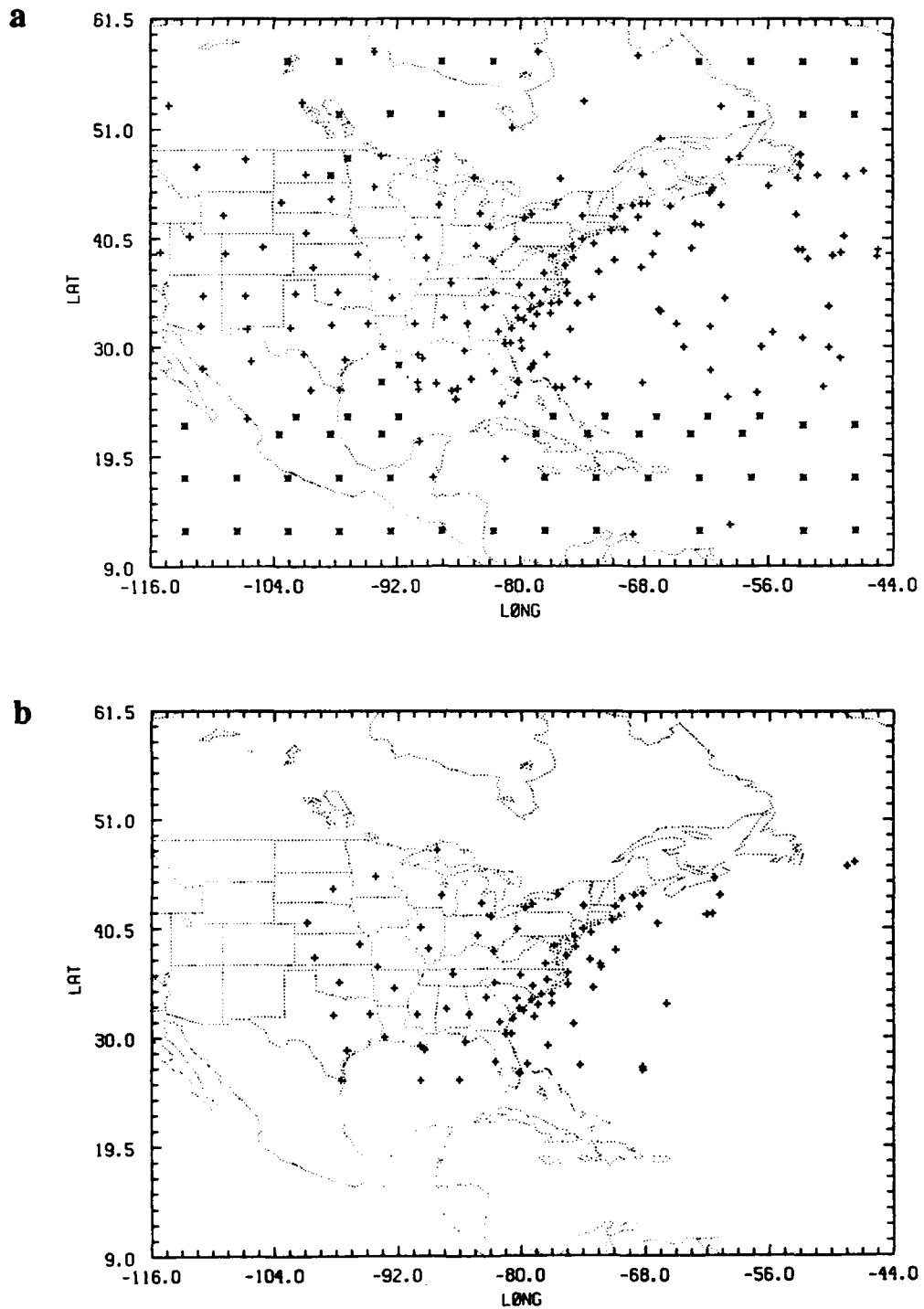


Figure 6.1. The locations of surface (a and b) and upper-air (c and d) data at 26/00Z and 26/03Z, respectively. The observations are indicated by the '+', while bogus values are indicated by '\*'. The analysis grid is indicated by the tick marks along the domain boundary.

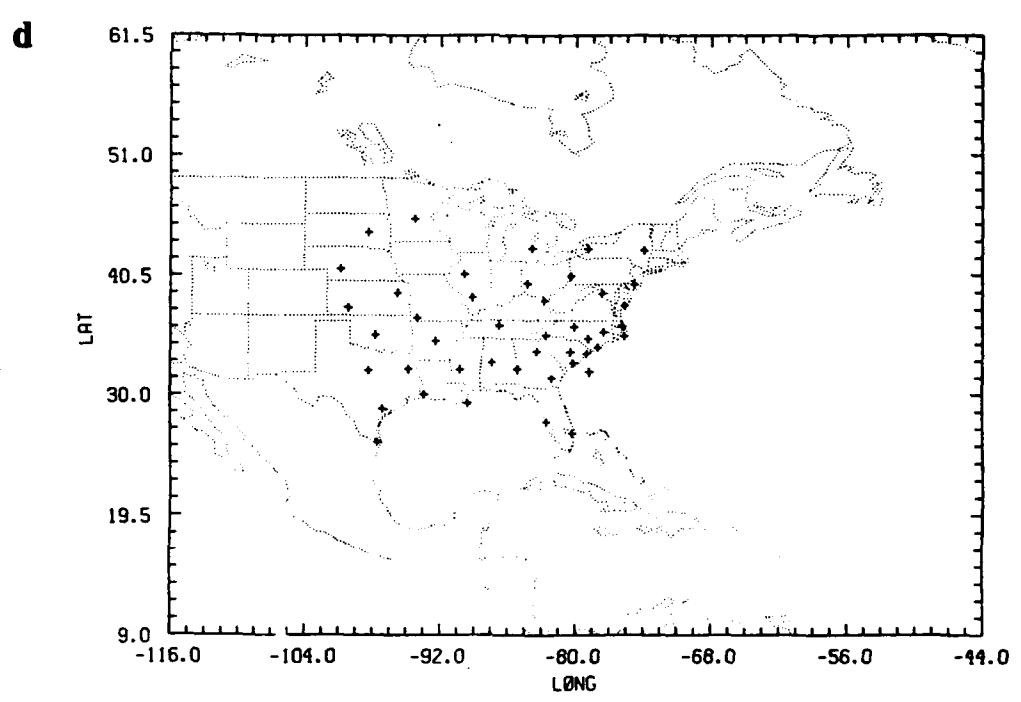
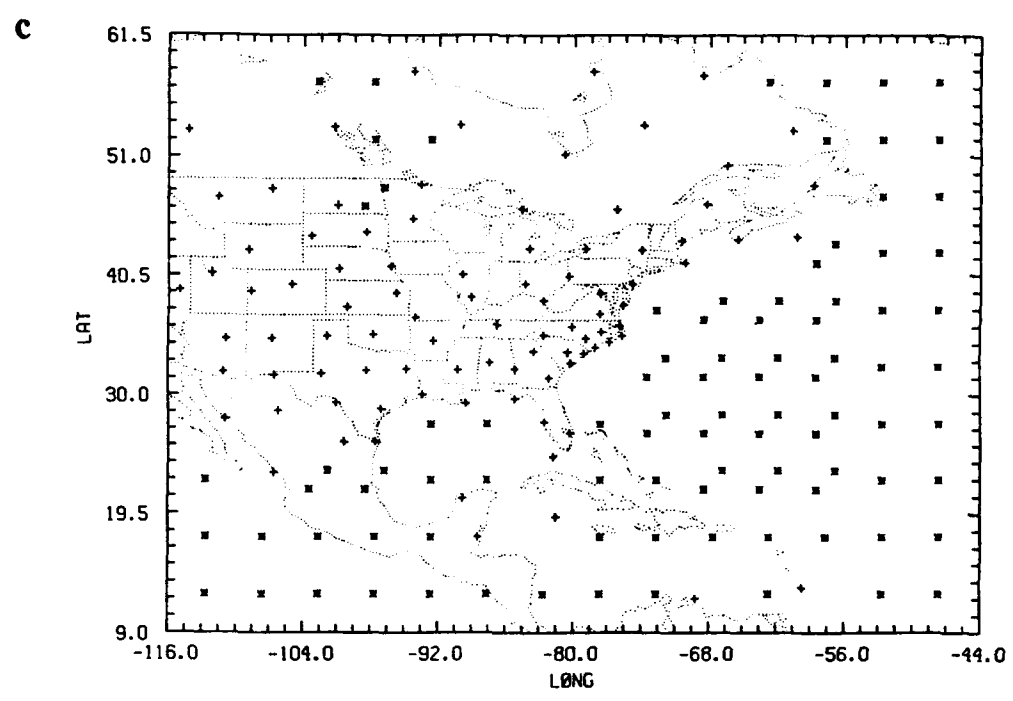


Figure 6.1. Continued.

TABLE 6.1. Average number of observations, before and after quality control and creation of super observations, in each analysis time window. Average number of bogus observations is in parentheses

<u>Analysis Time</u>	<u>Upper-air</u>			<u>Surface</u>		
0000 UTC	101	89	(93)	337	170	(64)
0300 UTC	49	42		226	85	
0600 UTC	51	44		277	120	
0900 UTC	48	42		232	87	
1200 UTC	113	103	(76)	376	198	(42)
1500 UTC	47	40		232	87	
1800 UTC	49	42		308	138	
2100 UTC	41	35		225	81	

Drexel University were bilinearly interpolated to the fine grid of the NRL/NCSU model. Values for the coarse grid were then obtained by computing a 9-point average using fine grid values. These raingauge data were supplemented, or merged, with the satellite-derived rainfall analyses provided by the University of Wisconsin (Martin et al. 1988). These satellite-derived rainfall values were available as 6-h accumulations on a one degree latitude by one degree longitude grid which extended from approximately 25°N to 46°N and 60°W to 85°W. The 6-h derived amounts were temporally interpolated to obtain 3-h accumulations, which were then bilinearly interpolated to the model grids. These interpolated fields of satellite-derived rainfall were merged with the GALE raingauge data to produce our "observed" 3-h rainfall data. When and where available, the raingauge values were kept; otherwise, the merged values were represented by the satellite-derived rainfall.

To test the effectiveness of the NRL/NCSU data-assimilation system and to assess the impact, if any, of the 3-hourly GALE data on the assimilation and subsequent forecasts initialized from our assimilated states, five experimental cases were performed, as outlined in Table 6.2. In experiment 1, 12-hourly National Meteorological Center 2.5° hemispheric analyses (NMC analyses) for the period 25/12Z to 28/00Z are used. No re-analysis was performed to incorporate the high-density GALE data; therefore, these NMC analyses represent our "no assimilation" case and serve as the control experiment for comparison with analyses from the assimilation experiments. Differences in the assimilated analyses from the control analyses are attributable to both the assimilation of the 3-hourly data and the use of the high horizontal resolution NRL/NCSU mesoscale model in the assimilation process.

The 25/00Z NMC analysis was used to cold start the remaining experiments. The first analysis of GALE data occurs at 25/12Z in these assimilation runs. The 25/00Z NMC analysis was initialized and then the model was integrated for 12 h. The 12-h

TABLE 6.2. Data Assimilation Experiments.

Experiment	Assimilation Cycle	Initialization Type	Remarks
1 - Control	N / A	*AVMI	No assimilation--uses NMC analyses
2 - 12DI	12 Hours	*DVMI	Assimilation without asynoptic GALE data
3 - 06DI	6 Hours	DVMI	Assimilation with 6-hourly GALE data
4 - 03DI	3 Hours	DVMI	Assimilation with 3-hourly GALE data
5 - 06AI	6 Hours	AVMI	Assimilation with 6-hourly GALE data; no diabatic heating in model initialization

\*AVMI -- Adiabatic vertical mode initialization

\*DVMI -- Diabatic vertical mode initialization

forecast served as the first-guess field for the initial analysis in the assimilation sequences. In experiment 2, the intermittent data assimilation was performed from 25/12Z to 28/00Z with a 12-h update cycle, where only synoptic data entered into the analyses. An update cycle of 6 h was used in experiment 3. GALE data valid at 00, 06, 12, and 18Z were incorporated. Like experiment 2, the assimilation is performed for a 2 1/2-day period. Due to extremely limited sounding data at 25/15Z and 25/21Z, the assimilation run in experiment 4 began at 26/00Z, using the 26/00Z analysis from experiment 3 as its initial assimilated state. The update cycle here is 3 h to use all 3-hourly GALE data from 26/00Z to 28/00Z. Diabatic vertical mode initialization was used in experiments 2, 3, and 4. Experiment 5 was identical to experiment 3 with a 6-h update cycle, except diabatic heating was excluded from the vertical mode initialization. The assimilated states (analyses at each update cycle) from experiments 2 - 5 were saved for post-processing, i.e. *inter-comparisons* and comparisons with the NMC analyses. For all experiments, a 3-h data window centered on the analysis time was used.

From the assimilated fields valid at 26/00Z and 26/12Z of each experiment, 24-h forecasts were produced using the same model that was used in the assimilation. Prior to model integration, these assimilated analyses were initialized using the vertical mode initialization procedure. The model initialization using analyses from experiments 2, 3, and 4 included forcing due to diabatic heating. But for the sake of fairness, the diabatic heating was derived from only rainfall occurring prior to forecast start time (a 3-h accumulation), versus a 6-h accumulation centered on the analysis/initialization time as done in the assimilation runs.

## 6.4 Results

Evaluation of the experiments is performed by means of data-fitting statistics, where rms differences between observations and analyses and between observations and background forecast fields are compared. The evaluation also includes a more subjective comparison of synoptic-scale and mesoscale patterns, amplitudes, and positions of specific features from the analyses (assimilated states) and the subsequent 24-h forecasts.

### 6.4.1 Statistical Evaluation and Discussion

Root-mean-square errors for the fit of background forecasts and analyses to the observations at each cycle of the assimilation experiments were compiled. The data used here are those passed by the data checking procedures in the analysis scheme. The bogus data are not included in this statistical evaluation. These statistics were computed for each analysis variable (geopotential, u- and v- wind components, temperature, and relative humidity) at each of the 19 analysis levels from 1000 mb to 100 mb. Figure 6.2 shows the average analysis and average background forecast rms errors in geopotential for the assimilation analyses and forecasts valid at 0000 and 1200 UTC from experiments 2, 3, and 4 which had update cycles of 12, 6, and 3 h, respectively. By extracting the statistics at only the synoptic hours (cycles), the comparison is more equitable than if including statistics from all hours of experiments 3 and 4. In Fig. 6.2b, the rms error in the background geopotential at the synoptic hours was greatest at all levels when using the 12-h update cycle. In the upper troposphere and at the surface, the 3-h update cycle led to the least error with about 5 - 10 m less error than with the 12-h cycle. These results show that a positive impact is made on the first guess field of geopotential at the synoptic hours when 3-hourly GALE data are included. However, in the mid- and lower

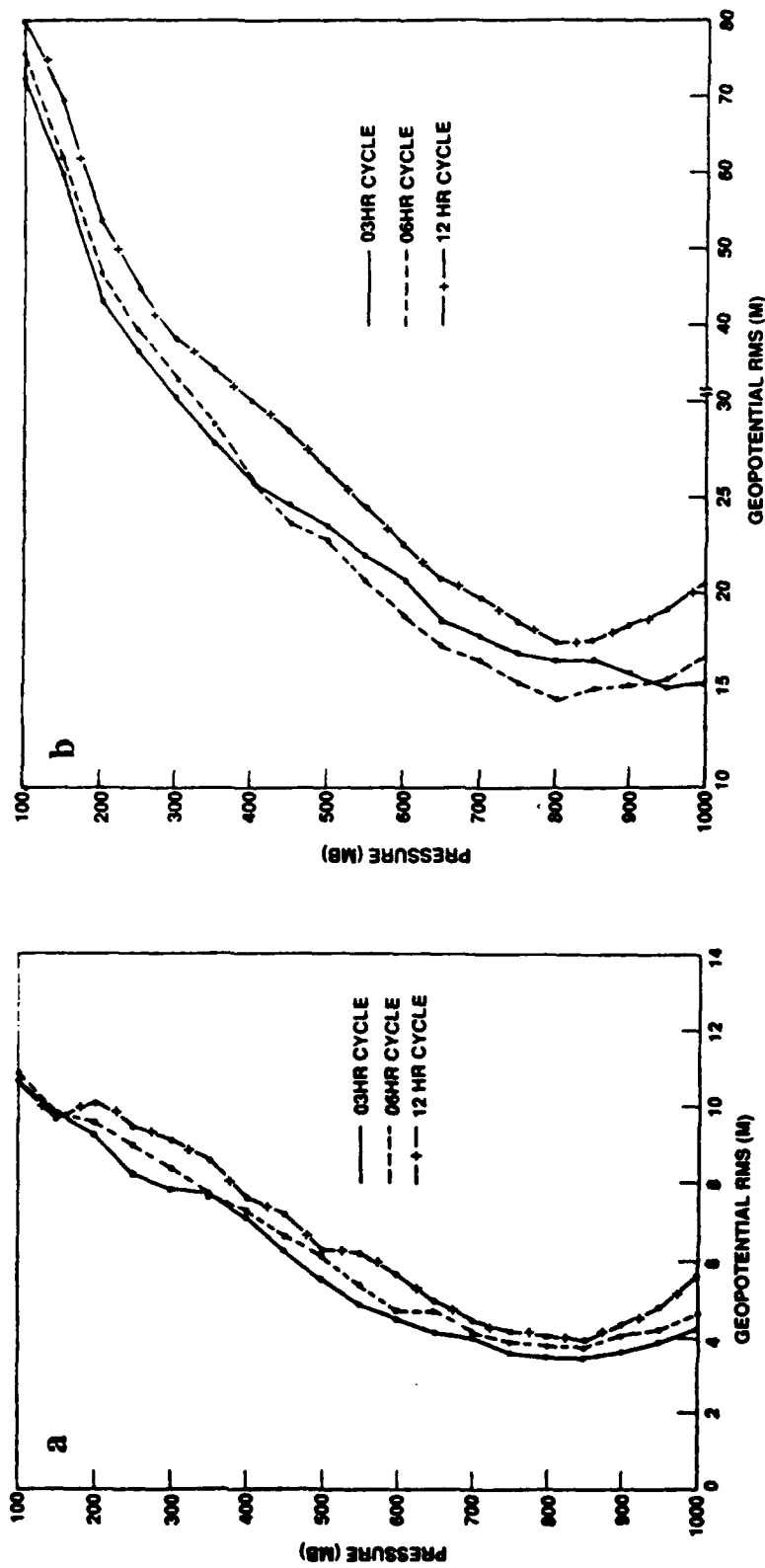


Figure 6.2. (a) Average analysis rms errors and (b) average background forecast rms errors for geopotential (m) from the 0000 and 1200 UTC update cycles of experiments 2 (12DI), 3 (06DI), and 4 (03DI).

troposphere, the 6-h update cycle gave slightly better results than when updating every 3 h. A possible explanation could be that the 3-h cycle may not allow sufficient time for model spinup in regions not updated by the 3-hourly asynoptic data. The corresponding average analysis rms errors at the synoptic hours, displayed in Fig. 6.2a, are significantly less, as expected, than the background errors. Here, the inclusion of the 3-hourly data led to a decrease in analysis errors throughout the troposphere, with the assimilation using the 3-h update cycle being better than the 6-h update cycle.

Error statistics were also compiled at the asynoptic hours of 0600 and 1800 UTC from experiments 3 and 4. As shown in Fig. 6.3, the background and analysis errors in geopotential decreased at all levels as additional 3-hourly data were assimilated; that is, the assimilation with an update cycle of 3 h showed an improvement over the case with a 6-h cycle. Clearly at the asynoptic hours, the improved background fields from the high-resolution forecast model are successful in carrying information from earlier asynoptic observations forward in time, leading to an improved analysis which then results in a better background forecast for the next update cycle of the assimilation.

Figures 6.4 - 6.6 illustrate the average rms statistics of u-, v-, and relative humidity from experiments 2 - 4 for the synoptic update cycles. Even though the analysis error in the wind and humidity fields remained essentially unchanged as the assimilation cycle decreased, the subsequent forecasts improved at all levels with the decreasing cycle length.

Average root-mean-square errors for geopotential from experiments 3 and 5 (all cycles included) are plotted in Fig. 6.7. Assimilation with diabatic heating included in the initialization procedure (06DI) resulted in background errors within the lower troposphere of about 1 m less than in the assimilation excluding the convective heating (06AI), but little or no improvement at higher levels. The analysis errors from these two experiments were almost identical. Similar results were found for the wind components and relative

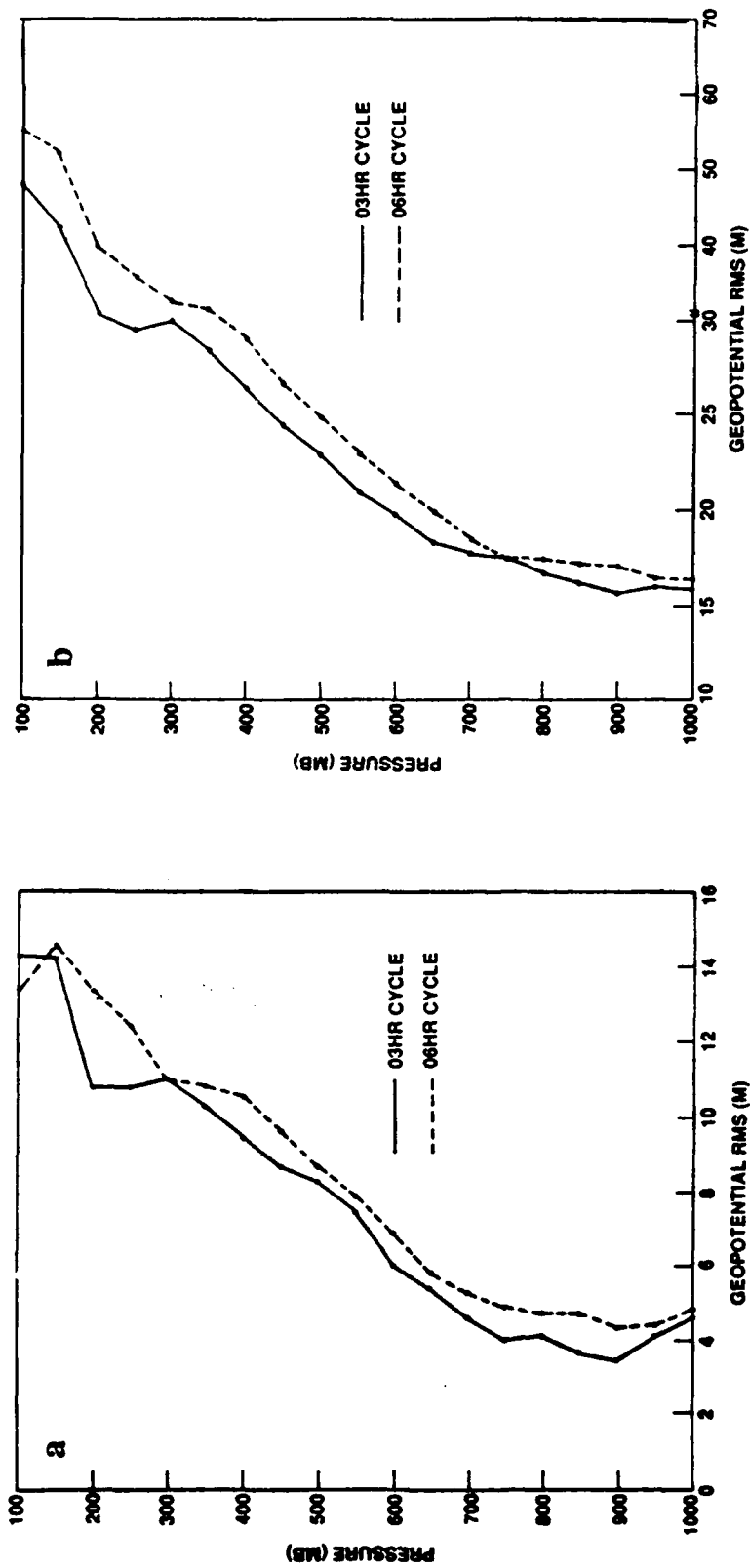


Figure 6.3. (a) Average analysis rms errors and (b) average background forecast rms errors for geopotential (m) from the 0600 and 1800 UTC update cycles of experiments 3 (06DI) and 4 (03DI).

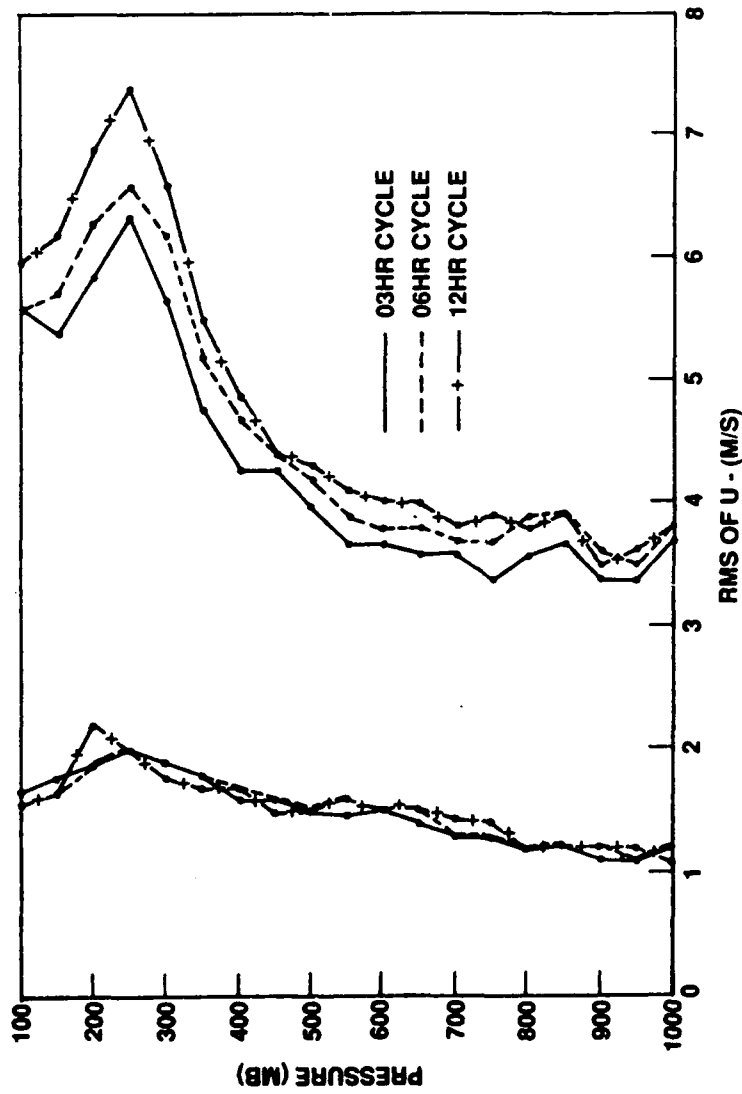


Figure 6.4. Average analysis and background forecast rms errors for the u- wind component ( $m s^{-1}$ ) from the 0000 and 1200 UTC update cycles of experiments 2 (12DI), 3 (06DD), and 4 (03DD). Analysis error plots are on the left side of the figure.

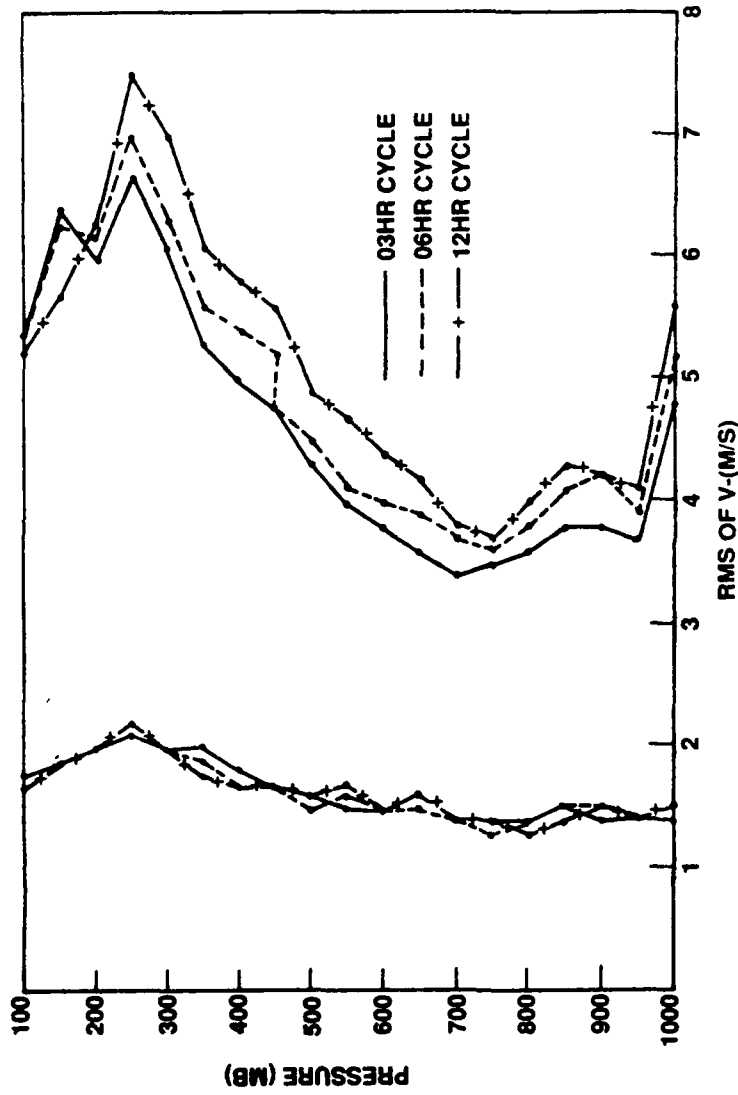


Figure 6.5. Average analysis and background forecast rms errors for the v-wind component ( $\text{m s}^{-1}$ ) from the 0000 and 1200 UTC update cycles of experiments 2 (12DI), 3 (06DI), and 4 (03DI). Analysis error plots are on the left side of the figure.

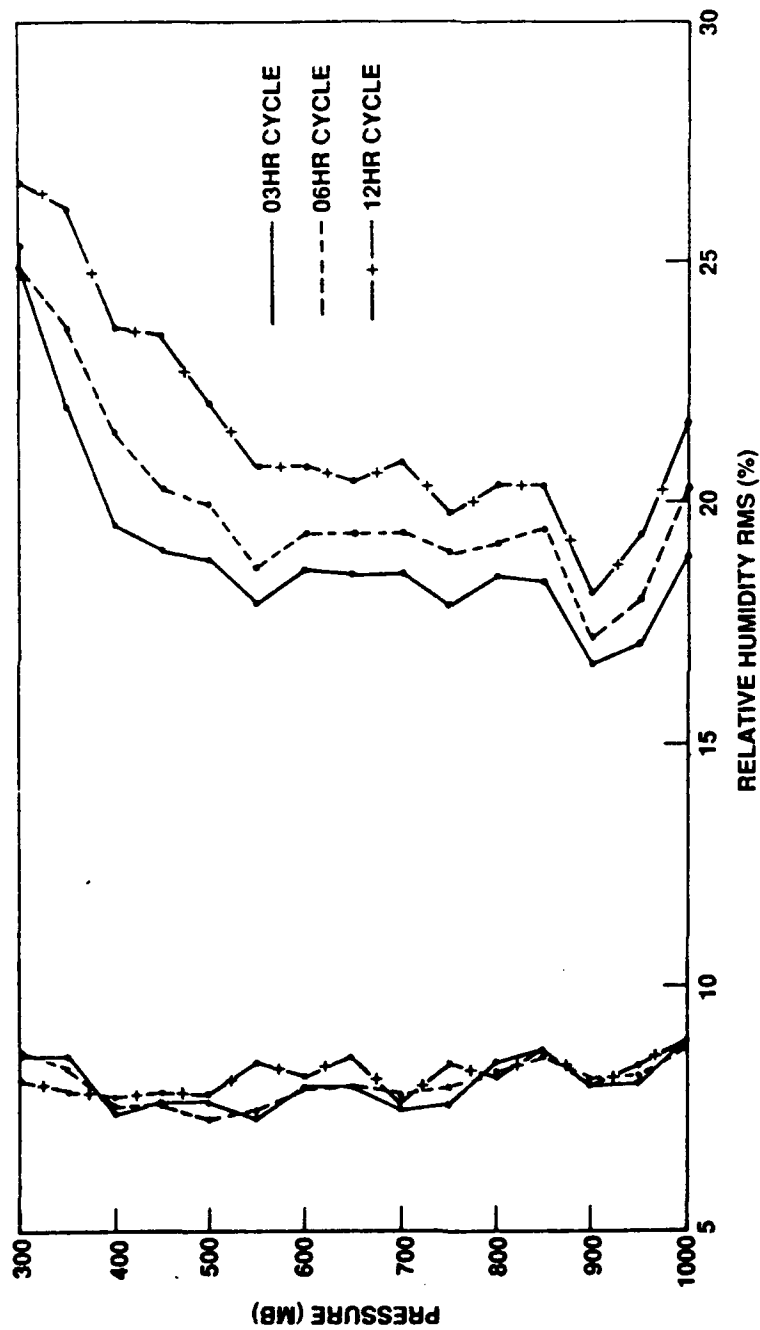


Figure 6.6. Average analysis and background forecast rms errors for relative humidity (%) from the 0000 and 1200 UTC update cycles of experiments 2 (12DI), 3 (06DI), and 4 (03DI). Analysis error plots are on the left side of the figure.

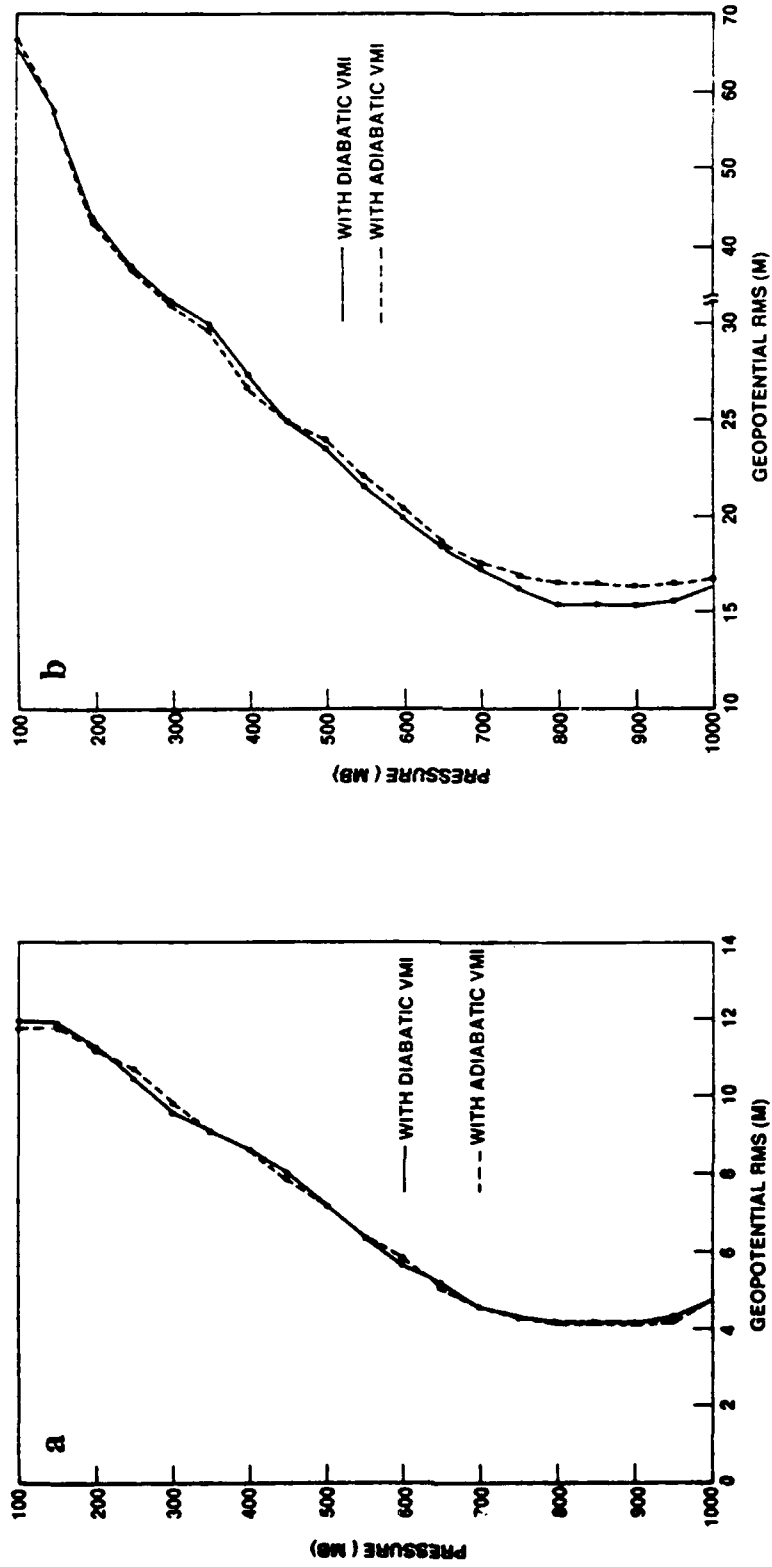


Figure 6.7. (a) Average analysis rms errors and (b) average background forecast rms errors for geopotential (m) from all update cycles of experiments 3 (06DI) and 5 (06AI).

humidity. These results suggest that the inclusion or exclusion of the diabatic forcing in the assimilation model initialization has minimal impact on the assimilation of these first order variables.

Generally, the background forecast errors at all levels (as shown in Figs. 6.2 - 6.7) are in good agreement with and verify our estimates of the standard deviations of the observations from the first guess forecasts (refer to Table 6.3). These estimates are a sum of the input observational error and a linear forecast growth error. With further testing, we can utilize statistics compiled over a longer period to further adjust these input error statistics for use in the analysis.

Further insight can be gained by investigating the time variation of the statistics in the case of the assimilation with update cycle of 3 h (experiment 4). Figure 6.8a shows plots of average rms analysis errors for the geopotential at 0300 and 1500 UTC, 0600 and 1800 UTC, 0900 and 2100 UTC, and 1200 and 0000 UTC from experiment 4. The analysis error (differences between analysis and observations) is less at the synoptic hours of 0000 and 1200 UTC than at the asynoptic hours. The larger errors noted by Rodgers et al. (1990) in the geopotential data from the supplemental GALE soundings along the east coast may have contributed to the higher rms errors at the asynoptic hours. At the synoptic hours, more data were used covering the whole analysis domain (see Fig. 6.1), and the average analysis error would be less. The average rms background errors for geopotential are shown in Fig. 6.8b. In general, the background fields for the 0000 and 1200 UTC analyses had the largest rms error, while those for the 0300 and 1500 UTC analyses possessed the least error. From the smaller analysis error and the larger data coverage at the synoptic hours, one would expect a more accurate background forecast for the 0300 and 1500 UTC analyses. At synoptic hours, the background in regions outside of the influence of the asynoptic data would be less accurate and the comparison with synoptic data would lead to larger errors. However, at 0600 and 1800

TABLE 6.3. Standard deviation of the observational errors and updated forecast error growth for a 6-h forecast period in parentheses. These are the input error statistics for the objective analysis.

Pressure (mb)	Height (m)	Temperature (°C)	Rel humidity (%)	u,v Wind (m s <sup>-1</sup> )
100	20 (25)	2.0 (0.7)	-----	3.5 (1.3)
150	18 (25)	1.8 (0.6)	-----	4.0 (1.4)
200	15 (20)	1.8 (0.5)	-----	4.0 (1.5)
250	14 (18)	1.5 (0.6)	-----	4.0 (1.6)
300	14 (16)	1.0 (0.6)	17 (4)	4.0 (1.6)
350	14 (14)	1.0 (0.5)	15 (4)	4.0 (1.7)
400	12 (12)	1.0 (0.5)	13 (4)	3.5 (1.7)
450	10 (11)	1.0 (0.4)	13 (4)	3.5 (1.6)
500	9 (10)	1.0 (0.3)	13 (4)	3.0 (1.6)
550	8 (10)	1.0 (0.3)	13 (3)	3.0 (1.5)
600	7 (9)	1.0 (0.3)	12 (3)	3.0 (1.4)
650	6 (8)	1.2 (0.3)	12 (3)	3.0 (1.3)
700	6 (8)	1.3 (0.3)	12 (2)	2.5 (1.2)
750	6 (8)	1.4 (0.3)	12 (2)	2.5 (1.2)
800	6 (8)	1.5 (0.4)	13 (2)	2.5 (1.1)
850	6 (8)	1.5 (0.5)	13 (2)	2.5 (1.1)
900	5 (8)	1.8 (0.5)	13 (2)	2.5 (1.1)
950	5 (8)	1.8 (0.6)	13 (2)	2.5 (1.1)
1000	5 (8)	1.8 (0.6)	13 (2)	2.5 (1.1)

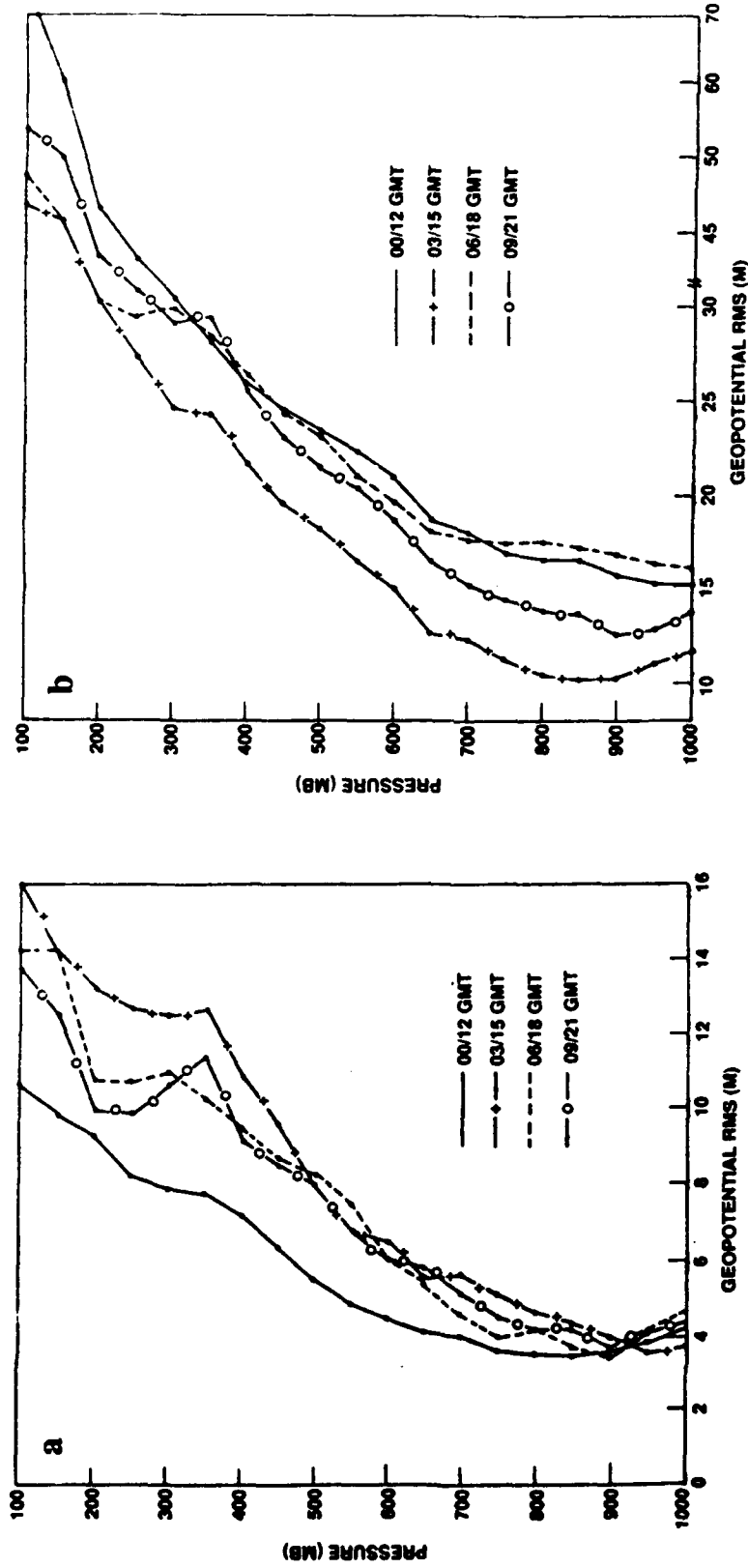


Figure 6.8. (a) Average analysis rms errors and (b) average background forecast rms errors for geopotential (m) from experiment 4 (03DI) at the 0300 / 1500 UTC, 0600 / 1800 UTC, 0900 / 2100 UTC, and 1200 / 0000 UTC update cycles.

UTC, the errors in the background fields were larger than the errors in the first-guess fields valid at 0900 and 2100 UTC.

Similar statistics were compiled from experiment 4 for the u- and v- wind components and relative humidity (not shown). However, the results are not as clear cut as in the case of geopotential. The background error at the 0300 and 1500 UTC cycles was generally less than that at the synoptic cycles, and likewise the analysis error at the 0300 and 1500 UTC cycles was generally larger than that at the 0000 and 1200 UTC update cycles. But the errors of the two sets of intermediate cycles (0600/1800 UTC and 0900/2100 UTC) were very random, with values not always falling between the errors from the 0300/1500 cycles and the synoptic cycles as in the case with geopotential.

These results can be useful in adjusting the input background forecast error growth rate used in the objective analysis scheme. Currently, the analysis error and the error growth are fixed values for all cycles within a given assimilation sequence. When considering the above results, it may be prudent in the future to adjust the analysis error and the forecast error growth, particularly for geopotential, in a fashion that allows the input background error to be largest at the 0000 and 1200 UTC update cycles and least at the 0300 and 1500 UTC cycles.

#### 6.4.2 Subjective Evaluation and Discussion

Some synoptic analysis of the results is beneficial for understanding the impact of four-dimensional data assimilation on synoptic and mesoscale features, i.e. in the present study, the impact of assimilating the 3-hourly GALE observations. Here, emphasis is placed on a few significant events in the surface and 500-mb analyses and the forecast precipitation fields. Precipitation forecasts are verified against our observed precipitation (raingauge / satellite-derived rainfall). Precipitation verification is especially valuable

since rainfall is the result of many complex physical processes and is usually characterized by considerable small-scale variability. Since rainfall is dependent on divergence and vertical motion, it is also a good indicator of the accuracy of the model's dynamic balance and intervariable consistency.

a) Analysis aspects

Sea-level pressure and 1000-mb wind and temperature analysis fields from the "no assimilation" case and the assimilation with a 12-h update cycle (12DI) at 25/12Z are shown in Fig. 6.9. The 12DI analysis, shown in Fig. 6.9b, captured the strong temperature gradient associated with the coastal front along the Carolina coast and also the cold air damming with strong ridging east of the Appalachians. The 25/12Z Bosart surface analysis (Fig. 6.10) verifies the existence of these mesoscale features. However, the "no assimilation" analysis, shown in Fig. 6.9a, has a weaker thermal gradient along the coast. Strong onshore flow, which is readily apparent in Bosart's analysis, was also present in the assimilated analysis. Figure 6.11 shows the 1000-mb specific humidity fields from experiments 1 and 2. The low-level moisture gradients at the coastal front and with the short wave over the western Gulf of Mexico are much greater in the 12DI analysis than in the "no assimilation" analysis.

At 26/00Z, surface and 500-mb analyses from experiments 1, 2, 3, and 5 were examined. Compared to the "no assimilation" analyses, the assimilated surface fields possessed much stronger thermal and low-level moisture gradients across the coastal front, with little distinction between the three assimilations of varying update cycles (not shown). The 500-mb relative humidity analyses, shown in Fig. 6.12, reveal a better distinction. While rain was falling over central North Carolina at 26/00Z, an upper-level moisture maxima was present there in the assimilated fields. However, the analysis from

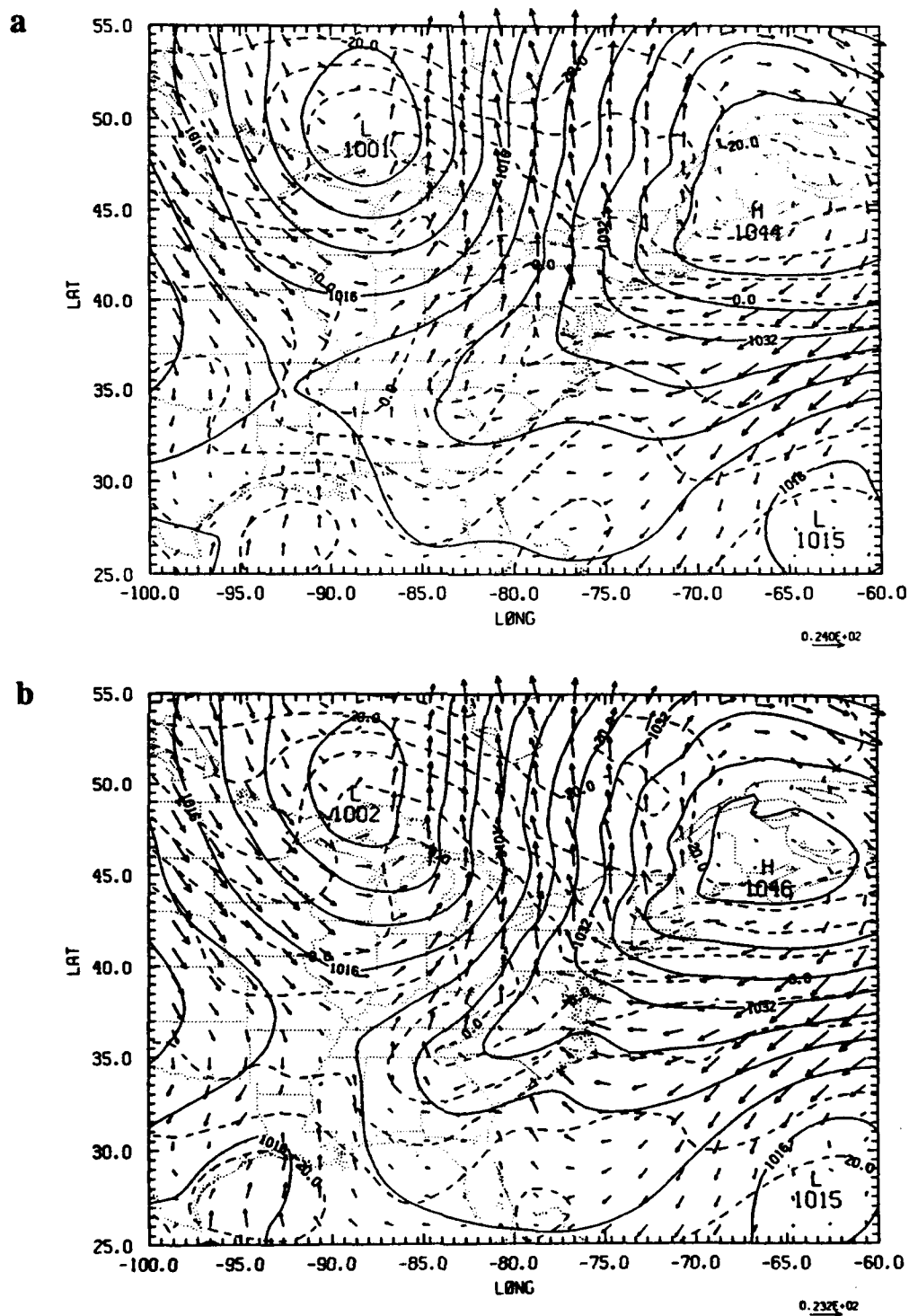


Figure 6.9. Sea-level pressure (mb), 1000-mb temperature ( $^{\circ}\text{C}$ ) and wind analyses at 25/12Z from (a) experiment 1 (no assimilation) and (b) experiment 2 (12DI). Contours of sea level pressure and temperature at 1000 mb are 4 mb and  $5^{\circ}\text{C}$ , respectively.

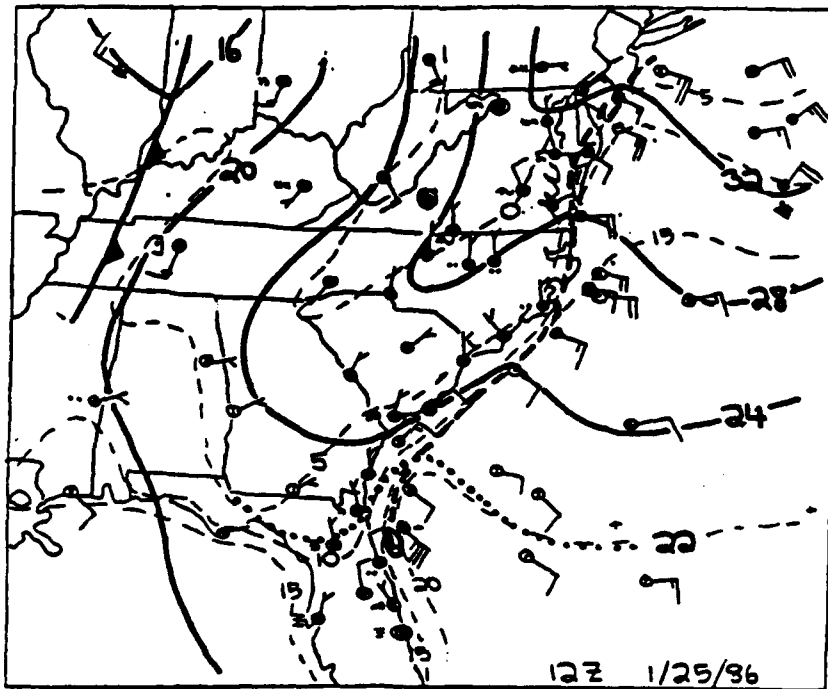


Figure 6.10. GALE analysis of sea-level pressure deviation (from 1000 mb), surface temperature ( $^{\circ}\text{C}$ ) and wind for 25/12Z by Bosart (1988). Surface temperature contours every  $5^{\circ}\text{C}$ .

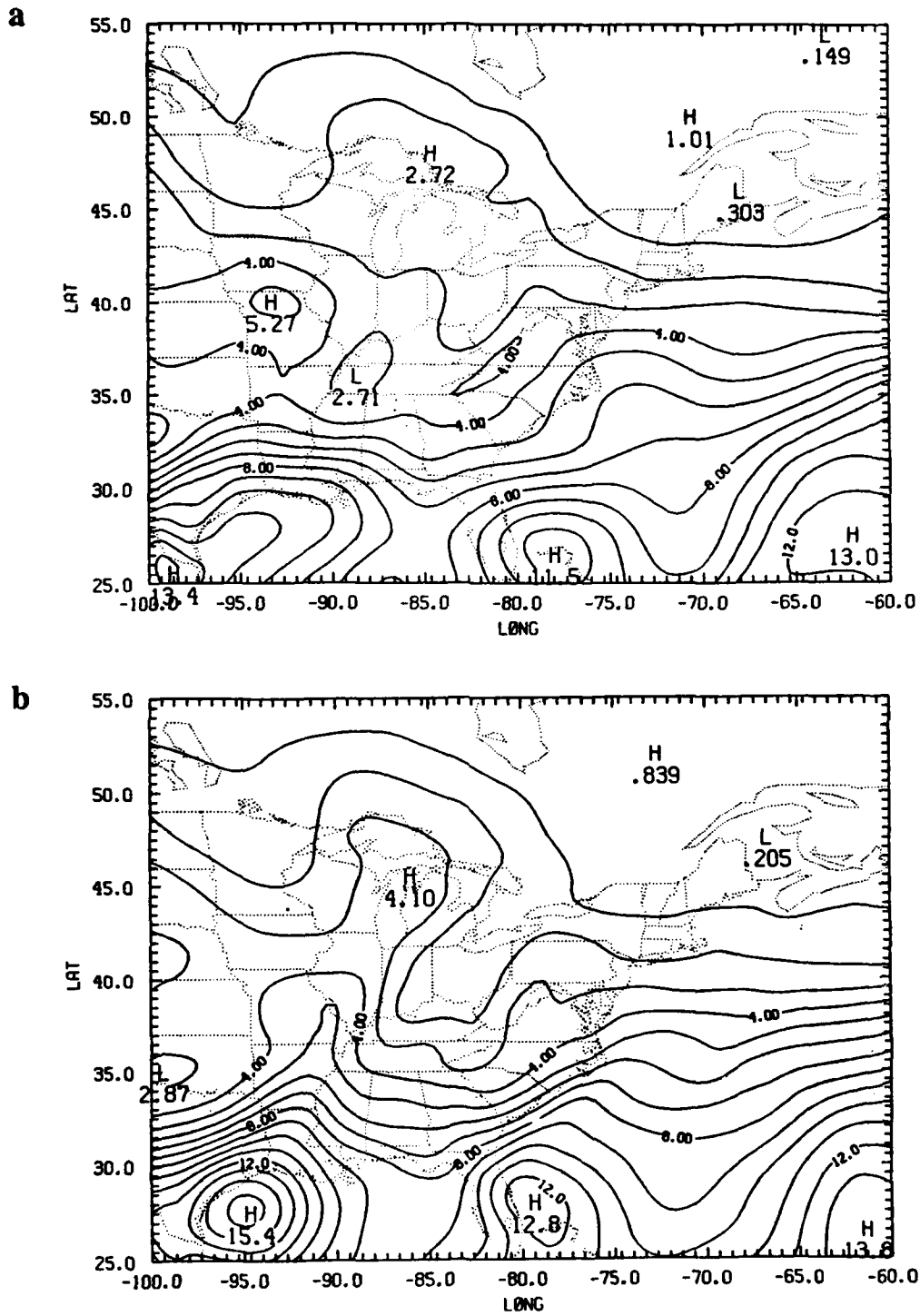


Figure 6.11. 1000-mb specific humidity ( $\text{g kg}^{-1}$ ) analyses at 25/12Z from (a) experiment 1 (no assimilation) and (b) experiment 2 (12DI). Contours are every  $1 \text{ g kg}^{-1}$ .

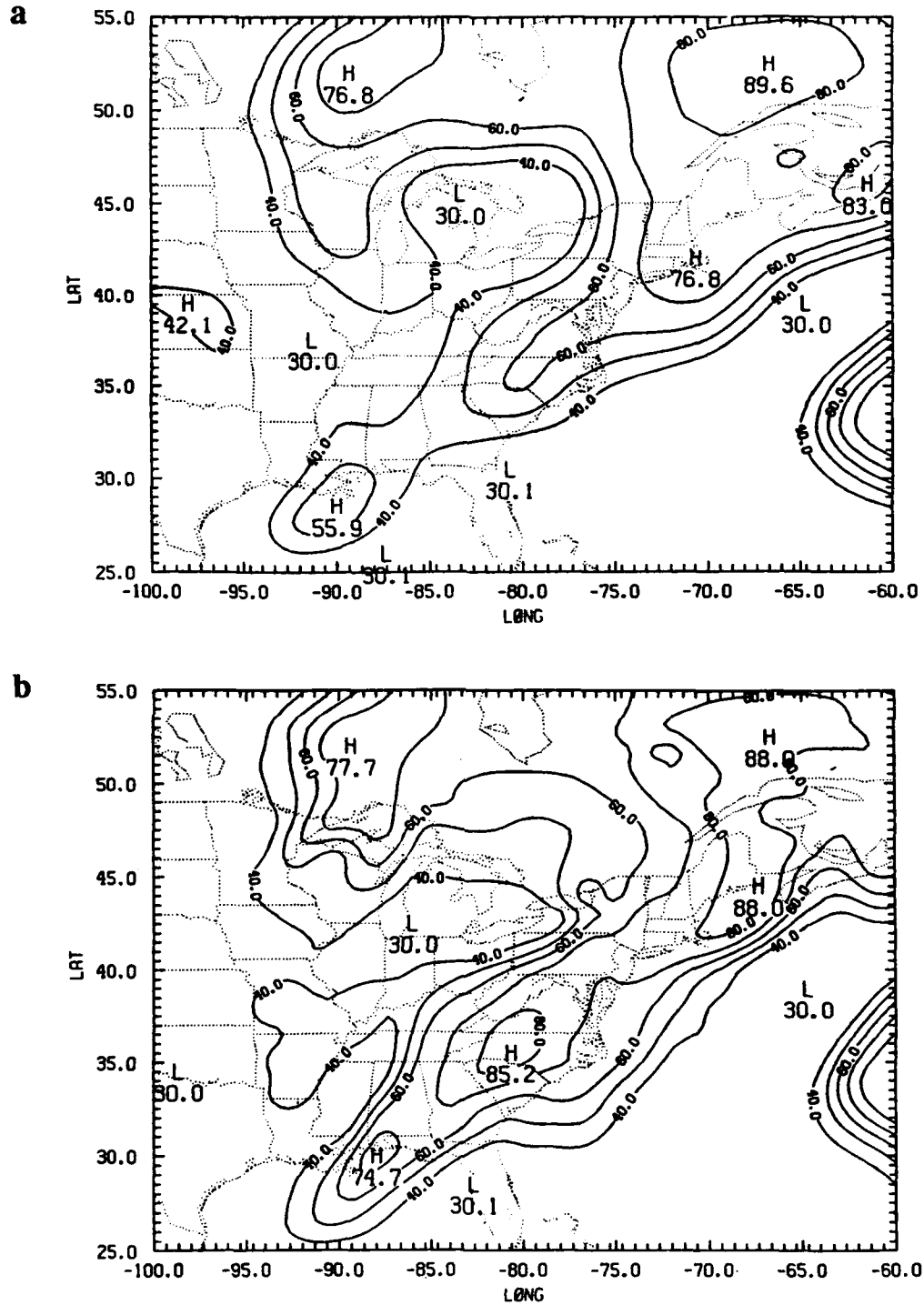


Figure 6.12. 500-mb relative humidity (%) analyses at 26/00Z from (a) experiment 1 (no assimilation), (b) experiment 2 (12DI), (c) experiment 3 (05DI), and (d) experiment 5 (06AI). Contours are every 10%.

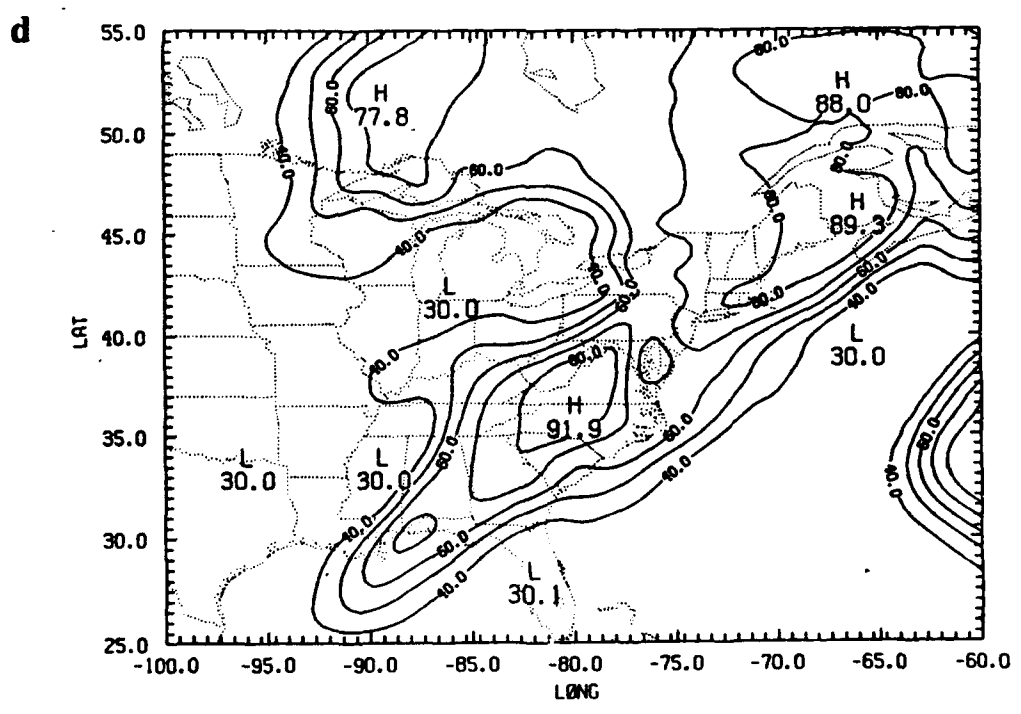
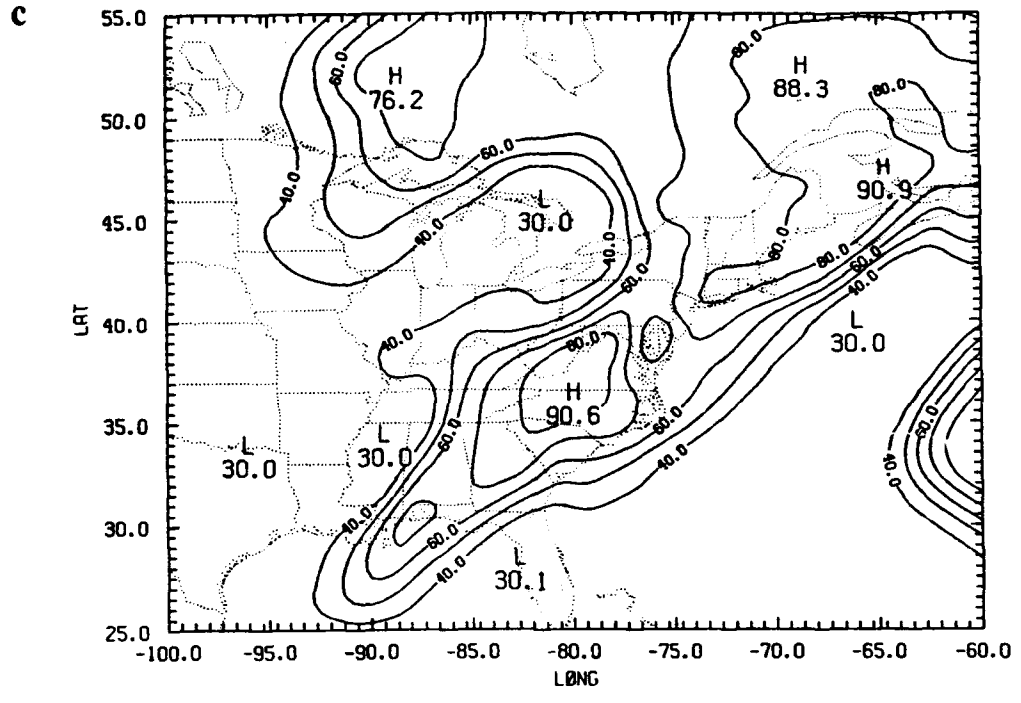


Figure 6.12. Continued.

the 6-h update cycle had the greatest value showing that asynoptic GALE data, in this case, led to an improvement over the assimilation with 12-h updates. Over the central Gulf coast, all three assimilations produced a moisture tongue (with relative humidity over 70%) associated with an eastward-moving short-wave disturbance. The "no assimilation" analysis showed a maxima of only 56% in this region where rainfall was occurring. The overall upper-level moisture pattern from the 06AI assimilation (i.e., VMI without diabatic heating) was very close to the other assimilated states. As noted in the previous section, the inclusion of diabatic heating in the vertical mode initialization led to little change in the first order field. This is not necessarily true in the case of vertical motion, which is related directly to diabatic heating. From the vertical velocity fields, shown in Fig. 6.13, a clear distinction between the experiment with diabatic VMI (experiment 3) and that with adiabatic VMI (experiment 5) can be seen. The assimilation with diabatic heating included in VMI shows a stronger vertical circulation at the coastal front at 26/00Z. The vertical motion along the east coast from the assimilated experiments was much stronger and had much more detail than that from the "no assimilation" case, with the 06DI assimilation producing slightly greater vertical motions at the coastal front than did the assimilation with a 12-h update cycle. Also, stronger vertical velocities are present over the central Gulf coast associated with the developing wave in all the assimilated states as compared to the "no assimilation" analysis.

Cross sections were produced to further investigate the ageostrophic circulation associated with the coastal front and an advancing upper-level jet. Cross section 2 (CS2 from 90°W, 43.5°N to 68.7°W, 26°N) cuts across the entrance region of the jet over the southeast U.S. and extends across the Carolina coast (see Fig. 4.5c). Figure 6.14 shows the magnitude of the wind speed normal to the cross section from the "no assimilation" case and the 12DI assimilation for 26/00Z. The ageostrophic circulations in the plane of CS2 for these two cases are depicted in Fig. 6.15. The mesoscale circulation of the

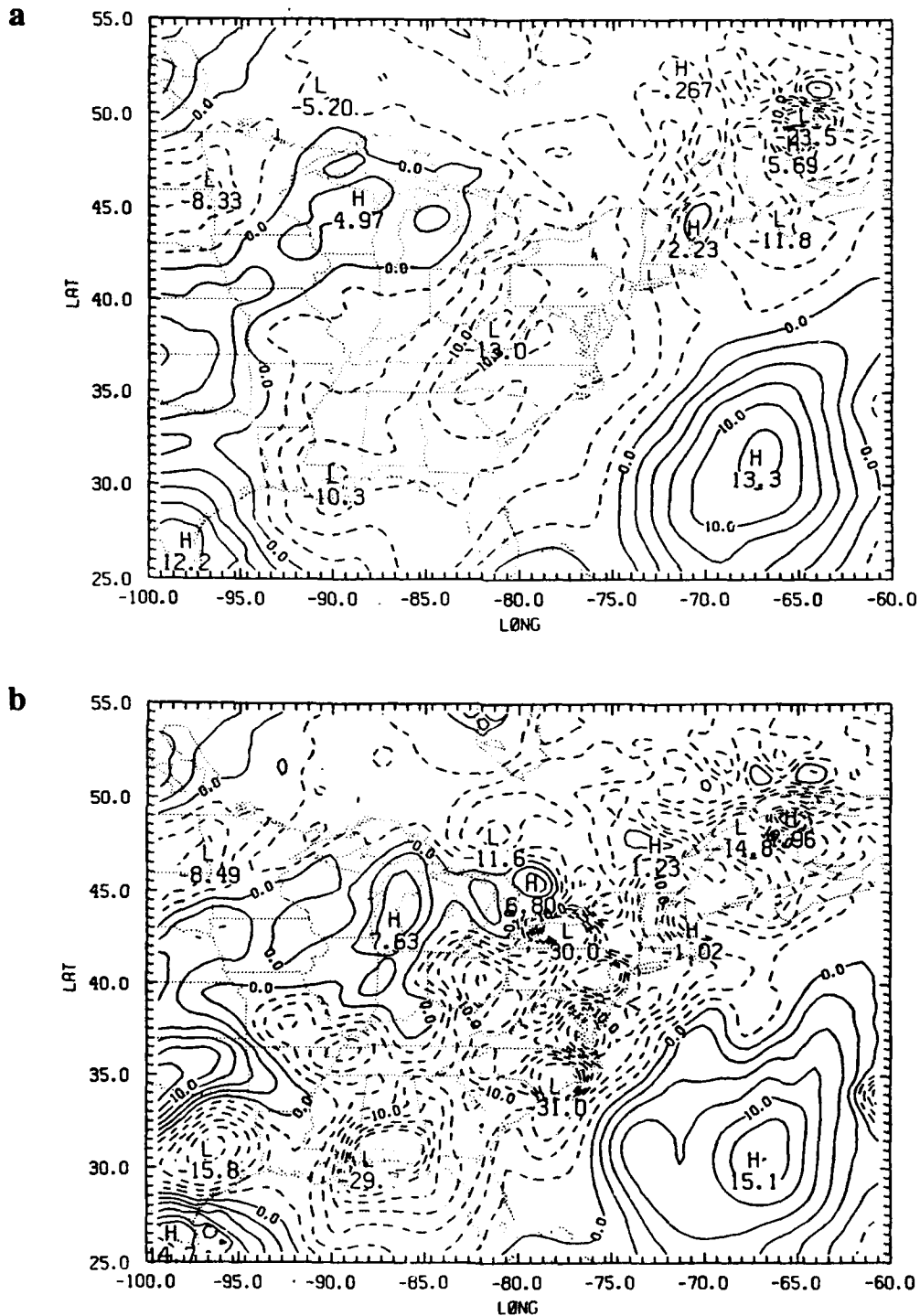


Figure 6.13. 500-mb vertical velocity ( $\text{mb h}^{-1}$ ) analyses at 26/00Z from (a) experiment 1 (no assimilation), (b) experiment 2 (12DI), (c) experiment 3 (06DI), and (d) experiment 5 (06AI). Vertical motion of magnitude of  $-20 \text{ mb h}^{-1}$  or more are contoured every  $2.5 \text{ mb h}^{-1}$ .

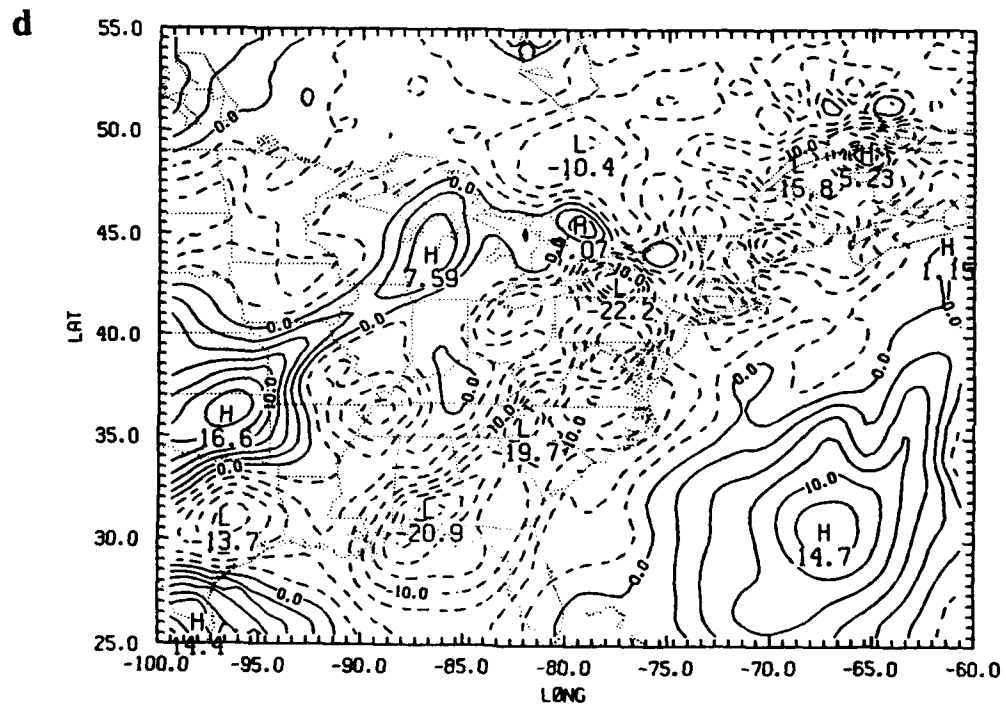
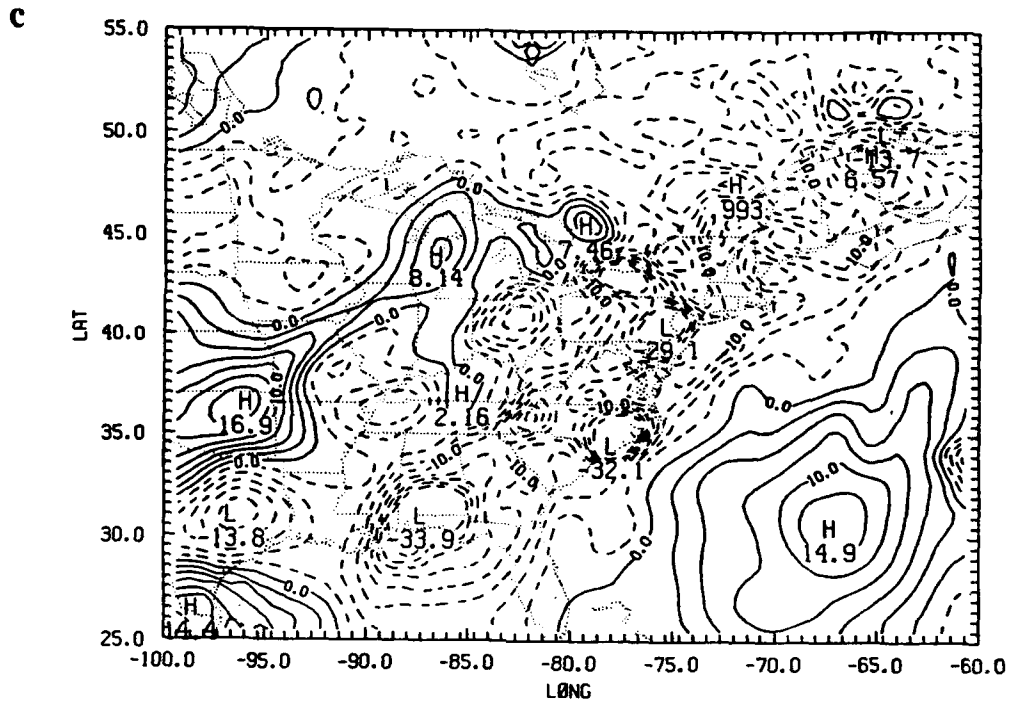


Figure 6.13. Continued.

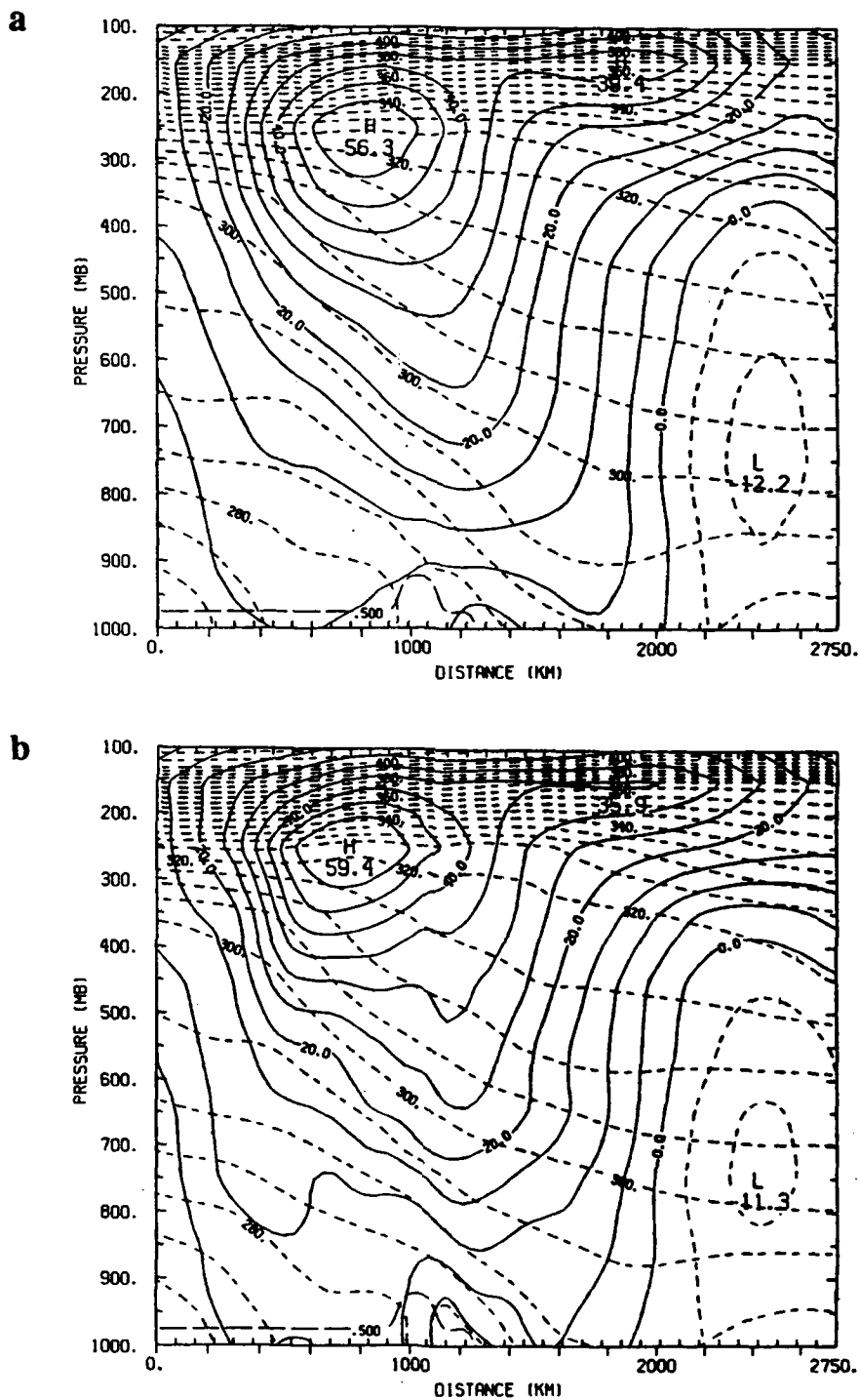


Figure 6.14. Wind speed ( $\text{m s}^{-1}$ ) normal to the plane of CS2 at 26/00Z from (a) experiment 1 (no assimilation) and (b) experiment 2 (12DI). Contours are every  $5 \text{ m s}^{-1}$ . The potential temperature ( $^{\circ}\text{K}$ ) is also shown by the dashed contours every  $5 \text{ }^{\circ}\text{K}$ .

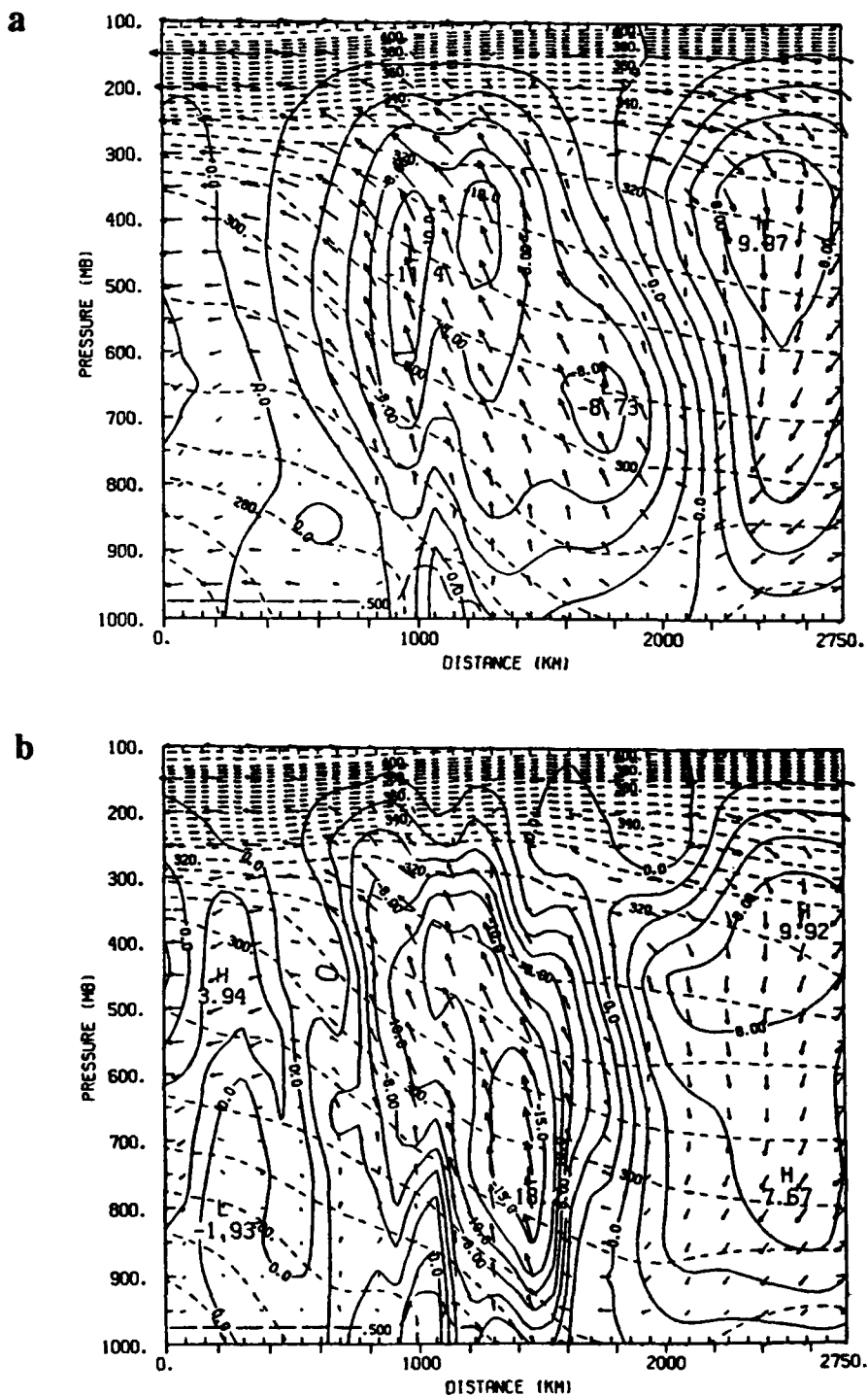


Figure 6.15. Vertical motion ( $\text{mb h}^{-1}$ ) and ageostrophic wind ( $\text{m s}^{-1}$ ) in the plane of CS2 at 26/00Z from (a) experiment 1 (no assimilation) and (b) experiment 2 (12DI). The magnitude of the vertical motion is represented by the solid contours at -40, -25, -20, -15, -12.5 and every 2  $\text{mb h}^{-1}$  for -10 and above.

coastal front is still a distinct feature within the 12DI analysis. However, the jet's secondary circulation has begun to absorb and deepen the coastal front's ageostrophic circulation as shown in the cross section. The ageostrophic circulation at 26/00Z due to the coastal front is much stronger and sharper in the 12DI as compared to the control analysis, with maximum ascents of  $-18.2$  and  $-8.7$   $\text{mb h}^{-1}$  at the coastal front, respectively. The 06DI assimilation (cross section not shown) strengthened the ageostrophic circulation, but only by a small amount ( $-19.1$   $\text{mb h}^{-1}$  vs.  $-18.2$   $\text{mb h}^{-1}$ ).

At 26/12Z, there is little difference in the surface temperature, wind, and pressure fields from the various assimilations sequences. In the 1000-mb specific humidity fields, the moisture gradient along the front on the east coast was sharpest in the 3-h cycle assimilation, followed by 06DI, then 12DI, with the "no assimilation" analysis having the weakest gradient. The 500-mb relative humidity analyses from experiments 1 - 4 again depicted the tongue of upper-level moisture extending over the eastern U.S. from Georgia to Maine. As in the lower troposphere, the 03DI assimilation generated the sharpest gradient and largest maxima and the "no assimilation" case produced the weakest. Little difference was found in the vertical motion fields resulting from the assimilation runs, with all displaying much greater maxima and detail than in the "no assimilation" experiment.

At 27/00Z and 27/12Z, the assimilated fields from experiments 2, 3, and 4 are very similar. The influence of the 3-hourly GALE data seems to be impacting the assimilation primarily when mesoscale circulations are predominant, i.e., there is a positive impact in the small-scale. When the synoptic-scale circulation became stronger and essentially engulfed the coastal front, less impact was noted. However, each of the assimilations still produced analyses which were noticeably different from the "no assimilation" case. One surface feature worth noting at 27/00Z is the positions of the low pressure centers from each experiment. By 27/00Z the disturbance, which had moved from the northern

Gulf of Mexico across southern Georgia, again appeared as a closed surface low in the assimilation analyses; rapid cyclogenesis had just begun (Fig. 6.16a). The low pressure center which was earlier associated with the coastal front had moved north and would soon merge with a weak northern low, associated with a short-wave trough which had advanced eastward from the Great Lakes region into New England. However, the "no assimilation" analysis does not distinguish those circulations, instead only the deepening low pressure center is depicted in a position farther up the east coast (Fig. 6.16b). By 27/03Z, the 03DI assimilation had deepened the cyclone's central pressure by 3 mb (Fig. 6.16c) and moved it just off the Delaware coast in close proximity with the "no assimilation" position at 27/00Z. This would seem to suggest that only a slight timing error in the development of the strengthening cyclone differentiates the "no assimilation" analysis from the assimilation case. However, investigation of the ageostrophic circulations along the east coast proves otherwise. As in other cases of rapid cyclogenesis (Uccellini and Kocin 1987, for example), the rapid development is being aided by the indirect circulations of an exiting upper-level jet to the north and an approaching jet located south of the low. In this case, the northern jet has also been strengthened by the short-wave trough from the Great Lakes. These jets are evident in Fig. 6.17a which is a cross section (CS7, see Fig. 6.16a) along the east coast ( $69.3^{\circ}\text{W}$ ,  $49.5^{\circ}\text{N}$  to  $80.0^{\circ}\text{W}$ ,  $26.5^{\circ}\text{N}$ ) of the normal wind speed at 27/00Z. Figures 6.17b and 6.17c are cross sections of the ageostrophic circulations from the 03DI and "no assimilation" cases. The 03DI analysis shows the ascending motion associated with the northern low (point A of Fig. 6.17b), still retains the mesoscale circulation associated with the decaying coastal low (point B), and depicts the strong vertical circulation of the developing low at point C. The secondary circulation of the coastal low is being absorbed by the indirect circulation of the entrance region of the northern jet. The ageostrophic circulation from the "no assimilation" analysis (Fig. 6.17c) fails to capture

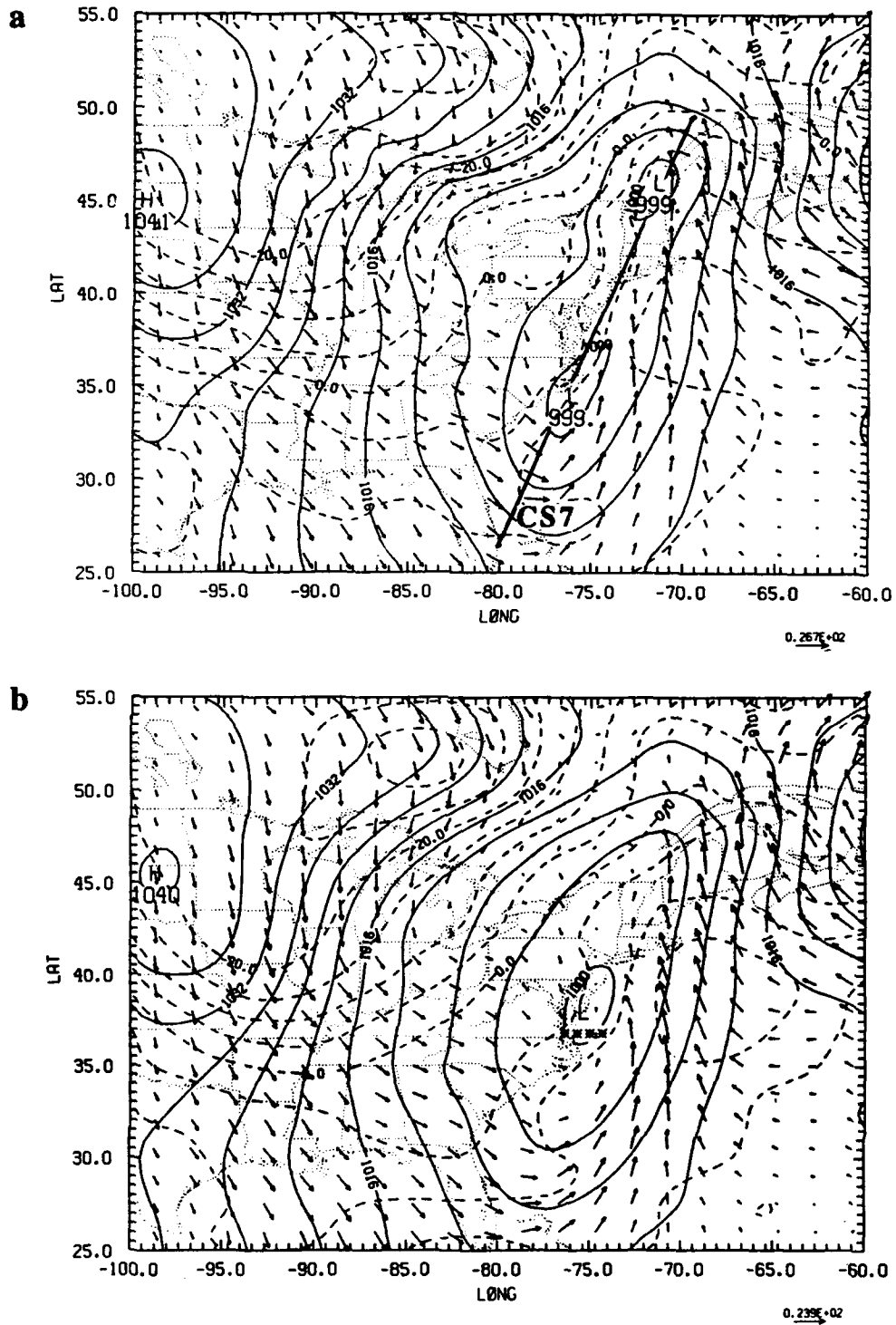


Figure 6.16. Sea-level pressure (mb), 1000-mb temperature ( $^{\circ}\text{C}$ ) and wind analyses at 27/00Z from (a) experiment 4 (03DI) and (b) experiment 1 (no assimilation), and at 27/03Z from (c) experiment 4 (03DI). Contours as in Fig. 6.9.

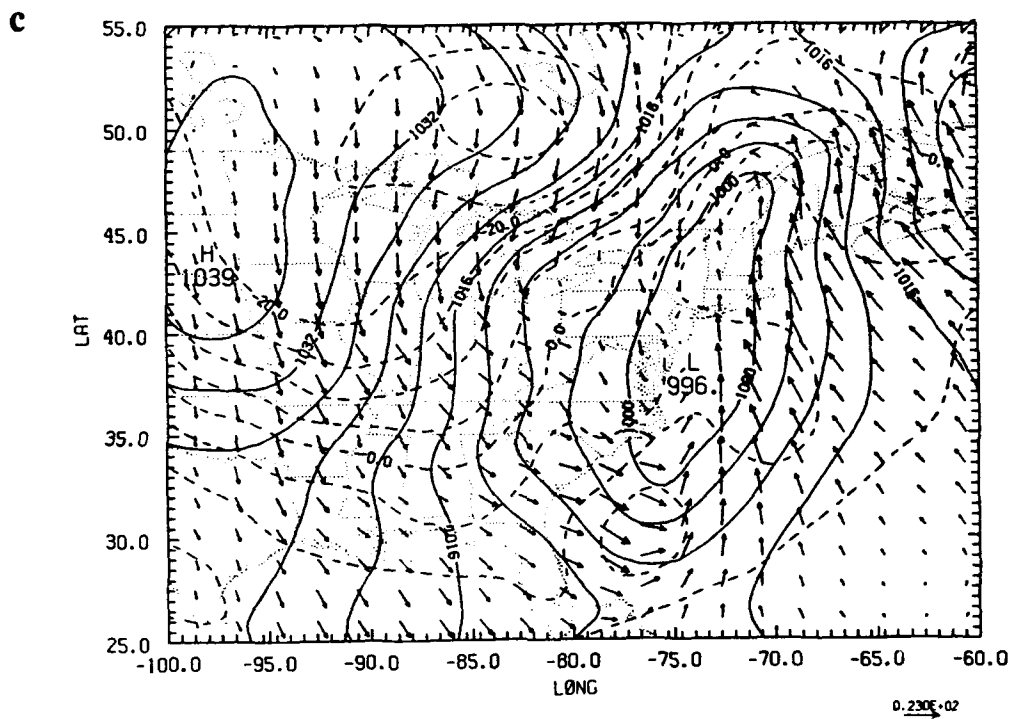


Figure 6.16. Continued.



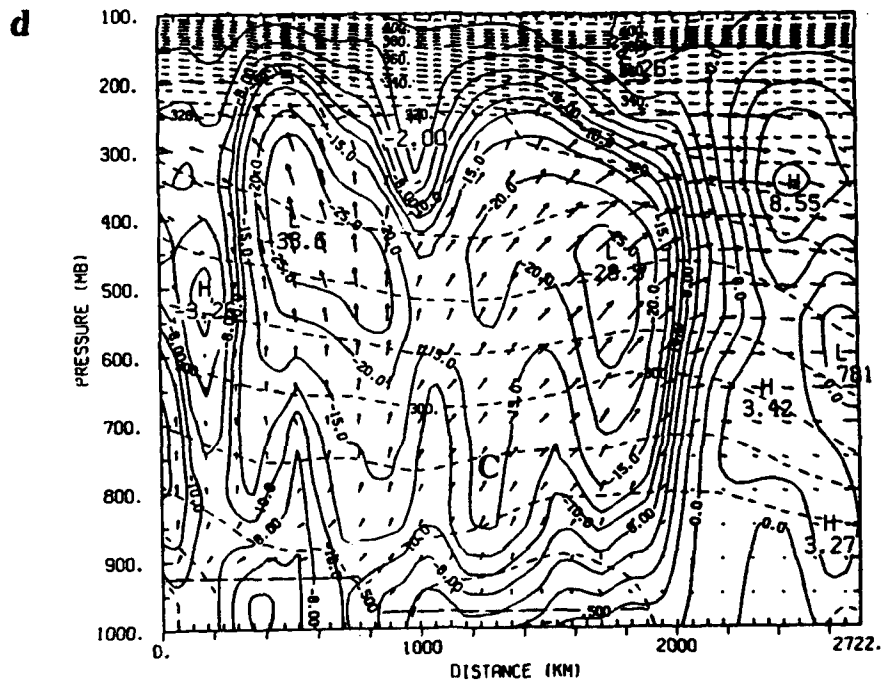
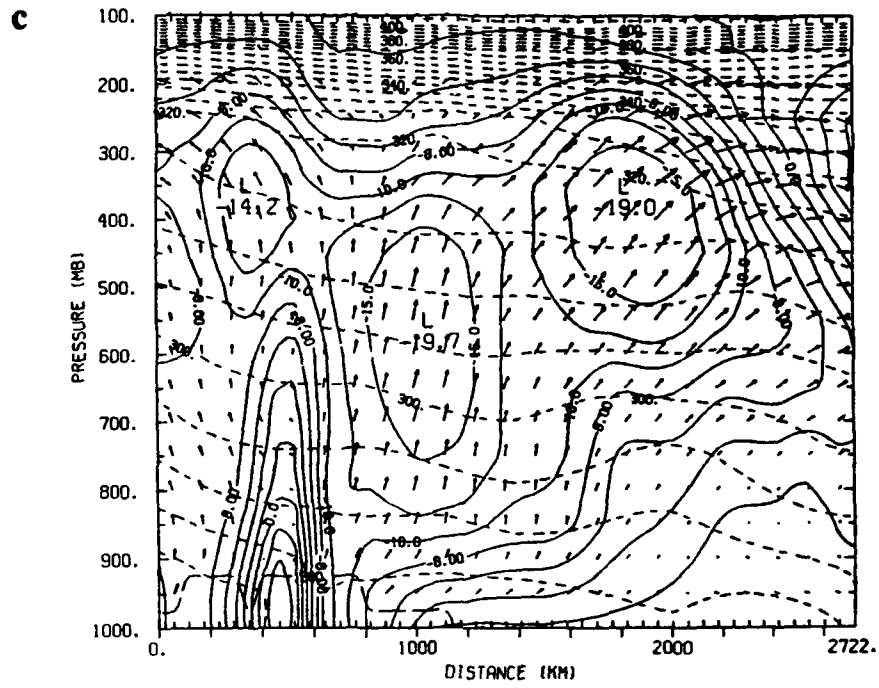


Figure 6.17. Continued.

these various features. It simply depicts the strong vertical motion of the deepening low, being supported by the indirect circulations of the two jets. Figure 6.17d shows the 03DI ageostrophic circulation at 27/03Z. By this time, the analyzed deepening low had moved a little farther north (point C). The circulations associated with the northern low and coastal low are merging and continue to be engulfed by the jet's secondary circulation.

By 27/12Z, the rapidly deepening cyclone had tracked northeast to New England in both the "no assimilation" and 03DI cases (Figs. 6.18a and 6.18b). With the support of the secondary circulations of the two jets, the low had deepened by 15 mb in the "no assimilation" analysis and 17 mb in the 03DI analysis. The synoptic scale circulation of the cyclone was now totally dominant, with the mesoscale circulation of the coastal low being completely absorbed in the large-scale circulation. As a result, the pattern of the ageostrophic circulation along CS6 (68.7°W, 55.5°N to 76.7°W, 25.5°N; see Fig. 4.24b) from the 03DI assimilation (Fig. 6.19b) is very similar to that from the "no assimilation" case (Fig. 6.19a). But the cyclone's vertical motion from the assimilation case is much stronger, with a maximum of  $-45 \text{ mb h}^{-1}$  versus  $-26.2 \text{ mb h}^{-1}$ .

#### b) Subsequent forecast aspects

The true test of the goodness of any data assimilation designed for the purpose of providing initial conditions for a numerical weather prediction model is the accuracy of the forecasts produced from the assimilated states. Twenty-four-hour forecasts starting at 26/00Z were generated from analyses in experiments 1 (no assimilation), 2 (12DI), 3 (06DI), and 5 (06AI). Comparisons among these forecasts were made and are now discussed.

Six-hour forecasts, valid at 26/06Z, of sea-level pressure, surface air temperature and winds are shown in Fig. 6.20. The forecasts originating from the assimilated fields

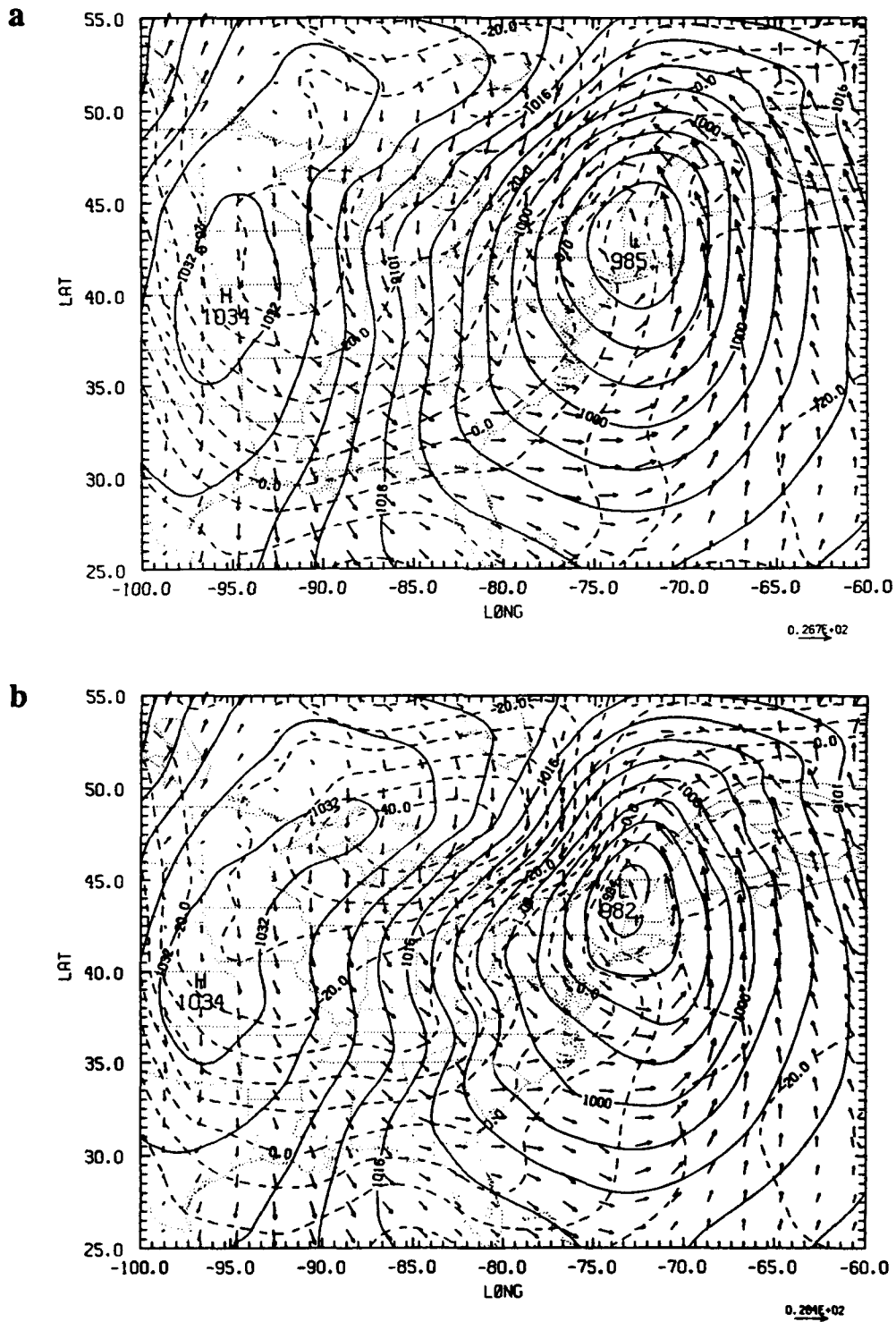


Figure 6.18. Sea-level pressure (mb), 1000-mb temperature ( $^{\circ}\text{C}$ ) and wind analyses at 27/12Z from (a) experiment 1 (no assimilation) and (b) experiment 4 (03DI). Contours as in Fig. 6.9.

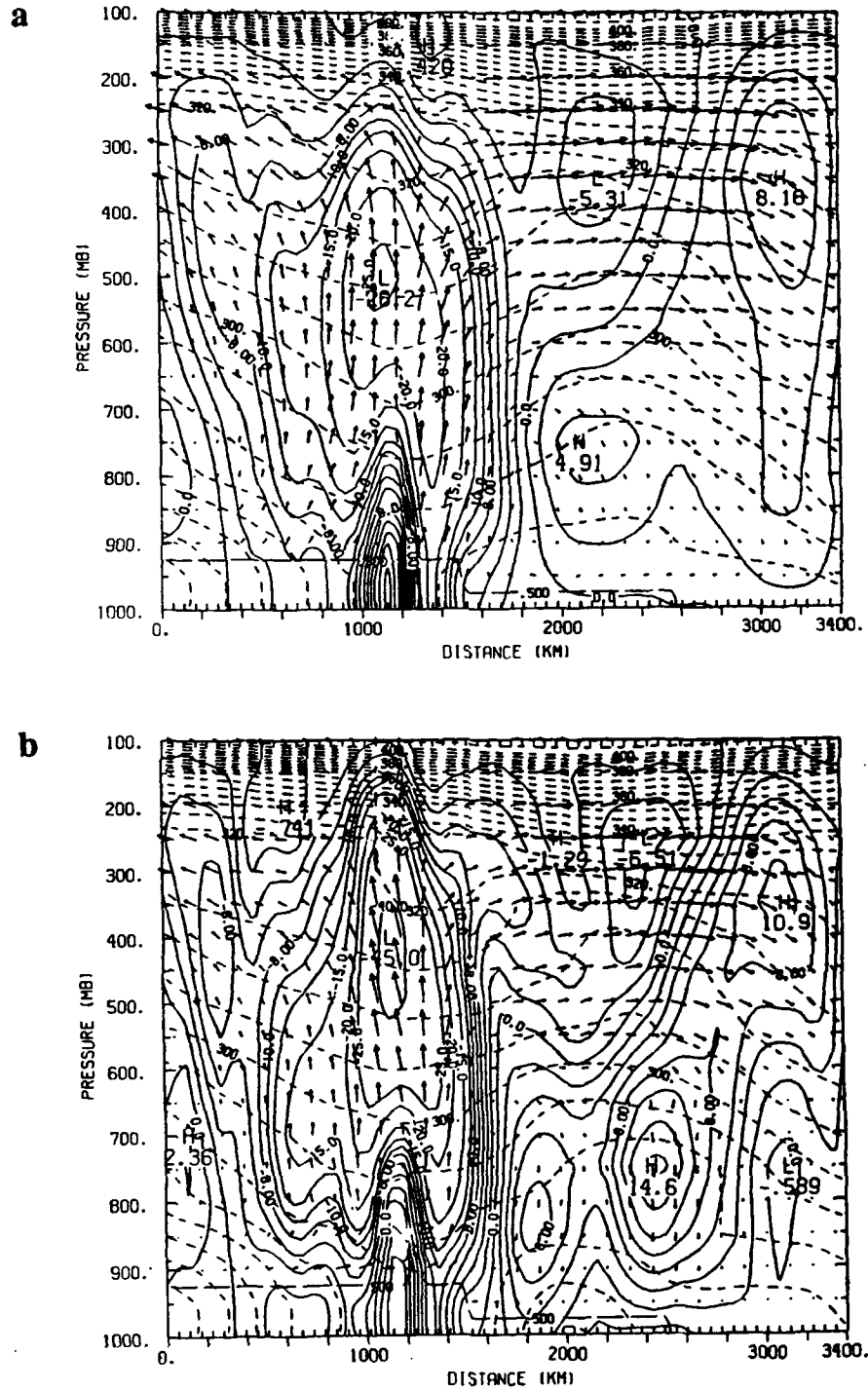


Figure 6.19. Cross sections (CS6) of the ageostrophic circulation at 27/12Z from (a) experiment 1 (no assimilation) and (b) experiment 4 (03DI). Contours as in Fig. 6.15.

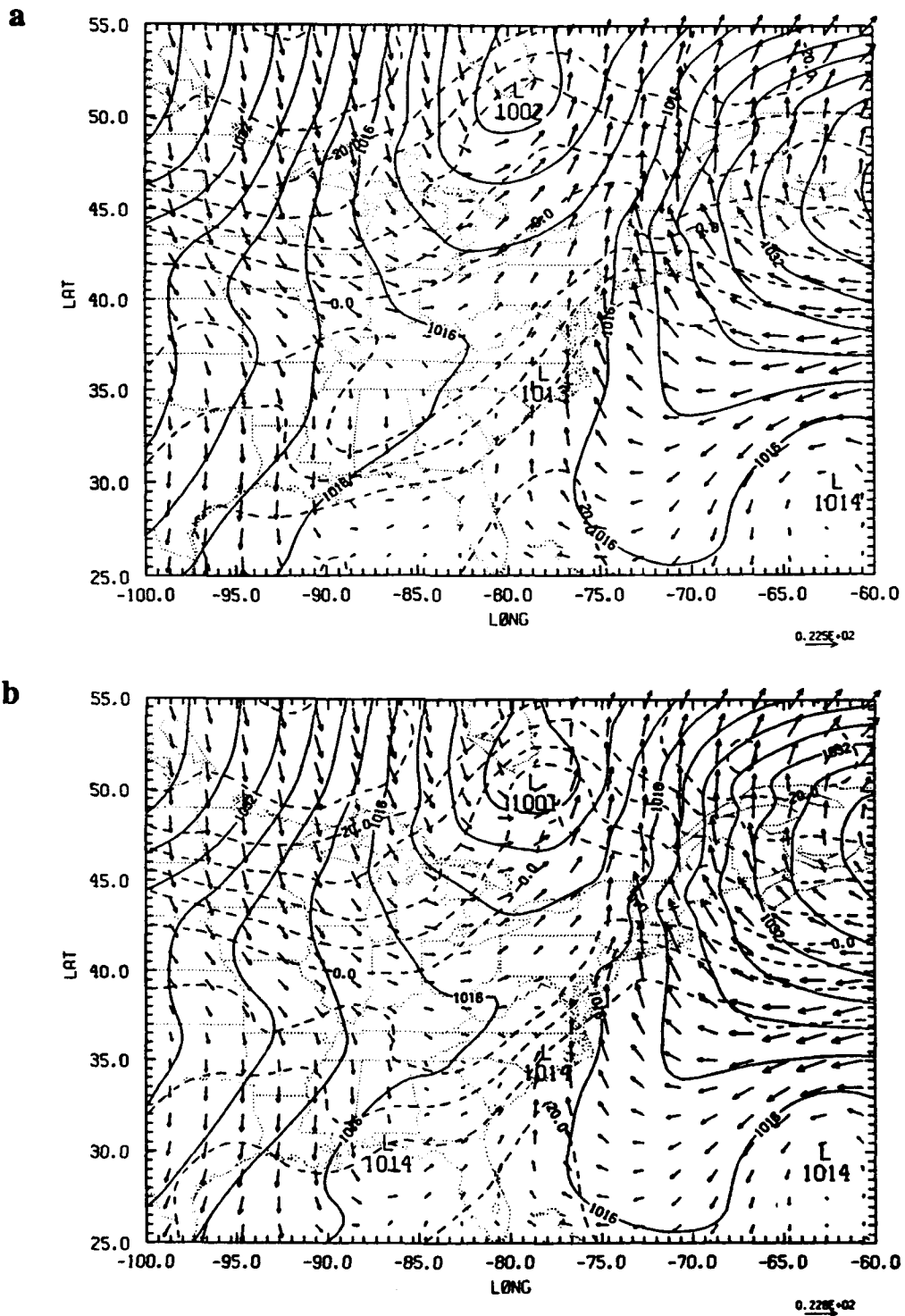


Figure 6.20. Six-hour forecasts of sea-level pressure (mb), surface air temperature ( $^{\circ}$ C), and 1000-mb winds valid at 26/06Z from (a) experiment 1 (no assimilation), (b) experiment 2 (12DI), and (c) experiment 3 (06DI). Contours and in Fig. 6.9.

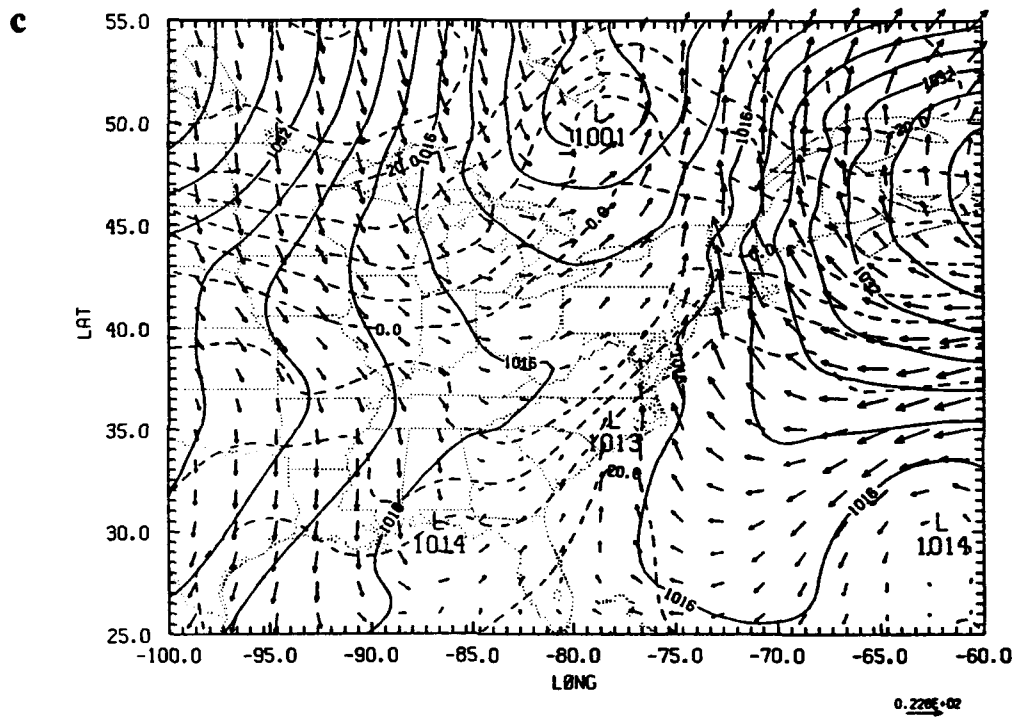


Figure 6.20. Continued.

have much tighter temperature gradients along the Carolina coast in the vicinity of the coastal front than does the forecast from the "no assimilation" case. The frontal temperature gradients resulting from experiments 2 and 3 are in very good agreement with the Bosart hand analysis (Fig. 6.21) with a temperature contrast of approximately 15°C from Charlotte, North Carolina to a position just off the South Carolina coast. Bosart's analysis shows a low of 1012 mb on the Florida panhandle and a low of less than 1012 mb which had formed on the southern end of the coastal front. In reference to these low pressure centers, the 12DI forecast verifies the best in regards to central pressure, but the 06DI forecast predicts the positions more accurately. As in the case of the analyses, the forecasts from the assimilated states produce a much tighter low level moisture gradient at the coastal front than does the "no assimilation" forecast (not shown).

Six-hour observed rainfall and accumulated forecast rainfall (26/00Z - 26/06Z) for experiments 1, 3, and 5 are shown in Fig. 6.22. The forecasts from the assimilated cases, 06DI (Fig. 6.22b) and 12DI (not shown), match the observed precipitation pattern (Fig. 6.22d) reasonably well and show much more rapid spinup of rainfall than does the "no assimilation" forecast. Here, the disadvantage of not having a mesoscale assimilation model to generate and maintain small-scale features is evident. The "no assimilation" forecast must spinup these circulations and, as a result, gives a poor short-range rainfall prediction. The forecast from experiment 5 (06AI in Fig. 6.22c) fails to capture any rainfall over the Gulf coast associated with the developing short wave. The absence of diabatic heating from the VMI has caused a spinup problem in this case.

The 12-h surface and low-level moisture forecasts (valid at 26/12Z) from the various assimilations are very similar and, like the 6-h forecasts, have much stronger gradients along the east coast of the U.S. than does the "no assimilation" forecast. Figure 6.23 depicts the 6-h accumulated rainfall ending at 26/12Z. The forecasts from

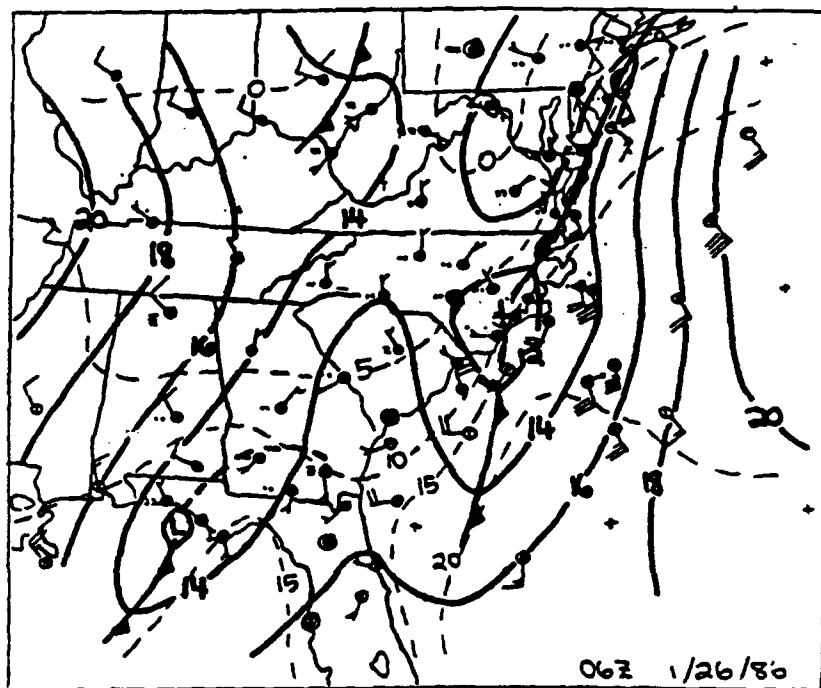


Figure 6.21. GALE analysis of sea-level pressure deviation (from 1000 mb), surface temperature ( $^{\circ}\text{C}$ ) and wind for 26/06Z by Bosart (1988). Surface temperature contours every  $5^{\circ}\text{C}$ .

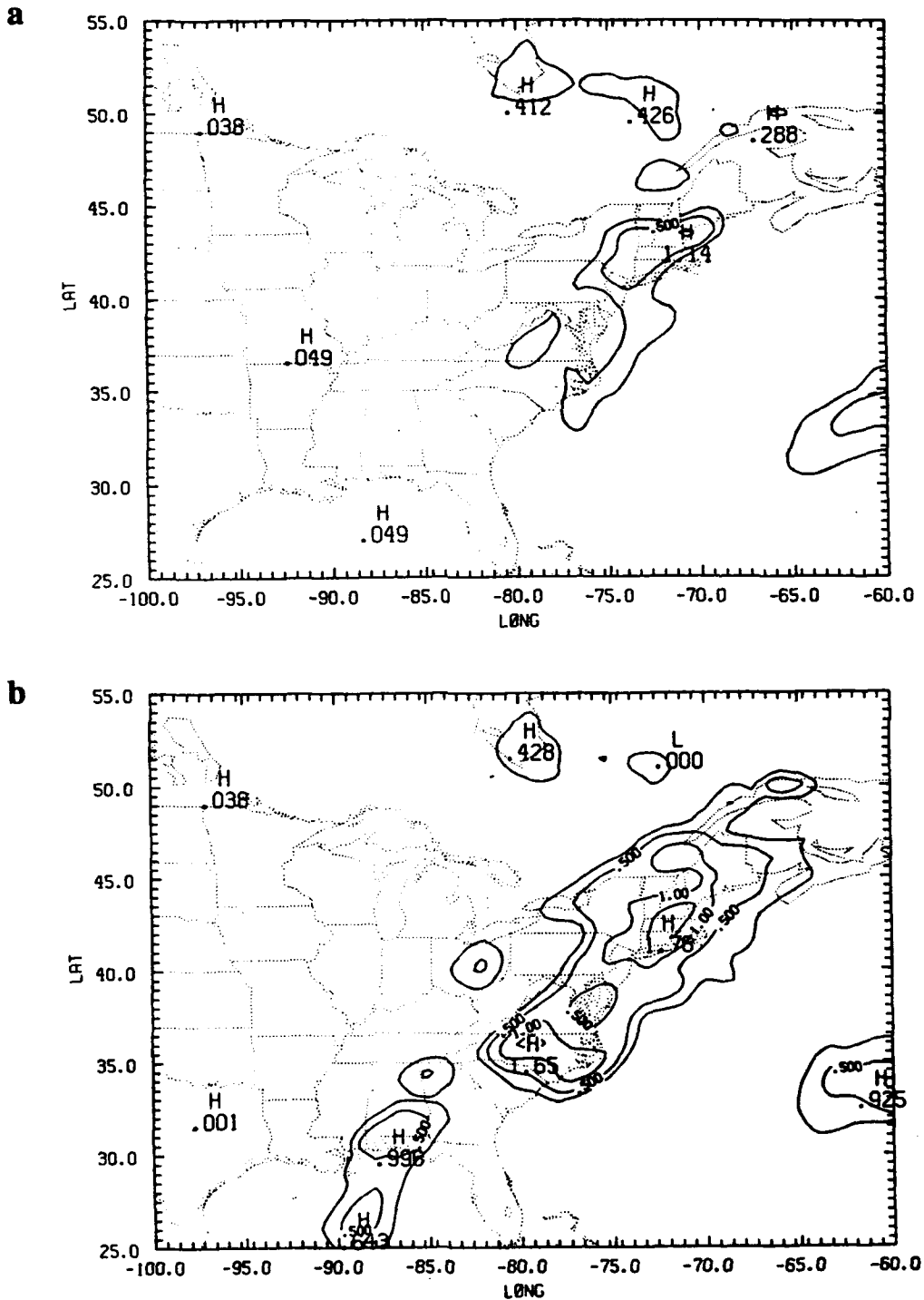


Figure 6.22. Forecasts of accumulated total precipitation in cm (26/00Z - 26/06Z) from (a) experiment 1 (no assimilation), (b) experiment 3 (06DI), and (c) experiment 5 (06AI). (d) Observed precipitation in cm (26/00Z - 26/06Z). Contours at 0.25 cm and every 0.5 cm for 0.5 and above.



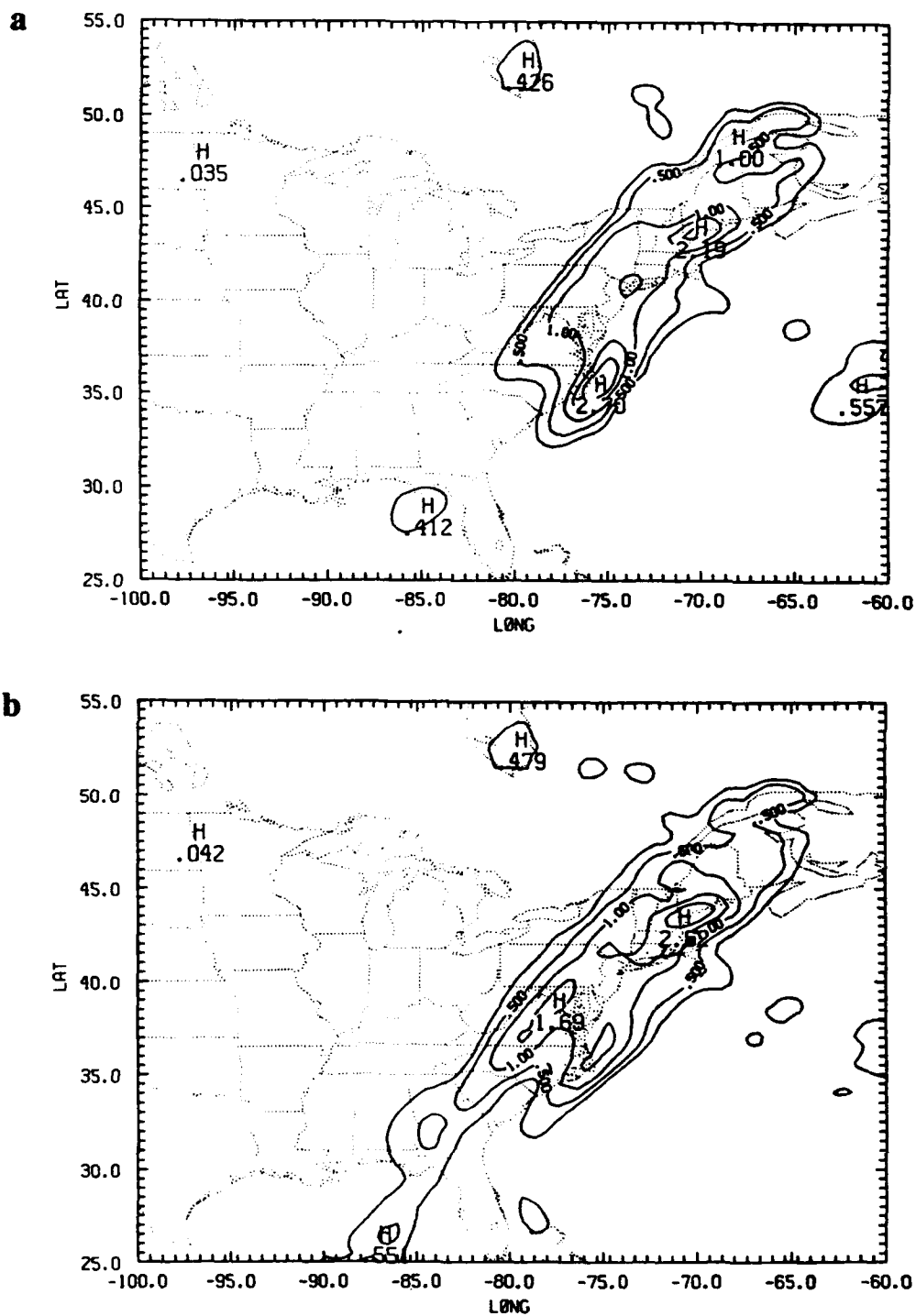


Figure 6.23. Forecasts of accumulated total precipitation in cm (26/06Z - 26/12Z) from (a) experiment 1 (no assimilation), (b) experiment 2 (12DI), and (c) experiment 3 (06DI). (d) Observed precipitation in cm (26/06Z - 26/12Z). Contours same as in Fig. 6.22.

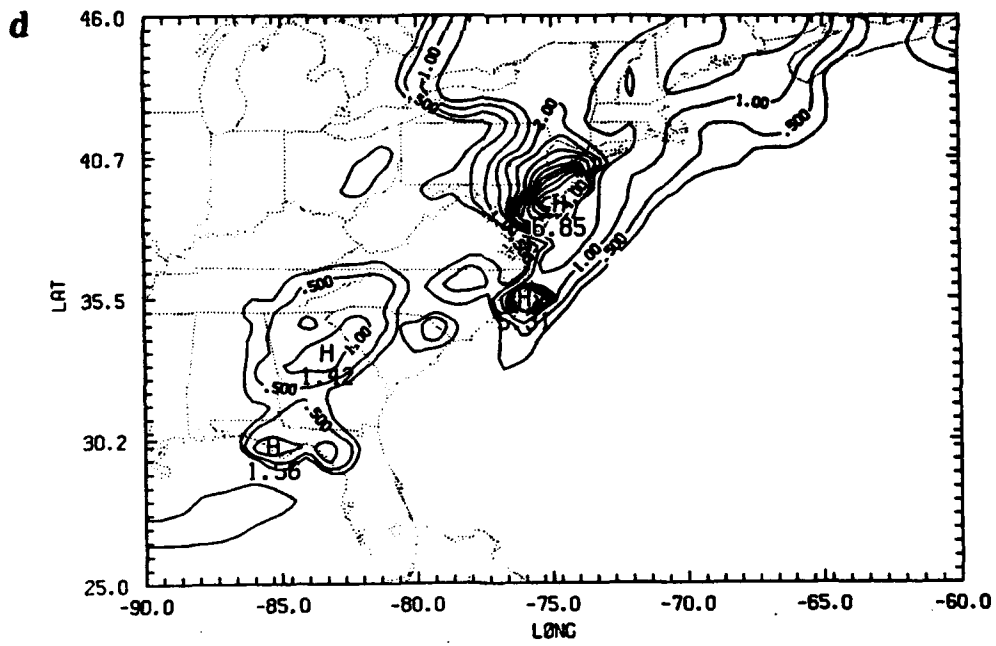
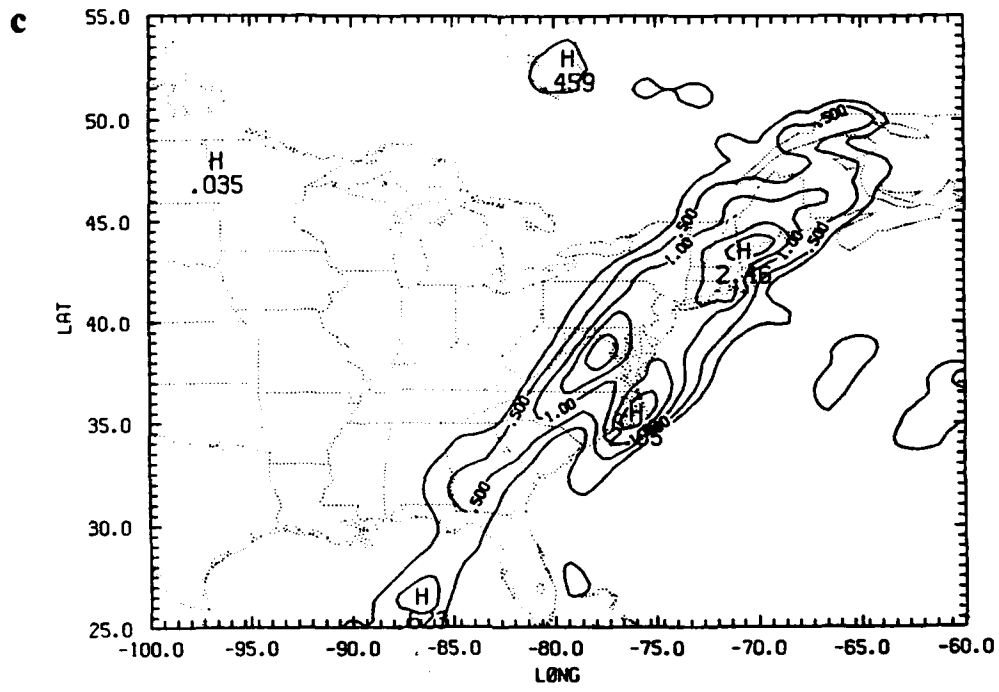


Figure 6.23. Continued.

06DI and 12DI are much better than that from the "no assimilation" case and verify reasonably well with the observed rainfall. However, the forecast from 12DI produced a maximum of only 1.5 cm near Cape Hatteras, whereas the 06DI forecast maximum was nearly 3 cm, a value much closer to the observed maximum of 5.31 cm. The rainfall forecast from experiment 5 (06AI) continued to be too weak on the southern extent of the precipitation area and the "no assimilation" case almost totally missed this feature. The forecasts from all the experiments completely missed the maximum of 6.85 cm in New Jersey as depicted in Fig. 6.23d. The horizontal resolution of even our fine-resolution mesoscale model is insufficient to resolve individual convective cells. The model's cumulus parameterization can not be expected to duplicate the observed precipitation maxima resulting from these sub-grid scale convective storms.

By 26/18Z the accumulated 6-h precipitation forecasts (Fig. 6.24) had become more similar with each extending the rainfall area across central Florida. However, the 06DI and 12DI forecasts did extent the precipitation area over most of North Carolina and South Carolina in agreement with the observed pattern, whereas the "no assimilation" forecast had moved all precipitation offshore for latitudes south of Virginia.

A second set of forecasts with an initiation time of 26/12Z were produced from experiments 1 - 4. Figure 6.25 depicts 6-h forecasts of sea-level pressure and 1000-mb temperature and wind fields; these forecasts, including the one from the "no assimilation" analysis, are very similar. Note similarities in temperature gradients along the east coast of U.S. and the locations of the coastal low defined by the center of the low pressure over southeast New York state. The coastal low is seen merging with a trough of low pressure to the northwest. The new cyclone center is forming near Cape Hatteras in the extended trough along the coast. The low-level moisture fields (not shown) are equally similar, particularly the sharp gradient associated with the frontal system along the east coast. The 6-h accumulated rainfall forecasts ending at 26/18Z originating from the

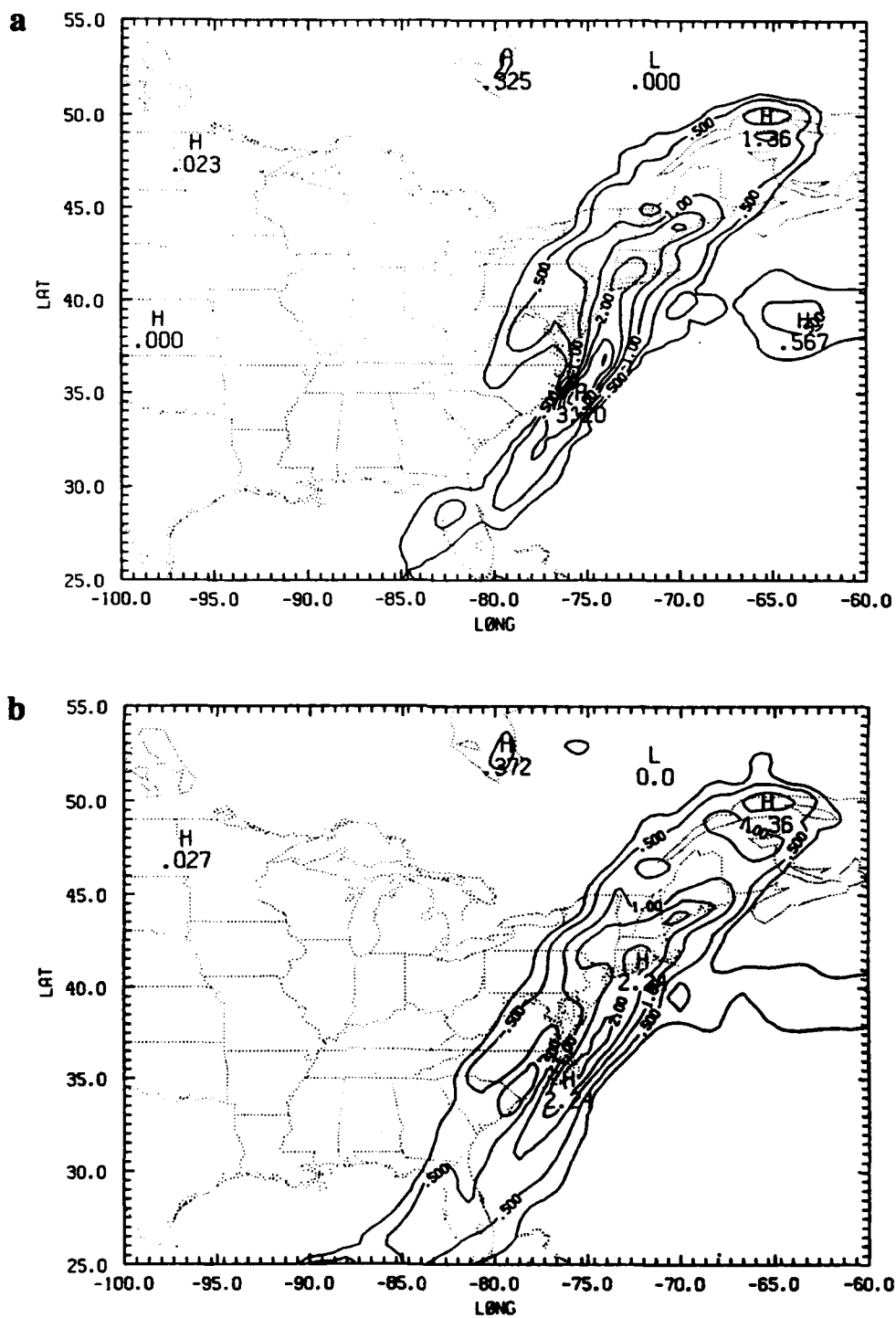


Figure 6.24. Forecasts of accumulated total precipitation in cm (26/12Z - 26/18Z) from (a) experiment 1 (no assimilation), (b) experiment 2 (12DI), and (c) experiment 3 (06DI). (d) Observed precipitation in cm (26/12Z - 26/18Z). Contours same as in Fig. 6.22.

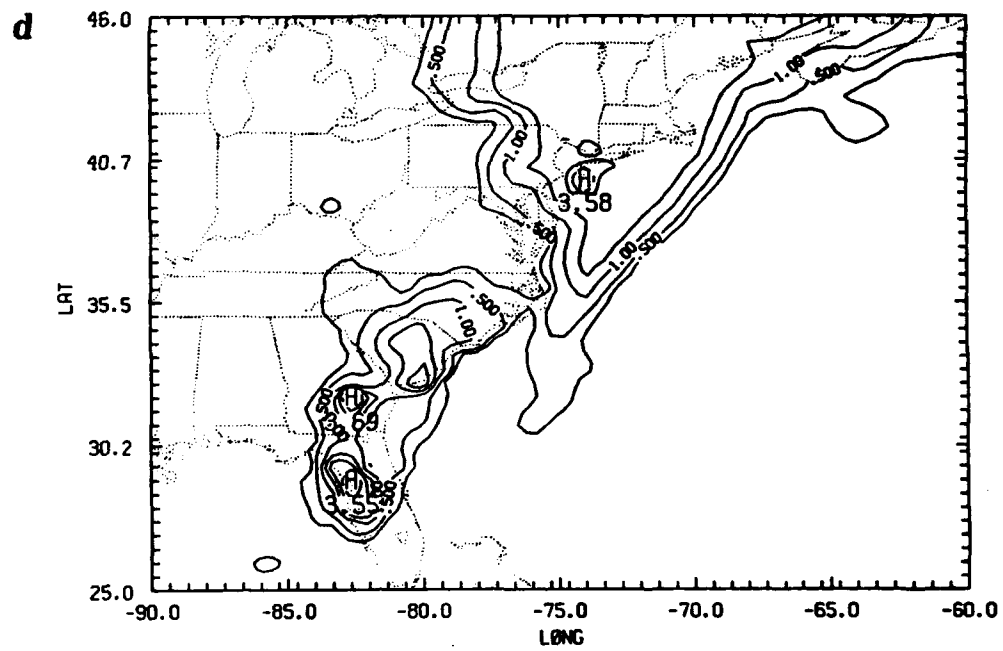
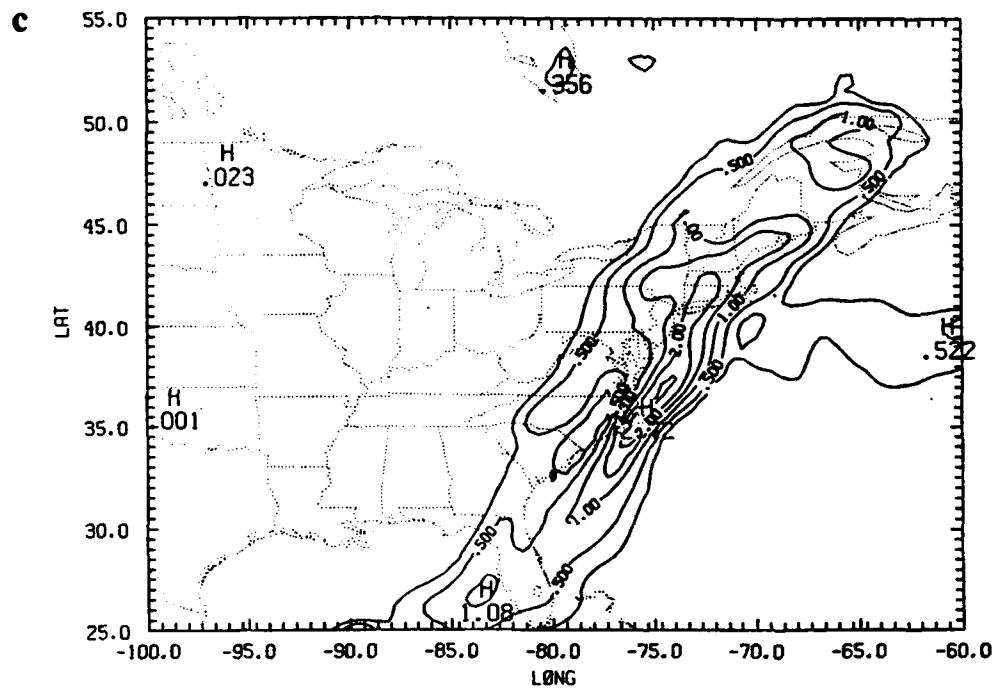


Figure 6.24. Continued.

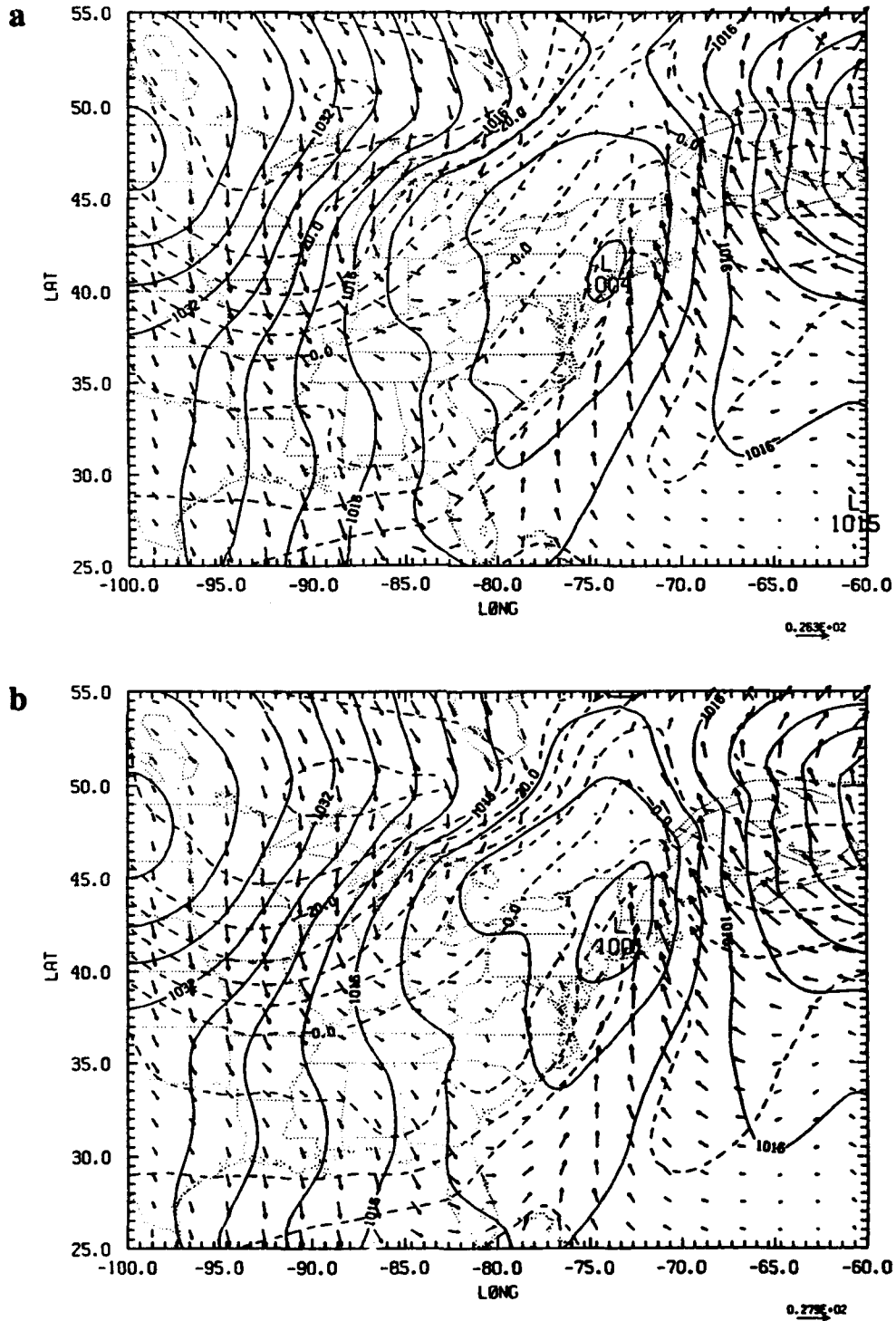


Figure 6.25. Six-hour forecasts of sea-level pressure (mb) and 1000-mb temperature ( $^{\circ}\text{C}$ ) and wind valid at 26/18Z from (a) experiment 1 (no assimilation), (b) experiment 2 (12DI), (c) experiment 3 (06DI), and (d) experiment 4 (03DI).

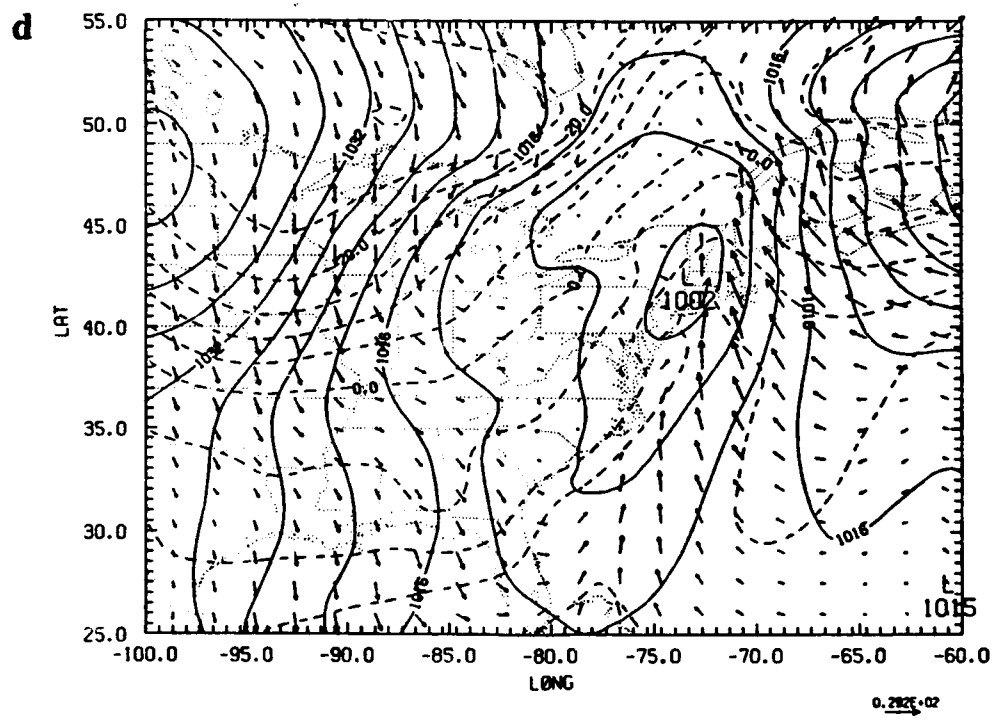
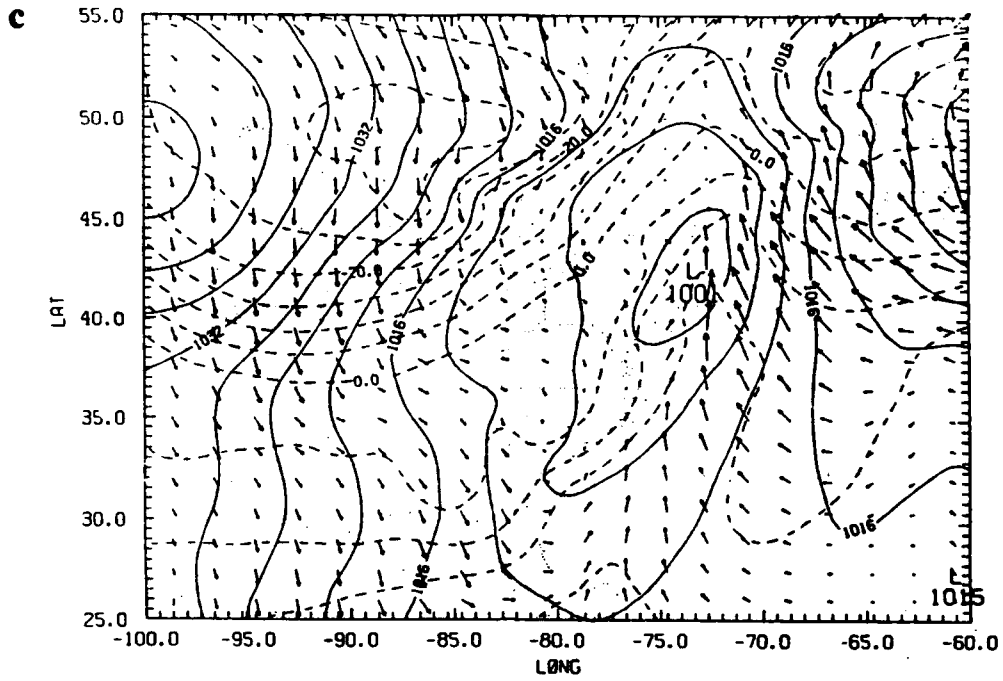


Figure 6.25. Continued.

assimilated fields are much better than the forecast originating from the "no assimilation" analysis, with the forecasts from the 3-h (03DI, not shown) and 6-h (06DI) cycle assimilations being the closest to and in good agreement with the observed rainfall pattern (Fig. 6.26). In other words, the assimilation process had an impact: there is a definite improvement over the "no assimilation" case, and the assimilation of asynoptic 3-hourly GALE data had at least a minor impact in the rainfall since the assimilations with the 3-h and 6-h cycles led to slightly better forecast precipitation fields than the case from the 12-h cycle assimilation.

During the remainder of the prediction period, the synoptic-scale circulation of this developing east coast cyclone was dominant and the forecast patterns from the different experiments were quite similar. The 12- and 24-h forecast precipitation fields from each case, including the "no assimilation" experiment, were similar and in reasonable agreement with the observed precipitation. By 27/00Z, a low pressure center appeared off the North Carolina coast and deepened rapidly as it moved along the coast (Fig. 6.27). In the 12-h forecasts (valid at 27/00Z) from the assimilated fields, the region of low pressure extends farther north and indicates two different northern centers (Fig. 6.27b), which compare more favorably with the assimilated analysis shown in Fig. 6.16a. The 24-h surface forecasts from the control and 03DI cases are shown in Figs. 6.27c and d. These forecasts are very similar, except that the center of the low has a better position in the assimilated case when compared with the analysis in Fig. 6.18b. It seems that the assimilation of the GALE data had less impact particularly in the precipitation during the latter part of the forecast period. The rainfall was being forced primarily by the large synoptic-scale circulation of the developing east coast cyclone, enabling the control forecast to produce adequate results. However, the 12- and 24-h surface pressure forecasts, with the assimilation of the GALE data, show more

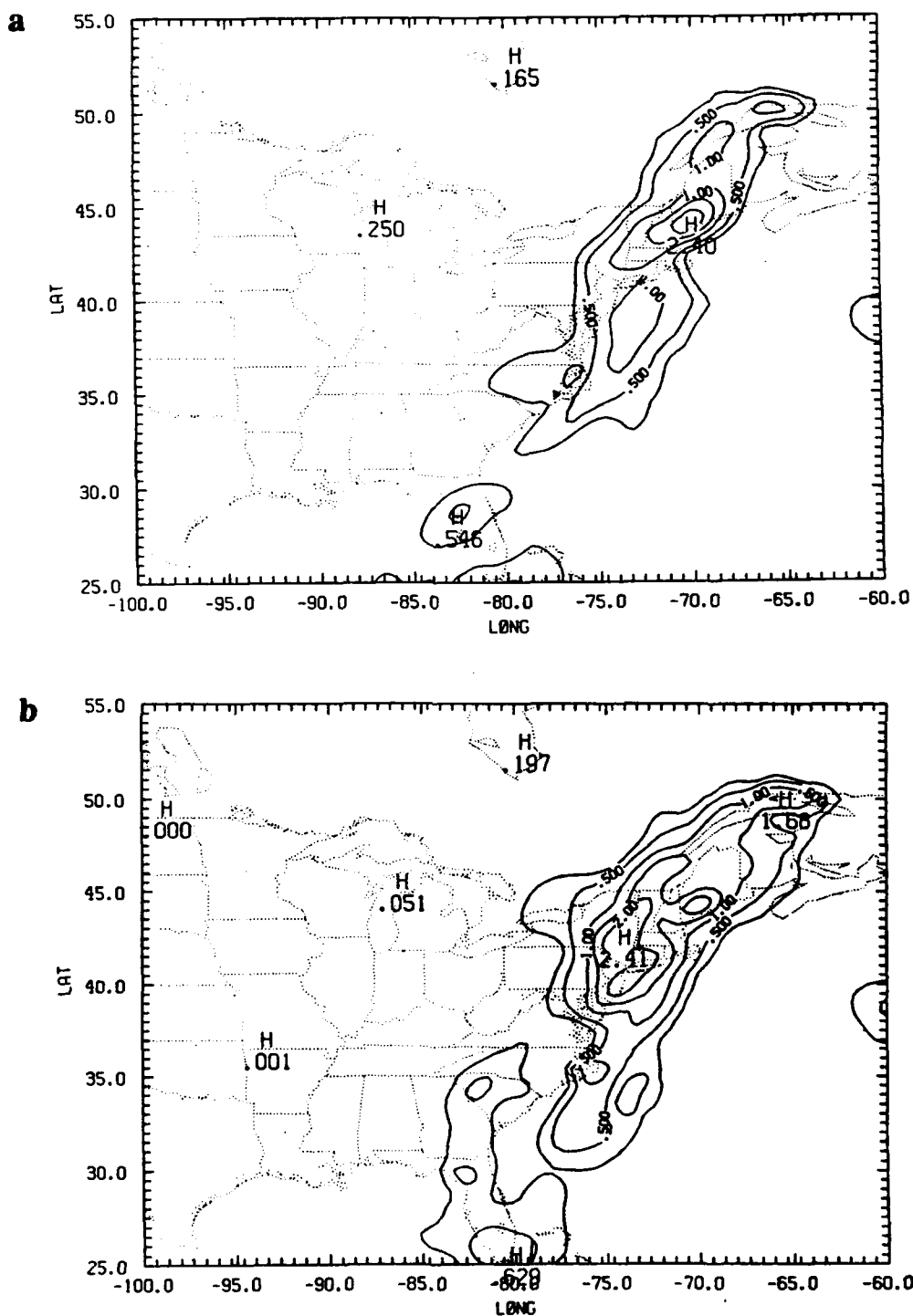


Figure 6.26. Forecasts of accumulated total precipitation in cm (26/12Z - 26/18Z) from (a) experiment 1 (no assimilation), (b) experiment 2 (12DI), and (c) experiment 3 (06DI), with forecast start time of 26/12Z. (d) Observed precipitation in cm (26/12Z - 26/18Z). Contours same as in Fig. 6.22.

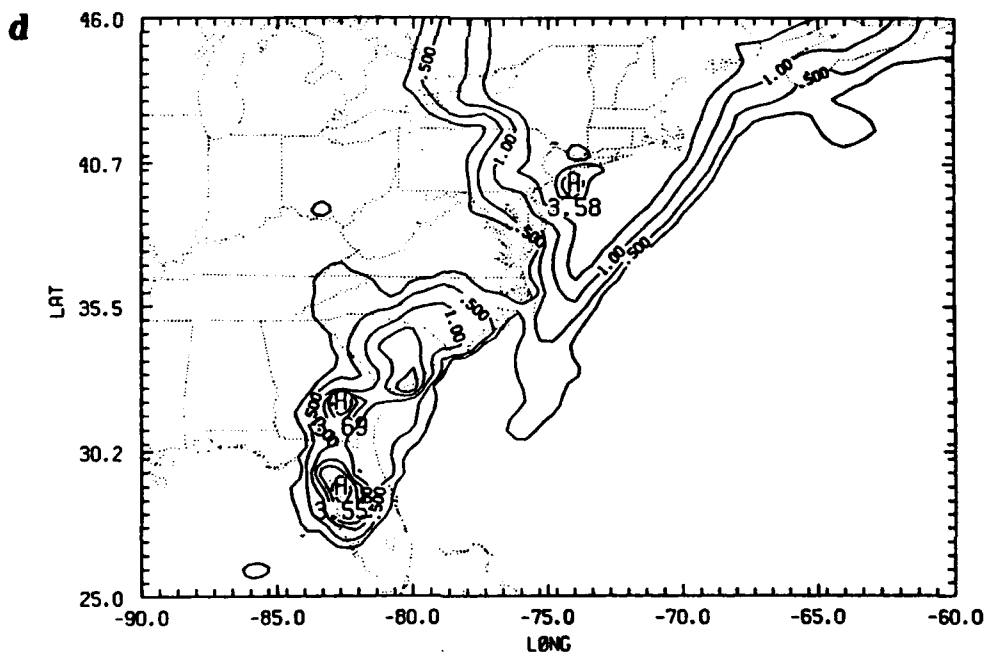
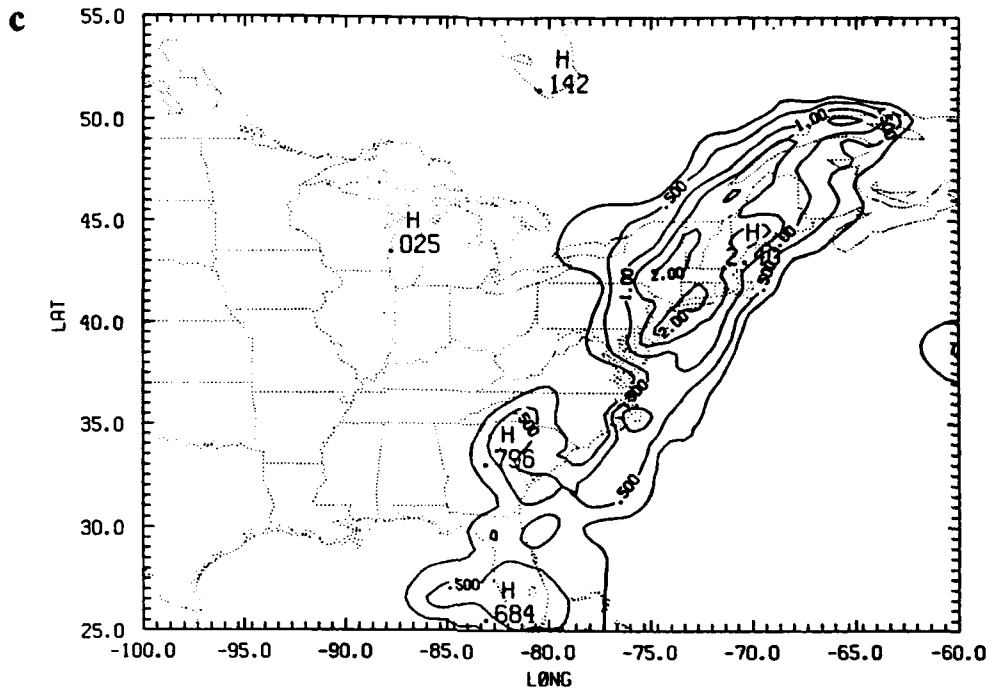


Figure 6.26. Continued.

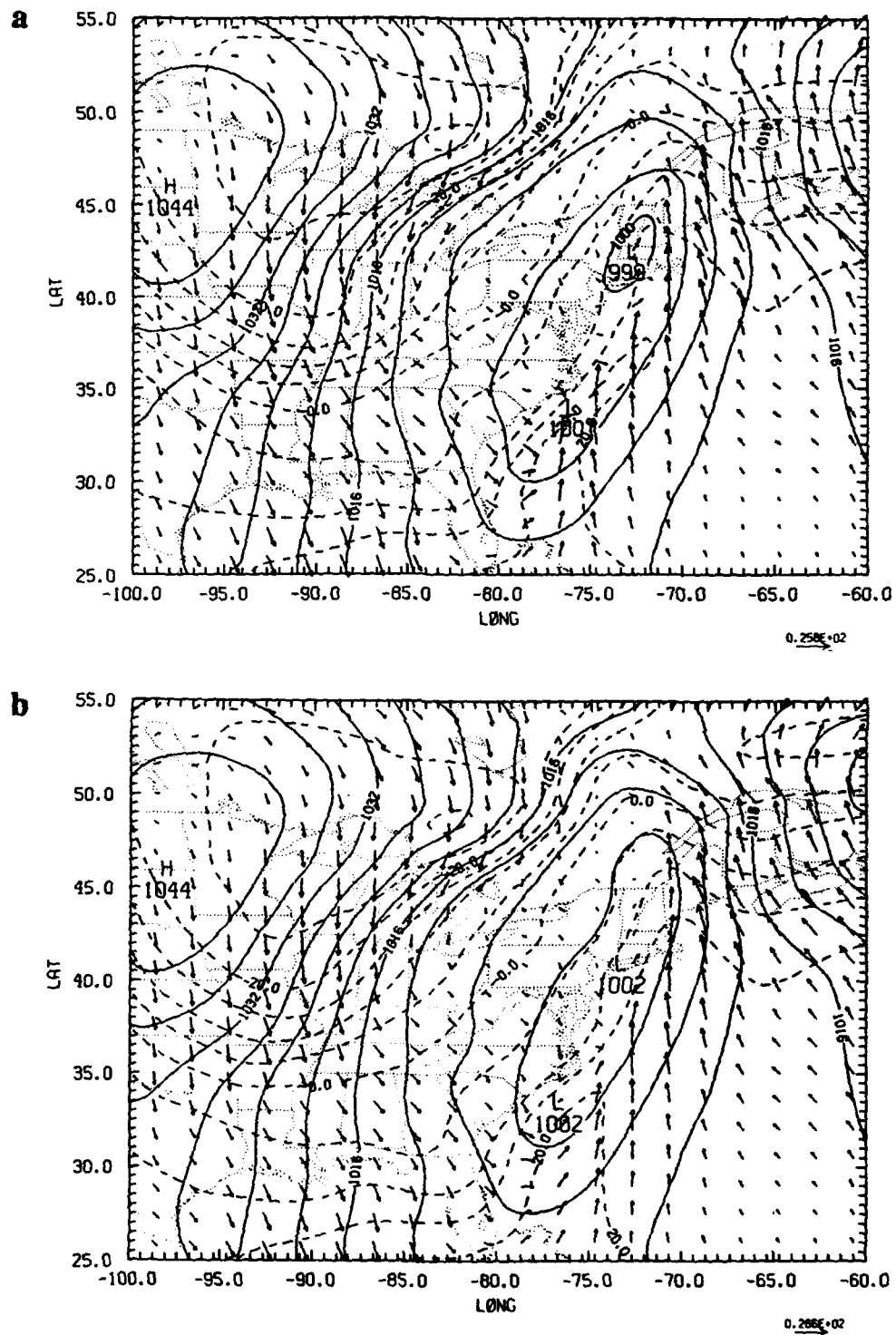


Figure 6.27. 12-h forecasts of sea-level pressure (mb) and 1000-mb temperature ( $^{\circ}\text{C}$ ) and wind valid at 27/00Z from (a) experiment 1 (no assimilation) and (b) experiment 4 (03DI), and 24-h forecasts valid at 27/12Z from (c) experiment 1 (no assimilation) and (d) experiment 4 (03DI).

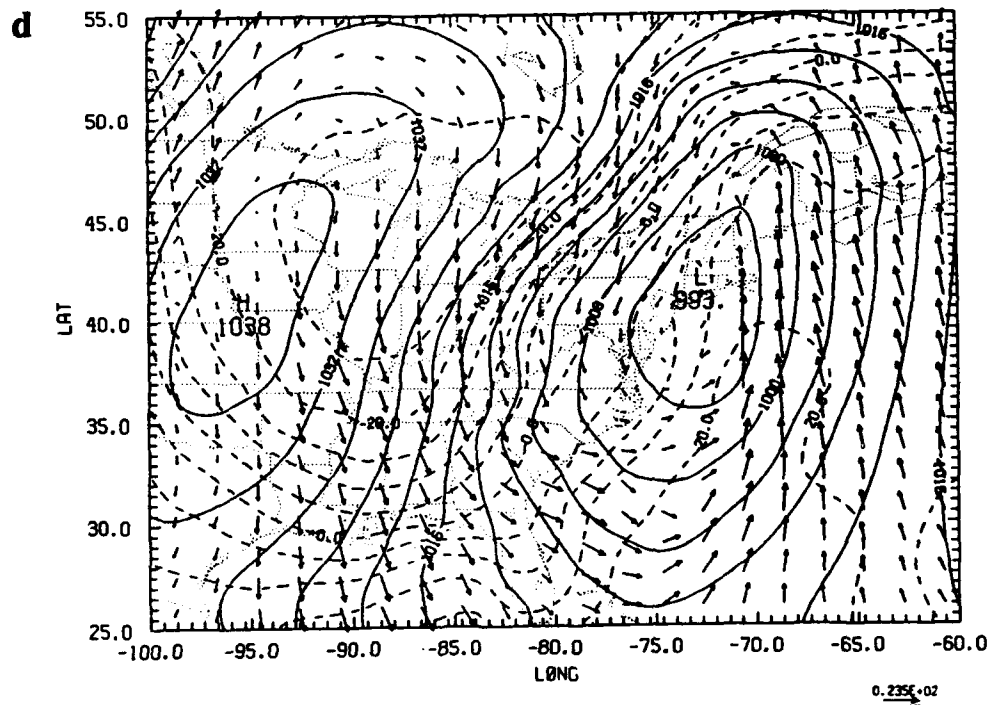
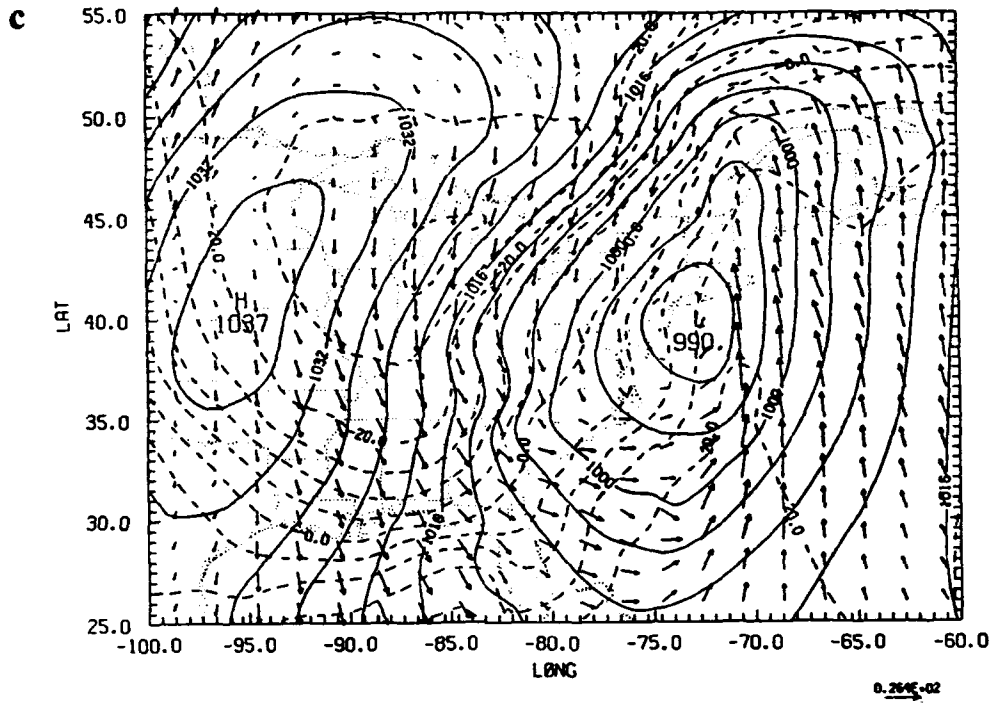


Figure 6.27. Continued.

consistency with the assimilated analyses than the control forecasts do with the NMC analyses.

## 7. CONCLUSIONS

Four-dimensional data-assimilation methodology has been applied to high-frequency observational data using a multivariate, successive correction objective analysis scheme, a diabatic vertical mode initialization procedure, and a fine-resolution mesoscale numerical weather prediction model. With only a limited number of iterations, the NRL/NCSU objective analysis scheme, based on Bratseth weighting functions, converges to the optimal interpolation solution. This scheme produces accurate analysis fields by using wind information to achieve gradients of geopotential through the geostrophic relationship. It is also successful in correcting the phase of the first-guess temperature field, improving the second-order fields of absolute vorticity and vertical motion, strengthening the first-guess upper-level jet, and resolving mesoscale circulations.

When diabatic vertical mode initialization is performed on these analysis fields, model spinup is reduced. With the inclusion of diabatic heating, which forces convective precipitation, the VMI retains the divergence, and therefore vertical motion, associated with the convection. This diabatic initialization procedure is used to initialize the background forecasts at each cycle of the assimilation process. Observed rainfall, coupled with "spunup" model rainfall, is used to derive three-dimensional heating fields. The method ensures temporal consistency of the diabatic heating rates by using rainfall rates which are time-centered (-3H to +3H) on the analysis/initialization valid time. This procedure also ensures that the heating rates in the initial integration of the subsequent assimilated background forecast are representative of the "observed" heating.

The performance of the assimilation system was evaluated by means of data-fitting statistics and subjective comparisons of assimilated states and subsequent forecasts. The

assimilated background forecast rms error for all analysis variables decreased significantly as the length of the update cycle shortened, i.e. as additional asynoptic, high-density GALE data were assimilated. The same was true for the analysis error of geopotential. This decrease in background and analysis error clearly shows that the inclusion of the 3-hourly GALE data had a positive impact on the assimilation. The analysis errors of the wind components and relative humidity varied little between the different experiments, due most likely to relatively large observational error in the wind and humidity. The background and analysis rms errors changed little when diabatic heating was included in the vertical mode initialization, suggesting that the inclusion or exclusion has minimal impact on the assimilation of these first-order variables. The assimilation with a 3-h update cycle revealed that the background forecast error generally increases as the period from the previous synoptic update to the current analysis/forecast cycle increases. With only small insertions of data at the asynoptic cycles (as compared to complete datasets at the synoptic hours), the effectual background forecast duration of successive update cycles increases between synoptic updates for geopotential.

A subjective evaluation of the assimilation system was conducted by comparing surface and 500-mb analyses and forecast fields. The analyses and subsequent forecasts from each of the assimilation experiments were consistently better than the "no assimilation" analyses (NMC analyses) and subsequent forecasts. A temporal consistency was achieved between the assimilated analyses and forecasts, which was not achieved without assimilation. Stronger thermal and moisture gradients and vertical motions were evident at the coastal front in the assimilated fields. There was less difference between the various assimilations which included the diabatic VMI. The surface analyses of pressure, wind, and temperature and vertical motion fields were generally very similar. However, the 03DI and 06DI lower- and upper-level moisture analyses showed some improvement over the 12DI analyses. Here, the inclusion of the

3-hourly GALE data made a positive impact on the moisture analyses. Excluding diabatic heating from the VMI (06AI) led to no noticeable detriment in the analyses of first order variables, but did result in weaker vertical velocities associated with the mesoscale circulation of the coastal front and upper-level jet streaks. This result is reasonable since vertical motion is directly related to diabatic heating.

A subjective verification of forecast 6-h accumulated precipitation was conducted. Precipitation verification is a valuable measure of the forecast "goodness" since rainfall is dependent on many complex physical processes; as a result, it is much more difficult to predict accurately than the other modelled variables. The forecast originating from the assimilated states verified reasonably well with the observed rainfall and were much better than the "no assimilation" forecasts, showing much faster spinup of forecast precipitation than did the control case. The assimilations with shorter update cycles (included asynoptic GALE data) led to slightly improved precipitation forecast as compared to the 12DI forecasts.

The results of this study show that the assimilation of GALE data in a mesoscale model is successful in producing significantly improved analyses and subsequent forecasts which are more consistent in time. The results also indicate that a small area of higher temporal data resolution can, when assimilated with high-resolution mesoscale prediction model, lead to improved assimilated states and better forecasts. However, the impact of the GALE data on the forecasts was generally greater when mesoscale circulations were important, such as in the interaction of the coastal front and the upper-level jet during the period prior to rapid cyclogenesis. When the large-scale synoptic system became dominant, the 3-hourly data had less impact in the subsequent forecasts.

In the present study, only diabatic heating associated with convective precipitation is considered. Future work should include the investigation of latent heating resulting from large-scale, non-convective rainfall. Also, forecast precipitation totals in areas of

strong convection were sometimes far from the observed amounts even when the 3-hourly GALE data were assimilated. The extremely small scale of the convective activity precluded our model from resolving these features. Work has begun to increase the model's horizontal and vertical resolutions and to include vertical accelerations. That is, the NRL/NCSU model will be converted to a 16-layer, non-hydrostatic model with horizontal grid spacing on the order of 5 to 10 km. Significant improvement in rainfall forecasts should result.

## 8. LIST OF REFERENCES

- Alaka, M. A., and R. C. Elvander, 1972: Optimum interpolation from observations of mixed quality. *Mon. Wea. Rev.*, **100**, 612-624.
- Andersen, J. H., 1977: A routine for normal mode initialization with non-linear correction for a multi-level spectral model with triangular truncation. ECMWF Internal Report No. 15, European Centre for Medium Range Weather Forecasts, Bracknell, U. K., 41 pp.
- Anthes, R. A., 1974: Data assimilation and initialization of hurricane prediction models. *J. Atmos. Sci.*, **31**, 702-719.
- , 1977: A cumulus parameterization scheme utilizing a one-dimensional cloud model. *Mon. Wea. Rev.*, **105**, 270-286.
- Arakawa, A., and V. R. Lamb, 1977: Computational design of the basic dynamical processes of the UCLA general circulation model. *Methods in Computational Physics*, Vol 17, General Circulation Models of the Atmosphere, J. Chang, Ed., Academic Press, New York, 173-265.
- Arkin, P. A., 1983: A diagnostic precipitation index from infrared satellite imagery. *Tropical Ocean - Atmosphere Newsletter*, **17**, 5-7. (Available from JISAO, U. of Washington, AK-40, Seattle, WA 98105).
- Baer, F., 1977: Adjustments of initial conditions required to suppress gravity oscillations in non-linear flows. *Beitr. Phys. Atmos.*, **50**, 350-366.
- Barnes, S.L., 1973: Mesoscale objective map analysis using weighted time-series observations. NOAA Technical Memorandum, ERL NSSL-62, Norman, OK, 60 pp.
- Bell, R. S., 1986: The Meteorological Office fine-mesh data assimilation scheme. *Meteor. Mag.*, **115**, 161-177.
- Belousov, S. L., L. S. Gandin, and S. A. Mashkovich, 1968: Computer processing of current meteorological data. *Hydrometeoizdat* [Meteor. Trans. No. 18, 1972. Canada Dept. of the Environment, Atmospheric Environment Service, Downsview, Ontario], 227 pp. (in Russian).
- Bengtsson, L., 1975a: Four-dimensional data assimilation of meteorological observations. GARP Publ. Ser., No. 15, WMO/ICSU, Geneva, 76 pp.
- , 1975b: Problems in four-dimensional data assimilation. *Seminars of Scientific Foundation of Medium Range Weather Forecasts, Part I*, Reading, September 1975, 113-138.

- , 1981: Current problems in four-dimensional data assimilation. *Data Assimilation Methods. ECMWF Seminar 1980*, 195-217. (Available from the European Centre for Medium Range Weather Forecasts, Shinfield Park, Reading RG29AX, England.)
- , 1985: Medium range forecasting at the ECMWF. *Adv. Geophys.*, **28B**, 3-56.
- , and J. Shukla, 1988: Integration of space and in situ observations to study global climate change. *Bull. Amer. Meteor. Soc.*, **69**, 1130-1143.
- Benjamin, S.G., 1989: An isentropic meso-scale analysis system and its sensitivity to aircraft and surface observations. *Mon. Wea. Rev.*, **117**, 1586-1603.
- , and N.L. Seaman, 1985: A simple scheme for objective analysis in curved flow. *Mon. Wea. Rev.*, **113**, 1184-1198.
- Bergthorsson, P., and B. R. Döös, 1955: Numerical weather map analysis. *Tellus*, **7**, 329-340.
- Bosart, L. F., 1988: Coastal frontogenesis and cyclogenesis during GALE IOP #2. Preliminary Reports, GALE/CASP Workshop, November 2-6 1987, Virginia Beach, VA, 75-93 (available from GALE Project Office, PO Box 3000, Boulder CO 80807).
- Bourke, W., and J. L. McGregor, 1983: A nonlinear vertical mode initialization scheme for a limited area prediction model. *Mon. Wea. Rev.*, **111**, 2285-2297.
- , R. Seaman, and K. Puri, 1985: Data assimilation. *Adv. Geophys.*, **28B**, 124-149.
- Bratseth, A. M., 1982: A simple and efficient approach to the initialization of weather prediction models. *Tellus*, **34**, 352-357.
- , 1986: Statistical interpolation by means of successive corrections. *Tellus*, **38A**, 439-447.
- Chang, S. W., 1981: Test of a planetary boundary-layer parameterization based on a generalized similarity theory in tropical cyclone models. *Mon. Wea. Rev.*, **109**, 843-853.
- , K. Brehme, R. Madala, and K. Sashegyi, 1989: A numerical study of the East Coast snow storm of February 10-12, 1983. *Mon. Wea. Rev.*, **117**, 1768-1778.
- Charney, J., M. Halem, and R. Jastrow, 1969: Use of incomplete historical data to infer the present state of the atmosphere. *J. Atmos. Sci.*, **26**, 1160-1163.
- Cressman, G., 1959: An operational objective analysis system. *Mon. Wea. Rev.*, **87**, 367-374.

- Daley, R., 1979: The application of non-linear normal mode initialization to an operational forecast model. *Atmos. Ocean*, **17**, 97-124.
- , 1981: Predictability experiments with a baroclinic model. *Atmos. Ocean*, **19**, 77-109.
- , 1991: *Atmospheric Data Analysis*. Cambridge University Press, Cambridge, 457 pp.
- , and K. Puri, 1980: Four dimensional data assimilation and the slow manifold. *Mon. Wea. Rev.*, **108**, 85-99.
- Davies, H. C., 1976: A lateral boundary formulation for multi-level prediction models. *Quart. J. Roy. Meteor. Soc.*, **102**, 405-418.
- , 1983: Limitations of some common lateral boundary schemes used in regional NWP models. *Mon. Wea. Mon.*, **111**, 1002-1012.
- , and R. E. Turner, 1977: Updating prediction models by dynamical relaxation: An examination of the technique. *Quart. J. Roy. Meteor. Soc.*, **103**, 225-245.
- Dickinson, R. E., and D. L. Williamson, 1972: Free oscillations of a discrete stratified fluid with application to numerical weather prediction. *J. Atmos. Sci.*, **29**, 623-640.
- DiMego, G. J., 1988: The National Meteorological Center regional analysis system. *Mon. Wea. Rev.*, **116**, 977-1000.
- , J. P. Gerrity, R. A. Petersen, and E. Rogers, 1989: Intermittent assimilation of emulated wind profiler data with the NMC Regional Data Assimilation System (RDAS). Preprints, 12th Conference on Weather Analysis and Forecasting, Amer. Meteor. Soc., Monterey, CA, October 2-6, 1989.
- Dirks, R. A., J. P. Kuettner, and J. A. Moore, 1988: Genesis of Atlantic Lows Experiment (GALE): An overview. *Bull. Amer. Meteor. Soc.*, **69**, 148-160.
- Dixon, R., 1976: An objective analysis system using orthogonal polynomials. GARP WGNE Report No. 11, 73-85. [Available from WMO, Geneva].
- , E. Spackman, I. Jones, and A. Francis, 1972: The global analysis of meteorological data using orthogonal polynomial base functions. *J. Atmos. Sci.*, **29**, 609-622.
- Donner, L. J., 1988: An initialization for cumulus convection in numerical weather prediction models. *Mon. Wea. Rev.*, **116**, 377-385.
- Doyle, J. D., and T. T. Warner, 1990: Mesoscale coastal processes during GALE IOP 2. *Mon. Wea. Rev.*, **118**, 283-308.
- Eddy, A., 1973: The objective analysis of atmospheric structure. *J. Meteor. Soc. Jpn.*, **51**, 450-457.

- Eliassen, A., 1954: Provisional report on calculation of spatial covariance and autocorrelation of the pressure field. Rept. No. 5, Institute of Weather and Climate Res., Academy of Science Oslo, 11 pp., (reprinted in *Dynamic Meteorology: Data Assimilation Methods*, L. Bengtsson, M. Ghil, and E. Kallen, Eds., Springer-Verlag, New York, 319-330).
- Errico, R. M., and P. J. Rasch, 1988: A comparison of various normal-mode initialization schemes and the inclusion of diabatic processes. *Tellus*, **40A**, 1-25.
- Flattery, T., 1971: Spectral models for global analysis and forecasting. *Proc. Sixth AWS Technical Exchange Conf.*, Air Weather Service Technical Report No. 242, 42-54.
- Gandin, L. S., 1963: Objective analysis of meteorological fields. *Hydrometeoizdat* (in Russian), English translation by Israel Program for Scientific Translations, Jerusalem, 1965, 242 pp. [Available from NTIS, as N66-18047].
- , 1988: Complex quality control of meteorological observations. *Mon. Wea. Rev.*, **116**, 1137-1156.
- Ghil, M., 1989: Meteorological data assimilation for oceanographers, Part I: Description and theoretical framework. *Dyn. of Atmos. and Oceans*, **13**, 171-218.
- , S. Cohn, J. Tavantzis, K. Bube, and E. Issacson, 1981: Applications of estimation theory to numerical weather prediction. *Dynamic Meteorology: Data Assimilation Methods*, L. Bengtsson, M. Ghil, and E. Kallen, Eds., Springer-Verlag, New York, 139-224.
- , M. Halem, and R. Atlas, 1979: Time-continuous assimilation of remote-sounding data and its effect on weather forecasting. *Mon. Wea. Rev.*, **107**, 140-171.
- Gilchrist, B., and G. P. Cressman, 1954: An experiment in objective analysis. *Tellus*, **6**, 97-101.
- Girard, C., and M. Jarraud, 1982: Short and medium range forecast differences between a spectral and grid point model: An extensive quasi-operational comparison. Tech. Rep. No. 32, European Centre for Medium Range Weather Forecasts, 176 pp. (Available from ECMWF, Shinfield Park, Reading, England).
- Gronas, S., A. Foss, and M. Lystad, 1987: Numerical simulations of polar lows in the Norwegian Sea. *Tellus*, **39A**, 334-353.
- , and K. H. Midtbo, 1986: Operational multivariate analyses by successive corrections. Collection of papers presented at WMO/TUGG numerical weather prediction symposium, Tokyo, 4-8 August 1986. *J. Meteor. Soc. Jpn.*, 61-74.
- Gustavsson, N., 1981: A review of methods for objective analysis. *Dynamic Meteorology: Data Assimilation Methods*, L. Bengtsson, M. Ghil, and E. Kallen, Eds., Springer-Verlag, New York, 17-76.

- Haltiner, G. J., and R. T. Williams, 1980: *Numerical Prediction and Dynamic Meteorology*. Second ed., John Wiley and Sons, New York, 477 pp.
- Harms, D. E., R. V. Madala, S. Raman, and K. D. Sashegyi, 1992a: Diabatic initialization experiments with convective heating. Submitted to *Meteor. and Atmos. Phys.*
- , S. Raman, and R. V. Madala, 1992b: An examination of four-dimensional data-assimilation techniques for numerical weather prediction. *Bull. Amer. Meteor. Soc.*, **73**, 425-440.
- , K. D. Sashegyi, R. V. Madala, and S. Raman, 1992c: Impact of assimilating 3-hourly GALE data using a mesoscale weather prediction model. Submitted to *Mon. Wea. Rev.*
- Hayden, C. M., 1976: Satellite reference level experiments with VTRR and the NMC global spectral analyses. GARP WGNE Report No. 11, 57-72. [Available from WMO, Geneva].
- Heckley, W. A., 1985: Systematic errors of the ECMWF operational forecasting model in tropical regions. *Quart. J. Roy. Meteor. Soc.*, **111**, 709-738.
- Hoke, J. E., and R. A. Anthes, 1976: The initialization of numerical models by a dynamical initialization technique. *Mon. Wea. Rev.*, **104**, 1551-1556.
- , and -----, 1977: Dynamic initialization of a three-dimensional primitive-equation model of Hurricane Alma of 1962. *Mon. Wea. Rev.*, **105**, 1266-1280.
- , N. A. Phillips, G. J. DiMego, J. J. Tuccillo, and J. G. Sela, 1989: The Regional Analysis and Forecast System of the National Meteorological Center. *Weather and Forecasting*, **4**, 323-334.
- Hollingsworth, A., 1986: Objective analysis for numerical weather prediction. *Short and Medium-Range Weather Prediction, Proc. WMO/IUGG NWP Symposium*, Tokyo, 11-59.
- , and P. Lonnberg, 1986: The statistical structure of short-range forecast errors as determined from radiosonde data. Part I: The wind field. *Tellus*, **38A**, 111-136.
- Holt, T., S. Chang, and S. Raman, 1990: A numerical study of the coastal cyclogenesis in GALE IOP 2: Sensitivity to PBL parameterizations. *Mon. Wea. Rev.*, **118**, 234-257.
- Jastrow, R., and M. Halem, 1970: Simulation studies related to GARP. *Bull. Amer. Meteor. Soc.*, **51**, 490-513.
- Juvanon du Vachat, R., 1986: A general formulation of normal modes for limited-area models: Application to initialization. *Mon. Wea. Rev.*, **114**, 2478-2487.
- Kalman, R. E., 1960: A new approach to linear filtering and prediction problems. *Trans. ASME, J. Basic Eng.*, **82D**, 35-45.

- , and R. S. Bucy, 1961: New results in linear filtering and prediction theory. *Trans. ASME, J. Basic Eng.*, **83D**, 95-108.
- Kanamitsu, M., 1989: Description of the NMC global data assimilation and forecast system. *Weather and Forecasting*, **4**, 335-342.
- Kao, C.-Y. J., and T. Yamada, 1988: Use of the CAPTEX data for evaluations of a long-range transport numerical model with a four-dimensional data assimilation technique. *Mon. Wea. Rev.*, **116**, 293-306.
- Kasahara, A., R. C. Balgovind, and B. B. Katz, 1988: Use of satellite radiometric imagery data for improvement in the analysis of divergent wind in the tropics. *Mon. Wea. Rev.*, **116**, 866-883.
- Kistler, R. E., 1974: A study of data assimilation techniques in an autobarotropic primitive equation channel model. M. S. thesis, The Pennsylvania State University, 84 pp.
- , and R. D. McPherson, 1975: On the use of a local wind correction technique in four-dimensional data assimilation. *Mon. Wea. Rev.*, **103**, 445-449.
- Kitade, T., 1983: Nonlinear normal mode initialization with physics. *Mon. Wea. Rev.*, **111**, 2194-2213.
- Koch, S. E., M. DesJardins, and P. J. Kocin, 1983: An interactive Barnes objective map analysis scheme for use with satellite and conventional data. *J. Clim. Appl. Meteor.*, **22**, 1487-1503.
- Kreiss, H.-O., 1979: Problems with different time scales for ordinary differential equations. *SIAM J. Num. Anal.*, **16**, 980-998.
- Krishnamurti, T. N., H. S. Bedi, W. Heckley, and K. Ingles, 1988: Reduction of the spinup time for evaporation and precipitation in a spectral model. *Mon. Wea. Rev.*, **116**, 907-920.
- Kuo, H.-L., 1974: Further studies of the influence of cumulus convection on large-scale flow. *J. Atmos. Sci.*, **31**, 1232-1240.
- Kuo, Y.-H., and Y.-R. Guo, 1989: Dynamic initialization using observations from a network of profilers. *Mon. Wea. Rev.*, **117**, 1975-1998.
- Lange, A., and E. Hellsten, 1986: Results of the WMO/CAS NWP data study and intercomparison project for forecasts for the Northern Hemisphere in 1981-82. WMO Short- and Medium-Range Weather Prediction Research, Publication Series No. 2, WMO, Geneva.
- Lejenas, H., 1980: On the influence of the technique of nonlinear normal mode initialization on the nonconvective precipitation rate. *Mon. Wea. Rev.*, **108**, 1465-1468.

- Lewis, J. M., 1972: An operational upper air analysis using the variational method. *Tellus*, **24**, 514-530.
- , and J. C. Derber, 1985: The use of adjoint equations to solve a variational adjustment problem with advective constraints. *Tellus*, **37A**, 309-322.
- Lorenc, A., 1981: A global three-dimensional multivariate statistical interpolation scheme. *Mon. Wea. Rev.*, **109**, 701-721.
- , 1985: Analysis methods for the quality control of observations. *Workshop on the Use and Quality Control of Meteorological Observations*, Reading, U. K., European Centre for Medium Range Weather Forecasts, 397-428.
- , 1986: Analysis methods for numerical weather prediction. *Quart. J. Roy. Meteor. Soc.*, **112**, 1177-1194.
- , 1988: A practical approximation to optimal four-dimensional objective analysis. *Mon. Wea. Rev.*, **116**, 730-745.
- , R. S. Bell, and B. MacPherson, 1991: The Meteorological Office analysis correction data assimilation scheme. *Quart. J. Roy. Meteor. Soc.*, **117**, 59-89.
- , and O. Hammon, 1988: Objective quality control of observations using Bayesian methods. Theory and a practical implementation. *Quart. J. Roy. Meteor. Soc.*, **114**, 515-543.
- , I. Rutherford, and G. Larsen, 1977: The ECMWF analysis and data assimilation scheme--Analysis of mass and wind fields. European Centre for Medium-Range Weather Forecasts, Reading, Berkshire, U. K., Tech. Rep. No. 6.
- Lorenz, E. N., 1982: Atmospheric predictability experiments with a large numerical model. *Tellus*, **34**, 505-513.
- Lynch, P., 1985a: Initialization using Laplace transforms. *Quart. J. Roy. Meteor. Soc.*, **111**, 243-258.
- , 1985b: Initialization of a barotropic limited-area model using the Laplace transform technique. *Mon. Wea. Rev.*, **113**, 1338-1344.
- , 1991: Filtering integration schemes based on the Laplace and Z- transforms. *Mon. Wea. Rev.*, **119**, 653-666.
- Lyne, W. H., R. Swinbank, and N. T. Birch, 1982: A data assimilation experiment and the global circulation during the FGGE special observing periods. *Quart. J. Roy. Meteor. Soc.*, **108**, 575-594.
- Machenhauer, B., 1977: On the dynamics of gravity oscillations in a shallow water model with applications to normal mode initialization. *Beitr. Phys. Atmos.*, **50**, 253-271.

- Madala, R. V., 1981: Efficient time integration schemes for atmosphere and ocean models. *Finite Difference Techniques for Vectorized Fluid Dynamic Calculations*, Chpt. 4, Springer Verlag, pp 56-74.
- , S. W. Chang, U. C. Mohanty, S. C. Madan, R. K. Paliwal, V. B. Sarin, T. Holt, and S. Raman, 1987: Description of the Naval Research Laboratory Limited Area Dynamical Weather Prediction Model. NRL Memorandum Report, No. 5992, Naval Research Laboratory, Washington, D.C., 131 pp.
- Manabe, S., J. Smagorinsky, and R.F. Strickler, 1965: Simulated climatology of a general circulation model with a hydrologic cycle. *Mon. Wea. Rev.*, **93**, 769-798.
- Martin, D. W., B. Auvine, and B. Hinton, 1988: Atlantic Ocean Rain Maps for GALE. Report on Contract NAG5-742, Space Science and Engineering Center, Madison, WI 53706, 98 pp.
- McPherson, R. D., 1975: Progress, problems, and prospects in meteorological data assimilation. *Bull. Amer. Meteor. Soc.*, **56**, 1154-1166.
- , 1976: Operational objective analysis techniques and potential applications for mesoscale meteorology. *Mesoscale Meteorology and Forecasting*, P. S. Ray, Ed., Amer. Meteor. Soc., Boston, 151-172.
- Mercer, T. J., 1987: Genesis of Atlantic Lows Experiment (GALE): Data Users Guide. Available from GALE Data Center, Department of Physics and Atmospheric Science, Drexel University, Philadelphia, PA, 19104.
- , T. J., and C. W. Kreitzberg, 1986: Genesis of Atlantic Lows Experiment (GALE): Field Program Summary. Available from GALE Data Center, Department of Physics and Atmospheric Science, Drexel University, Philadelphia, PA, 19104.
- Mills, G. A., and R. S. Seaman, 1990: The BMRC regional data assimilation system. *Mon. Wea. Rev.*, **118**, 1217-1237.
- Miyakoda, K., and R. Moyer, 1968: A method of initialization for dynamical weather forecasting. *Tellus*, **20**, 115-128.
- , R. F. Stricker, and J. Chludinsky, 1978: Initialization with the data assimilation method. *Tellus*, **30**, 32-54.
- Mohanty, U. C., A. Kasahara, and R. Errico, 1986: The impact of diabatic heating on the initialization of a global forecast model. *J. Meteor. Soc. Jpn.*, **64**, 805-817.
- Morel, P., 1981: An overview of meteorological data assimilation. *Dynamic Meteorology: Data Assimilation Methods*, L. Bengtsson, M. Ghil, and E. Kallen, Eds., Springer-Verlag, New York, 5-16.
- , and O. Talagrand, 1974: Dynamic approach to meteorological data assimilation. *Tellus*, **26**, 334-344.

- Panofsky, H., 1949: Objective weather map analysis. *J. Meteor.*, **6**, 386-392.
- Petersen, D. P., 1968: On the concept and implementation of sequential analysis for linear random fields. *Tellus*, **20**, 673-686.
- Phillips, N. A., 1957: A coordinate system having some special advantages for numerical forecasting. *J. of Meteor.*, **14**, 184-185.
- , 1976: The impact of synoptic observing and analysis systems on flow pattern forecasts. *Bull. Amer. Meteor. Soc.*, **57**, 1225-1250.
- Puri, K., 1987: Some experiments on the use of tropical diabatic heating information for initial state specification. *Mon. Wea. Rev.*, **115**, 1394-1406.
- , and W. Bourke, 1982: A scheme to retain the Hadley circulation during nonlinear normal mode initialization. *Mon. Wea. Rev.*, **110**, 327-335.
- , and M. J. Miller, 1990: The use of satellite data in the specification of convective heating for diabatic initialization and moisture adjustment in numerical weather prediction models. *Mon. Wea. Rev.*, **118**, 67-93.
- Ramamurthy, M. K., and F. H. Carr, 1987: Four-dimensional data assimilation in the monsoon region, Part I: Experiments with wind data. *Mon. Wea. Rev.*, **115**, 1678-1706.
- Raman, S., and A.J. Riordan, 1988: Genesis of Atlantic Lows Experiment: The Planetary-Boundary-layer subprogram of GALE. *Bull. Amer. Meteor. Soc.*, **69**, 161-172.
- Reynolds, R.W., 1982: A monthly averaged climatology of sea surface temperatures. NOAA Technical Report, NWS-31, Climate Analysis Center, National Weather Service, Washington, D.C., 35pp.
- Riordan, A. J., 1990: Examination of the mesoscale features of the GALE coastal front of 25-26 January 1986. *Mon. Wea. Rev.*, **118**, 258-282.
- Robinson, A. R., 1986: Data assimilation, mesoscale dynamics and dynamical forecasting. *Advanced Physical Oceanographic Numerical Modelling*, J. J. O'Brien, Ed., D. Reidel Pub. Co., 465-483.
- Rodgers, E., G. J. DiMego, J. P. Gerrity, R. A. Petersen, B. D. Schmidt, and D. M. Kann, 1990: Preliminary experiments using GALE observations at the National Meteorological Center. *Bull. Amer. Meteor. Soc.*, **71**, 319-333.
- Rutherford, I. D., 1972: Data assimilation by statistical interpolation of forecast error fields. *J. Atmos. Sci.*, **29**, 809-815.
- , 1976: An operational three-dimensional multivariate objective analysis scheme. *Proc. GARP Conf. on Four Dimensional Data Assimilation*, Paris, GARP WGNE Rep. No. 11, 98-121.

- Sasaki, Y., 1958: An objective analysis based on the variational method. *J. Meteor. Soc. Jpn.*, **36**, 77-88.
- , 1969: Proposed inclusion of time variation terms, observational in numerical variational objective analysis. *J. Meteor. Soc. Jpn.*, **47**, 115-124.
- Sashegyi, K. D., D. E. Harms, R. V. Madala, and S. Raman, 1992: Application of the Bratseth scheme for the analysis of GALE data using a mesoscale model. Conditionally accepted for publication in *Mon. Wea. Rev.*
- , and R. V. Madala, 1990: Tests of initialization procedures with the NRL limited area numerical weather prediction model. NRL Memorandum Report 6648, Washington, D. C., 88 pp.
- , and -----, 1992a: Application of vertical mode initialization to a limited area model in flux form. *Mon. Wea. Rev.* (in press).
- , and -----, 1992b: Test of a nested mesoscale model for the case of the development of an extratropical cyclone during GALE. Technical Memorandum Report, Naval Research Laboratory, Washington D.C.
- Satomura, I., 1988: Dynamic normal mode initialization of a limited-area model. *J. Meteor. Soc. Jpn.*, **66**, 261-276.
- Saucier, W. J.; 1955: *Principles of Meteorological Analysis*. The University of Chicago Press. Chicago, 438 pp. (p 56-59).
- Schlatter, T. W., 1988: Past and present trends in the objective analysis of meteorological data for nowcasting and numerical forecasting. Preprints, 8th Conference on Numerical Weather Prediction, Amer. Meteor. Soc., Feb 22-26, Baltimore, MD, J9-J25.
- Seaman, R. S., 1988: Some real data tests of the interpolation accuracy of Bratseth's successive correction method. *Tellus*, **40A**, 173-176.
- Shaw, D. B., P. Lonnerberg, A. Hollingsworth, and P. Uden, 1987: Data assimilation: The 1984/85 revisions of the ECMWF mass and wind analysis. *Quart. J. Roy. Meteor. Soc.*, **113**, 533-566.
- Shi, J. J., S. Chang, K. Sashegyi, and S. Raman, 1991: Enhancement of objective analysis of hurricane Florence (1988) with dropsonde data. Preprints, 19th Conference on Hurricanes and Tropical Meteorology, Amer. Meteor. Soc., May 6-10, Miami, FL, 335-337.
- Smagorinsky, J., K. Miyakoda, and R. Strickler, 1970: The relative importance of variables in initial conditions for dynamical weather prediction. *Tellus*, **22**, 141-157.

- Stauffer, D. R., and N. L. Seaman, 1987: A real-data numerical study and four-dimensional data assimilation application for mesobeta-scale flow in complex terrain. *Proc. Symp. Mesoscale Analysis and Forecasting*, Vancouver, ESA, 533-538.
- , and -----, 1990: Use of four-dimensional data assimilation in a limited-area mesoscale model, Part I: Experiments with synoptic-scale data. *Mon. Wea. Rev.*, **118**, 1250-1277.
- , T. T. Warner, and N. L. Seaman, 1985: A Newtonian "nudging" approach in four-dimensional data assimilation: Use of SESAME-IV data in a mesoscale model. *Preprints, Seventh Conf. on Numerical Weather Prediction*, Montreal, Amer. Meteor. Soc., 77-82.
- Stephens, J., 1970: Variational initialization of the balance equation. *J. Appl. Meteor.*, **9**, 732-739.
- Sugi, M., 1986: Dynamic normal mode initialization. *J. Meteor. Soc. Jpn.*, **64**, 623-632.
- Temperton, C., 1984: Orthogonal vertical modes for a multilevel model. *Mon. Wea. Rev.*, **112**, 503-509.
- , 1988: Implicit normal mode initialization. *Mon. Wea. Rev.*, **116**, 1013-1031.
- , and D. L. Williamson, 1981: Normal mode initialization for a multilevel grid-point model, Part I: Linear aspects. *Mon. Wea. Rev.*, **109**, 729-743.
- Turpeinen, O. M., L. Garand, R. Benoit, and M. Roch, 1990: Diabatic initialization of the Canadian Regional Finite-Element (RFE) model using satellite data. Part I: Methodology and application to a winter storm. *Mon. Wea. Rev.*, **118**, 1381-1395.
- Uccellini, L. W., and P. J. Kocin, 1987: The interaction of jet streak circulations during heavy snow events along the east coast of the United States. *Weather and Forecasting*, **2**, 289-308.
- , -----, R.A. Petersen, C. H. Wash, and K. F. Brill, 1984: The Presidents' Day cyclone of 18-19 February 1979: Synoptic overview and analysis of the subtropical jet streak influencing the pre-cyclogenetic period. *Mon. Wea. Rev.*, **112**, 31-55.
- Wang, W., and T. T. Warner, 1988: Use of four-dimensional data assimilation by Newtonian relaxation and latent heat forcing to improve a mesoscale-model precipitation forecast, a case study. *Mon. Wea. Rev.*, **116**, 2593-2613.
- Warner, T. T., 1987: Four-dimensional initialization of mesoscale models. *Proc. Symp. Mesoscale Analysis and Forecasting*, Vancouver, Canada, 17-19 August 1987, ESA SP-282, pp. 663-665.

- Wergen, W., 1982: Incorporation of diabatic effects in non-linear normal mode initialization. In *The GARP Programme on Numerical Experimentation*, Rep. No. 3, GARP/WCRP, WMO/ICSU, Geneva, pp. 2.8-2.10.
- , 1983: Initialization. Interpretation of Numerical Weather Prediction Products, ECMWF Seminar/Workshop 1982, 31-57. (Available from the European Centre for Medium Range Weather Forecasts; Shinfield Park, England RG29AX, England.)
- , 1987: Diabatic nonlinear normal mode initialization for a spectral model with a hybrid vertical coordinate. ECMWF Technical Report No. 59, ECMWF, 83 pp.
- Williamson, D. L., and C. Temperton, 1981: Normal mode initialization for a multilevel grid-point model. Part II: Nonlinear aspects. *Mon. Wea. Rev.*, **109**, 744-757.
- Wolcott, S. W., and T. T. Warner, 1981: A humidity initialization utilizing surface and satellite data. *Mon. Wea. Rev.*, **109**, 1989-1998.
- Yamada, T., 1976: On the similarity functions A, B and C of the planetary boundary layer. *Mon. Wea. Rev.*, **33**, 781-793.
- , 1979: PBL similarity profiles determined from a level-2 turbulence-closure model. *Bound. Layer Meteor.*, **17**, 333-351.